SUPRAMOLECULAR ASSEMBLY, CHIRALITY, AND ELECTRONIC PROPERTIES OF RUBRENE STUDIED BY STM AND STS

THÈSE N^{O} 3487 (2006)

PRÉSENTÉE LE 24 MARS 2006

À LA FACULTÉ SCIENCES DE BASE

Laboratoire de physique des surfaces

SECTION DE PHYSIQUE

ÉCOLE POLYTECHNIQUE FÉDÉRALE DE LAUSANNE

POUR L'OBTENTION DU GRADE DE DOCTEUR ÈS SCIENCES

PAR

Marie-Christine BLÜM

Dipl.Phys., Rheinische Friedrich-Wilhelms-Universität, Bonn, Allemagne
et de nationalité allemande

acceptée sur proposition du jury:

Dr G. Gremaud, président du jury
Prof. W.-D. Schneider, directeur de thèse
Dr K.-H. Ernst, rapporteur
Prof. J.I. Pascual, rapporteur
Prof. R. Raval, rapporteur

ÉCOLE POLYTECHNIQUE
FÉDÉRALE DE LAUSANNE

Lausanne, EPFL
2006

SUPRAMOLECULAR ASSEMBLY, CHIRALITY, AND ELECTRONIC PROPERTIES OF RUBRENE STUDIED BY STM AND STS

Thèse présentée à la faculté sciences de base, section de physique
École Polytechnique Fédérale de Lausanne, Suisse

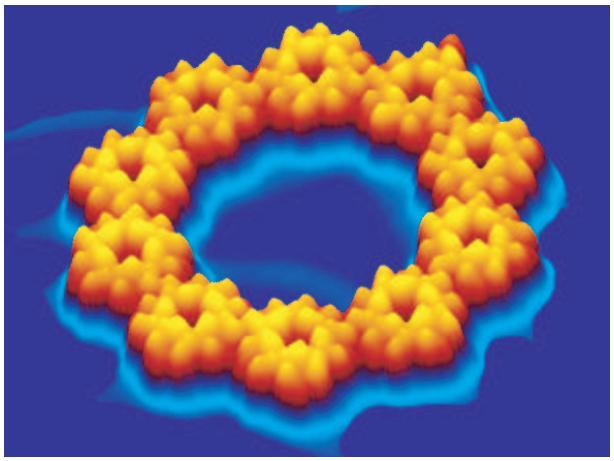

by

Marie-Christine BLÜM

Directeur de thèse:	Prof. W.-D. Schneider
Président du jury:	Dr. G. Grémaud
Rapporteurs:	Dr. K.-H. Ernst
	Prof. J. I. Pascual
	Prof. R. Raval

Contents

Abstract

This thesis presents the first experimental results of a scanning tunneling microscopy (STM) and scanning tunneling spectroscopy (STS) investigation of rubrene at the supramolecular, molecular and submolecular level. Based on its semiconducting and fluorescent properties, this molecule is of particular interest in view of the emerging fields of molecular electronics and optoelectronics which could one day replace the conventional technology relying on semiconductors such as silicon and gallium arsenide. The goal is the substitution of these inorganic materials by cheap and flexible layers of semiconducting organic molecules for a new class of diodes and transistors, as well as the realization of electronic switches based on individual molecules. One fundamental approach is to take advantage of the molecular self-assembly behavior which results in the creation of well-ordered supramolecular structures.

The investigations of the self-assembly of rubrene adsorbed on metal surfaces (Au(111), Au(100), Ag(111), and Ag(100)), which were carried out within the framework of this thesis, show a surprising diversity of supramolecular structures. Amongst other shapes, the molecules organize themselves into geometries of perfect hexagonal and pentagonal symmetry and create multifaceted patterns on the surface. A fascinating peculiarity consists in the spontaneous construction of nested structures which are built up by a hierarchical self-assembly of individual molecules into pentagonal supermolecules which form in a second step perfect supramolecular decagons.

The geometric shape of rubrene is characterized by a structural asymmetry leading to the existence of two mirror imaged versions of the molecule which are not superimposable to each other, such as for instance our left and right hand or the helical DNA. The aspect of chirality is crucial for basic processes in living systems and calls for a fundamental understanding of the interaction mechanisms occurring between chiral molecules. The experiments on rubrene reveal that the intermolecular bonding differentiates between the two chiral types of the molecule (chiral recognition), yielding the self-organization into homochiral structures. These assemblies exhibit a geometry which is again chiral, demonstrating a propagation of chirality throughout the three stages of the supramolecular hierarchy.

The semiconducting behavior of rubrene is furthermore probed by STS measurements detecting the energetic positions of the highest occupied molecular orbital (HOMO) and the lowest unoccupied molecular orbital (LUMO). The experimental data uncover that different adsorption conformations exhibit characteristic HOMO energies and reveal adsorption conformations of rubrene which preserve the intrinsic electronic structure of the free molecule. Furthermore, a switching of the molecular conformation and the electronic structure of one rubrene conformer is induced with the STM.

Keywords: Scanning tunneling microscopy (STM), scanning tunneling spectroscopy (STS), rubrene, molecular adsorption, self-assembly, supramolecular structures, chirality, chiral recognition, highest occupied molecular orbital (HOMO), lowest unoccupied molecular orbital (LUMO)

Version abrégée

Ce travail de thèse présente les premiers résultats expérimentaux de mesures par microscopie à effet tunnel (STM) et spectroscopie tunnel (STS) du rubrène à l'échelle nanométrique. Cette molécule est d'un intérêt particulier pour les domaines émergeants que sont l'électronique moléculaire et l'optoélectronique grâce à ses propriétés semiconductrices et fluorescentes. Ces technologies pourraient un jour remplacer les procédés traditionnels basés sur le silicium et l'arséniure de gallium; le but étant de substituer à ces matières inorganiques des films flexibles et bons marchés de matières semiconductrices organiques. Cela permettrait la création de nouveaux types de diodes et transistors ainsi que d'interrupteurs moléculaires. Dans ce sens, une approche est d'utiliser les capacités d'autoassemblage afin d'obtenir des structures supramoléculaires ordonnées.

L'étude de l'autoassemblage du rubrène sur des surfaces métalliques (Au(111), Au(100), Ag(111) et Ag(100)) effectuée dans le cadre de cette thèse montre une diversité surprenante de structures supramoléculaires. Entre autres, les molécules se lient en des symétries hexagonales et pentagonales parfaites et forment de multiples dessins sur la surface. Une particularité fascinante est la création spontanée de structures imbriquées. Celles-ci sont formées par l'assemblage hiérarchique de molécules individuelles en pentagones puis de ces supermolécules en décagones supramoléculaires.

La forme géométrique du rubrène se caractérise par une asymétrie de structure donnant lieu à deux versions de la molécule, images miroirs l'une de l'autre, qui ne sont pas superposables. Nos mains ainsi que l'hélice de l'ADN sont des exemples courants possédant cette propriété. La chiralité est un aspect crucial des processus en jeu dans le vivant, ce qui motive la compréhension des mécanismes d'interaction entre molécules chirales. Les expériences sur le rubrène montre que les liens intermoléculaires distinguent les deux types de chiralités de la molécule (reconnaissance chirale) aboutissant à l'autoorganisation en des structures homochirales. Ces assemblages ont une chiralité propre démontrant la propagation de chiralité à travers les trois niveaux de la hiérarchie supramoléculaire.

Le comportement semiconducteur du rubrène a été étudié par des mesures STS qui ont permis de détecter la position énergétique de la plus haute orbitale moléculaire occupée (HOMO) ainsi que de l'orbitale moléculaire vacante la plus basse (LUMO). Les données expérimentales montrent que les différentes conformation d'adsorbtion présentent des énergies de HOMO caractéristiques. Ces mesures spectroscopiques révèlent que certaines conformations du rubrène laissent leur structure électronique intrinsèque essentiellement non perturbée. De plus, un changement de conformation et de la structure électronique a été induit par STM.

Mots clés: Microscopie à effet tunnel (STM), spectroscopie à effet tunnel (STS), rubrène, adsorption moléculaire, autoassemblage, structures supramoléculaires, chiralité, reconnaissance chirale, plus haute orbitale moléculaire occupée (HOMO), orbitale moléculaire vacante la plus basse (LUMO)

Kurzfassung

Diese Doktorarbeit stellt die ersten experimentellen Ergebnisse einer Studie mittels Rastertunnelmikroskopie (STM) und Rastertunnelspektroskopie (STS) von Rubren im Nanobereich vor. Das Molekül ist aufgrund seiner halbleitenden und fluoreszierenden Eigenschaften von besonderem Interesse im Hinblick auf die neu entstehenden Gebiete der molekularen Elektronik und Optoelektronik, die eines Tages die auf Halbleitern wie zum Beispiel Silizium und Galliumarsenid basierende konventionelle Technologie ersetzen könnten. Als Ziel wird der Ersatz dieser anorganischen Materialien durch billige und flexible Schichten von halbleitenden organischen Molekülen angestrebt, um einen neuen Typ von Dioden und Transistoren zu bauen, sowohl als auch die Realisierung von auf einzelnen Molekülen basierenden elektronischen Schaltern. Ein grundlegender Ansatz besteht darin, die molekulare Selbstorganisation auszunutzen, die zur Bildung von geordneten supramolekularen Strukturen führt.

Die im Rahmen dieser Doktorarbeit durchgeführten Untersuchungen der Selbstorganisation von Rubren, das auf Metalloberflächen (Au(111), Au(100), Ag(111) und Ag(100)) adsorbiert wird, zeigen eine überraschende Vielfalt von supramolekularen Strukturen. Die Moleküle organisieren sich unter anderem in Strukturen von perfekter hexagonaler und pentagonaler Symmetrie und bilden vielseitige Muster auf der Oberfläche. Eine faszinierende Besonderheit besteht in der spontanen Erzeugung von verschachtelten Strukturen, die durch eine hierarchisch aufgebaute Selbstorganisation von einzelnen Molekülen zu Supermolekülen entstehen, die sich anschließend zu supramolekularen Zehnecken verbinden.

Die geometrische Form von Rubren ist gekennzeichnet durch eine strukturelle Asymmetrie, die zu einem Vorhandensein von zwei spiegelbildlichen, nicht deckungsgleichen, Molekülvarianten führt, wie zum Beispiel unsere linke und rechte Hand oder die spiralförmige DNA. Der Aspekt der Chiralität (Händigkeit) ist äußerst wichtig für grundlegende Prozesse der biologischen Welt und erfordert ein fundamentales Verständnis der Interaktionsmechanismen, die zwischen chiralen Molekülen stattfinden. Die Experimente mit Rubren zeigen, dass bei der Bildung von intermolekularen Bindungen zwischen den beiden Chiralitätsformen des Moleküls unterschieden wird (chirale Erkennung), was dazu führt, dass die Moleküle supramolekulare Strukturen bilden, die ausschließlich eine Chiralität beinhalten. Die Geometry dieser Anordnungen ist wiederum chiral, womit die Chiralität einer Stufe der supramolekularen Hierarchie von der vorherigen bestimmt wird (Induktion von Chiralität).

Die halbleitenden Eigenschaften von Rubren wurden des Weiteren mit Hilfe von STS untersucht, die die energetische Position des höchsten besetzten Molekülorbitals (HOMO) und des niedrigsten unbesetzten Molekülorbitals (LUMO) bestimmt. Die experimentellen Daten zeigen, dass die unterschiedlichen Adsorptionskonformationen, die die Moleküle auf der Oberfläche einnehmen, verschiedene Energien des HOMOs aufweisen. Diese spektroskopischen Messungen zeigen Adsorptionskonformationen von Rubren, die die spezifische elektronische Struktur des freien Moleküls bewahren. Zusätzlich wurde ein Umschalten der geometrischen und elektronischen Struktur von einem Rubrenkonformer zu einem anderen mittels STM induziert.

Schlüsselwörter: Rastertunnelmikroskopie (STM), Rastertunnelspektroskopie (STS), Rubren, molekulare Adsorption, Selbstorganisation, supramolekulare Strukturen, Chiralität, chirale Erkennung, höchstes besetztes Molekülorbital (HOMO), niedrigstes unbesetztes Molekülorbital (LUMO)

Un grand merci...

au Prof. Wolf-Dieter Schneider qui m'a offert la possibilité de travailler dans son excellent groupe de recherche et qui m'a laissé la liberté de choisir un sujet fascinant

*

aux membres du jury: Dr. Karl-Heinz Ernst, Prof. Jose Ignatio Pascual et Prof. Rasmita Raval qui ont accepté la tâche de juger cette thèse

*

aux gens qui étaient toujours au laboratoire pour m'aider: Dr. François Patthey, Jean-François Jeanneret et en particulier Dr. Marina Pivetta qui a partagé avec moi une grande partie du travail au laboratoire

*

à mes collègues qui ont partagé les soucis et les joies qu'impliquent le travail expérimental et la préparation d'une thèse: Elizabeta, Hans-Christoph qui a lu attentivement ce manuscript et Markus, en particulier pour les discussions concernant la spectroscopie

*

à Gil Felley pour ses cours de taïzo et à Jean Lechim pour ses cours de yoga qui sont devenus les joyaux de la semaine

*

à Inès, d'avoir été une colocataire parfaite

*

aux amis qui m'ont accompagnés pendant ces quatres ans à Lausanne: Céline, Horace, Ilaria, Jessen, Kiko, Maxime et Nicolas pour les belles soirées et des longues heures de discussion

*

à tous ceux avec lesquels j'ai passé des nombreux bons moments en montagne, à des fêtes ou à d'autres soirées

*

à mes amis loin de la Suisse: Andrea, Axel, Cédric, Steffi et Markus qui me sont restés proches malgré la distance

*

à Maik pour son enthousiasme et ses idées

*

à M. et Mme Buluschek pour leur chaleureux accueil et les fruits de leur jardin

*

à mes parents, ma sœur Béatrix, mon frère Jean-Christian et ma grand-mère pour leur amour et leur soutien

*

et avant tout à Philipp pour son amour et le bonheur qu'on vit ensemble

* * *

à Grand-Père et à Oma

pour leur affection et leur estime qu'ils m'ont témoigné

Chapter 1

Introduction

1.1 Outline of the thesis

The aim of this thesis is the investigation of the geometric and electronic properties of individual and self-assembled rubrene ($C_{42}H_{28}$) molecules which are adsorbed on different metal surfaces. The experiments are performed with a scanning tunneling microscope (STM) [1, 2] operated in ultrahigh vacuum (UHV) and at low temperatures, allowing for a study of single molecules with submolecular resolution. The first molecules observed with the STM were phthalocyanine [3] and benzene [4] in 1987 and 1988. Since then, a great variety of molecules of different sizes have been studied, analyzing the intramolecular structure, the adsorption conformation and the supramolecular self-assembly [5, 6].

Considering chiral molecules, the latter aspect becomes of particular importance in view of the continuous quest for methods to separate the two chiral forms of the molecule present in a chiral mixture. The mirror-imaged stereoisomers (enantiomers) often exhibit different functionalities, especially inside of the human body which provoked dramatic consequences in the case of the drug thalidomide in the early sixties [7]. Starting with the first determination of the chirality of individual molecules in 1998 [8, 9], the study of the supramolecular self-organization of chiral molecules on a surface demonstrate the realization of a spontaneous resolution of a racemic mixture into homochiral molecular dimers and rows [10, 11, 12, 13]. These STM observations of an enantioselective assembly enlighten the fundamental processes of chiral recognition on which rely the basic mechanisms of living systems. Furthermore, the creation of enantiomorphic domains and complete monolayers of molecules bestowing chirality to an achiral surface [14, 15, 16] is of particular relevance for heterogeneous enantioselective catalysis [17].

Apart from imaging the individual molecules and following the supramolecular self-assembly, an analysis of the electronic levels of single molecules is accomplished by means of scanning tunneling spectroscopy (STS). Differential conductance (dI/dV) spectra on molecules have been first recorded in 1993 on C_{60} [18] and ethylene [19], but since then the spectroscopic investigations have been extended to a large number of different systems. However, a probing of unperturbed molecular levels, such as the highest occupied molecular orbital (HOMO) and the lowest unoccupied molecular orbital (LUMO) is hampered due to the interactions with the surface (e.g. chemisorption or electronic coupling of molecular π levels to the substrate states), leading to a broadening and shifting of the levels. In the case of physisorbed molecules, the interaction is caused by π systems of the molecules which are oriented parallel and close to the metal surfaces. To reduce this effect of electronic coupling, an ultrathin insulating film acting as a spacer layer between a planar π conjugated molecule and a metal was used by Repp *et al.* [20]. Using methods related to the manipulating mode of operation of STM demonstrated for the first time

in 1991 [21], specific adsorption conformations of the molecules which are determined by the STM images [22] have been reversibly switched by mechanical contact of the tip, field-assisted processes, or inelastic electron tunneling [23, 24].

This thesis is organized as follows:

Chapter 1 introduces the molecule rubrene which is investigated in this thesis, regarding existing applications, the specific three-dimensional and chiral geometry, and the optical and electronic properties known from the literature. A short introduction to the concept of chirality is given, followed by an outline of the adsorption of molecules on surfaces.

Chapter 2 discusses the theoretical principles of the scanning tunneling microscope for imaging (STM) and spectroscopy (STS) with a special focus on the implications of large voltage ranges for STS measurements. A short introduction to the problem of imaging adsorbed molecules is given, as well as a presentation of the used experimental set-up and techniques.

Chapter 3 presents the STM measurements of the supramolecular self-assembly of rubrene on Au(111), composed of phases of different geometry and symmetry for submonolayer, as well as multilayer coverage. Based on the experimental results, an explanation of the intermolecular bonding which stabilizes the different supramolecular structures is proposed.

Chapter 4 includes the aspect of chirality by the determination of the chiral signature of individual rubrene molecules by STM and shows the crucial importance of chiral recognition processes on the hierarchical self-assembly of rubrene on Au(111).

Chapter 5 presents results of a study of the distribution of chirality in extended molecular islands and gives an organization of the supramolecular phases observed on Au(111) in terms of a coverage dependent growth which is explained by taking into account the different geometries and the chirality.

Chapter 6 discusses the STS results recorded on different adsorption conformations of rubrene on Au(111) which are distinguished by their submolecular contrast in the STM images. From the dI/dV spectra, HOMO and LUMO energies corresponding to the different conformers are determined and compared to known values of the molecule. Furthermore, STS measurements of rubrene on Au(100), Ag(111), and Ag(100) complete the consistent interpretation of the adsorption mechanism of rubrene on all four metal surfaces. The switching of the geometric and electronic structure of a rubrene conformer on Au(111) induced by STM and STS is demonstrated.

Chapter 7 gives the results of a comparative STM study of the adsorption of rubrene on Au(111), Au(100), Ag(100), and Ag(111) which demonstrate the impact of the underlying surface on the supramolecular self-assembly.

Chapter 8 summarizes the results of this thesis.

Chapter 9 gives an outlook for further work on the investigated subjects.

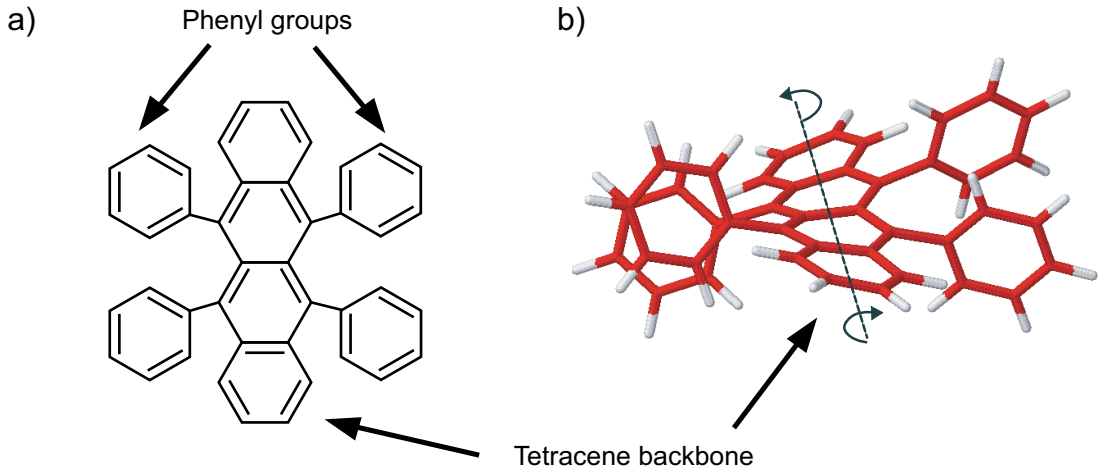

Figure 1.1: Rubrene ($C_{42}H_{28}$). a) Chemical structure showing the central tetracene backbone and four attached phenyl groups. b) Three dimensional model. Steric hindrance leads to a rotation of the phenyl groups out of the plane and furthermore to a helical twisting of the tetracene backbone.

1.2 Rubrene

The organic molecule which is investigated in this thesis is the fluorescent molecule 5,6,11,12-tetraphenylnaphthacene (rubrene, $C_{42}H_{28}$). Rubrene belongs to the family of polycyclic aromatic hydrocarbons (PAH) which are characterized by an extended system of delocalized π-electrons. This electronic structure establishes the enhanced stability of the molecules and provides the basis for the interesting optical and electronic properties of PAHs due to a relatively small (insulating) energy gap with high lying ionization potentials (IP) or low lying electron affinities (EA) which are close to the work functions of metals. Consequently, the energetic positions of the molecular levels offer ideal conditions for an integration of PAHs into molecular electronic and optoelectronic devices [25, 26, 27, 28, 29] which require a contacting to electrodes as well as optical transitions in the visible.

These requirements are fulfilled by the electronic properties of rubrene establishing its recent successful application for organic light emitting diodes (OLED) and organic field effect transistors (OFET). Added as a dopant into the hole transport layer, rubrene increases the efficiency and stability of the devices [30, 31]. Furthermore, red OLEDs are realized by the energy transfer from rubrene to a red emitting dopant [32] while white emitting OLEDs mix the yellow-orange light from rubrene with a blue emission from an adjacent layer [33, 34]. The very high charge carrier mobility of typically 15-20 cm^2/Vs measured at the surface of rubrene crystals lead to its integration into p-type OFETs [35, 36, 37, 38].

1.2.1 Geometry of rubrene

The chemical structure of rubrene is shown in Fig. 1.1 together with its three-dimensional (3D) representation[1]. The molecule consists of a tetracene backbone with four phenyl groups which are rotated out of the molecular plane due to steric hindrance between the phenyls. Furthermore, this molecular structure forces a twisting of the tetracene backbone by 42° [39] which establishes an axial chirality of the molecule in the gas phase. The dimensions of the molecule are determined

[1] 3D Mol file from http://webbook.nist.gov/chemistry/.

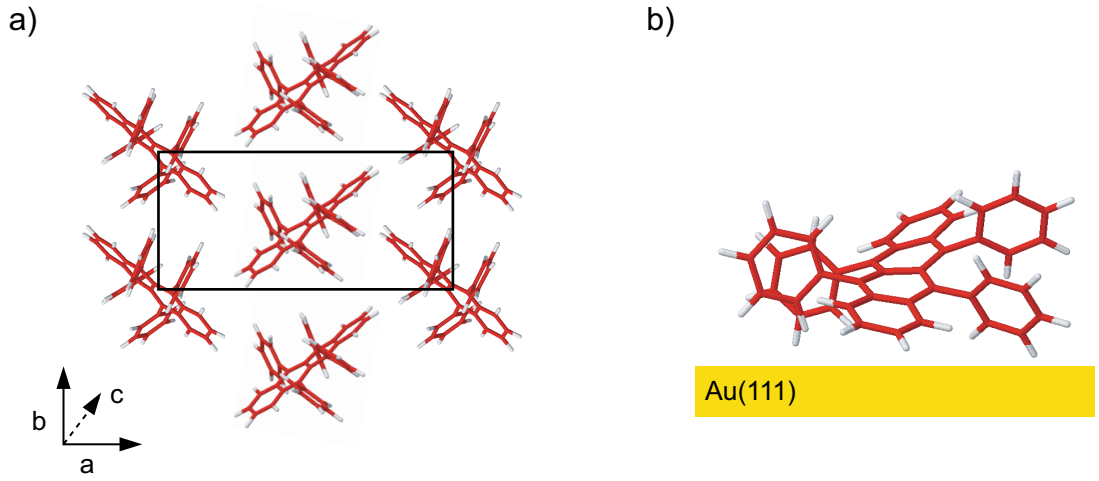

Figure 1.2: a) Orthorhombic crystal structure of rubrene based on [36]. The herringbone motif is constructed with a=14.4 Å, b=7.2 Å, c=27 Å. b) Proposed adsorption geometry of rubrene on Au(111) based on [39]. The inclination of the tetracene backbone with respect to the surface is $\approx 38°$.

to 13.6 Å (along long tetracene axis), 15.7 Å (along short tetracene axis) and 4.3 Å (perpendicular to the tetracene plane) [40].

The crystallization of rubrene is reported to result in different structures depending on the growth conditions: monoclinic [41], triclinic [42] and orthorhombic [43]. The latter crystal structure with lattice constants $a = 14.4$ Å, $b = 7.2$ Å, $c = 27$ Å is described in the two-dimensional (a-b) plane by a herringbone motif shown in Fig. 1.2 (a) and is confirmed by recent studies [36, 44, 45]. Near edge x-ray absorption fine structure (NEXAFS) analysis revealed that the crystallization leads to a planarization of the tetracene backbone for a thickness above 9 monolayers (ML) [39] which enhances the packing efficiency of the molecules. This arrangement yields a π-π stacking along the b direction of the van der Waals (vdW) crystal which is at the origin of the higher charge carrier mobility measured along this axis [36]. Moreover, the NEXAFS studies unraveled an inclined orientation of the twisted rubrene adsorbed on Au(111) with a tilt angle of $\approx 38°$ between the tetracene backbone and the surface as shown in Fig. 1.2 (b).

1.2.2 Optical and electronic properties

Rubrene is a highly efficient fluorescent dye which emits yellow-orange light in the visible (maximum $\approx$ 560 nm, 2.2 eV) by a radiative $S_1 \rightarrow S_0$ transition[2] between the unoccupied π^* and occupied π states of the molecule. The powder and the crystals are of orange-red color due to an absorption which is reaching from the UV-blue to the green part of the spectrum [46, 47]. The light emission from rubrene is stimulated by different processes: photon absorption (fluorescence), electron-hole injection (electroluminescence) and energy transfer from chemical reactions (chemiluminescence). Irradiating rubrene with light in the presence of air quenches the emitted luminescence in the visible. However, the fluorescence is recovered by heating the oxidized product which leads to a release of the oxygen (thermostimulated chemiluminescence) [48, 49].

This mechanism is important for the understanding of the electronic structure of rubrene since it shows that the HOMO-LUMO transition responsible for the fluorescence is concentrated on the tetracene backbone of rubrene. The O_2 insertion divides the tetracene into a benzene and

[2]Transition from the first excited state S_1 (singlet) to the ground state S_0 (singlet).

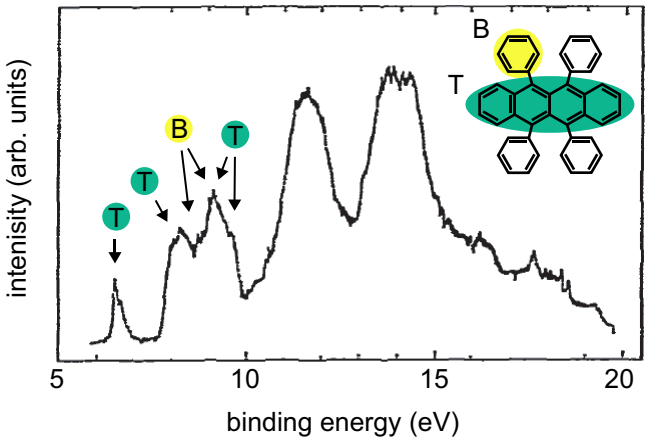

Figure 1.3: UPS He(I) spectrum of rubrene in the gas phase. Peaks are denoted by T or B depending on their origin from the tetracene or benzene part of the molecule [49, 50].

a naphthalene part whose HOMO-LUMO transitions are in the ultraviolet part of the spectrum, just like those of the four phenyl groups. The tetracene dominance on the fluorescence mechanism is reflected by the strong resemblance of the spectra of tetracene and rubrene revealing the same features, which are red-shifted to lower energies due to the influence of the phenyl groups [47].

A comparison of the peak positions found in the ultraviolet photoelectron spectrum (UPS) of rubrene (Fig. 1.3) with known values from tetracene and benzene allows for an assignment of the occupied molecular orbitals of rubrene to the corresponding ones of tetracene (T) and benzene (B) [49, 50]. From the position of the first peak, the HOMO energy of rubrene is determined to 6.4 eV (adiabatic IP) which is shifted by 0.6 eV with respect to the value of tetracene (7.0 eV [51]). This shift is due to the contribution of the phenyl groups to the HOMO originating from the overlap of their π systems with those of the tetracene backbone. This effect is relatively small due to the rotation of the phenyl substituents by $\approx 60°$ with respect to the tetracene plane [52], leading to a small contribution of the phenyl groups to the HOMO and LUMO of rubrene (see Fig. 1.4). The LUMO of rubrene is studied by NEXAFS measurements, revealing that the lowest lying peaks in the unoccupied spectrum originate from the tetracene backbone and the phenyl groups [39]. The spectra presented in Fig. 1.5 (a) compare the signal obtained from a multilayer of rubrene on Au(111), with the corresponding curves of benzene and tetracene, showing that the LUMO of rubrene (α) is due to the tetracene backbone. The spectrum obtained from submonolayer coverage of rubrene on Au(111) is displayed in Fig. 1.5 (b) and reveals an additional peak α' close to α. This new feature is assigned to the different electronic structure of rubrene molecules with a twisted tetracene backbone for a submonolayer and thin films compared to the case of a planar geometry as in the case of thick films and crystals.

The change of the electronic structure of the molecules upon crystallization into a solid is schematically depicted in Fig. 1.6. Due to the small vdW forces acting between the molecules inside an organic crystal, most of the molecular orbitals stay localized in the potential wells of the individual molecules, in contrast to the situation of delocalization encountered in inorganic semiconductor crystals. The electronic levels of an (ionized) molecule are probed by UPS and inverse photoelectron spectroscopy (IPES) where electrons are extracted from occupied or injected into unoccupied molecular levels. The extraction of an electron from a molecule in the bulk will create a hole which induces a polarization of the surrounding molecules. This effect leads to a reduction of the HOMO energy by a polarization energy P_{h} (see Fig. 1.7). The cor-

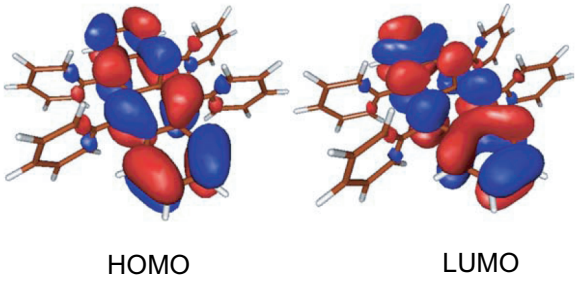

Figure 1.4: HOMO and LUMO plots of rubrene calculated by DFT showing the main contribution of the tetracene backbone to the frontier orbitals [53].

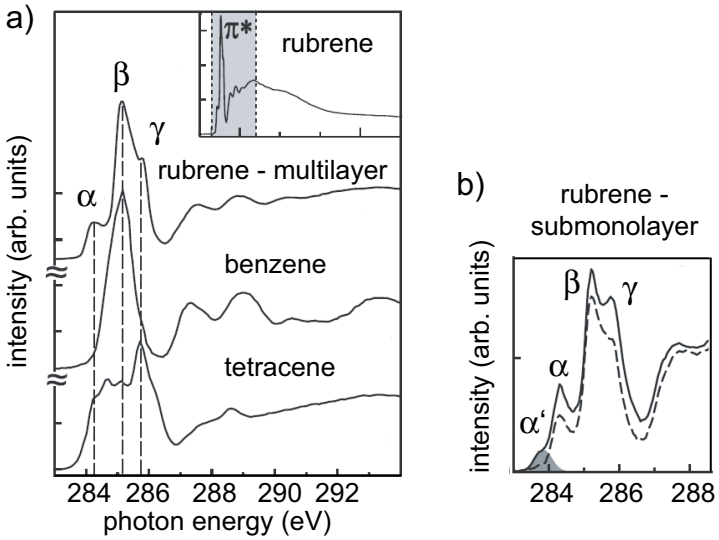

Figure 1.5: NEXAFS study probing the LUMO of rubrene for multilayer (a) and submonolayer (b) coverage on Au(111). a) The comparison with the corresponding spectra from benzene and tetracene allow for an assignment of the peaks α and γ to a contribution from the tetracene backbone and β to the signal from the phenyl groups. b) At submonolayer coverage, an additional peak α' appears, which originates from the changed electronic structure of the twisted tetracene backbone in the case of a submonolayer. [39].

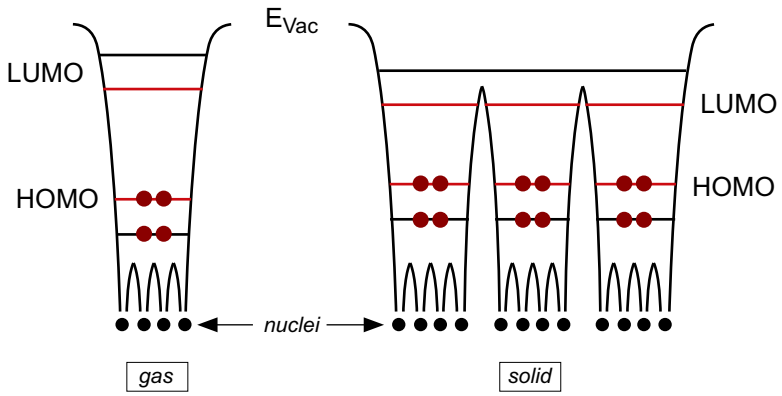

Figure 1.6: Energy levels in potential wells for an isolated molecule and a molecular solid (adapted from [54]).

	E_{HOMO}	E_{LUMO}	E_{t}
gas phase	6.4 eV	$\approx$ 1.9 eV	$\approx$ 4.5 eV
solid phase	5.3 eV	$\approx$ 2.6 eV	$\approx$ 2.7 eV

Table 1.1: Energy values for rubrene in the gas phase and in the solid. The values of E_{HOMO} are measured values from UPS and the values of E_{LUMO} and E_{t} are estimated values (see text).

responding increase of the E_{LUMO} by a polarization energy P_{e} is due to the additional electron in the LUMO. This change of the electronic levels results in a reduced HOMO-LUMO gap of the molecular crystal with respect to the energy gap of the free molecule. From a comparison of gas and solid phase UPS spectra one can determine the polarization energy P_{h} as the difference between the adiabatic IP of the free molecule and the threshold IP of the crystal. For rubrene, this evaluation yields $P_{\mathrm{h}} = 1.1$ eV with $E_{\mathrm{HOMO}} = 6.4$ eV for the gas and $E_{\mathrm{HOMO}} = 5.3$ eV for the solid phase [55]. Absorption and electron energy loss spectroscopy (EELS) reveal an optical HOMO-LUMO gap E_{a} of 2.3 eV which gives an estimate of the LUMO value of the solid by adding an exciton binding energy[3] E_{b} to E_{a} [56, 57, 58]. For rubrene, E_{b} should be slightly smaller than the value of 0.4 eV for tetracene due to the larger size of rubrene which is expected to reduce E_{b} [56]. This yields an electronic (transport) gap of $E_{\mathrm{t}} \approx 2.7$ eV and, consequently, a value of E_{LUMO} for the solid of ≈ 2.6 eV. The corresponding gas phase value is roughly estimated to ≈ 1.9 eV by the subtraction of $P_{\mathrm{e}} = 0.7$ eV, which is approximated by considering that for tetracene, the polarization energy P_{e} is about 0.4 eV smaller than P_{h} [59]. These energies are schematized in Fig. 1.7 with the corresponding values for rubrene given in Tab. 1.1.

Until recently, the macroscopic investigations of rubrene which analyzed the fluorescent, crystallographic, and electronic properties of the molecule in the gas and solid phase discarded the aspect of chirality of the molecule. The NEXAFS measurements justified this approach for the case of the rubrene crystals by demonstrating that the crystallization of rubrene lifts the characteristic twisting of the tetracene backbone for film thicknesses larger than 9 ML [39]. They confirmed however, that the chirality is preserved upon adsorption on a Au(111) surface, raising

[3] In organic layers, this optical gap is characterized by the formation of exciton-hole pair which is localized on the individual molecule (Frenkel exciton).

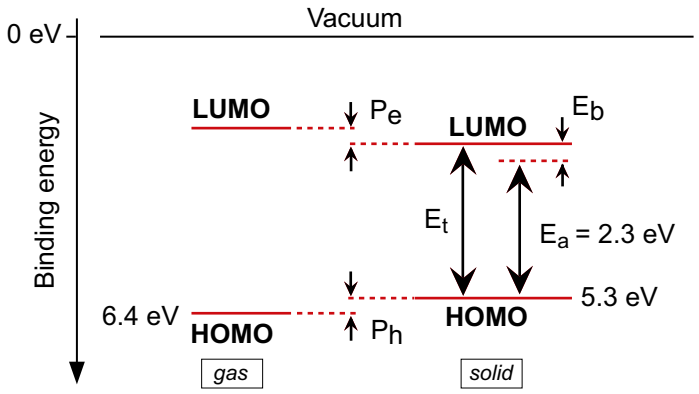

Figure 1.7: Energy level scheme showing the HOMO-LUMO gap of the free molecule and the solid with an optical gap E_a and transport gap E_t of the solid. Experimental values are given for the HOMO energies and the optical energy gap.

the question of how this property will appear in a local investigation of the individual molecules. Furthermore, the deposition of a chiral mixture of molecules offers different possible outcomes for the interaction between the adsorbates on the surface. The following section will give a - very brief - introduction to the main notions and implications of chirality.

1.3 Chirality

The fascination for chirality and the ongoing importance of scientific research[4] on chiral substances and enantioselective processes stems from its ubiquitous presence in living organisms. The word *chiral* (derived from the Greek word $\chi\epsilon\iota\rho$ - *cheir*, meaning hand) refers to all objects which cannot be superimposed to their mirror image, such as the snail shells shown in Fig. 1.8. Other examples are found everywhere in nature: our hands, molecules like the lactic acid and the DNA are chiral and can exist in two versions, denoted in the following by **L** and **R** type. Thus, the combination of two objects out of a racemic mixture (i.e. containing **L** and **R** species) has four possible outcomes: **LL**, **RR** (homochiral) and **LR**, **RL** (heterochiral). The fact that homochiral products behave completely different from heterochiral ones establishes the importance of chiral recognition in biological systems [60]. This mechanism is based on the fact that the molecules distinguish between their two versions (enantiomers) for the formation of intermolecular bonds. The discovery of the existence of chiral molecules and chiral recognition has been made by Louis Pasteur in his famous experiment in 1848 [61], where he determined and separated the two enantiomers of sodium ammonium tartrate crystals. From his results he deduced that the chirality of the crystal is originating from the molecular building units. The still unexplained predominance of one enantiomer of a molecule in the human body [62] establishes the crucial importance for the pharmaceutical industry to separate the "right" enantiomer of a drug which interacts correctly with the human physiology from the other one, which might be harmful [7]. These dramatic consequences motivate the continuous quest for novel techniques to resolve a racemic mixture of a molecule into enantiopure (containing only one enantiomer) compounds or to perform an asymmetric catalysis producing directly an excess of the desired enantiomer.

[4] Nobel Prize in Chemistry 2001.

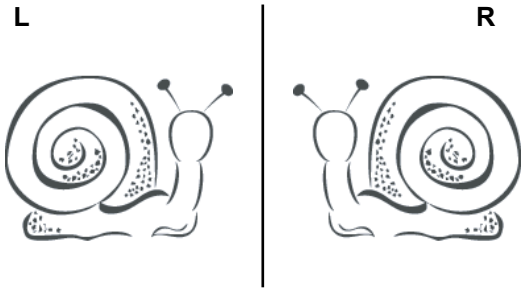

Figure 1.8: Snail as an example for a chiral object. The **L**-snail and its mirror image of **R**-type are not superimposable by any rotation.

The study of chiral molecules on surfaces has become of importance since the recent development of the heterogeneous catalysis [17] which uses a chiral modifier on a metal surface to induce an enantioselective synthesis. Molecular adsorption on surfaces is however a challenging subject with many open questions. The following section outlines the fundamental theoretical principles which try to explain the basic interactions of the molecules with the substrate. These mechanisms affect the molecular properties with respect to their geometric conformations and electronic characteristics.

1.4 Adsorption of molecules on metal surfaces

The adsorption of molecules on metal surfaces is a complex process which is still lacking a complete and consistent understanding. A simplistic classification of the basic processes which take place distinguishes *physisorption*, where the adsorbate preserves its electronic structure from *chemisorption*, resulting in modified electronic levels of the adsorbate due to a strong interaction with the surface [63].

The mechanism of chemisorption is characterized by strong ionic or covalent bonds due to charge transfer from and to the adsorbate [64]. The process of ionic bonding is displayed in Fig. 1.9 revealing that the crossing of the Fermi level (E_{F}) by broadened molecular orbitals, such as the HOMO or LUMO, is at the origin of this interaction. A second mechanism consists of the overlap and hybridization of partially unoccupied molecular orbitals with partially filled d bands of transition metals [65]. The adsorption energy of chemisorption in the order of 1 eV is much higher than for physisorption and the intrinsic electronic structure of the chemisorbed molecule is substantially changed.

The adsorption of rare gas atoms on metal surfaces constitutes the typical example of physisorption. Their completely filled valence shell of binding energies well below metallic Fermi levels prohibits a charge transfer interaction or hybridization with the surface states. Nevertheless a bonding is established due to vdW forces which describe the interaction between the fluctuating dipole of the adsorbate and the induced dipole moment in the metal. An atom can be represented by electrons oscillating around the nucleus. The positive (nucleus) and negative (electrons) charges induce image charges in the polarizable metal. This situation is schematized in Fig. 1.10 by an atom which is adsorbed at a distance z from a metal surface. The interaction energy is the sum of the Coulomb energies $-q^2/(4\pi\epsilon_0 2z)$ resulting from the attractive and repulsive forces between the charges q and their induced charges $-q$. An expansion of this sum yields that the attractive bonding energy of an adsorbate on a metal surface depends in a first

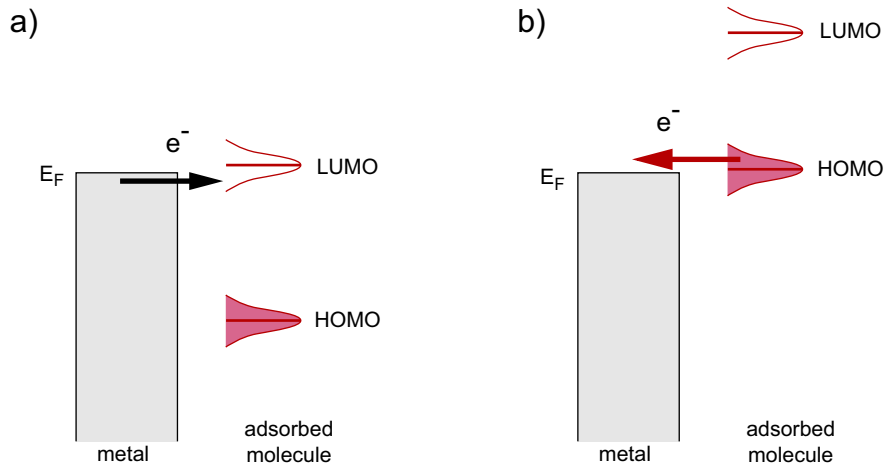

Figure 1.9: Charge transfer process leading to chemisorption of the molecule. a) The unfilled LUMO resonance crosses E_F, enabling a transfer of electrons from the surface to the molecule. b) Electrons from the filled HOMO of the molecule go into the unoccupied levels of the surface.

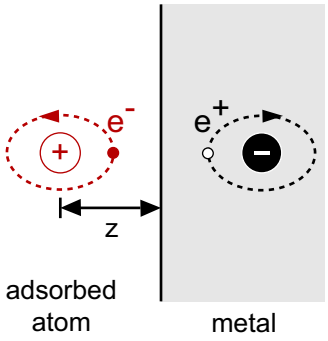

Figure 1.10: Schematic representation of a physisorbed atom on a metal surface. The positive charge of the nucleus and the negative charge of the electron induce image charges in the metal resulting in an attractive Coulomb interaction between the atom and its image.

approximation on $-z^{-3}$, which is in contrast to the corresponding value of $-z^{-6}$ for vdW interaction between molecules. At closer distances a repulsive force due to the Pauli exclusion arises from the interaction of the surface charge distribution with the charge density of the closed-shell atom [63]. A different description of the physisorption of rare gases on metals leading to similar results is given by local density approximation (LDA) in density functional theory (DFT) [66].

Chapter 2

Experimental techniques

2.1 Scanning tunneling microscopy

The development of the scanning tunneling microscope (STM) by Binnig and Rohrer[1] in 1982 [1, 2] opened up a new field in surface science, permitting a real-space investigation of atomically resolved metal and semiconductor surfaces and the study of individual atomic and molecular adsorbates. The imaging mechanism of the STM is based on the quantum mechanical tunneling effect which enables electrons to cross the vacuum barrier between the tip and the surface, resulting in a tunneling current I which strongly depends on the distance z between tip and sample. A sharp tip is brought very close to a surface and scans a small area by means of a piezo to which the tip is attached. High voltage ramps applied to the piezo drive the x and y movements while the z direction is controlled by a feedback loop which compares I to a given set-point value for each position (x, y) and applies an appropriate voltage to the z-piezo which approaches or retracts the tip in order to keep I constant (constant current mode).

The quantum mechanical tunneling is based on the wavelike nature of electrons. This property leads to a finite probability for electrons to cross a potential barrier V_0 which is higher than their kinetic energy E. For a rectangular barrier, the barrier transmission coefficient $\mathcal{T}$ is exponentially dependent on z and the square root of the effective barrier height $V_0 - E$

$$\mathcal{T} \propto e^{-2\kappa z} \quad \text{with} \quad \kappa = [2m(V_0 - E)]^{1/2}/\hbar. \tag{2.1}$$

In a first-order perturbative treatment of tunneling for a three-dimensional barrier, the tunneling current I between two independent planar electrodes is evaluated for a weak wave function overlap to (see Fig. 2.1)

$$I(V) = \frac{2\pi e}{\hbar} \sum_{\mu,\nu} |M_{\mu\nu}|^2 \delta(E_\mu - (E_\nu + eV)) \times$$
$$\Big[f(E_\mu, T)[1 - f(E_\nu, T)] - f(E_\nu, T)[1 - f(E_\mu, T)] \Big] \tag{2.2}$$

for an applied voltage V between the electrodes and a summation over all eigenfunctions Ψ_μ and Ψ_ν of tip and sample having eigenenergies E_μ and E_ν with respect to their Fermi levels $E_{\mathrm{F,t}}$ and $E_{\mathrm{F,s}}$. The Fermi-Dirac function $f(E, T)$ gives the probability that an electronic state of energy E is occupied at the temperature T and the δ-function accounts for an elastic tunneling process. Energy diagrams of the tunneling junction without and with an applied voltage V are depicted in Fig. 2.1.

[1] Nobel Prize in Physics, 1986.

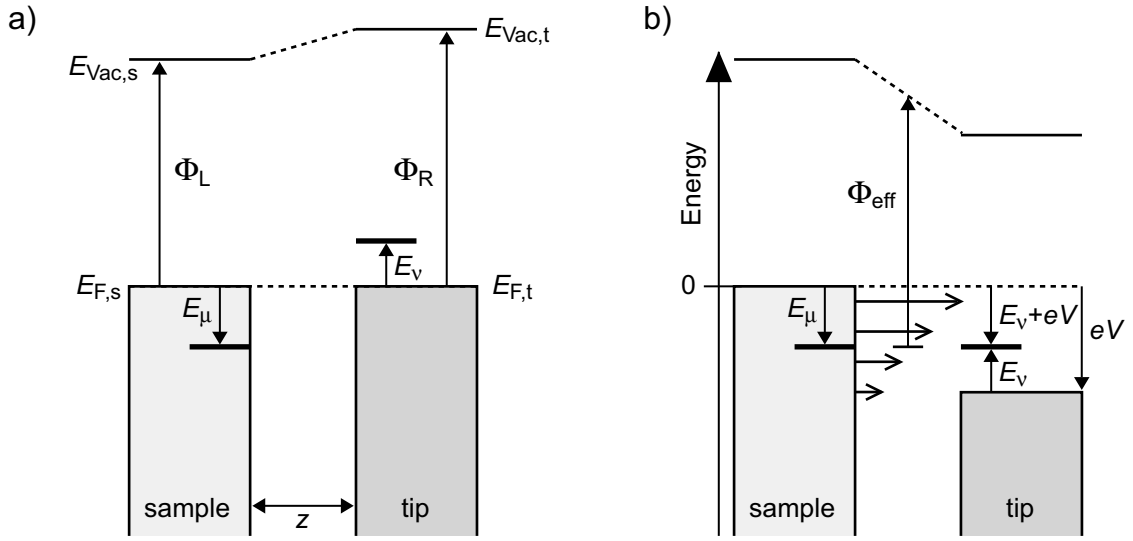

Figure 2.1: Schematic energy diagram of the tunnel junction a) without an applied bias voltage b) with an applied voltage *V* between tip and sample.

Bardeen [67] showed that the tunneling matrix $M_{\mu\nu}$ which evaluates the overlap of the wavefunctions Ψ_μ and Ψ_ν in the gap region can be expressed as

$$M_{\mu\nu} = \frac{-\hbar^2}{2m} \int_S (\Psi_\mu^* \vec{\nabla} \Psi_\nu - \Psi_\nu \vec{\nabla} \Psi_\mu^*) \, d\vec{S} \tag{2.3}$$

where the integration is over a surface lying inside the gap.

Tersoff and Hamann applied this approach to the calculation of the tunneling current in STM and simplified it by restricting the external conditions to a locally spherical tip having only s-type wavefunctions and to the regime of low temperatures and small voltages V which reduces Eq. 2.2 to [68]

$$I(V) = \frac{2\pi e^2}{\hbar} V \cdot \sum_{\mu,\nu} |M_{\mu\nu}|^2 \delta(E_\mu - E_F) \cdot \delta(E_\nu - E_F). \tag{2.4}$$

The application of explicit wave functions for the sample and an idealized tip with a radius of curvature R at a position $\vec{r}_0$ simplifies Eq. 2.4 to

$$I(V) \propto V \cdot \rho_t(E_F) \, e^{2\kappa R} \sum_\mu |\Psi_\mu(\vec{r}_0)|^2 \delta(E_\mu - E_F) \tag{2.5}$$

with $\kappa = \sqrt{2m\Phi_{eff}}/\hbar$ being the inverse decay length for the wave functions in vacuum, Φ_{eff} the effective local potential barrier height and $\rho_t(E)$ the density of states of the tip. Consequently, for constant V the tunneling current I is proportional to the local density of states (LDOS) of the sample $\rho_s(\vec{r}, E)$ at the position $\vec{r}_0$:

$$I \propto \rho_s(\vec{r}_0, E_F) \quad \text{with} \quad \rho_s(\vec{r}_0, E) \equiv \sum_\mu |\Psi_\mu(\vec{r}_0)|^2 \delta(E_\mu - E). \tag{2.6}$$

Eq. 2.6 gives an interpretation of the contrast in STM images for scanning at constant current and small voltage in terms of a contour of constant LDOS of the sample at E_F. The exponential

decay of the wave functions in the z-direction normal to the surface yields $|\Psi_\mu(\vec{r}_0)|^2 = e^{-2\kappa(z+R)}$. A substitution into Eq. 2.5 gives

$$I \propto e^{-2\kappa z} \tag{2.7}$$

describing the exponential dependence of I on the tip-sample distance z.

2.2 Spectroscopy - STS

A further important technique using STM consist of the spectroscopic analysis probing the electronic structure of the surface [69, 70, 71, 72]. The above deduced proportionality of I and $\rho_s(E_F)$ (Eq. 2.6) is only valid for small voltages, thus probing the surface LDOS at E_F. Information about the electronic structure of the sample at finite bias voltage V is obtained by a generalization of the expression for I by Tersoff and Hamann and the determination of the derivative dI/dV [73, 74].

An integration over all states E which contribute to the tunneling current in the energy range between $E_F = 0$ and eV results in

$$I(V) \propto \int_0^{eV} \rho_t(E - eV)\, \rho_s(E)\, \mathcal{T}(z, E, eV)\, dE \tag{2.8}$$

with an exponential transmission coefficient $\mathcal{T}(z, E, eV)$ for a trapezoidal barrier

$$\mathcal{T}(z, E, eV) = e^{-2(z+R)\kappa} \quad \text{with} \quad \kappa = \sqrt{\frac{2m\Phi_{\text{eff}}}{\hbar^2}} \tag{2.9}$$

$$\text{and} \quad \Phi_{\text{eff}} = \frac{1}{2}(\Phi_s + \Phi_t + eV) - E \tag{2.10}$$

where Φ_{eff} is the bias voltage dependent effective barrier height [72]. The exponential dependence of $\mathcal{T}$ on Φ_{eff} expresses the predominant tunneling from occupied electronic states of the sample close to E_F due to the reduced effective barrier height $\Phi_{\text{eff}} = (\Phi_s + \Phi_t - e|V|)/2$ for those electrons (see Fig. 2.1). However, tunneling into unoccupied states of the sample is strongest for states close to eV where Φ_{eff} is smallest (see Fig. 2.2). The differential conductance is then given by

$$\begin{aligned} \frac{dI(V)}{dV} &\propto \rho_t(0)\, \rho_s(eV)\, \mathcal{T}(z, eV, eV) \\ &+ \int_0^{eV} \rho_t(E - eV)\, \rho_s(E)\, \frac{d\mathcal{T}(z, E, eV)}{dV}\, dE \\ &+ \int_0^{eV} \frac{d\rho_t(E - eV)}{dV}\, \rho_s(E)\, \mathcal{T}(z, E, eV)\, dE \end{aligned} \tag{2.11}$$

Assuming a constant ρ_t, the third term vanishes and the first term shows the proportionality $dI/dV \propto \rho_s(eV)$ while the $d\mathcal{T}/dV$ dependent term provides a smoothly changing background signal in the case of small voltages. From this equation follows that the measurement of the differential conductance dI/dV gives information about the surface LDOS ρ_s at eV.

The experimental measurement of the surface LDOS is realized by recording the dI/dV signal for a specific voltage range by the application of a small sinusoidal voltage modulation $V_{\text{mod}} \cdot sin(\omega t)$ to the tunneling voltage V_0 between tip and sample. The voltage modulation induces an in-phase modulated contribution to the current whose amplitude $\frac{dI(V_0)}{dV} \cdot V_{\text{mod}}$ is

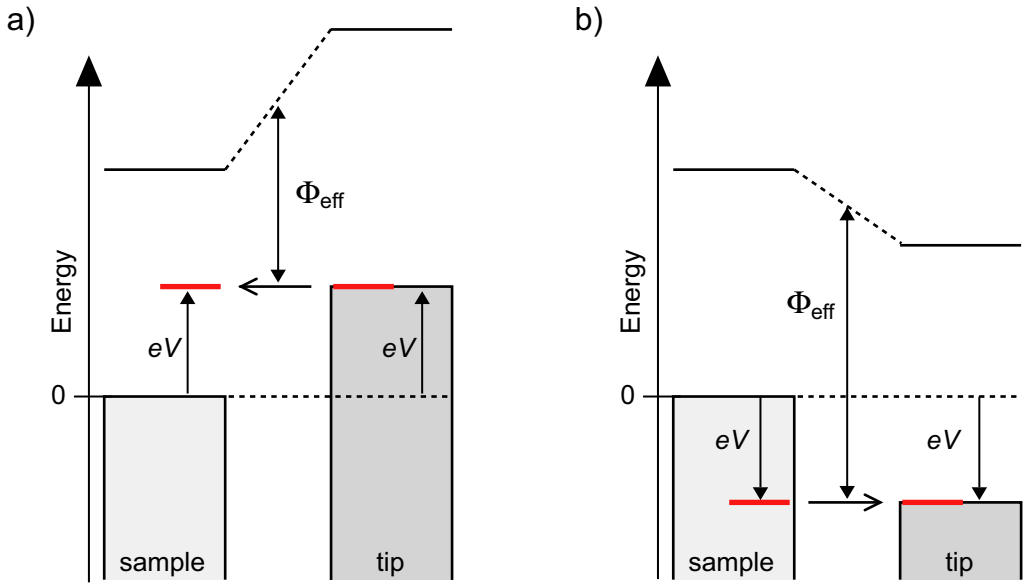

Figure 2.2: Schematic energy diagram revealing the asymmetry of the tunnel junction a) for a negatively polarized tip (negative bias voltage) b) for a positively polarized tip (positive bias voltage).

detected by a lock-in amplifier. The contribution of dI/dV to the tunneling current can be seen by expanding I in a Taylor series

$$\begin{aligned} I(V_0 + V_{\mathrm{mod}} sin(\omega t)) &= I(V_0) + \frac{dI(V_0)}{dV} \cdot V_{\mathrm{mod}} \cdot sin(\omega t) \\ &+ \frac{d^2 I(V_0)}{dV^2} \cdot V_{\mathrm{mod}}^2 \cdot sin^2(\omega t) + ... \end{aligned} \tag{2.12}$$

The third term which depends on $sin^2(\omega t)$ is the second derivative of the tunneling current dI^2/dV^2. The measurement of this quantity as a function of V reveals peaks in the corresponding spectrum, if the current I contains contributions originating from inelastic tunneling processes. The latter mechanism explains the excitation of localized surface plasmons [75], vibrational modes of molecules [76] or spin-flips of atoms [77]. Recording the first derivative dI/dV allows to probe the LDOS of a sample using two different methods:

- Feedback loop OFF (small voltages $|V| \leq 1$): The tip-sample distance z is fixed and the dI/dV signal reveals $\rho_s(eV)$ which dominates over a smoothly changing background originating from the $d\mathcal{T}/dV$ dependent term.

- Feedback loop ON (wide voltage range): The modulation frequency is higher than the response frequency of the feedback loop, allowing for a detection of the dI/dV signal [69, 70]. This technique is used to account for the fact that for voltages in the range of electronvolts, the dependence of the transmission coefficient $\mathcal{T}$ on V becomes important. Since the influence is different for positive and negative voltages, the two cases have to be treated separately.

  For a positively biased sample ($V > 0$), $\mathcal{T}$ is maximal for states at eV due to a minimal effective barrier height $\Phi_{\mathrm{eff}} = (\Phi_s + \Phi_t - e|V|)/2$ (see Eq. 2.10 and Fig. 2.2 (a)). Thus, the first term in Eq. 2.11 dominates over the second term. To counterbalance the exponential

increase of $\mathcal{T}(z, eV, eV)$ with the (positive) voltage V, the tip is retracted from the surface by leaving the feedback loop enabled during the voltage ramp in order to keep $I(V)$ constant.

For a negatively polarized sample ($V < 0$), the first term of Eq. 2.11 is strongly diminished by the lower transmission for states at eV due to the increased effective barrier height $\Phi_{\text{eff}} = (\Phi_s + \Phi_t + e|V|)/2$ (see Eq. 2.10 and Fig. 2.2). The second term gains in importance, since the integration goes over all states from 0 to eV, thus including the states at E_F (i.e. $E = 0$) for which $\mathcal{T}(z, 0, eV)$ increases exponentially with the magnitude of the applied voltage due to the reduced $\Phi_{\text{eff}} = (\Phi_s + \Phi_t - e|V|)/2$ at E_F. This strong increase is again compensated by the withdrawal of the tip driven by the closed feedback loop. However, the small value of the first term for high negative voltages results in a reduced tunneling from low lying occupied states of the sample [72].

The second technique of recording dI/dV spectra with the feedback loop enabled is of importance for spectroscopic measurements probing the electronic structure of molecules. The molecular adsorbates are often characterized by a large separation between the HOMO and the LUMO, requiring a large voltage range for the dI/dV measurements which becomes possible with the method described above. The specific (semiconducting) property of a large number of molecules suggests that they should be transparent for the STM which scans contours of constant DOS. The experiments show however that most of the specimen can be imaged with molecular and submolecular contrast.

2.3 Imaging adsorbed molecules

Since the first observation of adsorbed phthalocyanine [3, 78] and benzene [4] with the STM, different molecules on various metal surfaces have been investigated. However, the precise mechanism which renders the adsorbates visible in the STM images remains partially unclear.

The question arises from the interpretation of constant current images at small voltages as contours of constant LDOS at E_F at the position $\vec{r}_0$ of the tip (see Eq. 2.6). This explanation suggests that most of the small molecules would appear invisible in the images due to their large energy gap between the HOMO and LUMO levels which are separated by typically several eV from E_F. However, the successful imaging of adsorbates is due to a contribution of atomic or molecular levels to the LDOS at E_F, as calculated for adsorbed xenon [79] and benzene [80, 81]. The broadening of an adsorbate level located far away from E_F results in an extended tail of this resonance which contributes to the LDOS at E_F. Interestingly, depending on the specific adsorption mechanism (see Sec. 1.4) the electronic interaction of adsorbate and sample can also lead to a depletion of the Fermi-level state density like for helium [82], carbon [83] and carbon monoxide [21, 84, 85, 86] adsorbed on a metal. Consequently, those molecules figure as depressions in the images which demonstrates that the plots of constant-current recorded with STM do not provide topographic information of adsorbed molecules in a straightforward manner.

The extension of the theoretical description of I for finite voltages (Eq. 2.8) shows that the constant current images for a chosen voltage V_t map the contours of the electronic density which is an integration over all $\rho_s(E)$ from E_F to eV_t. Thus, for resonant tunneling at a voltage V_t which aligns a molecular level with E_F of the tip, STM images and dI/dV maps of C_{60} [87, 88, 89] and flat-lying π-conjugated molecules [78, 90, 91, 92, 93] show a spatial distribution of density of states closely resembling calculated HOMO or LUMO plots or simulated STM images by DFT using the generalized gradient approximation for exchange correlation. However, the latter calculations are not suitable for weakly interacting systems like vdW bonded molecules [24].

For three-dimensional molecules with out-of plane rotated bulky substituents, such as for instance Cu-tetra[3,5 di-*t*-butylphenyl]porphyrin (Cu-TBPP) [94], hexa-*t*-butyl decacyclene (HtBDC) [95], and the "Lander" molecule [96], the constant current imaging mechanism is different. Due to the fact that the molecular π system is held at a larger distance or in a non-parallel orientation from the surface, the contribution from these orbitals to the imaging current is negligible and a dominant tunneling takes place through the *t*-butyl(phenyl) groups. This explanation gives the elastic scattering quantum chemistry (ESQC) approach [97, 98, 99] which has reproduced STM images of large molecules by the evaluation of the full scattering matrix of the STM tunnel junction, including the substrate, the adsorbate and the tip. The STM images are calculated from first principles, considering the optimization of the structural rigidity and conformations of the molecules on the substrate. Furthermore, the strong contribution to the imaging current from even small individual hydrogen atoms attached to the molecules is demonstrated by a dramatic change of the molecular appearance upon a tip-induced dehydrogenation of Co-phthalocyanine (CoPc) [100].

2.4 Experimental set-up

The experiments presented in this thesis were carried out with a home-built STM (similar to the one presented in Ref. [101]) operated in ultrahigh vacuum (UHV) at temperatures of 5 K (liquid helium) and 50 K (solid nitrogen). The UHV system guarantees the cleanliness of the investigated surface and encloses the STM (base pressure $\approx 2 \cdot 10^{-11}$ mbar) and the preparation chamber (10^{-10} mbar). Furthermore, the instrument is equipped with a photon collection instrumentation allowing for the detection and spectroscopic resolution of light emitted from metal surfaces and supported molecules [102, 103]. Low temperatures are a prerequisite for the study of organic molecules to prevent diffusion of the weakly adsorbed molecules. In addition, the resulting small thermal broadening (low value of $k_{\mathrm{B}}T$) permits well-resolved spectroscopic measurement of electronic structures of surfaces and adsorbates. In the preparation chamber, the metal surfaces are cleaned by cycles of Argon ion sputtering and subsequent annealing.

Rubrene molecules (purchased from *Aldrich*) were degassed and then sublimated from a resistively heated evaporator inside the STM chamber onto a sample held at a temperature of 5 or 50 K, followed by an annealing to ≈ 300 K (preparation P1). In a second preparation method, the deposition of the molecules takes place at room temperature or above inside the preparation chamber (preparation P2). In this case, the sample is transferred in-situ from the preparation chamber to the cold STM chamber, yielding a cooling time of ≈ 60 min for measurements performed at 50 K and ≈ 10 min for a temperature of 5 K.[2] The cut Pt-Ir tips yield regular atomic resolution and reproducible spectra and are used over extended measurement periods. The used metal substrates were Au(111) and Ag(111) films evaporated onto MICA, and single crystal Au(100), Ag(111), and Ag(100) surfaces. Typical tunneling parameters for the measurement of rubrene molecules adsorbed in the submonolayer regime were $V = -0.8$ V and $I = 20$ pA. The low current values ensured a high tunneling resistance of 40 GΩ, minimizing tip-induced molecular diffusion. The measurements of multilayers on Au(111) required elevated voltages of $V \leq -2.2$ V.

The spectroscopic measurements probing the electronic structure of the molecular adsorbates and the bare metal surfaces are realized by applying a small voltage modulation V_{mod} of typically 20 mV peak-to-peak to the voltage between tip and sample at a modulation frequency of

[2] The much faster cooling rate at 5 K is due to the strongly increased thermal conductivity of copper at this temperature, compared to the corresponding value at 50 K.

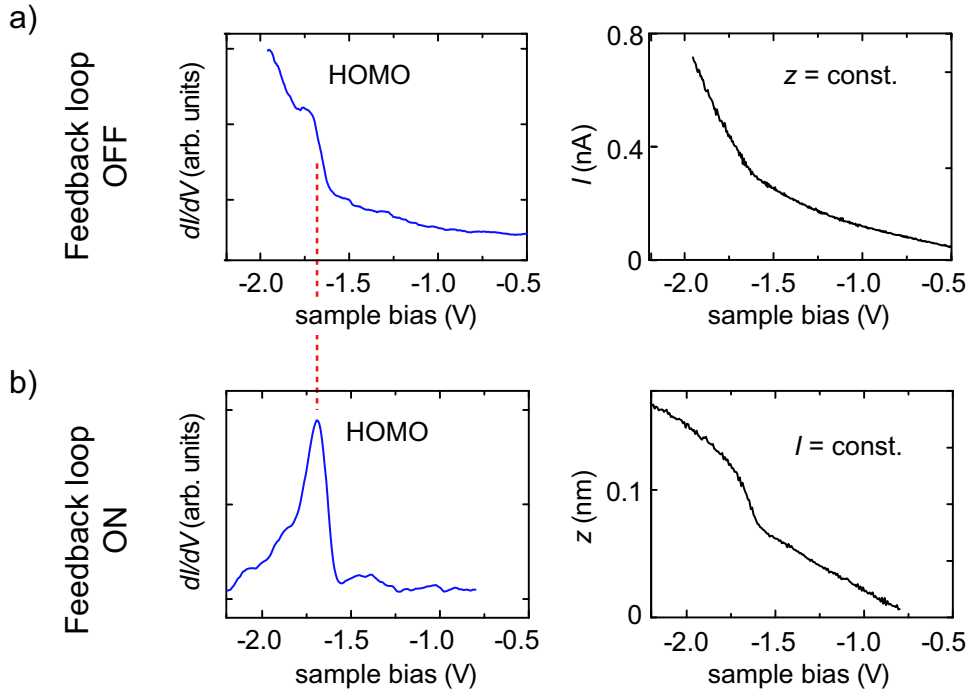

Figure 2.3: STS measurements probing the HOMO of rubrene with disabled (a) and enabled (b) feedback loop. The blue curves (left side) show the *dI/dV* signal from the molecule. The black curves (right side) give the corresponding data of the varying current (a) and tip displacement (b). ($I = 50$ pA, voltage modulation: 1.5 kHz, 20 mV peak-to-peak)

$\approx$ 1.5 kHz. The lock-in amplifier records the amplitude of the resulting modulation of the tunneling current which is in-phase with V_{mod}. The detected signal is proportional to the quantity dI/dV which is related to the local density of states of the sample (see Sec. 2.2). Recording the spectra at constant current by leaving the feedback loop enabled allows for the measurement of a large voltage range (see the corresponding discussion in Sec. 2.2). This is necessary since the molecular orbitals of the molecules are separated by typically several eV from each other and are located far away from the Fermi level of the metal.

The dI/dV spectra in Fig. 2.3 measure the same molecular level with disabled (a) and enabled (b) feedback loop, together with the corresponding current and z displacement curves. While the HOMO peak in the open loop spectrum is buried in the strong increase of the current, the dI/dV spectrum recorded at constant current renders the position of the peak maximum clearly visible. The technique requires separate STS measurements for the negative and positive voltage range in order to record a complete spectrum including the HOMO and the LUMO of the molecules. The peak positions at higher absolute voltages are subject to shifts originating from the Stark effect which move the levels away from E_{F} of the substrate and vary with the effective electric field. Depending on the tip-sample distance (i.e. tunneling resistance) and the applied voltage, shifts of the order of 1 eV have been reported for image potential states close to E_{Vac} [70, 69], while the surface state onsets close to E_{F} measured on Ag(111), Cu(111), and Au(111) are displaced by $\approx$ 10 meV [104, 105]. These shifts have been recorded for small tunneling gaps at tunneling resistances of the order of $\approx$ 1 MΩ. In contrast to these results, the STS measurements presented in this thesis are acquired at large tip-sample distances resulting from low (constant) currents of $\approx$ 20 pA and very high tunneling resistances of $\approx$ 50 GΩ which leads to reduced electrical

fields, compared to the values in the cited references. Consequently, the shifting of the molecular orbitals observed in the dI/dV curves due to the Stark effect is estimated to be smaller than 0.1 V for the relevant voltage range of $-2.4 \leq V \leq +3.0$ V, in analogy to the experiments presented in [20]. This value lies within the measured uncertainty of 0.1 V of the experimental data. However, the shifts of levels at higher absolute voltages of $|V| > 3$ V might be larger than 0.1 V.

Chapter 3

Supramolecular self-assembly of rubrene on Au (111)

The spontaneous self-organization of molecules adsorbed in the submonolayer regime on surfaces leads to a manifold of supramolecular structures [106, 5, 107]. The weak intermolecular forces drive an assembly into extended islands of regularly arranged molecules or direct the creation of small free-standing supramolecular structures of higher organizational complexity. For instance, compact close packed islands are formed by molecules such as C_{60} [18, 108], HBC [109], Cu- and H_2-TBPP [22, 110], Co- and Cu-Pc [111], PTCDA [112, 113], anthracene [91], benzene [114], HB-HPB and HB-HBC [115], and guanine [116]. An interesting alternative in view of the design of molecular electronics is demonstrated by the spontaneous creation of magic clusters of 1-nitronaphthalene [92], the controlled design of size selected structures by the substitution of porphyrin molecules [117] and the formation of one-dimensional supramolecular chains out of benzoic acid [11] and pentacene molecules [118].

3.1 The reconstructed Au (111) surface

The Au(111) surface represents a suitable substrate for molecular adsorption in the submonolayer regime due to its surface reconstruction which offers favorable adsorption sites by the presence of an additional periodic corrugation, different dislocations and variable interatomic distances [119]. The rearrangement of the last atomic layer of Au(111) is unique for close packed surfaces and consists of a contraction of the interatomic distance of the surface atoms along the $[1\bar{1}0]$ direction from the bulk value of 2.89 Å to an average value of 2.75 Å. This anisotropic contraction is due to the fact that 23 gold atoms of the surface layer are arranged over 22 bulk lattice sites in this direction, leading to a $23 \times \sqrt{3}$ overlayer structure and the creation of alternating domains of hexagonal close packed (hcp) and face centered cubic (fcc) stacking (see Fig. 3.1). The fcc and hcp areas are separated by ≈ 0.2 Å high domain walls which are formed by surface atoms located near bridge sites. The direction of the boundaries along the $[11\bar{2}]$ direction is periodically rotated by 120°, forming the characteristic herringbone (chevron) pattern [120]. The elbows of the zigzag shaped troughs exhibit two different appearances which are characterized by a broader hcp or fcc region in the turning point, denoted by x and y, respectively in Fig. 3.1. Chambliss et al. [121, 122] proposed that the sharper edge of the x-type elbow is due to a point dislocation which leads to higher protruding atoms. An influence of the reconstruction on the adsorption of atoms and molecules on Au(111) is demonstrated for different systems by a preferred nucleation at the elbows or a commensurability with the herringbone structure [121, 122, 123, 92, 10, 110, 117, 124, 125]

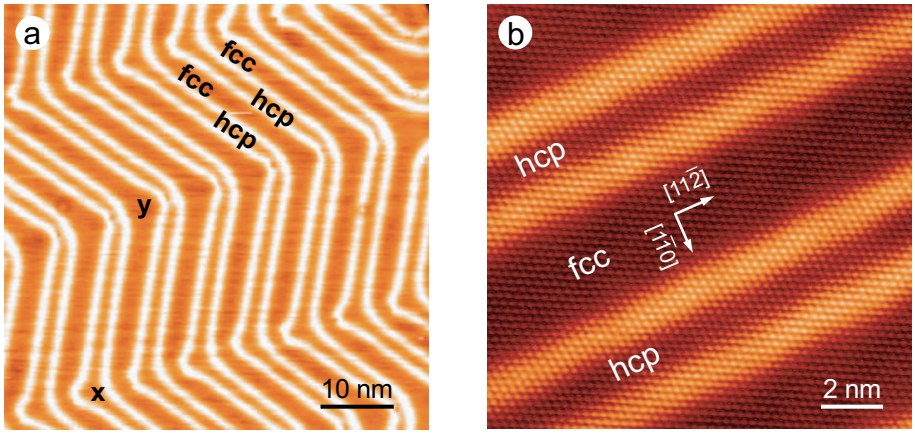

Figure 3.1: STM image showing the herringbone reconstructed Au(111) surface. a) Alternating fcc and hcp stacking domains, as well as *x*- and *y*-type elbows are visible. b) Atomically resolved STM image, revealing the slightly distorted hexagonal arrangement of the surface atoms together with the domain walls separating fcc and hcp stacking. The interatomic distances along $[11\bar{2}]$ and $[1\bar{1}0]$ are 2.88 Å and $\approx$ 2.75 Å, respectively. (Tunneling parameters: a) $V = -0.7$ V, $I = 0.2$ nA; b) $V = -0.02$ V, $I = 1.3$ nA)

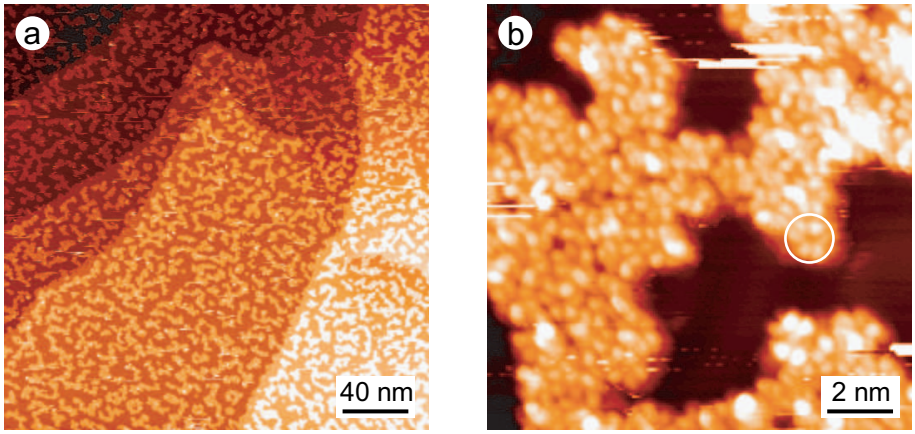

Figure 3.2: STM images showing two-dimensional molecular clusters of rubrene on Au(111) formed after the deposition onto a sample held at 50 K without an additional annealing. a) Overview image of the clusters distributed over several gold terraces. b) Closeup view of a cluster showing the densely packed, disordered arrangement. An individual molecule is encircled and shows submolecular features.

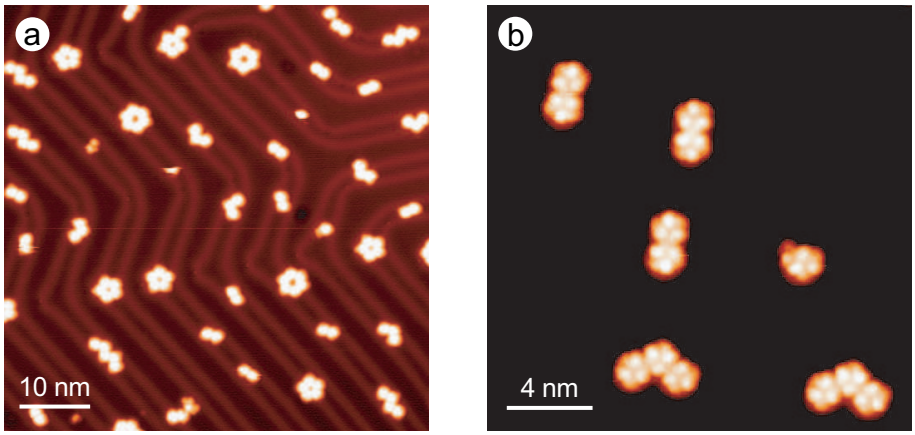

Figure 3.3: Small structures at low coverage. a) Small self-assembled structures from dimers to hexamers uniformly distributed on the Au(111) surface. b) Monomer, dimers, and trimers of rubrene.

The adsorption of rubrene on Au(111) is only weakly influenced by the herringbone pattern of the reconstruction. Even at a sample temperature upon evaporation of 5 K, the molecules move to the step edges where they are stabilized, leaving the terraces empty in the case of a very low coverage. At higher coverage, two-dimensional molecular clusters nucleate on the terraces, consisting of densely packed molecules which reveal submolecular features, as shown in the STM images of Fig. 3.2. However, complex, well ordered supramolecular patterns are obtained by annealing the sample to approximately 300 K (preparation P1) since it provides the necessary energy to enable the molecules to diffuse freely on the surface and to adopt energetically more favorable adsorption conformations. The second preparation method P2 (i.e. deposition of the molecules on a sample at room temperature) leads directly to this molecular motion and flexibility. The resulting supramolecular structures show either a slight preference for the elbows of the reconstruction (circular assemblies) or exhibit a rough orientation along the hcp troughs (elongated assemblies).

3.2 Small structures from monomers to hexamers

The deposition of ≈ 0.04 ML of rubrene on Au(111) (corresponding to 4% of a full hcp coverage of molecules) results in the presence of adsorbed monomers, and the formation of dimers, trimers, tetramers, pentamers and hexamers. The STM image[1] displayed in Fig. 3.3 (a) shows small structures along hcp domains and circular shapes which adsorb at the domain boundaries of the hcp troughs and at x-type elbows. The smaller scale image in Fig. 3.3 (b) unveils a single molecule and the smallest units of supramolecular structures: dimers and trimers. The monomer appears as a round protrusion of about 2.4 Å height which exhibits mainly three maxima of approximately threefold symmetry with smaller intermediate features between the maxima (this submolecular appearance will be discussed in Sec. 4.2.1). The dimers and trimers show that the molecule preserves its characteristic geometric features upon bonding to other molecules to form small supramolecular structures.

The STM images in Fig. 3.4 show the progressive self-assembly into small structures which consist of two to six molecules. While the dimer is a linear object, the trimer forms an angle of

[1] Tunneling parameters for STM imaging throughout this thesis are -0.8 V to -1.0 V and 0.2 pA to 0.5 pA, if not stated differently in the figure caption.

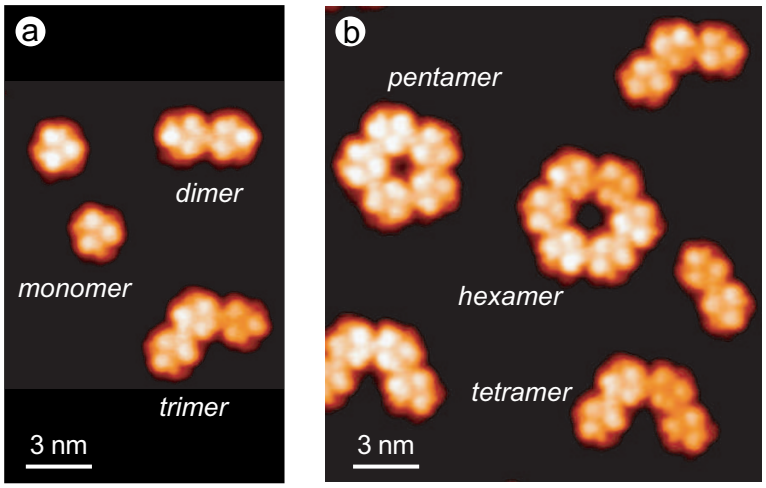

Figure 3.4: STM images showing a) monomers, dimers, and trimers and b) tetramers, a pentamer, and hexamer.

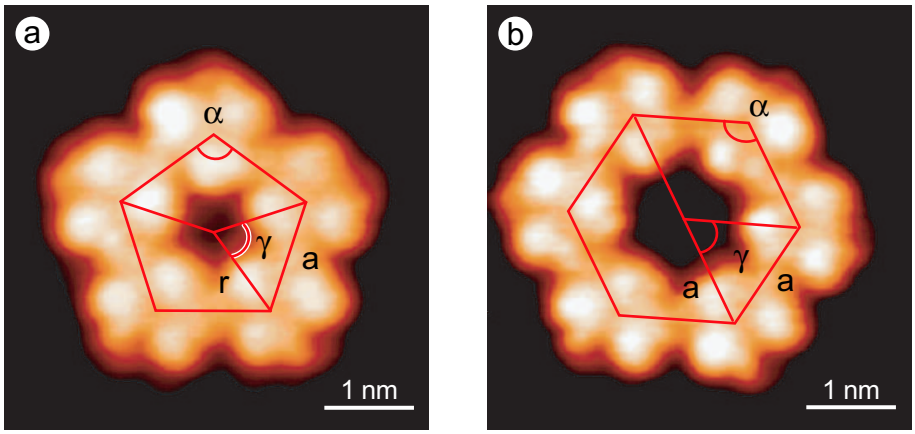

Figure 3.5: STM image of a) a pentagonal supermolecule (α =108°, γ =72°, r=1.0±0.1 nm) and b) a hexagonal supermolecule (α =120°, γ =60°, r=a=1.2±0.1 nm). The intermolecular distance a=1.2 nm is equivalent for both structures.

120°. This surprisingly exact geometry of the intermolecular binding into a trimer reflects the threefold character of the molecule with three apparently equivalent "docking" sites, to which other molecules can link at angular separations of 120°. The tetramer, pentamer and hexamer in the STM image of Fig. 3.4 (b) are of more circular shape. The two closed structures are made out of five and six molecules and reveal clearly a fivefold and sixfold symmetry. These supramolecular regular pentagons and hexagons have a side length $a = 1.2 \pm 0.1$ nm (corresponding to the intermolecular distance in all types of self-assembled structures) and radii of 1.0 ± 0.1 and 1.2 ± 0.1 nm, respectively. These geometric lengths are denoted in Fig. 3.5, together with the characteristic angles of a pentagon ($\alpha = 108°,\ \gamma = 72°$) and a hexagon ($\alpha = 120°,\ \gamma = 60°$). The formation of supramolecular pentagons is surprising, since the presence of a fivefold axis in the solid state is limited to the case of quasicrystals [126], due to the impossibility to fill a plane with pentagons without leaving gaps. Furthermore, the coexistence of C_5 and C_6 symmetry groups in the supramolecular assemblies of the same molecule is a novel observation which shows the flexibility of the intermolecular bonding of rubrene. The ability of the molecules to adapt to their local environment leads to the formation of structures with an angle of 120° or 108°.

The contraction of the angle formed by three adjacent molecules which results in the creation of a pentagonal supermolecule is a result of the process described in Fig. 3.6. The first steps of intermolecular bonding lead to the construction of linear dimers, then to supramolecular trimers and tetramers with angles of 120° between the two intermolecular bonds. This structural design implies that the structures are built up on a hexagonal geometry as indicated in Fig. 3.6 (a). Joining a fifth molecule to the tetramer would lead to an almost closed structure where the molecules which form open ends with a separation of $d = a/\sqrt{2} \approx 0.9$ nm between their potential bonding sites. The absence of this type of pentamer, which would be the logical successor of the existing tetramers, gives rise to the conclusion that the attractive forces acting between the two molecules are strong enough to induce a closure of the pentamer. This transformation affects all the molecules, given that the resulting structure has the geometry of a regular pentagon with angles of 108° instead of 120° as for the tetramer.

Taking into account that a hexagonal pentamer is presumably an unstable structure, the construction of a hexagonal supermolecule has to undergo a different process than joining one molecule after the other to a growing assembly. A possible mechanism is the linking of small supramolecular fragments, i.e. a dimer bonding to a tetramer (see Fig. 3.7) or the combination of two trimers. Correspondingly, a pentagon could be built up by a assembly of a dimer with a trimer into a hexagonal pentamer which undergoes an angular contraction to 108° in order to form a stable pentagonal supermolecule.

3.3 Honeycomb islets

The deposition of about 0.1 ML of rubrene favors the development of hexagonal structures in the self-assembly process. This is visible in the STM image of Fig. 3.8 (a), showing a predominance of small honeycomb like patterns which are distributed uniformly over the Au(111) surface. These islets exist in a manifold of different shapes, from mathematical geometries like triangles, trapezoids and parallelograms having angles of 60° and 120° (see for example the STM images in Fig. 3.8 (b) and Fig. 3.10 (b)) to assemblies of mixed hexa-pentagonal structures. In these mixed structures, hexagons and pentagons share two of their molecules which confirms the equivalence of the intermolecular distance in the fivefold and sixfold patterns and the flexible bonding directions of the molecules. This situation is schematically described in Fig. 3.9, revealing that the three sites in the molecule which are available for an intermolecular bonding are separated by angles of 120° in the case of mixed hexagons and by 108°, 120° and 132° for a fusion of a hexagon with

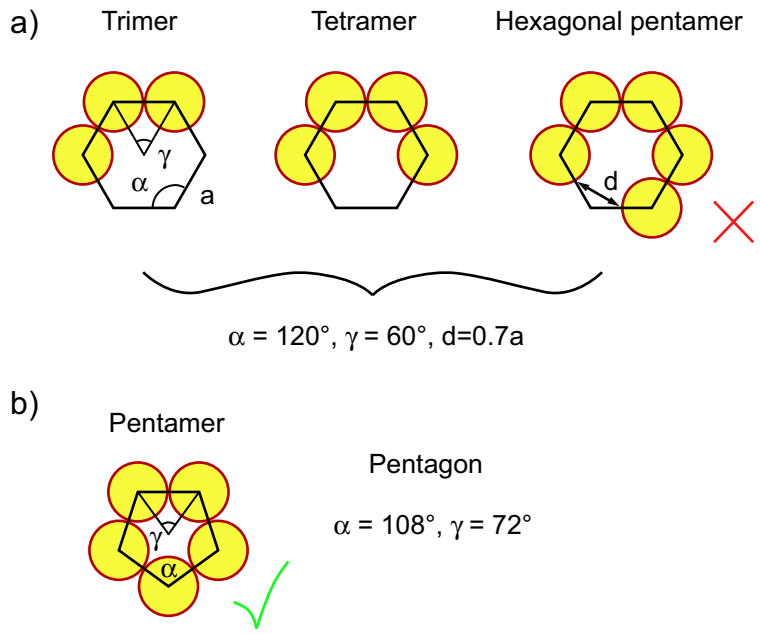

Figure 3.6: Schematics of the self-assembly into small structures. a) Three adjacent molecules form angles of 120°. A pentamer constructed on a hexagonal basis has not been observed. b) Five molecules form a pentagonal supermolecule with angles of 108° between three neighbors.

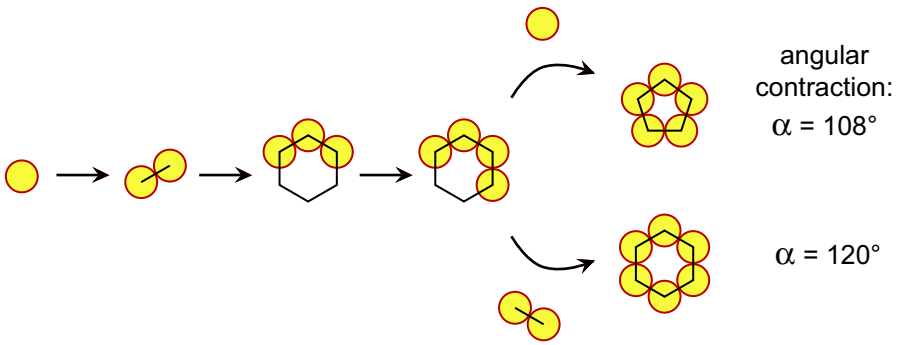

Figure 3.7: Proposed model describing one possible self-assembly leading to the creation of pentagonal or hexagonal assemblies. Since the hexagonal pentamer is unstable, the supramolecular hexagon has to be built up by a linking of hexagonal fragments.

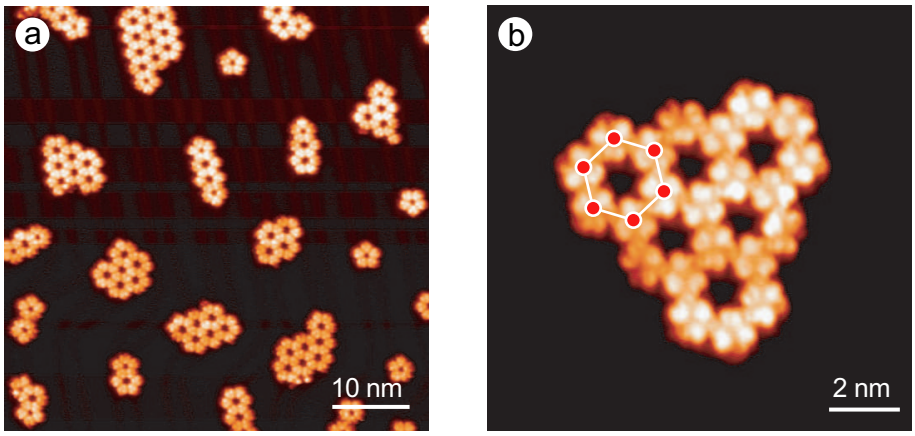

Figure 3.8: a) Supramolecular honeycomb islets, distributed uniformly on the Au(111) surface. b) Honeycomb pattern of hexagonally arranged rubrene molecules forming a supramolecular, equilateral triangle.

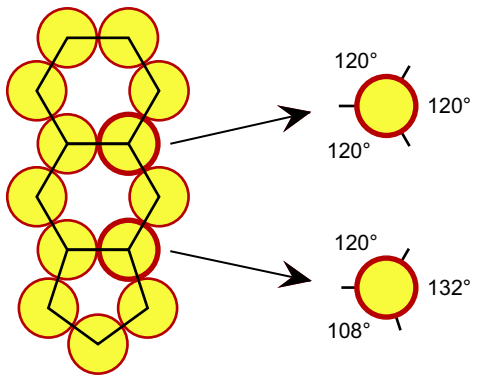

Figure 3.9: Schematic construction of a merged hexagonal-pentagonal assembly. The angular flexibility of intermolecular bonds are shown by the different angles between the bonding sites for molecules at a hexagon-hexagon and a hexagon-pentagon interface.

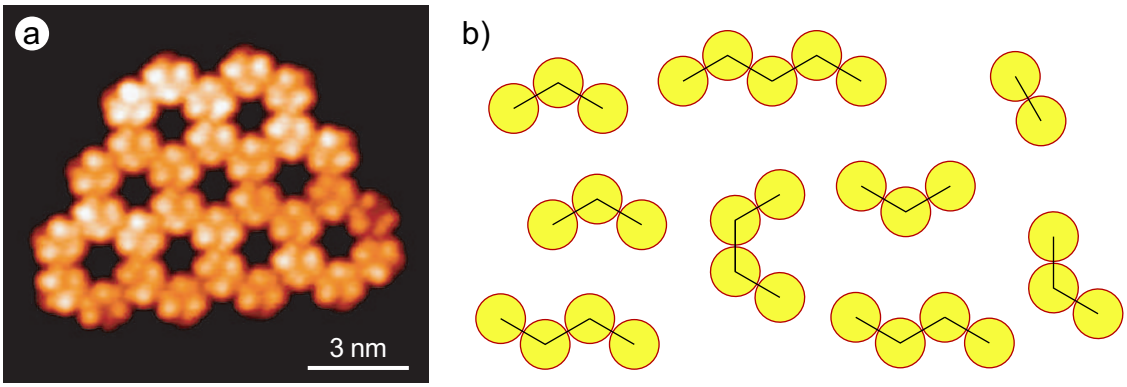

Figure 3.10: a) STM images of a trapezoidal honeycomb structure. b) Possible building units for the creation of the shown honeycomb pattern.

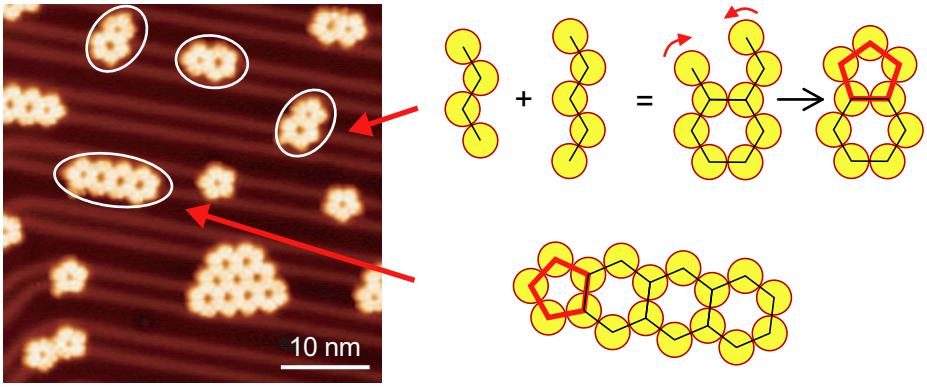

Figure 3.11: STM image of honeycomb islets, pentagonal supermolecules and (encircled) mixed pentagonal-hexagonal structures. The assembly into these mixed geometries is a result of the bonding of mismatching zigzag structures, leading to on open pentamer which closes and thus forms a pentagon at the end of the hexagonal structure.

a pentagon. A closer look to the honeycomb patterns reveals that they are not the result of an assembly of supramolecular hexagons, i.e. two hexagons of the honeycomb structure are made out of only ten molecules, since they share two molecules. This fact suggests that these assemblies are mainly formed by a linking of dimers, trimers and longer zigzag shaped structures, and not by complete supramolecular hexagons. The STM image in Fig. 3.10 (a) shows a trapezoidal honeycomb structure which could be constructed by many different combinations of variously shaped small fragments. As an example, the linking of the building blocks which are presented in Fig. 3.10 (b) would result in the formation of the shown honeycomb islet.

Moreover, this assembly mechanism of open supramolecular fragments explains the observed frequent occurrence of honeycomb patterns which are terminated by pentagons, such as those shown in the STM image of Fig. 3.11. The situation is coherent by taking into account that the dimers, trimers and zigzag chains consist of different numbers of molecules and that an assembly of those structures might result in a honeycomb formation with open ends which are formed by not bonded molecules at angles of 120°. Accordingly to the discussion in Sec. 3.2, these unstable pentamers contract into stable pentagons which leads to a mixed hexagonal-pentagonal assembly as shown schematically in Fig. 3.11. Furthermore, the combination of

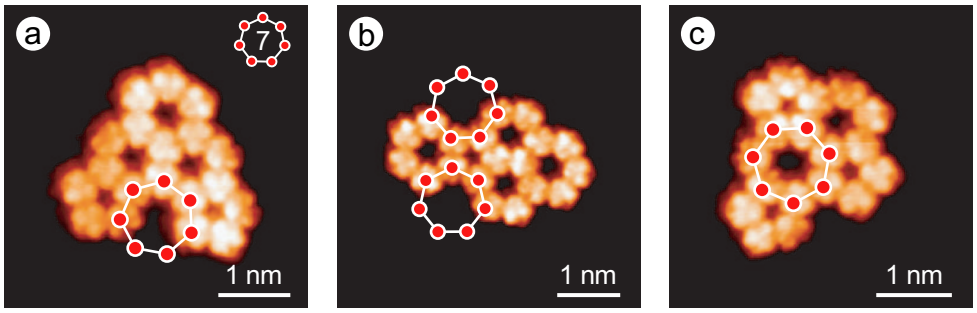

Figure 3.12: STM images of mixed structures made out of pentagons and hexagons, as well as open (a), (b) and closed (c) heptagons.

different small supramolecular parts of different shapes result in the formation of mixed assemblies which exhibit in addition to the five- and sixfold symmetry also sevenfold patterns. This is shown in the STM images displayed in Fig. 3.12, where the mixing of hexagonal and pentagonal supramolecular parts creates an arrangement of molecules which are located at the corners of a heptagon (sevenfold polygon). The appearance of this sevenfold symmetry is not surprising, given that the intermolecular bonding of a molecule at the interface of a hexagon and a pentagon leads to an outward angle of 132° (see Fig. 3.9) which is close to the angle $\alpha \approx 129°$ formed at the edges of a regular heptagon. This coexistence of five-, six- and (slightly distorted) sevenfold symmetry gives rise to a fascinating plane-filling supramolecular phase which is described in Sec. 3.6.

3.4 Chains of pentagonal supermolecules

Upon deposition of ≈ 0.15 ML of rubrene on Au(111), the sample reveals a patterning by chain-like structures which are uniformly distributed over the surface, as shown in Fig. 3.13 (a). These partially straight and partially curled supramolecular structures exhibit a slight influence of the underlying herringbone reconstruction by giving the structures a rough orientation along the lines of the domain walls. The smaller scale STM image in Fig. 3.13 (b) unveils that the supramolecular structures are combinations of narrow honeycomb patterns and supramolecular pentagons (see Sec. 3.2). An examination of these specimen results in the finding that the honeycomb parts are predominantly of the width of just one hexagon, i.e. two zigzag lines, and are terminated by pentagons.

The deposition of slightly more molecules (≈ 0.2 ML) eliminates the honeycomb patterned parts and results in the formation of purely pentagonal chains. These structures extend to lengths of more than 50 pentagons, corresponding to ≈ 150 nm, and form beautifully meandering labyrinths on the Au(111) surface such as the one shown in Fig. 3.14 (a). The zoomed image of a detail of such a supramolecular chain displayed in Fig. 3.14 (b) resolves the individual molecules which form the pentagonal supermolecules. A study of the appearance of the rubrene molecules inside these purely pentagonal chains uncovers that the submolecular features differ from those observed in the single molecules and the constituent molecules of small self-assemblies. This important property will be discussed in detail in Sec. 6.1, including also a treatment of the molecules in the honeycomb patterns.

The small-scale STM image shown in Fig. 3.14 (b) indicates furthermore that the pentagonal supermolecules bond to each other like small molecular gearwheels. This comparison originates

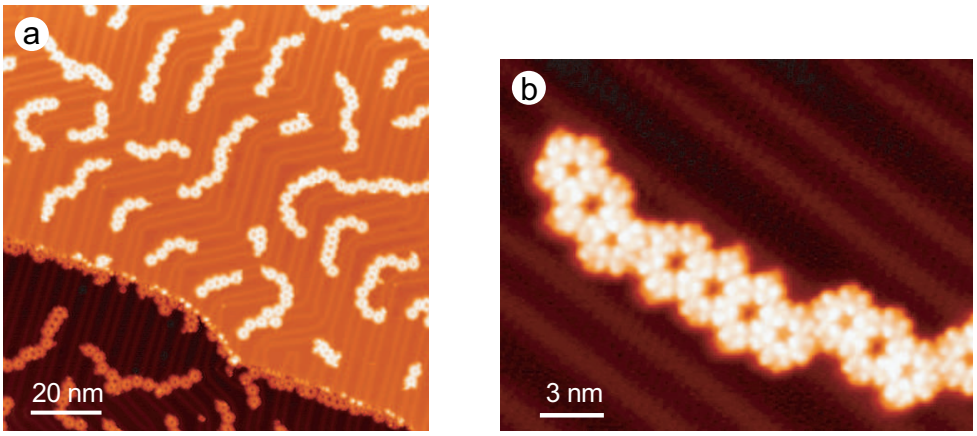

Figure 3.13: STM images showing the result of an assembly into elongated supramolecular structures. a) Overview image of the uniform distribution of the chains on two Au(111) terraces separated by an atomic step of the gold surface. b) Zoom of a mixed honeycomb - pentagonal structure.

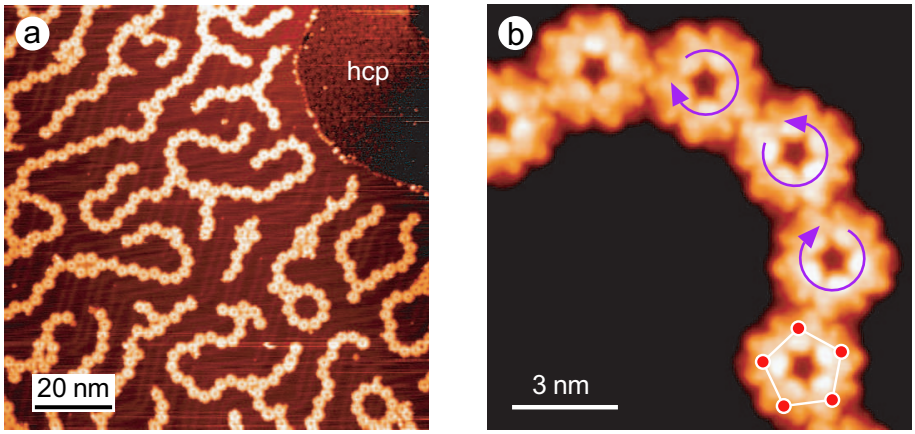

Figure 3.14: STM images of supramolecular chains formed by pentagonal supermolecules. a) Large scale image showing meandering chains constructing a labyrinth. In the upper right part of the image, a step of the gold substrate is seen, separating the upper terrace with the pentagonal chains from the lower terrace covered with an hcp island of rubrene. b) The zoom reveals that the building blocks of the supramolecular chains are pentagonal supermolecules which interlock like small gearwheels. The arrows indicate the rotational motion which would be induced in all pentagons by an initiating rotation of one molecular gearwheel.

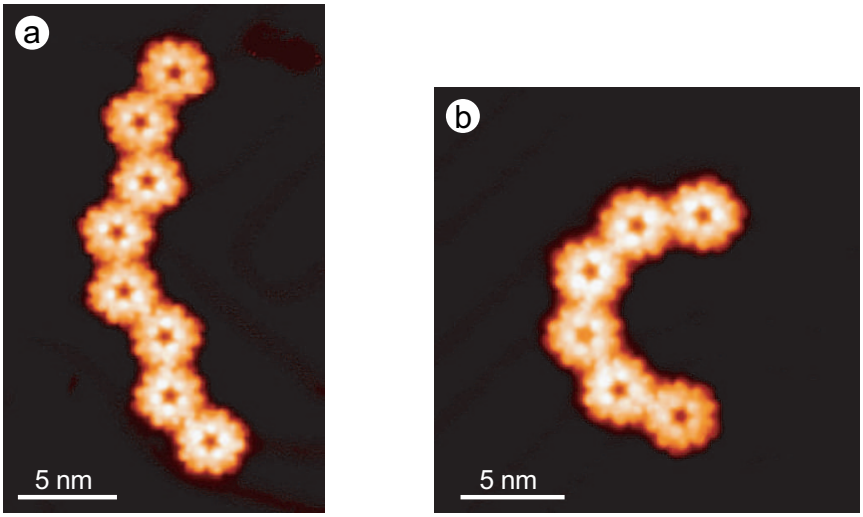

Figure 3.15: STM images of supramolecular chains which are jagged and elongated (a) or bent into circular structures (b).

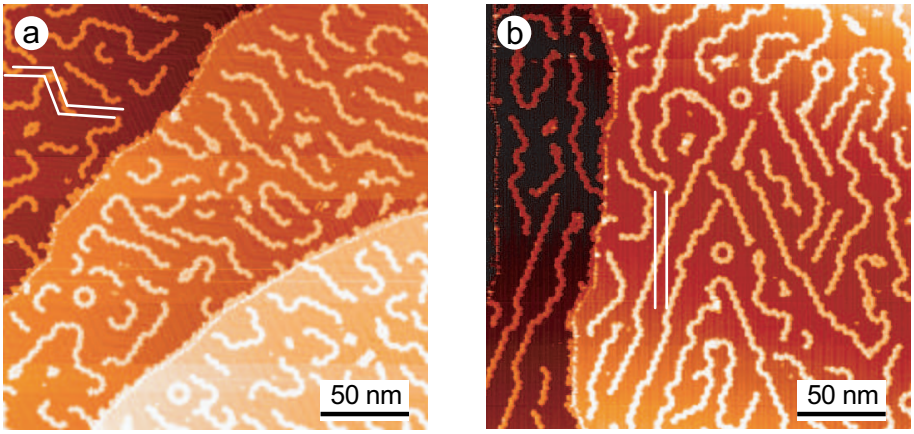

Figure 3.16: STM images of supramolecular labyrinths made out of pentagonal chains showing an influence of the herringbone reconstruction. a) The presence of the zigzag shaped reconstruction leads to shorter, more jagged and curved structures. b) The unusual reconstruction of straight running hcp/fcc troughs favors the creation of long and remarkably straight supramolecular chains. The white lines indicate exemplarily the distinct shape of the surface reconstruction in the different areas of (a) and (b).

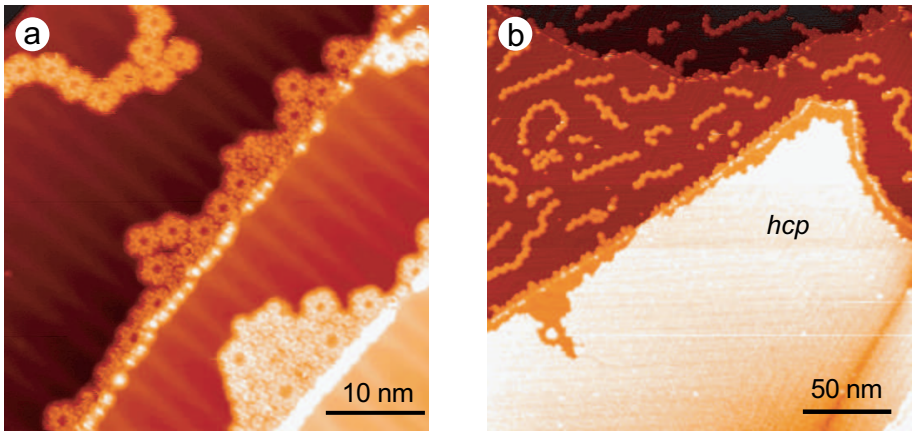

Figure 3.17: STM images showing a supramolecular assembly at the phase transition between pentagonal chains and hcp islands. a) Evolution of a small hcp island growing from the lower terrace of an atomic step. b) Coexisting pentagonal chains and extended hcp island which covers a whole terrace by leaving a narrow spacing to the step edge.

from the observation that the pentagons which form the supramolecular chain are interlocked in such a way that the rotation of one molecular gearwheel around its center would induce an oppositely oriented rotation of the second pentagon, provoking the spinning of the third one and so on. Consequently, the rotation of a pentagonal supermolecule at one end would drive a rotation of all members of the supramolecular chain. The mechanism of interlocking supermolecules leads to the creation of a variety of differently modeled chains as shown in the STM images of Fig. 3.14 to Fig. 3.16. The process is exemplified in the STM images of Fig. 3.15, showing small pentagonal chains of almost straight and circularly bent shape. A detailed investigation of the inter-supermolecular bonding reveals that for each pentagon which joins an existing chain, there exist two available bonding sites on the pentagon which is located at the end of the structure (see Sec. 4.1). This leads to a very high number of possible formations of supramolecular chains, i.e. a linking of 20 pentagonal supermolecules has $2^{18} \approx 3 \cdot 10^5$ differently shaped outcomes[2]. However, the design of pentagonal chains is driven by other parameters than just the laws of probability. This is seen in the STM images displayed in Fig. 3.16 which show the supramolecular labyrinths of the same sample, but at different areas of the surface and indicate the influence of the herringbone reconstruction on the design of the pentagonal chains. The area shown in Fig. 3.16 (a) is characterized by a gold reconstruction of zigzag shape which results in the formation of jagged and curved supramolecular structures. In contrast to this behavior, the straight running hcp/fcc troughs of the reconstruction present in the STM image of Fig. 3.16 (b) seem to be at the origin of the much longer and very straight supramolecular chains.

Looking at the step edges of the Au(111) terraces, an interesting feature appears which is related to the phase transition from honeycomb patterns to purely pentagonal supermolecules described above. With the disappearance of honeycomb fragments in the chains due to an increasing rubrene coverage, the growth of molecular islands starts at the step edges. At low coverage, the steps are decorated exclusively by individual molecules and small structures, but from a critical density on, there is an island growth from the step edge on which extends over the lower terrace of the step. The situation is shown in the STM image of Fig. 3.17 (a), revealing that

[2]By taking into account that there is only one possible result for the creation of a dimer and that the bonding happens always at one end of the chain.

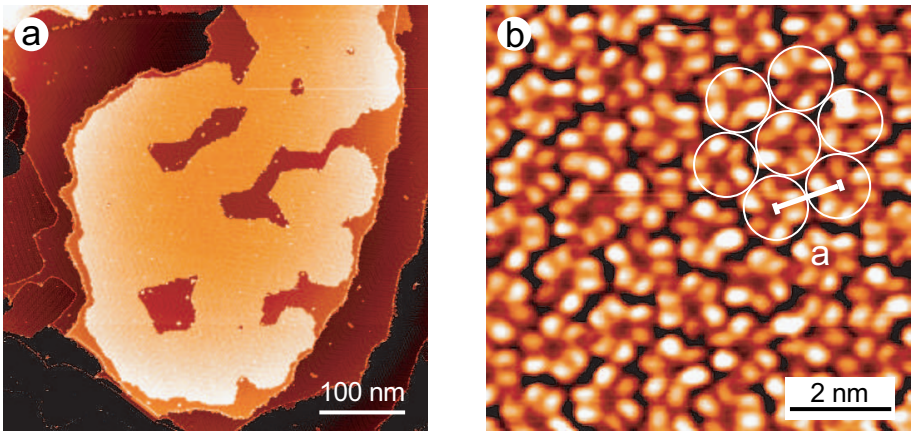

Figure 3.18: a) Extended densely packed molecular island, growing from a step edge (not seen) over a gold terrace. b) Closeup view of an island showing the hcp arrangement of rubrene molecules with submolecular resolution. The individual molecules are encircled and reveal an intermolecular distance of a ≈1.3 nm. The image is high pass filtered to eliminate the herringbone corrugation of the underlying Au(111) surface.

the small islands consist of densely packed molecules, existing next to supramolecular pentagons and hexagons. With increasing coverage, the dimensions of these islands increase until they extend over the whole terrace, just stopping before a decorated upper step edge, such as shown in the STM image of Fig 3.18 (a). This behavior demonstrates the presence of a repulsion from the upper step edge (or from the molecule decorating it), reminding the Ehrlich-Schwoebel barrier experienced for atoms on metal surfaces [127, 128, 129].

3.5 Hexagonal close packed islands

The deposition of ≈ 0.25 ML of rubrene molecules on Au(111) leads to increasing hcp island sizes, going along with a decreasing number of pentagonal chains of more and more reduced lengths. Finally, at a coverage of about 0.3 ML, all the molecules are either adsorbed at step edges or are densely packed into extended hcp islands. This situation is depicted in the STM image of Fig. 3.18 (a), showing a huge hcp island with dimensions of several hundred nanometers. The growth of the islands starts again at the lower edge of gold steps and goes on by extending over the lower terrace until it is almost covered. The STM images reveal that the islands are repelled by upper step edges which are decorated with molecules, as well as by larger contaminants on the surface.

The molecularly resolved STM image displayed in Fig. 3.18 (b) shows the hexagonal close packed arrangement of rubrene molecules inside the islands with an intermolecular nearest neighbor distance $a = 1.3 \pm 0.1$ nm. This intermolecular separation is about 1 Å larger than in the honeycomb patterns and leads to a wider hexagonal mesh in the hcp islands. Thus, the supramolecular hexagons are large enough to accommodate a sevenths molecule, which is not possible in the case of the honeycomb islets. The submolecular appearance of the molecules in Fig. 3.18 (b) differs from the appearances of the molecules presented up to now. The adsorbates reveal three pairs of two lobes in the shown STM image which are different in height and size. A detailed study uncovers that there exist unequal types of hcp islands showing different submolecular features in the molecules, e.g. the molecules in Fig. 3.18 (b) appear different than those in

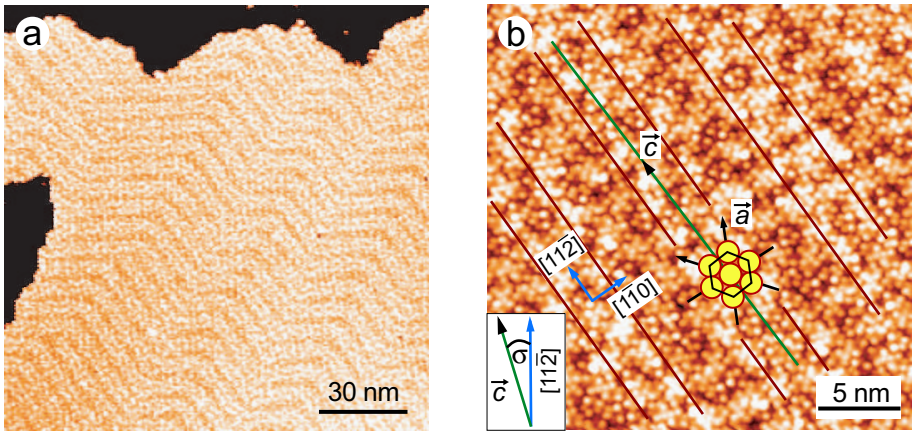

Figure 3.19: a) STM image of an extended hcp island revealing the zigzag pattern of the underlying herringbone reconstruction of Au(111). b) Molecularly resolved image exhibiting the domain walls along the [11$\bar{2}$] direction of Au(111) (brown lines) which are visible through the rubrene island. The two-dimensional hcp packing of the molecules is indicated together with the three nearest neighbor directions $\vec{a}$ and a second nearest neighbor direction $\vec{c}$. There is a small angular mismatch σ between the $\vec{c}$ orientation of rubrene and the [11$\bar{2}$] direction of gold, indicating the incommensurability of the hcp with the gold reconstruction and the gold(111) periodicity.

Fig.3.19 (b). This property and its implication on the electronic structure of the molecules will be discussed in detail in Sec. 6.1.

The very weak physisorption of rubrene on Au(111) is expressed by the incommensurability of the supramolecular assemblies with the periodicity of the underlying gold surface. This is obvious in the case of the assembly into pentagonal and hexagonal structures since the fivefold symmetry of a pentagon is incommensurate with a hexagonal (111) lattice. Moreover, the fact that the honeycomb patters adsorb with various inclinations with respect to the hcp troughs of the herringbone motif (see Fig. 3.8 (a) and Fig. 3.11), indicate that the molecules in these structures are neither in registry with the periodicity of the substrate. In the case of the extended hcp islands, the preservation of the herringbone reconstruction of the underlying gold indicates the weak interaction between the molecules and the substrate, in contrast to the reported lifting of the surface rearrangement by the formation of C_{60} islands [130]. Furthermore the hexagonal arrangement of the molecular island shows no dependence on the orientation of the reconstruction domains. This feature is shown in Fig. 3.19 (a), displaying the characteristic zigzag pattern of the surface reconstruction of Au(111) (see Fig. 3.1) under the hcp islands. Molecularly resolved STM images allow for a comparison of the hexagonal close packed directions of rubrene and gold. The image shown in Fig. 3.19 (b) reveals a small angular mismatch σ between the [11$\bar{2}$] direction of Au(111) and the second nearest neighbor direction $\vec{c}$ of the hcp arrangement of rubrene. This angle σ takes all values between 0° and 30° for different islands and thus demonstrates that the hcp ordering of rubrene is not commensurate with the gold surface, neither with the reconstruction, nor with the (111) periodicity.

The preference of the hcp islands to start their growth at the lower terraces of step edges leads to the typical behavior of the molecules to fill holes and valleys of the gold surface. This process results in partially filled spaces as shown in Fig. 3.20 (a) or in the complete filling of large valleys, demonstrating that the hcp islands are repelled exclusively from the upper level of decorated step edges and not from the lower one.

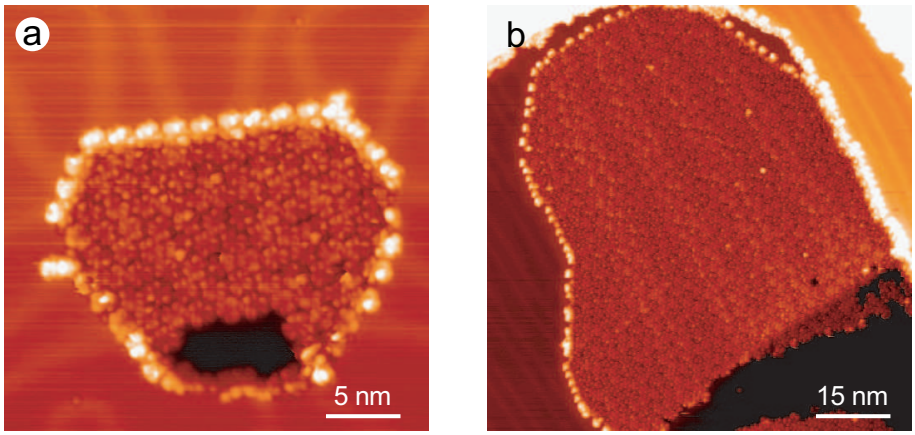

Figure 3.20: STM images showing the preference of hcp island growth from the step edge of the lower terrace. This results in a filling of holes and valleys in the gold surface.

3.6 Periodic and non-periodic plane-filling

The evaporation of a complete monolayer of rubrene on Au(111) yields an extension of the hcp islands over the whole surface. However, under different conditions of the sample preparation, e.g. for a deposition of the molecules outside the cryostat on a sample held at room temperature or above and a subsequent transfer of the sample into the cold STM chamber (preparation P2), the supramolecular self-assembly results in a new supramolecular phase (see Sec. 5.2). The STM image displayed in Fig. 3.21 (a) shows the resulting supramolecular self-assembly of the molecules on two terraces, separated by an atomic step. This overview reveals different areas showing variable packing densities and different degrees of supramolecular order. The zoomed image in Fig. 3.21 (b) shows three types of domains, denoted by A, B and C. While A and C appear as ordered arrangements, the inhomogeneous area B reveals no translational symmetry.

3.6.1 Non-periodic tiling with pentagons, hexagons and heptagons

This apparently non-periodic supramolecular phase is shown in Fig. 3.22 (a) and consists of a distribution of differently organized domains. The closeup view of such a loosely packed area displayed in Fig. 3.22 (b) evidences that it is composed of pentagons, hexagons and heptagons which appear to be randomly distributed over the surface. A consideration of the angles at the corners of a regular pentagon (108°), hexagon (120°) and heptagon ($180° - 360°/7 \approx 129°$) yields that only in the case of joining three hexagons with one common corner, the angular sum is exactly 360°. All other combinations would lead to a plane-filling with either uncovered gaps or overlapping polygons. There exist however three configurations which yield an angular sum close to 360° and are schematized in Fig. 3.23 (a). As expected, these three possibilities are indeed the most frequently realized in the non-periodic supramolecular tiling shown in Fig. 3.22 (b). The fact that the angular sum of the polygons involved in the patterning is either smaller or larger than the required 360° for a true plane-filling leads to small distortions of the side lengths and the angles of the objects, compared to regular polygons. The best suited combination is the combination of a pentagon, a hexagon and a heptagon which results in the smallest angular mismatch ($\approx 3°$). This is indeed the configuration which is most frequently observed in the non-periodic supramolecular phase and dominated over less frequent combinations such as two heptagons with a pentagon and two hexagons with a heptagon.

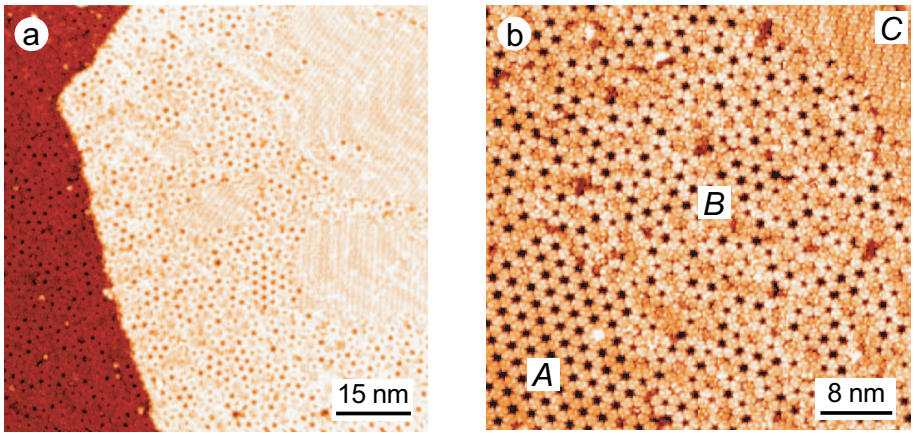

Figure 3.21: a) STM overview image showing a non-periodic plane-filling supramolecular self-assembly. The herringbone reconstruction of gold is visible in some areas. b) A closeup of one area reveals the coexistence of three different types of self-organization: honeycomb (*A*), non-periodic (*B*) and hcp (*C*) arrangement.

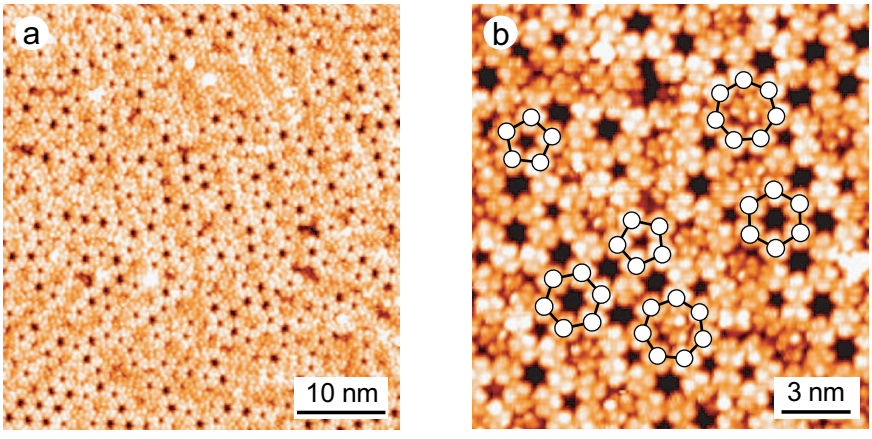

Figure 3.22: a) STM image of a non-periodic tiling. b) The zoomed area reveals the surface patterning with pentagons, hexagons and (filled) heptagons.

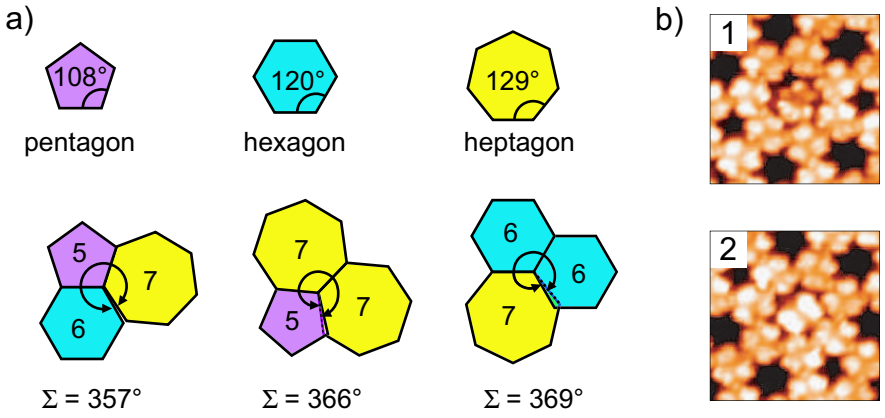

Figure 3.23: a) Schematic representation of an assembly of pentagons, hexagons and heptagons. Due to the respective angles of 108°, 120° and 180°−360°/7 ≈ 129°, a combination of these regular polygons results in three configurations which are close to the best case of the honeycomb arrangement (i.e three hexagons: Σ =360°). b) Closeup views (5 nm×5 nm) of heptagons which reveal the inclusion of an additional molecule inside the ring which appears either like molecules inside hcp patterns (1) or brighter and twofold (2).

The STM images displayed in Fig. 3.23 (b) uncover that the supramolecular heptagons in the non-periodic tiling accommodate an additional molecule in their center. This is in agreement with the observation that hexagons with an intermolecular distance and radius of 1.2 nm are not large enough to include a molecule in their center, while the hexagonal cell of the hcp islands offers enough space due to an intermolecular distance and radius of 1.3 nm. Since the radius of a heptagon with a side length of 1.2 nm is even wider, i.e. 1.4 nm, it is not surprising to find all holes of these polygons filled with molecules. These captured specimen appear in two different ways which are shown in the STM images displayed in Fig. 3.23 (b). While the additional molecule in the upper image resembles those observed in hcp islands, the lower image reveals a new conformation with a twofold and brighter appearance. These different molecular conformations are presumably due to the varying small deformations of the heptagon, offering more circular or more elliptical holes for the additional molecules.

3.6.2 Periodic tiling with pentagons, hexagons and heptagons

An arrangement of pentagons, hexagons and heptagons which is periodic throughout a whole domain is realized in another type of supramolecular phase present in this mixed surface coverage. An overview image of this tiling is given in Fig. 3.24 (a), showing a regularly appearing arrangement of differently sized holes in the supramolecular ordering. The blue bars indicate one possible repeating motif, which forms a centered rectangular two-dimensional lattice with alternating orientations of the supramolecular units along the diagonal of the unit cell, leading to a herringbone arrangement. The smaller scale image of Fig. 3.24 (b) reveals that these repeating supramolecular structures are pairs of hexagons which are inclined by an angle $\alpha = 90° - 360°/7 \approx 39°$ with respect to each other.

This inclination originates from the linking units between the pairs of hexagons which are made of pentagons and heptagons. This is shown in the schematic representation of the self-assembly into a periodic, plane-filling tiling which is displayed in Fig. 3.24 (c). Each hexagonal pair is surrounded by four pentagons and four heptagons, which need to be slightly deformed

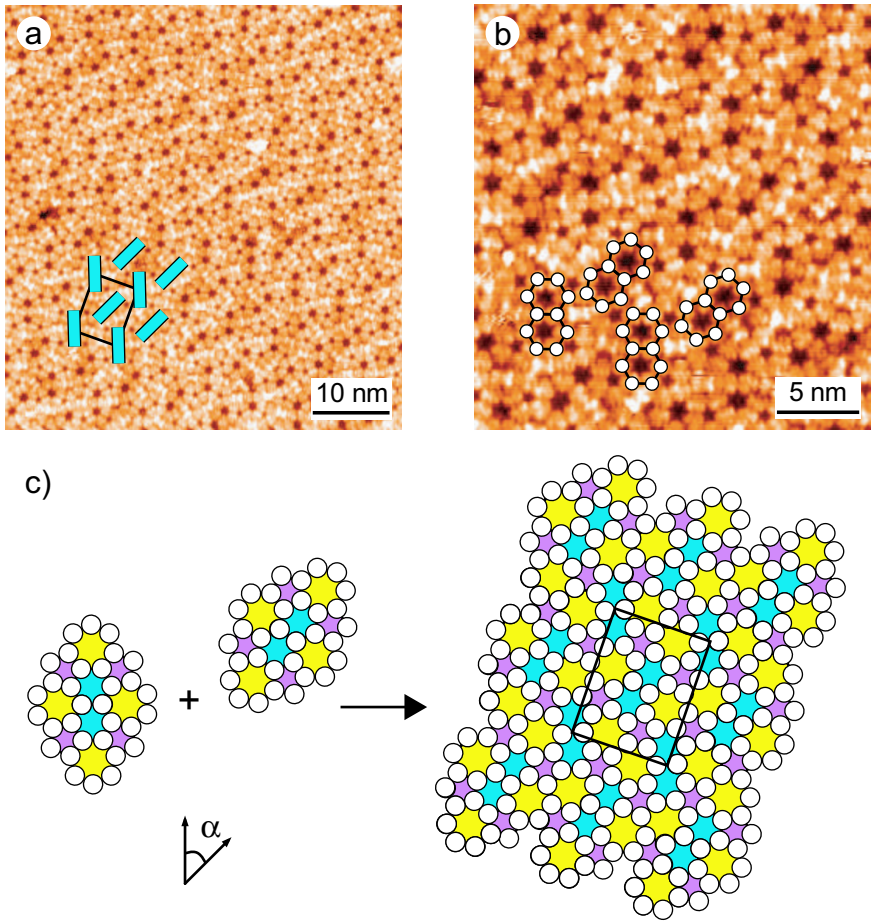

Figure 3.24: a) STM image of a periodic tiling consisting of a herringbone arrangement of supramolecular motifs which are indicated by blue bars. b) A magnified area reveals the periodic patterning of pentagons, hexagons and filled heptagons. The arrangement of hexagon-pairs are indicated by the superimposed drawings. c) Schematic representation of the supramolecular units found in the periodic tiling. A combination of these patterns into a herringbone arrangement leads to a plane filling supramolecular tiling.

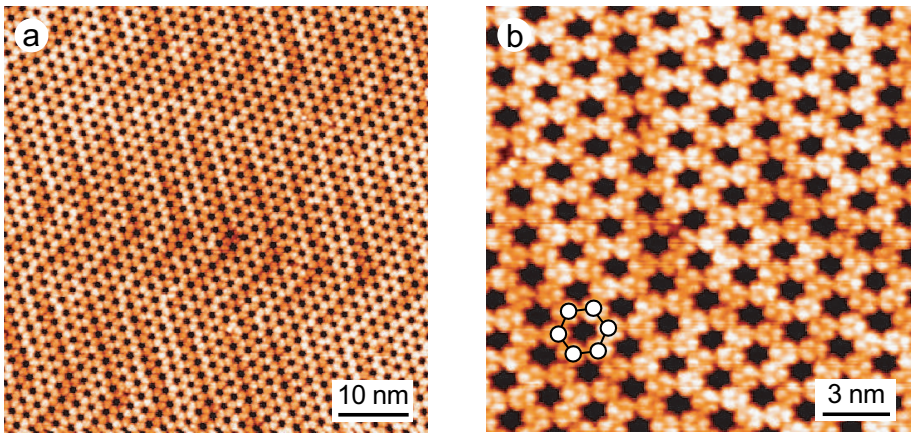

Figure 3.25: a) STM image showing an extended honeycomb patterned domain. The underlying herringbone reconstruction of gold is visible. b) Zoom into the honeycomb pattern revealing the periodic hexagonal arrangement with a nearest neighbor distance a=1.2±0.1 nm.

to compensate the angular mismatch of the adjacent angles. The fact that the value of α is connected to the corner angle of a heptagon reflects the fact that the linking unit between the pairs constitutes a heptagon. Arranging the pairs of hexagons in a herringbone motif with the angle α between the two different inclinations and filling up the space with pentagons and heptagons in a periodic way as shown in Fig. 3.24 (c) leads to a plane-filling periodic arrangement of the polygons. This tiling of the surface with pentagons, hexagons and heptagons uses those three configurations of the polygons which result in the smallest angular deviation from the ideal 360° (i.e. pentagon-hexagon-heptagon, heptagon-heptagon-pentagon and hexagon-hexagon-heptagon; see Sec. 3.6.1).

3.6.3 Supramolecular rosettes in honeycomb domains

The second type of ordered, periodic arrangement present in this patchwork-like surface tiling is an extension of the honeycomb islets presented in Sec. 3.3 and is already seen in the area A in Fig. 3.21 (b). While in the case of a deposition of rubrene onto a cold sample the dimensions of the obtained honeycomb patterns were in the order of tens of nanometers, the evaporation onto a sample at ≈ 300 K can lead to much larger islands. The STM image displayed in Fig. 3.25 (a) shows a large domain of perfectly ordered honeycomb arrangement. Such areas are found next to the non-periodic tiling discussed above and extend over hundreds of nanometers. The underlying reconstruction of gold is visible and reveals that the lines of hexagons in the honeycomb pattern are preferentially oriented along the domain boundaries. This is possible due to the fact that the zigzag shape of the herringbone has angles of 120°, which offers a matching with the sixfold symmetry of the honeycomb pattern. By taking into account that both, the uniaxial hcp/fcc domains, as well as the hexagonal lines of the honeycomb pattern, start preferentially perpendicular to the step edges of gold, this observation is coherent without compromising the conclusion of a substrate-independent supramolecular self-assembly (see Sec. 3.5).

A beautiful singularity existing inside these perfectly periodic domains is shown in the STM image of Fig. 3.26. The honeycomb pattern is locally interrupted by a circular replacement of the hexagons by a ring of alternating pentagons and heptagons, surrounding a core of seven hexagons. The closeup image shown in Fig. 3.27 (a) uncovers that the heptagons are again filled with additional molecules exhibiting the two different conformations, with a strong preference for the

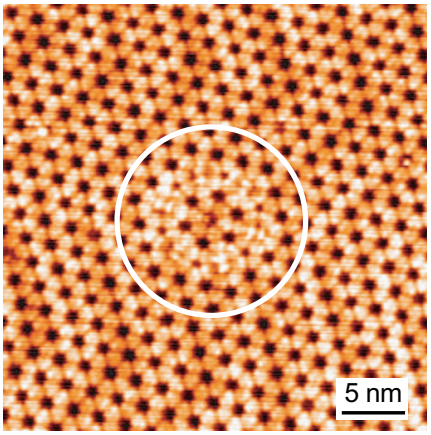

Figure 3.26: STM image showing a supramolecular rosette (encircled) inside an extended honeycomb pattern.

twofold geometry. The schematic representation of the rosette structure which superimposed to the STM image in Fig. 3.27 (b) reveals that this symmetric structure with six outer pentagons and heptagons forms a regular hexagon which is perfectly insertable into the surrounding honeycomb arrangement. However, due to the angular argument discussed in Sec. 3.6.1, a combination of a pentagon, hexagon and heptagon which share a common edge implies a distortion of at least one polygon. Since the ring of pentagons and heptagons suffer from this constriction from two sides due to the presence of an inner ring, as well as an outer ring of hexagons, this leads to a compression of both, the pentagons and the heptagons as indicated in Fig. 3.27 (c). Typically two or three supramolecular rosettes are found in each extended domain of honeycomb arrangement.

3.6.4 Hexagonal close packed domains of oriented molecules

A second periodic arrangement present in this patchwork phase consists of densely packed areas such as the one shown in the upper right corner of the STM image in Fig. 3.21 (b). In contrast to the hcp islands discussed in Sec. 3.5 where the molecular orientation within the hcp lattice was not well-defined, the molecules are organized into an ordered and locally periodic domains. Although the hexagonal symmetry is indicated in the image of Fig. 3.28 (a) and fixes the molecular centers at an intermolecular distance of 1.3 ± 0.1 nm, the molecules are furthermore organized into ordered rows which run parallel to lines appearing brighter. Inside of one row, the molecules having all the same fixed orientation, but this orientation is rotated by 180° in the adjacent rows. In addition, neighboring molecular lines are shifted by half of the intermolecular distance which leads to the hexagonal symmetry. These domains of alternating rows are interrupted by bright lines which are clearly visible in the images displayed in Fig. 3.28 and consist of molecules which appear different from the others. They run parallel within a domain of ordered hcp arrangement and unveil their importance by taking into account the chiral property of rubrene which is discussed in Sec. 4.2.1.

3.7 Multilayers of rubrene on Au (111): twin rows

The formation of multilayers changes the molecular self-assembly and the adsorption conformation drastically. The multilayers are obtained by a longer evaporation of rubrene molecules onto

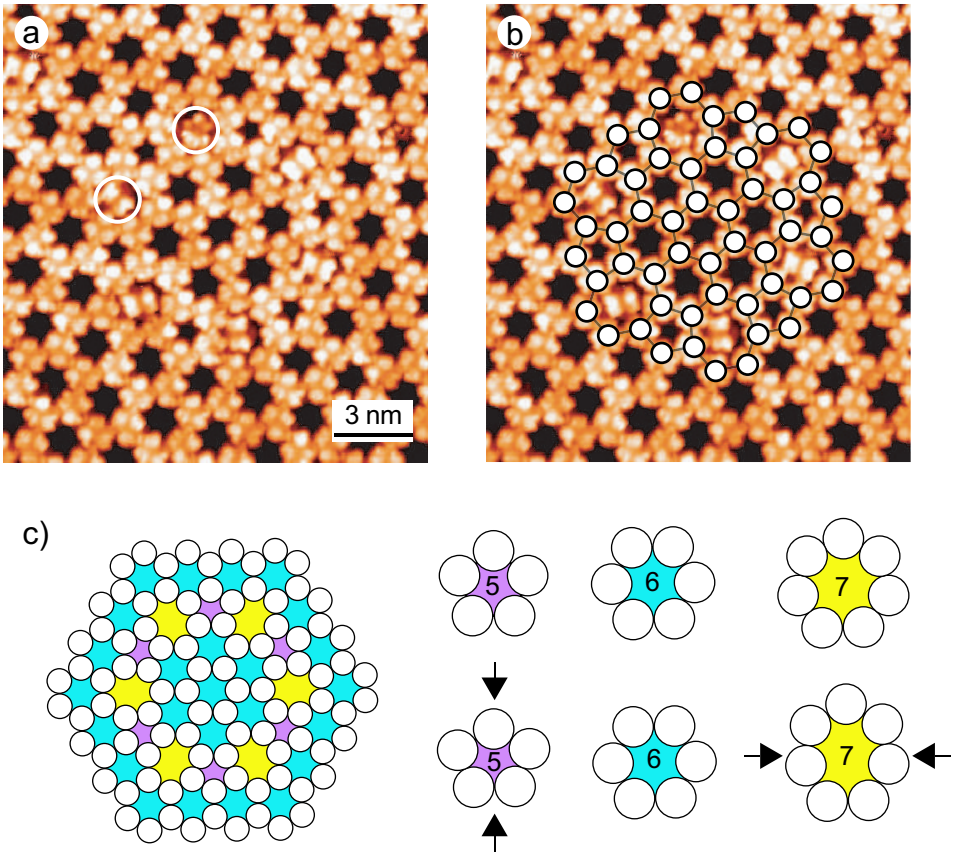

Figure 3.27: a) STM image of a supramolecular rosette. The white circles indicate the presence of additional molecules inside the heptagons. b) Schematic drawing of the rosette formation superimposed to the image (a). c) Schematic drawing of the supramolecular rosette, formed by 54 molecules which are building 7 hexagons, surrounded by 6 distorted pentagons and 6 distorted heptagons.

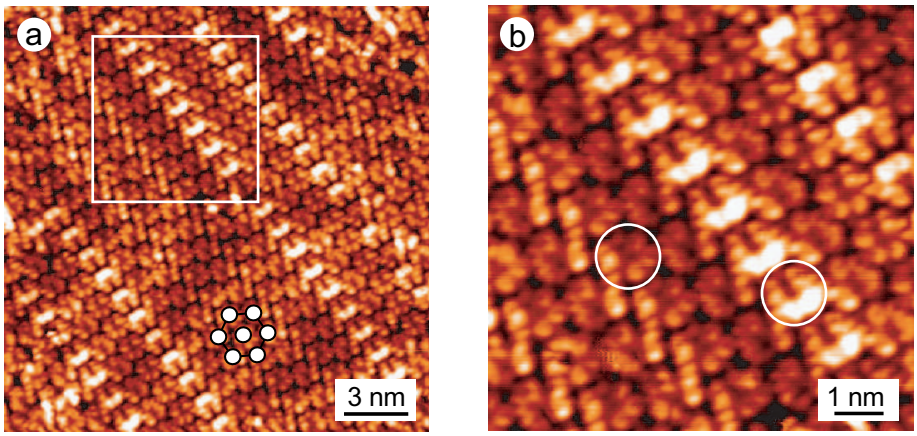

Figure 3.28: a) STM image of molecules assembled into a densely packed domain of oriented molecules. The local symmetry is hcp with an intermolecular distance of 1.3±0.1 nm. Parallel running brighter rows along one of the high symmetry directions of the hcp separate different domains of variable widths. The underlying surface reconstruction of gold is visible. b) Zoomed image of the area indicated by the square in (a) revealing that the individual molecules have different submolecular features in the bright lines than in the flat domains. The molecules are ordered into rows running parallel to the separation lines and having molecules of the same orientation within one row.

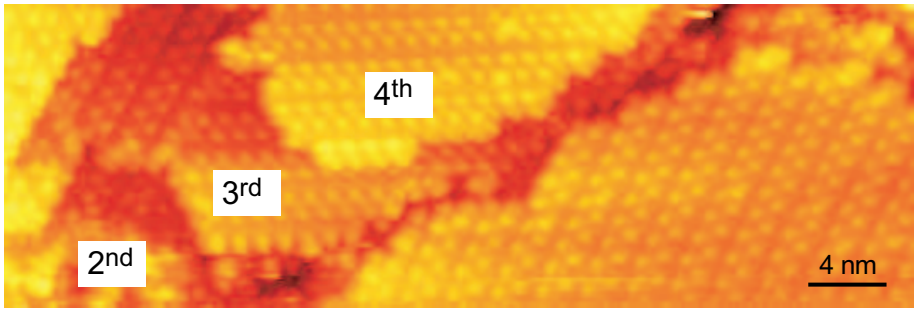

Figure 3.29: STM image showing a 2nd, 3rd and 4th layer of rubrene on Au(111) (Tunneling parameters: $V = -3.3$ V, $I = 20$ pA).

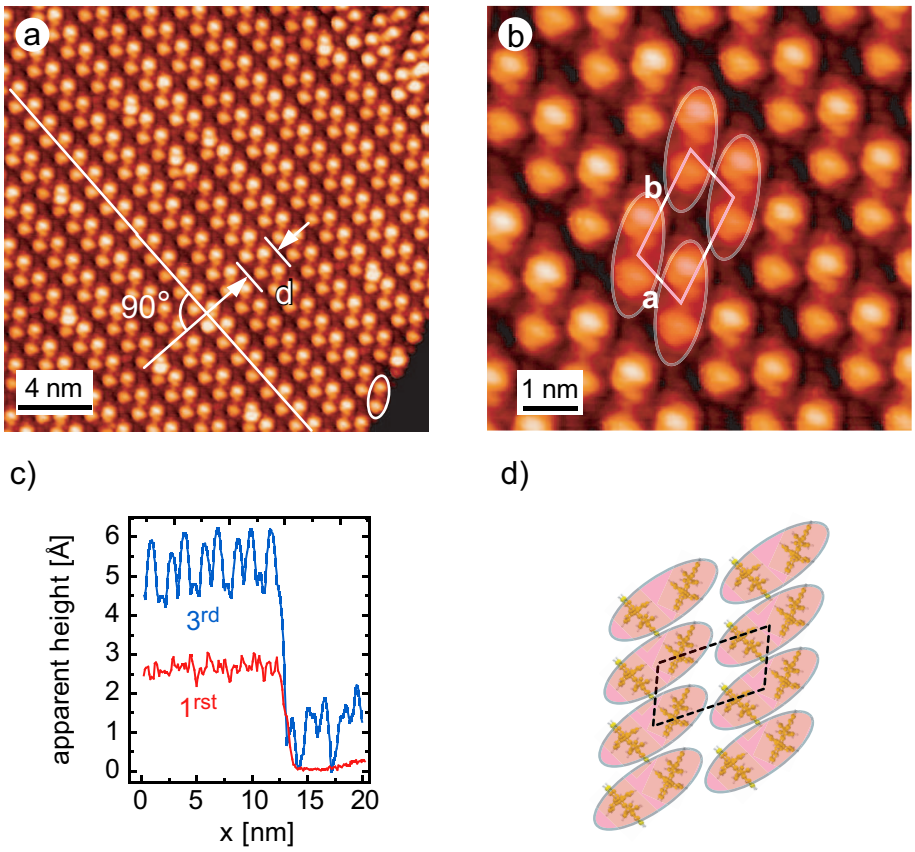

Figure 3.30: a) STM image showing the twin rows forming the second and higher layers of rubrene. The distance between the twin rows (perpendicular to the row axis) is d=2.0±0.1 nm. b) Detail of a domain shown in a). A unit cell is indicated with lattice parameters a=1.1±0.1 nm and b=2.2±0.1 nm. There are two molecules in a unit cell which are paired (encircled). (Tunneling parameters: a), b) $V = -3.3$ V, $I = 20$ pA) c) Line scans revealing the step height of a 3rd laver on a 2nd layer (blue) and of a monomolecular layer on gold (red). d) Proposed arrangement of the molecular pairs into an oblique unit cell.

the gold sample held at ambient temperature. The STM image displayed in Fig. 3.29 shows the 2nd, 3rd and 4th layer of rubrene on Au(111), measured at an elevated tunneling voltage of typically -3.3 V. In contrast to samples with a submonolayer coverage, imaging of the multilayers was only possible for a sample bias $V \leq -2.2$ V. The multilayers reveal parallel running rows, which are well resolved in Fig. 3.30 and reveal that each parallel line consists of a zigzag arrangement of circular protrusions. The distance between these twin rows (perpendicular to their orientation) is $d = 2.0 \pm 0.1$ nm.

The closeup view in Fig. 3.30 (b) reveals that the intermolecular distances in the zigzag rows are different for opposite directions along the rows. This observation leads to two possible ways to form pairs of molecules, building up the supramolecular line. A study of the layer edges reveals that the predominant termination of the rows is realized by pairs of molecules with the larger intermolecular distance (see Fig. 3.30 (a)). This observation suggest that these pairs of molecules constitute the building blocks of the twin rows. A possible unit cell with two molecules in each corner is superimposed to the STM image shown in Fig. 3.30 (b) and has side lengths $a = 1.1 \pm 0.1$ nm and $b = 2.2 \pm 0.1$ nm at an angle of about 110°. The molecules appear smaller

(diameter $<$ 1 nm) than the molecules which are adsorbed directly on the bare gold surface ($\approx$ 1.2 nm) and reveal no reproducible submolecular contrast[3]. This aspect, together with the different self-organization into twin rows, suggests that the rubrene molecules adopt a different conformation if they are adsorbed onto a molecular layer than in the case of an adsorption onto the bare metal surface.

The cross sections presented in Fig. 3.30 (c) show the step height of a 3$^{\text{rd}}$ layer[4], together with the one of a monolayer on gold. The comparison reveals that the apparent layer thickness[5] of the 3$^{\text{rd}}$ layer ($\approx$ 5.0 nm) is almost the double of the monolayer thickness ($\approx$ 2.5 nm) on the bare metal surface. This variation in height corroborates the supposed different adsorption behavior of rubrene on a rubrene layer, compared to the adsorption of rubrene on Au(111) and indicates that different forces act between the molecular layers than between molecules and the gold surface. However, the molecules bind to each other and appear in the same way in the case of layer formation onto the hcp arranged first monolayer, as for an adsorption onto twin rows of a second or third molecular layer. This indicates a small influence of the underlying molecular arrangement onto the adsorption and self-assembly mechanism in the multilayers.

The larger thickness of the twin row layers, together with the smaller lateral dimensions of the individual molecules suggest that the molecular conformation of adsorbed rubrene is more inclined than on Au(111) [39]. Consequently, there are two possible adsorption geometries for molecules inside multilayers: either with the tetracene backbone standing upright on the surface, or with its long axis parallel, but with the short axis perpendicular to the surface plane. The fact that in the second configuration, two phenyl groups on one side are establishing a bonding to the underlying molecules makes this version more reasonable than the upright orientation with only one of the six interacting molecular "corners" (the four phenyl groups and the two sides of the tetracene backbone; see Sec. 1.2.1). This presumable adsorption conformation reminds also the molecular packing in an orthorhombic rubrene crystal, resulting in a herringbone arrangement of the molecules inside the (a-b) plane (see Sec. 1.2.1). In analogy to this two-dimensional ordering with alternating molecular orientations, a possible unit cell of the twin row pattern has the shape of a parallelogram with side lengths $a = 1.1 \pm 0.1$ nm and $b = 2.2 \pm 0.1$ nm and pairs of molecules in the four corners as presented in Fig. 3.30 (c).

The STM image showing a step edge of a multilayer in Fig. 3.31 (a) demonstrates that each motif of this molecular arrangement is really composed of two rubrene molecules. While one side of the edge is terminated by the elongated building units of the rows, the left part reveals ends with an additional protrusion, which is consequently identified as an individual molecule. These unpaired molecules allow furthermore for the formation of boundaries which link together domains of different orientations. This property is seen in the closeup view of a transition region between twin row domains which are rotated by 60° with respect to each other.

The bonding of molecules into supramolecular arrangements forming perfectly parallel rows on the surface has been reported on various systems [14, 11, 13, 16]. The explanation of the interaction mechanisms between the molecules in this type of assembly appears more intuitive than for the multifaceted structures of rubrene observed at submonolayer coverage. The diversity of the existing geometries and the coexistence of different bonding angles suggest a subtle combination and competition of intermolecular forces directing the self-assembly of rubrene on Au(111).

[3] In monomolecular layers the molecules exhibit submolecular contrasts even at these high voltages (see Sec. 6.4).

[4] The step heights of the 2$^{\text{nd}}$ and 4$^{\text{th}}$ are close to this value.

[5] This value of the layer thickness is only the apparent height, measured with STM which is not implicitly equal to the geometric height of the molecules (see Sec. 2.3).

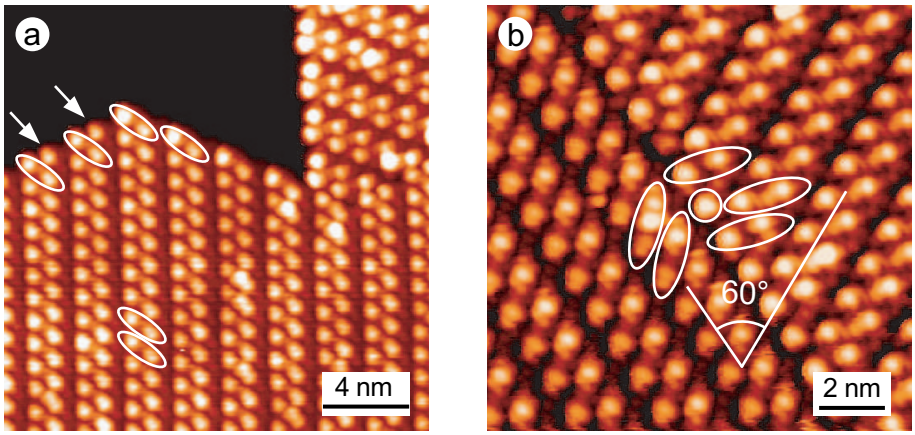

Figure 3.31: a) STM image showing the termination of a multilayer organized into twin rows. The ellipses indicate pairs of molecules and the arrows show that non-paired molecules form row ends, too. b) Detail of a boundary, separating two domains which are rotated by 60° with respect to each other and use unpaired, individual molecules (encircled) to form the transition between the domains. (Tunneling parameters: a), b) $V = -3.3$ V, $I = 20$ pA)

dipole-dipole[a]	quadr.-quadr.[a]	vdW[b]	XH···Y[c]	XH···π[d]	$\pi\cdots\pi$[e]
$\propto r^{-3}$	$\propto r^{-5}$	$\propto r^{-6}$	X-H → Y	(X-H) $\perp$ π-system	$\pi \parallel \pi$-system

Table 3.1: Attractive intermolecular forces and the dependence of their interaction potential on the distance r or the orientation of essential parts of the molecules.
[a] Maximal electrostatic interaction energy between permanent dipoles and quadrupoles.
[b] Van der Waals interaction due to the attraction between fluctuating dipoles.
[c] Hydrogen bonds between an X-H group (X,Y=F, N, O) pointing to an Y.
[d] Weak hydrogen bonds between an X-H group (X=N, O, C) and a π system.
[e] Interaction between π systems.

3.8 Intermolecular bonding of rubrene

Supramolecular chemistry is driving basic processes in living system and denotes the "chemistry of molecular assemblies and of the intermolecular bond" [6] [131]. While the strong *intra*molecular bonds are of ionic or covalent character, *inter*molecular bonds are mainly based on weak, non-covalent interactions such as dipole-dipole (or higher order multipole) forces, hydrogen bonding[7] or vdW interactions[8]. The weakness of these intermolecular forces results in less stable and more flexible assemblies than in the case of the intramolecular bonding of atoms into a molecule. Furthermore, the high number of possible non-covalent interactions makes a prediction of supramolecular structures difficult and might even result in the coexistence of different metastable supramolecular assemblies of similar energies [132].

The specific intermolecular forces which may contribute to an attraction between the molecules are summarized in Tab. 3.1 together with the corresponding dependence on distance r (for the

[6] J.-M. Lehn, Nobel Prize in Chemistry 1987.
[7] The physical origins of hydrogen bonds are actually electrostatic, vdW and ionic/covalent forces.
[8] The vdW forces are also called *London* or *dispersion* forces.

electrostatic forces) and the orientation of the interacting groups (in the case of vdW, $\pi\cdots\pi$ interactions and hydrogen bonds). The absence of charges and the negligible dipole moment in rubrene [53] excludes electrostatic forces between charges and dipoles. The same is valid for the hydrogen bonds of type XH$\cdots$Y (X,Y=F, N or O) which are discarded due to the absence of these highly electronegative atoms X in rubrene. However, higher order multipoles such as e.g. quadrupoles are presumably present, given that constituent parts of rubrene (i.e. benzene and tetracene) possess significant quadrupole moments. Consequently, the intermolecular bonding between rubrene molecules might have contributions from electrostatic quadrupole-quadrupole interactions, vdW forces, $\pi\cdots\pi$ bonding and CH$\cdots\pi$ interactions [133, 134, 135, 136].

The STM measurements of the self-assembled structures presented in this chapter demonstrate a competition of these forces for a decisive influence on the supramolecular assembly of rubrene. There are two cases of two-dimensional ordering to consider: On the one hand, the dense packing of the hcp islands exhibits non-directional interactions between the molecules, indicating a dominant contribution from the isotropic vdW forces. On the other hand, the directional assembly into small structures from trimers to pentamers and hexamers, as well as the honeycomb patterns strongly suggests an impact of anisotropic quadrupole-quadrupole interactions, $\pi\cdots\pi$ interactions and CH$\cdots\pi$ hydrogen bonds.

While the $\pi\cdots\pi$ contributions promote a parallel arrangement of the π systems, the CH$\cdots\pi$ bond is particularly strong for a perpendicular orientation of the CH group to a π system of another molecule [135]. Moreover, this hydrogen bond is stronger if the hydrogen is bonded to a sp^2 hybridized carbon. The structure of rubrene is a suitable candidate for the realization of those forces which rely on the existence of π systems, due to the four easily rotatable phenyl groups, the non-planar aromatic tetracene backbone and the presence of a total of 28 sp^2-hybridized CH bonds, pointing into three dimensions (see Fig. 1.1). The CH$\cdots\pi$ hydrogen bond is of importance for biological systems and influence the molecular packing in organic crystals [136]. In combination with the $\pi\cdots\pi$ interactions, this "non-conventional" hydrogen bond stabilizes the formation of the herringbone arrangement found in molecular solids like rubrene (see Fig. 1.2 (a)). The combination of all three anisotropic forces acting between different parts of the molecules at the same time is thus assumed to drive the directed assembly into strictly ordered pentagonal and hexagonal structures while the isotropic vdW forces might account for the densely packed hcp islands without a fixed molecular orientation.

The intermolecular bonding of rubrene molecules into pentagonal and hexagonal supermolecules, honeycomb islets and hcp islands is strong enough to keep the structures stable at temperatures of 50 K. Due to the high mobility of smaller assemblies, dimers, trimers and tetramers are not imaged at this temperature and could therefore not be studied. The stability of the closed structures is also confirmed by the application of strong tip-sample interactions due to low tunneling resistances (e.g. low bias voltage and high currents) which do not easily destroy the intermolecular bonds. Contrary to this behavior, supramolecular chains which are constructed out of pentagonal supermolecules into open structures are less stable than the constituent pentagons. While at 5 K the supramolecular chains stay complete, the situation is different at 50 K, where the thermal energy is high enough to break the bonds between those supramolecular pentagons which are not stabilized inside circular structures, such as nearly complete and complete decagons of pentagons. An evaluation of the thermal energy $k_{\mathrm{B}}T \approx 4$ meV of the molecules at 50 K leads to a rough estimation of the activation energies for bond breaking of individual molecules and pentagonal supermolecules inside of circular structures ($\gg 4$ meV) and of the much lower value for only singly bonded pentagons in open supramolecular chains (≈ 4 meV).

3.9 Conclusions

The self-assembly of rubrene on Au(111) creates supramolecular structures on the surface which are of unprecedented diversity concerning the large number of different phases obtained. A novel finding consists furthermore in the observation of fivefold and sevenfold symmetries which are present in these assemblies. In the submonolayer regime, individual molecules and small self-assembled dimers, trimers, tetramers, pentamers and hexamers are observed dispersed on the gold terraces for a temperature of 5 K. A surprising finding is the coexistence of hexagonal and pentagonal symmetry, the latter resulting from a contraction of a pentamer which is originally constructed by the same angles of 120° as the trimers, tetramers and hexamers. This change to 108° of the angle formed by three adjacent molecules demonstrates an angular flexibility of the intermolecular bonding which is extended to the occasional formation of heptagonal structures with an angle of 129°.

Larger self-assemblies consist of regular honeycomb islets and pentagonal supermolecules which interlock like small gearwheels to construct elongated curled chains forming beautiful supramolecular labyrinths on the gold surface. Upon an increased coverage, hcp islands grow from lower step edges on and show no regular orientation of the molecules inside of the islands. All assembled rubrene structures exhibit an almost complete independence of the substrate periodicity and herringbone reconstruction which is preserved and visible under the different patterns. However, the elbows of the surface reconstruction are slightly preferred adsorption sites for circular structures like the pentagonal supermolecules and the supramolecular decagons. Furthermore, the bridge sites between the hcp and fcc stacking influences the direction of longer structures.

The deposition of rubrene following preparation method P2 results in an additional supramolecular phase which covers completely the surface at a coverage of 1 ML. This patchwork phase is composed of different domains comprising extended regular honeycomb patterns with local perturbances formed by supramolecular rosettes. Other areas are patterned by non-periodic and periodic tilings formed by a plane-filling arrangement of slightly deformed pentagons, hexagons and heptagons which resemble the complex surfaces of quasicrystals [126, 137, 138]. Furthermore, hcp domains of molecules oriented into fixed directions are observed which differ in their organization from the hcp islands obtained by a sample preparation P1. The assembly of rubrene into multilayers on Au(111) differs from the submonolayer case, resulting in the formation of extended domains of regular twin rows, which are rotated by 60° with respect to each other. The individual molecules reveal a reduced submolecular contrast and much larger apparent height compared to the molecules directly adsorbed on gold.

The construction of various supramolecular structures which differ strongly regarding their geometric assembly suggests that different mechanism direct the respective intermolecular bonding. The precise angle of 120° of the small structures indicate the impact of directional forces originating from quadrupole-quadrupole interactions, $\pi \cdots \pi$ interactions, and $\mathrm{CH} \cdots \pi$ hydrogen bonds, which are however flexible enough to allow for a deformation into pentagonal and heptagonal angles. In contrast to this bonding, the densely packed and unoriented arrangement of the molecules inside of the hcp islands suggest the acting of anisotropic vdW forces.

Chapter 4

Chiral recognition in a hierarchical supramolecular self-assembly

Molecular and supramolecular chiral recognition governs fundamental processes in living systems [60, 139]. Its importance for disciplines such as biology, pharmaceutics, chemistry, and physics stems from the different properties the two chiral forms exhibit in the presence of chiral phenomena, such as, for example, chiral enzymes and drugs [7], β-rays [62], circularly polarized light [140], and spin-polarized electrons [141]. The differences in physical and chemical characteristics should become important for the design of molecular electronic and optoelectronic devices [28, 29, 27]. Pioneering work has been done by the determination of the chirality of individual molecules of 2-bromohexadecanoic acid [9] and alkene [8] with the STM, followed by the study of the enantiomeric composition and overall chirality of supramolecular assemblies [142, 143, 144]. Amongst others, investigations have been performed dealing with the aspect of chirality in the self-assembly of small molecules such as 1-nitronaphthalene [92, 145], tartaric and benzoic acid [14, 11], cysteine [12], adenine [13], and alanine [15]. Less studies have been performed until now on the impact of chirality on the self-organization of larger three-dimensional molecules, such as the hydrocarbons HtBDC ($C_{60}H_{66}$) [146] and heptahelicene ($C_{30}H_{18}$) [147, 148, 16]. However, the spontaneous resolution of a racemic mixture of adsorbed molecules into enantiopure structures is less frequent and restricted to the assembly of small molecules [10, 11, 12, 13, 149, 150]. The intriguing mechanism of a hierarchical self-assembly of molecular species on surfaces consists of the spontaneous organization of individual molecules into small two-dimensional clusters which, in a next step, build larger structures, and so on. This concept results in an autonomous creation of complex supramolecular structures. STM observations demonstrate the results of such a hierarchical organization constructed by two consecutive assembly steps [13, 151, 15].

4.1 Hierarchical self-assembly

One of the most intriguing findings on the self-assembly of rubrene on Au(111) at submonolayer coverage is the formation of symmetric structures which combine into complex supramolecular architectures. The formation of elongated, curled supramolecular chains is presented in Sec. 3.4 and described as an assembly of pentagonal supermolecules. The observation that part of the pentagonal chains are not stable at a temperature of 50 K and disintegrate into stable pentagons which diffuse on the surface suggests an explanation of the assembly in terms of a two-stepped assembly from molecules to pentagonal supermolecules, followed by the binding of the pentagons into supramolecular chains. Consequently, there are two consecutive bonding steps which obey different laws: the assembly of individual molecules into supramolecular pentagons, which is

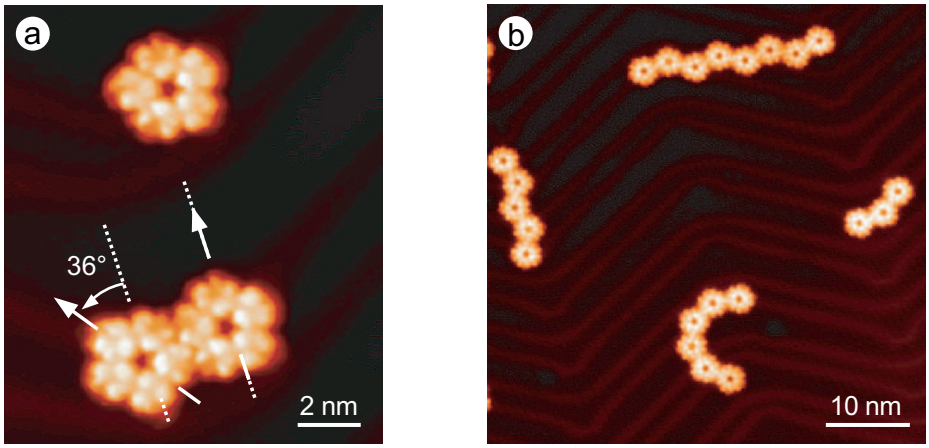

Figure 4.1: a) STM image of an individual pentagonal supermolecule and a dimer of pentagons which is formed by a rotation of 36° of one of the supermolecules with respect to the other. b) STM image showing different results of a self-assembly into pentagonal chains.

discussed in Sec. 3.2 and the linking of these supermolecules into pentagonal chains.

The mechanism of the second step is captured in the STM image displayed in Fig. 4.1 (a), showing a single pentagonal supermolecule next to a dimer of pentagons. As already mentioned in Sec. 3.4, the two supermolecules are interlocked like small gearwheels, but a closer look to the image reveals furthermore that the linking happens at a precise angle of 36° between the two interacting parts. The reason for this rotation lies in the peculiarity of the inter-pentagonal bonding, favoring a linking of the pentagons with their connecting sides oriented parallel to each other, such that four molecules interact with each other. The case of a bonding between only two molecules of the pentagons, i.e. with the pentagons facing each other with the corners and not with the sides[1], is occasionally observed at a temperature of 5 K, i.e. when the motion of the supermolecules is "frozen" and the activation energy for a breaking of this less-favorable bonding is higher than the thermal energy of the molecules. The dominant linking of two pentagons with parallel sides leads to an angle of 36° between the orientations of adjacent pentagons and results in the creation of chains of non-linear and diverse shape, such as shown in Fig. 4.1 (b). Joining pentagons one by one with a rotation of 36° between adjacent supermolecules, the first molecule offers five equal docking sites for a second pentagon, but from then on the last molecule possesses only two linking sites for additional supermolecules. This is schematized in Fig. 4.2, showing the assembly into the different possible shapes of the pentagonal chains up to a length of five pentagons. The process allows for one special assembly which takes place if the arriving pentagons choose exclusively the same bonding site on the last pentagon. The corresponding option is encircled in the schematic assembly of Fig. 4.2 and reveals a perfect circular bending of the structures.

This circular assembly into real supramolecular chains made of rubrene is observed in the STM images shown in Fig. 4.3 (a) and leads to the cyclic geometric structure formed by ten pentagons, which is presented at the end of the row. The STM image in Fig. 4.3 (b) shows such a supramolecular decamer which is constructed by an assembly of pentagonal supermolecules with angles of 36° between adjacent pentagons. The geometry of this structure is schematized in Fig. 4.3 (c) and demonstrates that the linking of ten regular pentagons leads to the formation

[1]This corresponds to a configuration with the two interacting molecules joining in the the same way as in the case of a dimer.

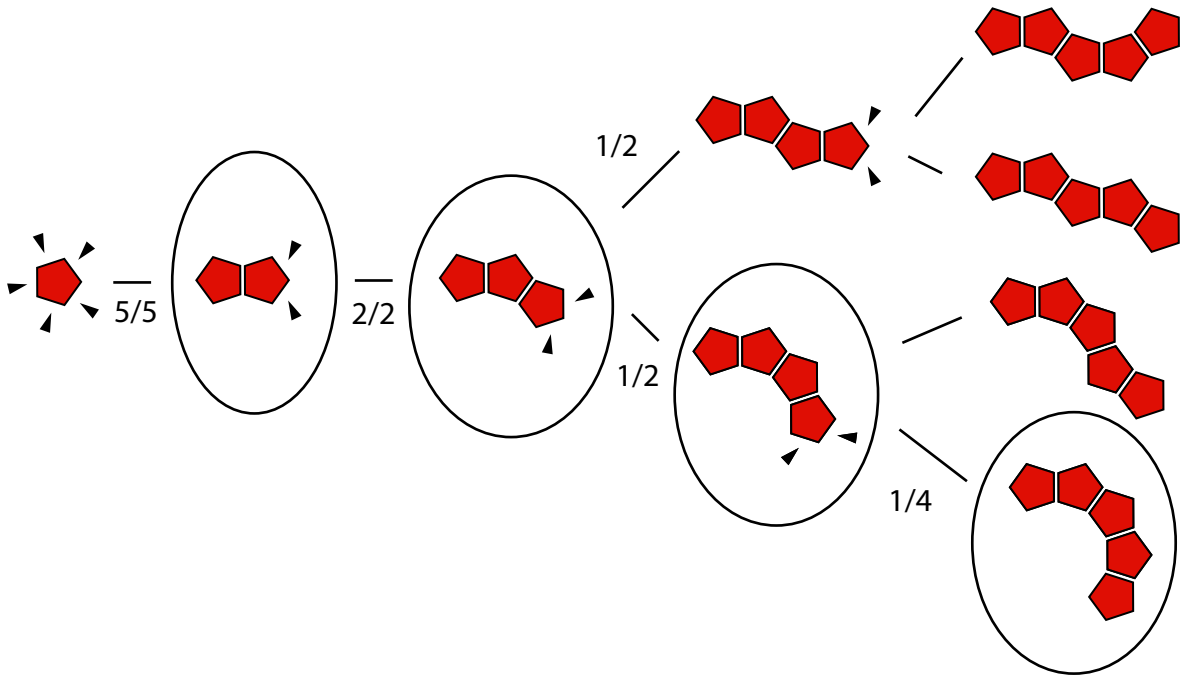

Figure 4.2: Schematic representation of the interlocking mechanism leading to the formation of differently shaped pentagonal chains. From the second pentagon on, each pentagon at the end of the chain offers two possible bonding sites (indicated by the black triangles) for an additional supermolecule. The choice between two possibilities results in a branching of the assembly from the tetramer on, favoring the creation of zigzag chains compared to the circular assembly.

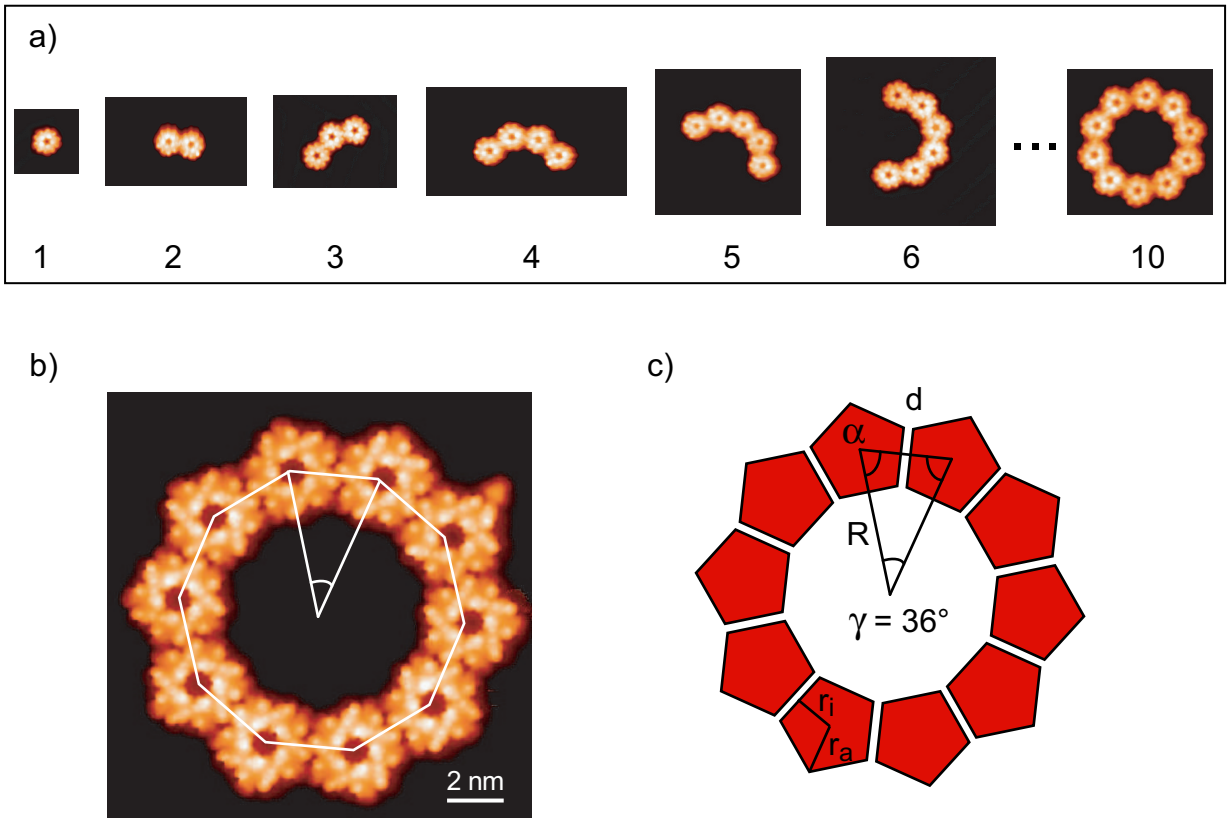

Figure 4.3: a) STM images showing the construction of a supramolecular decamer of pentagonal supermolecules. b) STM image of a closed structure forming a regular decagon (as indicated by the white line). c) Geometry of a regular decagon with γ =36°, α =72° and the values of the supramolecular decagon shown in (a): d=3.0±0.1 nm and R=5.0±0.1 nm.

of a regular decagon. Since the two angles α at the side d of the shown triangle are equal to 72°, the angle γ at the center of the triangle gets equal to 36° and thus is a factor of 360°. A superposition of a regular decagon with the STM image shown in Fig. 4.3 (b) confirms that this geometry describes the observed supramolecular structure and permits a determination of the dimensions of this polygon to the side length $d = 3.0 \pm 0.1$ nm (corresponding to the inter-supermolecular distance) and the radius $R = 5.0 \pm 0.1$ nm. The construction of these nested supramolecular decagons of pentagonal supermolecules (consisting on their own of individual molecules) is expected to have a low probability, taking into consideration the assembly scheme shown in Fig. 4.2 which predicts a probability of $(\frac{1}{2})^7 \approx 1\,\%$ for the assembly of ten pentagons into a closed ring. This value explains well the rarity of the nested structures in the case of a low density of supramolecular pentagons on the surface, where the assembly mechanism is presumably correctly described by the schematized one-by-one addition of pentagons. However, the presence of a large number of pentagonal supermolecules on the surface at higher densities might result in the formation of many fragments of decagons which might link to each other as a whole and thus increase significantly the probability of constructing a complete decagon. This rationalizes the much higher occurrence of those circular structures on surfaces which are covered with a high density of pentagonal supermolecules.

The formation of a regular polygon by an assembly of smaller regular polygons is an exceptional geometric phenomenon which exists in only six variants, shown in Fig. 4.4. The first two polygons are special cases since they are densely packed with the small polygons pointing with an edge in the center of the resulting polygon. They are different from the four other possible combinations, which create an "open" polygon with one of the sides of the small polygons facing the center of the large structure. These four polygons are the decagon of pentagons (c), the hexagon of hexagons (d), the square of octagons (e) and the triangle of dodecagons (f). The latter four cases are the only geometries which fulfill the condition that joining two polygons with one of their sides together, creates an angle between the prolongations of the respective inner radii r_i in the polygons which divides 360°.[2] Apart from the fact that the decagon of pentagons is the polygon of highest (i.e. tenfold) symmetry, it has a second property which is different from the other polygons and which is of importance for the supramolecular assembly of molecules on a surface. While all the other combinations are plane-filling patterns which can be continued periodically into two dimensions,[3] the decagonal geometry of the polygon of pentagons does not possess translational symmetry.

The bonding of individual molecules into small supermolecular structures, followed by the formation of larger supramolecular structures establishes a hierarchy of the self-assembly of rubrene which is presented in Fig. 4.5. The scheme denotes three different generations, consisting of the individual molecules, the small supramolecular structures and honeycomb islets, and the pentagonal chains, including in particular the nested structures of supramolecular decagons. The progression is vertically separated into a hexagonal and a pentagonal family, which is induced by the branching of the small structures of the second generation into two geometries which have either a hexagonal basis or contract into a pentagonal shape. The hexagonal fragments (dimers, trimers, up to zigzag chains) combine to form supramolecular pentagons and larger honeycomb patterned islets which belong to the same generation. In contrast to this assembly staying on the same level of the hierarchy, the pentagonal supermolecules are size-defined stable building units which join in a second assembly step into supramolecular chains of variable length and into decagons, thus building a third organizational level.

[2] This situation occurs if the angle α of a polygon satisfies the equation: $360° \mathrm{mod}(180° - 2 \cdot \alpha) = 0$.

[3] A tiling with hexagons of hexagons leads for example to the honeycomb pattern presented in Sec. 3.3.

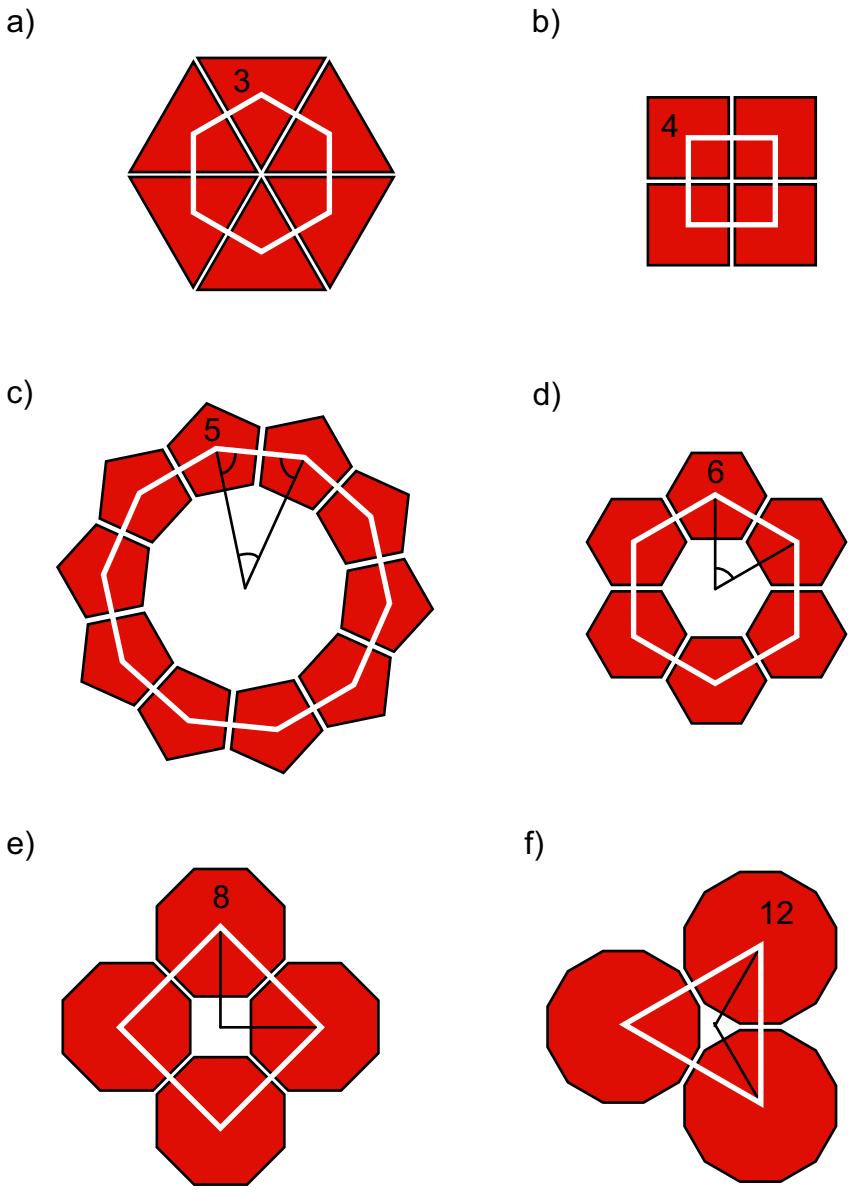

Figure 4.4: Schematic drawings showing the six possible assemblies of regular polygons into a regular polygonal geometry. a) Hexagon of triangles. b) Square of squares. c) Decagon of pentagons. d) Hexagon of hexagons. e) Square of octagons. f) Triangle of dodecagons.

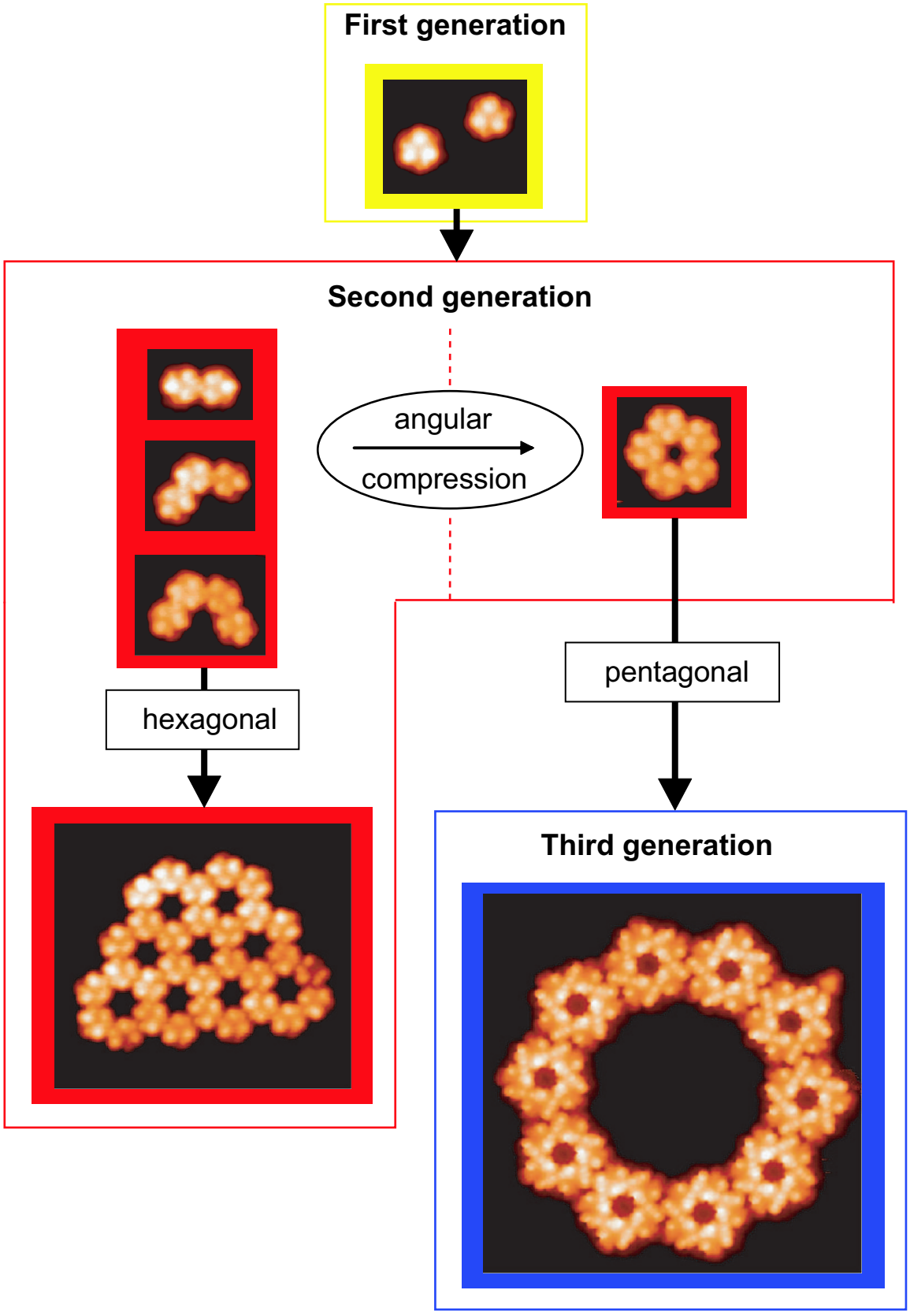

Figure 4.5: Hierarchy of the self-assembly, consisting of three generations of supramolecular structures which are divided vertically into a hexagonal and pentagonal family.

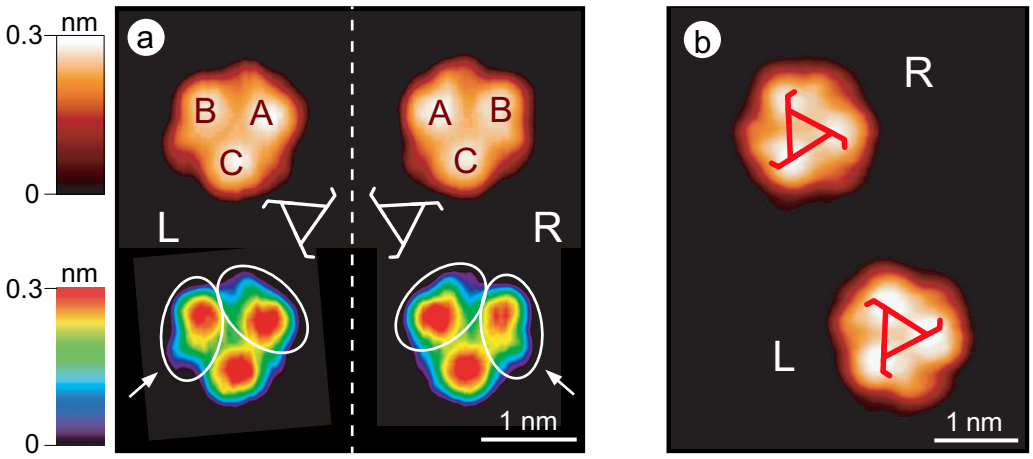

Figure 4.6: Chiral conformation of individual rubrene molecules seen in the STM images. a) The monomers possess three maxima A, B and C with shoulders which are visible in the lower panels. The **R**-type monomer (**L**-type) has a counterclockwise (clockwise) arrangement of the maxima ABC and the shoulders on the left (right) side of the maxima A and B (seen from the center of the molecule), schematized by the chiral triangles. b) Both enantiomers are adsorbed next to each other on the Au(111) surface.

4.2 Chiral recognition on all stages of a hierarchical self-assembly

In the preceding discussions about the supramolecular structures of rubrene on Au(111) and the progression of structures into a three-staged hierarchy, the chirality of rubrene (see Sec. 1.2.1) has not been taken into consideration. With the inclusion of this inherent property of the individual molecule, a new aspect enriches the investigation of the self-assembly of rubrene into hierarchically organized supramolecular structures.

4.2.1 Chiral conformation of single molecules

The chiral geometry of rubrene is conserved upon adsorption onto the Au(111) surface. This has been inferred from NEXAFS measurements [39] and is directly visible in the STM images of individual adsorbed molecules on the surface. This property is shown in the images displayed in Fig. 4.6 (a), revealing three unequally shaped features (denoted by A, B, and C) which are present in each molecule. The monomer on the left has a counterclockwise arrangement of these lobes (BAC), while the one on the right follows a clockwise orientation (ABC), thus the molecules are mirror images of each other and reflect the chiral conformation of the molecule in the gas phase. The same STM image represented in a different color coding in the lower part of Fig. 4.6 (a) reveals the existence of shoulders (green/blue bulges) belonging to the features A and B which appear either on the left side of each maximum or on the right side, as viewed from the center of the molecule. This characteristic arrangement of asymmetric features determines the molecular chirality and allows the classification of the adsorbed molecules as **L** or **R** enantiomers, as shown schematically by the chiral triangles. The analysis of the orientation of the shoulders allows for a determination of the absolute chirality of each monomer observed and reveals that the different enantiomers are distributed equally on the surface. Consequently, **L**-type monomers are found next to **R**-type ones, such as the ones shown in Fig. 4.6 (b).

Although the molecular conformation (and thereby the appearance in the STM images) is

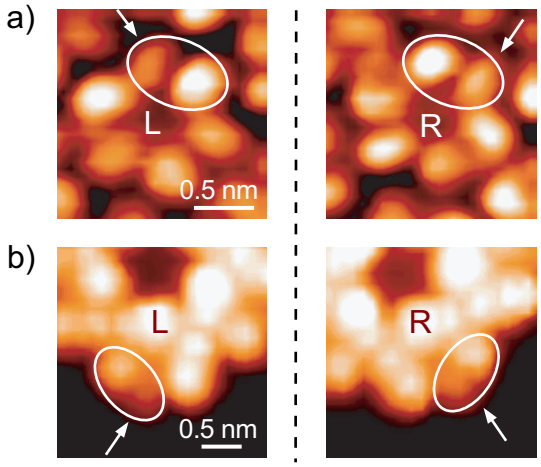

Figure 4.7: STM images revealing the chiral conformation of molecules inside self-assembled structures. The position of the dimmer feature with respect to brighter one defines the chirality. a) **L**- and **R**-type molecules in hcp islands revealing three pairs of higher and lower appearing lobes. b) Enantiomers in pentagonal chains revealing chiral submolecular features.

different for molecules in pentagonal chains and hcp structures, compared to the isolated molecule and the molecules in small structures (see Sec. 6.1), the chiral signature of the molecules is still visible. This is demonstrated in the STM images displayed in Fig. 4.7, showing enantiomers of molecules in hcp islands and within the pentagonal chains which are distinguished by the characteristic orientation of lower features with respect to the higher appearing neighboring submolecular maxima. While Fig. 4.7 (a) presents molecules with an arrangement of three similar pairs of clearly separated dimmer and brighter lobes, the submolecular contrast visible in Fig. 4.7 (b) resembles more the threefold pattern of the monomers, but with more unequal features of maxima and shoulders.

4.2.2 First step of chiral recognition: chiral dimers

The finding that the individual molecules adsorb in a chiral conformation on the gold surface gives rise to the question how different enantiomers interact with each other, leading either to homochiral (**LL** or **RR**) or heterochiral (**LR** or **RL**) supramolecular structures. The study of the smallest entities created in the self-assembly, i.e. the dimers, uncovers that they are exclusively formed by a bonding of molecules of the same chirality. The STM images of two different dimers in Fig. 4.8 represented in false colors to enhance the submolecular contrast demonstrates this property. The position of the shoulders (white arrows) with respect to the maxima are highlighted by the ellipses which encircle both features and reveals that the left dimer consists of two **L**-type molecules, while the right one is made up of two **R**-type specimen, thus the two dimers are mirror images of each other. This suggests a denotation of the homochiral **LL** and **RR** combination as a **L**-dimer and **R**-dimer, respectively.

The absence of any heterochiral configuration (**LR** and **RL**) is a very interesting phenomenon suggesting that the bonding of different enantiomers is energetically strongly disfavored, compared to the homochiral combination. The observation of exclusively enantiopure dimers may have two different origins: chiral recognition or chiral assimilation. While the first mechanism describes the selective bonding of molecules of the same chirality to each other, the second process implies a “flipping” of the chirality of one interacting partner in order to adopt to the chiral

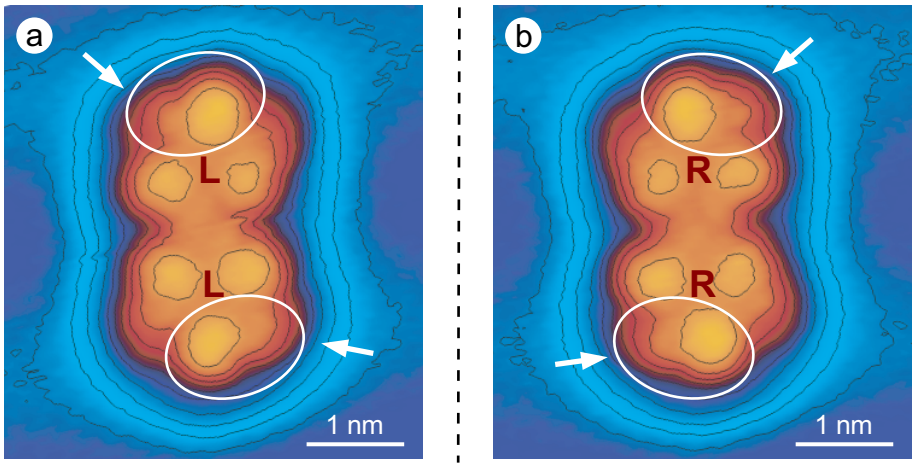

Figure 4.8: STM images of chiral dimers. **a)** **L**-type dimer of **L**-type molecules. **b)** **R**-type dimer of **R**-type molecules. The shoulders of the molecules are encircled, together with their corresponding maxima.

conformation of the other. However, the latter mechanism is improbable due to an energy of 210 meV which is required for the transition of a rubrene molecule from one enantiomeric form to the other[4] [39]. This value is about one order of magnitude larger than $k_{\mathrm{B}}T \approx 26$ meV at 300 K, thus making the "flipping" process improbable. Furthermore, the high mobility of the molecules enables the enantiomers to look for a suitable bonding partner, thus indicating that the self-assembly of rubrene molecules into homochiral dimers of **L**- or **R**-type is due to a chiral recognition process following a trial-and-error procedure of the diffusing molecules which results in the stable bonding of exclusively equal enantiomers. Consequently, the observation of the absence of chirally mixed dimers reveals that the interaction between enantiomers of opposite chirality is significantly different from the bonding mechanism which links enantiomerically equal monomers. This finding demonstrates that chiral recognition is of decisive importance for the self-assembly of rubrene on Au(111).

4.2.3 Chiral supermolecules

The self-assembly of rubrene molecules into structures forming the second generation of the hierarchy is subject to the same rules of chiral recognition than the enantioselective bonding into dimers. Consequently, the resulting supramolecular structures, such as trimers, tetramers, zigzag chains and pentamers are exclusively homochiral and therefore exist in two versions which are mirror images of each other. This leads to a local chiral segregation of the racemic mixture of individual molecules into small homochiral structures which are randomly distributed over the surface and thus constitute a chirally mixed surface coverage at the mesoscopic scale.

The study of the homochiral pentagonal supermolecules uncovers an additional interesting property, coming along with the geometry of the bonding between the molecules. The classification of the two enantiomers of chiral pentagons which are shown in the STM images displayed in Fig. 4.9 is carried out by a study of the contours of the molecules, unveiling the position of the shoulders and thus determining the chirality of the individual molecules in the pentagons. The orientation of the indicated molecular axis of the molecules (red arrows) with respect to the radius of the pentagons reveals that the **L**-pentagon is constructed by **L**-enantiomers which

[4]This energy is needed to force the molecule from its twisted conformation into the planar form, enabling subsequently a twisting into the opposite direction.

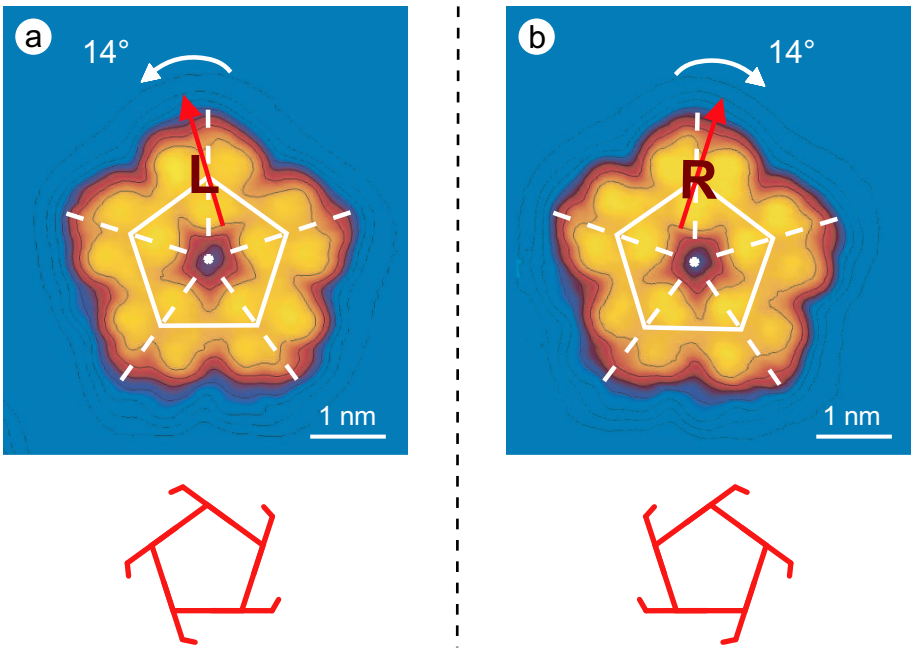

Figure 4.9: STM images of chiral pentagonal supermolecules. **a)** **L**-type pentagon of **L**-type molecules, rotated into the counterclockwise direction around their centers. **b)** **R**-type pentagon of **R**-type molecules, rotated into the clockwise direction around their centers. The red chiral pentagons schematize the chiral pentagonal supermolecules.

are rotated by $\approx 14°$ around their molecular center in the counterclockwise direction, while the **R**-type molecules are rotated into the opposite direction. This clockwise or counterclockwise inclination of the molecules provides an optimization of the intermolecular bonding and introduces an overall chiral signature to the pentagonal structure, schematized by the "hooked" pentagons shown in Fig. 4.9.

In analogy to the chiral self-assembly into homochiral pentagonal supermolecules, which are chiral on their own due to the clockwise or counterclockwise rotation of the constituent molecules, hexagonal supermolecules and honeycomb islets are created following the same building rules. This results in the creation of an equal amount of both enantiomers of hexagonal homochiral structures which are detectable by the rotations of the composing molecules, leading furthermore to chiral starlike holes inside the pattern. The STM image displayed in Fig. 4.10 gives an example of a small honeycomb islet of **R**-type, revealing the formation of holes of starlike shape which appear twirled into one direction due to the rotation of the individual molecules. Accordingly, honeycomb patterns of **L**-type uncover star-shaped holes of the opposite direction of rotation of the twirled deformation.

4.2.4 Second step of chiral recognition: chiral chains

The importance of the chiral property of the pentagonal supermolecules for the second step of the hierarchical self-assembly is determined by an investigation of the pentagonal chains, such as those shown in the STM image in Fig. 4.11. The closeup views of the indicated white squares displayed in Fig. 4.12 show details of two different supramolecular chains revealing by the submolecular structure of each molecule that all constituent pentagonal supermolecules of one chain are of the same chirality. Consequently, the left image presents a homochiral supramolecular

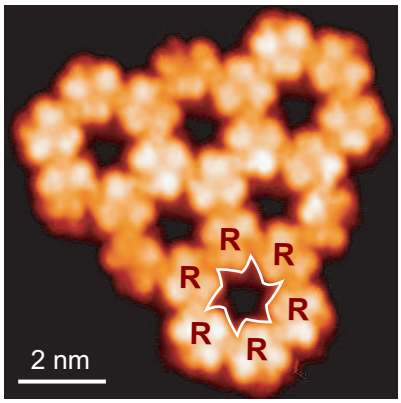

Figure 4.10: STM image of a chiral **R**-type honeycomb pattern built up by exclusively **R**-type molecules which are all rotated in the same direction of rotation (i.e. clockwise) around their center. This rotation creates chiral starlike holes inside the honeycomb pattern, as indicated by the twirled white star.

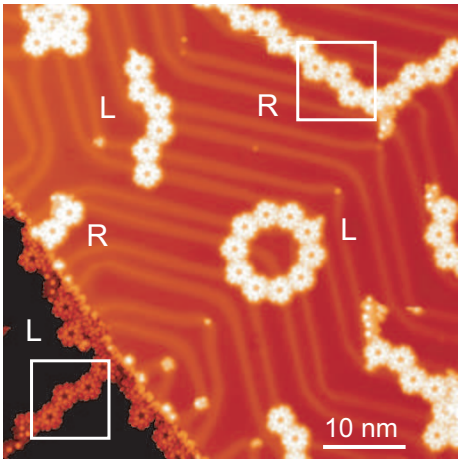

Figure 4.11: STM image showing two terraces, separated by an atomic step, with a distribution of homochiral pentagonal decagon and chains. The indicated squares are shown in Fig. 4.12

structure composed of **L**-pentagons, while the right one gives an example of a homochiral chain made out of **R**-type building blocks. An investigation of pentagonal chains present in a larger area brings forward that the chiral chains are uniformly distributed over the surface which is shown in the STM image displayed in Fig. 4.11 by the identification of **L**- and **R**-type structures.

The question whether this second step of the hierarchical self-assembly is driven by chiral recognition as the first step or by an assimilation procedure of the interlocking pentagons is evaluated by a consideration of the structural design of the individual pentagonal supermolecules. Chiral assimilation infers that one of the two enantiomers changes its chiral conformation to adapt its chirality to the one of the other enantiomer. In the actual case of the pentagonal supermolecules, this process would not only require an isomerization (i.e. chiral inter-conversion) of five molecules at the same time, but moreover a change of the rotational direction around the centers of each of these molecules. Contrary to this improbable mechanism, chiral recognition between the very mobile supermolecular pentagons appears as a reasonable process directing the second step of the self-assembly in the same way as the enantioselective assembly of the

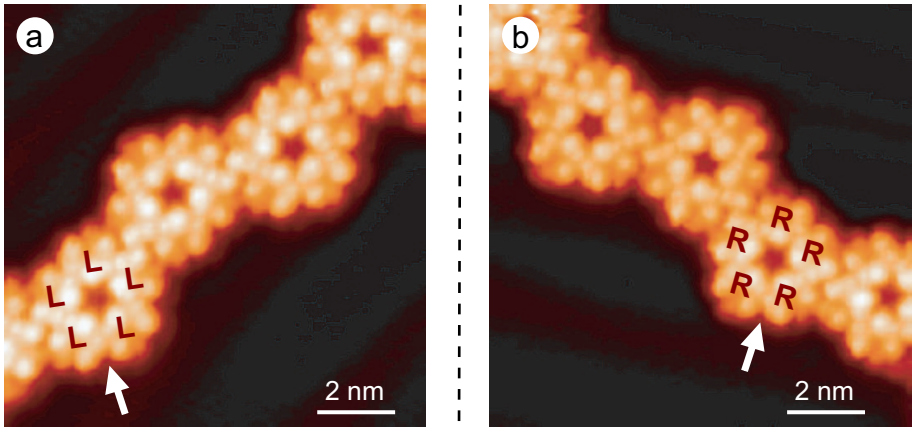

Figure 4.12: STM images of chiral pentagonal chains showing the magnified areas indicated by the white squares in Fig. 4.11. **a)** **L**-type chain of **L**-type pentagons. **b)** **R**-type chain of **R**-type pentagons.

individual molecules (see Sec. 4.2.2) into small supramolecular structures. Consequently, the third generation of this supramolecular hierarchy constitutes the outcome of a second step of chiral resolution by an enantioselective assembly of chirally mixed supermolecular pentagons into enantiopure chains extending over a maximal length of ≈ 150 nm.

4.2.5 Chiral supramolecular decagons

A particular aspect of the bonding between pentagonal supermolecules of the same chirality is pointed out in the formation of the nested supramolecular decagons, which are a special cyclic and size-defined case of the pentagonal chains discussed above. The STM images of two decagons, displayed in Fig. 4.13 confirm that they follow the same enantioselective self-organization as the chains by showing that they consist each of ten homochiral pentagonal supermolecules and thus form homochiral nested supramolecular assemblies. The additional characteristic of the self-organization of the pentagons is visible by studying the orientation of the individual supermolecules with respect to the radius of the decagon. The superimposed drawing shown in Fig. 4.13 (c) schematizes the finding that the **L**-type decagon consists of ten **L**-pentagons which are rotated by $\approx 12°$ into the counterclockwise direction around their centers. The respective **R**-decagon shown on the right side of Fig. 4.13 forms a mirror image due to its **R**-type pentagons which are rotated into the clockwise direction around their centers. Consequently, the direction of the molecular rotation introduces a new level of chirality to the whole supramolecular structure which thus form a third generation of size-defined chiral objects on the surface.

4.3 Conclusions

The surprisingly complex self-assembly of rubrene is organized into a three-staged hierarchy of supramolecular structures going from the individual molecules to small structures, pentagonal supermolecules and honeycomb islets and further on to the formation of chains of pentagons and nested decagons. The bonding mechanisms constructing this hierarchy are driven by chiral recognition processes on the molecular and supramolecular level, resolving the original racemic mixtures of individual rubrene molecules into homochiral structures of different dimensions.

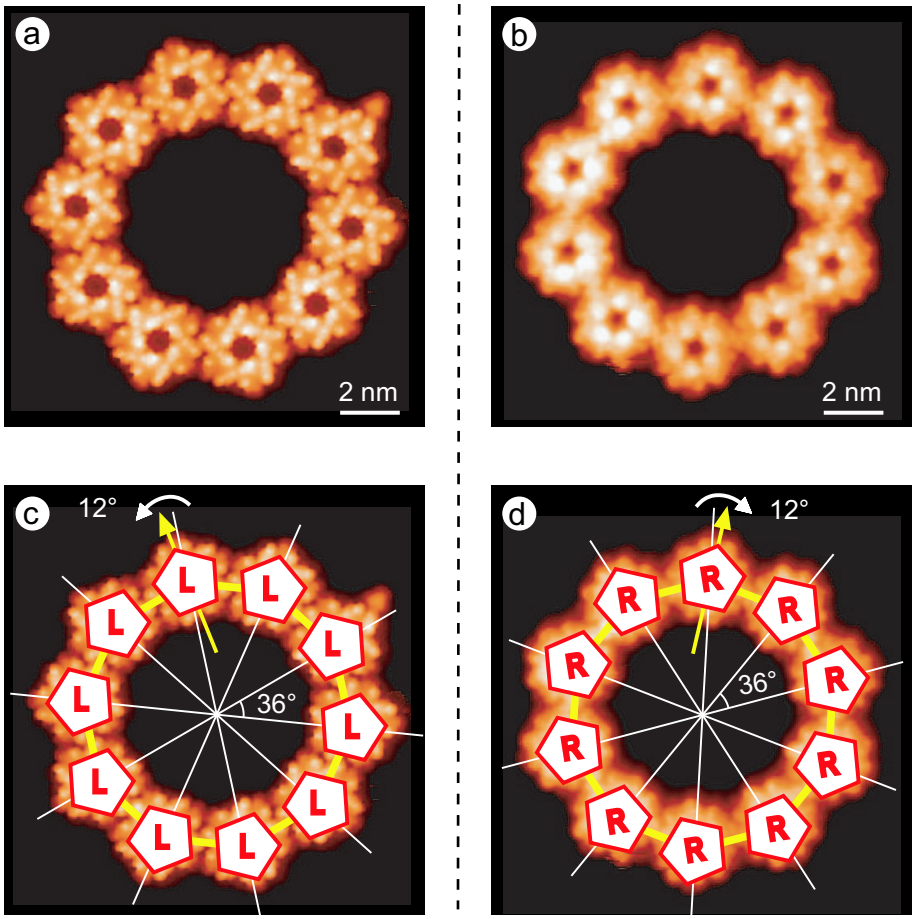

Figure 4.13: STM images of chiral supramolecular decagons which are mirror images of each other. **a)** **L**-type decagon of **L**-type pentagons which are rotated around their centers into the counterclockwise direction. **b)** **R**-type decagon of **R**-type pentagons which are rotated into the clockwise direction around their centers.

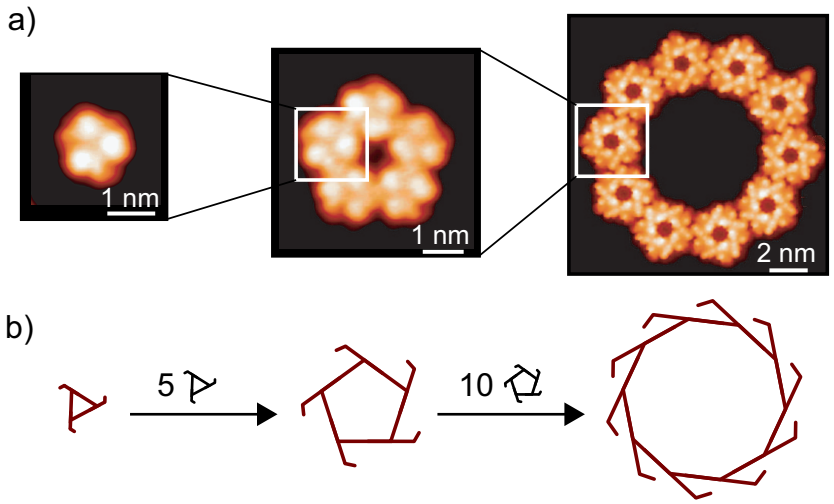

Figure 4.14: Progression of chirality in a two-staged supramolecular hierarchy. **a)** Hierarchy of supramolecular structures from monomers to pentagonal supermolecules and further on to nested supramolecular decagons. **b)** Conservation of the left-handedness from single chiral molecules to chiral **L**-pentagons and further on to chiral **L**-decagons.

The chirality of the individual molecules is determined by their appearance in the STM images and leads to specific rotations of the molecules inside of the supramolecular structures, as well as of the pentagonal supermolecules inside of the pentagonal chains and decagons. The orientation of the rotation is thereby fixed by the type of chirality of the molecular and supramolecular building block, resulting in an overall chirality of the complete structure. The STM observations show that the chirality of the rubrene molecules is preserved upon adsorption of the surface and furthermore transferred to the next level of the hierarchy. Three species of each generation are characterized by a defined number of molecules: the single molecules, the pentagonal supermolecules and the supramolecular decagons. The latter architecture is a doubly nested structure consisting of $10 \times 5 = 50$ molecules of the same chirality. This progression of supramolecular self-assembly and chiral recognition at the molecular and supramolecular level is summarized and schematized in Fig. 4.14, pointing out the most important properties of this remarkable phenomenon of a two-dimensional supramolecular self-assembly.

Chapter 5

Coverage dependent supramolecular self-assembly on Au (111)

Chiral recognition processes are directing the supramolecular self-assembly into a hierarchy of complex architectures, resulting in an enantioselective construction of pentagonal and hexagonal patterns. However, the hcp islands which start their growth from a coverage of approximately 0.25 ML on, do not reveal a homochiral composition, but, on the contrary, are a racemate of both enantiomers. The observation that the hcp islands are not following the rule of chiral separation suggests a possible explanation for the coverage dependent transition from well-ordered small supramolecular architectures to large, extended and loosely vdW bonded hcp islands. For a sample preparation consisting in a deposition of the molecules at low temperatures followed by an annealing (P1), the supramolecular structures are dependent on the coverage of rubrene and are therefore consistently described by a one-dimensional phase diagram. However, the evaporation of rubrene onto a sample held at ambient temperature (P2) yields deviations from this coverage dependent progression and results in different supramolecular phases which uncover a dependence of the assembly on other parameters. The self-assembly of one type of molecule on the same surface into low-density and high-density phases has been reported earlier to depend on the sample coverage [10, 152, 148, 153, 143, 154], the annealing temperature [116], and thermodynamic parameters [155].

5.1 Chirality in extended molecular islands

The hcp islands which have been presented in Sec. 3.5 reveal a different self-assembly mechanism than the hierarchically organized supramolecular structures discussed in the last chapter. In contrast to the well-defined and enantiopure pentagonal and hexagonal patterns which are characterized by directed intermolecular bonds, the hcp islands reveal a denser packing of arbitrarily rotated molecules, larger intermolecular distances, different submolecular appearance as well as a chiral mixture of **L**- and **R**-type molecules. The latter finding is illustrated in the STM image displayed in Fig. 5.1 (a) by an identification of the chirality of each individual molecule. As indicated in the figure, both enantiomers are present in the island, but of unequal number with an excess of **R**-species. An investigation of other hcp islands reveals that this disproportion of both chiralities is a locally changing phenomenon which depends on the investigated island and varies roughly between 30% and 70%.

In the case of the patchwork phase which has been discussed in Sec. 3.6, the different sample preparation resulted in extended domains of different tiling. One of these arrangements is a special type of hcp phase which is built up by an assembly of molecules with a fixed orienta-

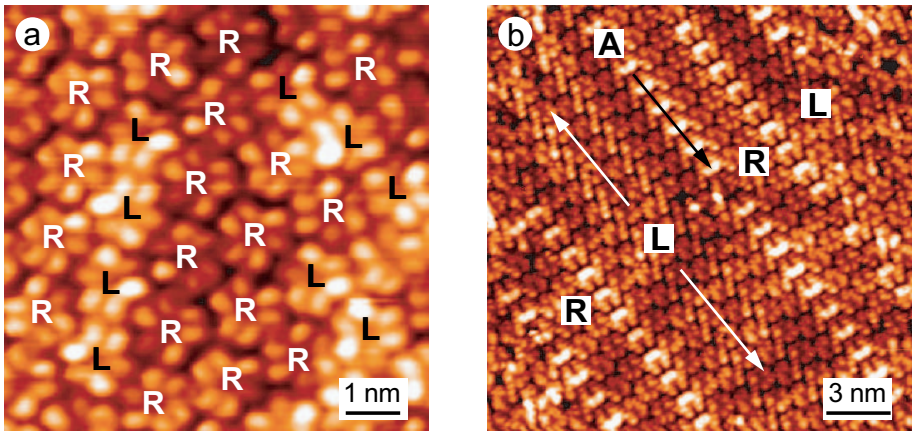

Figure 5.1: STM images of hcp islands on Au(111), revealing the chirality of the individual molecules. a) Chirally mixed distribution of **L**- and **R**-enantiomers. b) Hcp domain with oriented molecules in the patchwork phase revealing homochiral areas, separated by lines of achiral molecules.

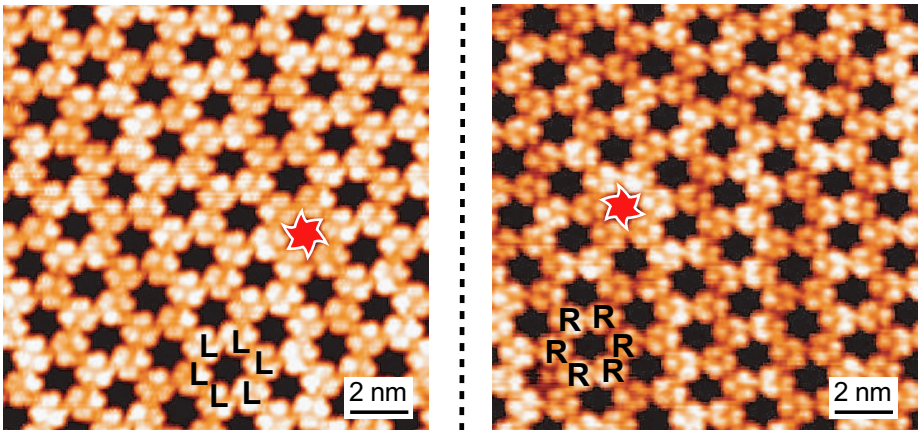

Figure 5.2: STM images of two different extended honeycomb islands revealing homochiral arrangements of **L**- and **R**-type molecules which represent mirror images.

tion with respect to their neighbors (see Sec. 3.6.4). In a range of tens of nanometers, these islands form different domains which are separated by brighter appearing, parallel running lines. The STM image displayed in Fig. 5.1 (b) illustrates the observation that the flat domains are homochiral hcp arrangements. Domains of opposite chirality are joint with the help of rows or achiral molecules which appear higher in the STM image. Each line of molecules which is parallel to these achiral chains consists of molecules which are oriented into the same direction with respect to the direction of the row. However, alternating rows are rotated by 180° with respect to each other. This arrangement of alternating rows establishes directed intermolecular bonding between molecules of neighboring rows. Since this interaction is well-defined, molecular lines of different chirality are not matching and are therefore linked by a row of molecules which change their chiral conformation to an achiral, symmetric shape in order to be able to bond to both types of enantiomers.

In contrast to these ordered hcp domains which are only locally homochiral, the other supramolecular arrangements which exist in this patchwork phase fill extended areas with ho-

mochiral patterns. This enantioselective growth results in the periodic and non-periodic tiling with pentagons, hexagons and heptagons, as well as in the extended honeycomb patterns, including the supramolecular rosettes. The STM images shown in Fig. 5.2 reveal the chirally twisted stars, already mentioned in Sec. 4.2.2, which are formed by the holes of the honeycomb arrangement and display the enantiopure assembly of the structures into two mirror domains. These homochiral patterns extend over hundreds of nanometers and the corresponding mirror-images are separated by transition areas of periodic or non-periodic tiling and hcp domains which allow a change of the chirality due to their arrangement including both enantiomers.

5.2 Coverage dependent growth

The exceptional self-assembly of rubrene on Au(111) creates a manifold of multifaceted architectures including small structures, pentagonal and hexagonal assemblies and different periodic and non-periodic phases extending over the whole surface. The supramolecular growth depends on different parameters of the sample preparation. Basically, the molecules are deposited either inside the cryostat onto a sample held at low temperatures of 50 K or 5 K (P1), or inside the preparation chamber onto a sample held at room temperature or above (P2). While in the latter preparation the molecules have enough energy to diffuse on the surface directly after their deposition, the first method P1 requires an annealing to $\approx$ 300 K in order to enable enough molecular mobility. A consequence of the preparation P1 is the fact that the two-step process results in different initial conditions influencing the self-assembly mechanism. Since the deposition of the molecules is already finished before the sample is annealed, the molecular density is maximal from the beginning of the molecular diffusion on. This different initial situation might be decisive for the outcome of the supramolecular assembly. Furthermore, the annealing procedure makes the sample preparation of type P1 independent of the deposition rate of the molecules which might be subject to small variations originating from instabilities of the evaporator.

In the case of a sample preparation of type P2 no specific supramolecular structures could be obtained in a reproducible manner. In contrast to this method, the sublimation of rubrene at low temperature, followed by an annealing to $\approx$ 300 K (P1) resulted in a reproducible progression of self-assembled phases. This specific sample preparation yields a coverage dependent evolution from small structures up to hcp islands extending over the whole surface for a coverage of 1 ML. This progression of the supramolecular assembly is shown in the STM images of Fig. 5.3 which presents the phases obtained by repeatedly adding molecules to a sample at 5 K and measuring the resulting samples after an annealing to $\approx$ 300 K. The images demonstrate the transition from small structures (δ) to honeycomb islands (η), then to mixed hexagonal-pentagonal chains (η/λ) which evolve into exclusively pentagonal chains (λ), leading finally to an hcp assembly of the molecules (ω). This evolution of supramolecular architectures is summarized in the scheme presented in the lower part of Fig. 5.3. The diagram shows the dominance of small structures (monomers to hexamers) up to $\approx$ 0.05 ML, changing into the honeycomb phase with a dominant hexagonal character, which merges from $\approx$ 0.15 ML on with a phase consisting of assemblies of pentagonal supermolecules. At a coverage of $\approx$ 0.25 ML, the number and lengths of the supramolecular chains decrease with an increasing growth of hcp islands, which are finally the only supramolecular assemblies present on the sample from a coverage of $\approx$ 0.3 ML on.

The different mechanisms of supramolecular self-organization as a function of the coverage of rubrene are tentatively rationalized by considering the distribution of molecules of different chirality on the surface at varying coverage. For a very low molecular density, the molecules diffuse unperturbed on the surface and interact with each other by a trial-and-error process which enables the chiral recognition between the same enantiomers. The creation of small homochiral

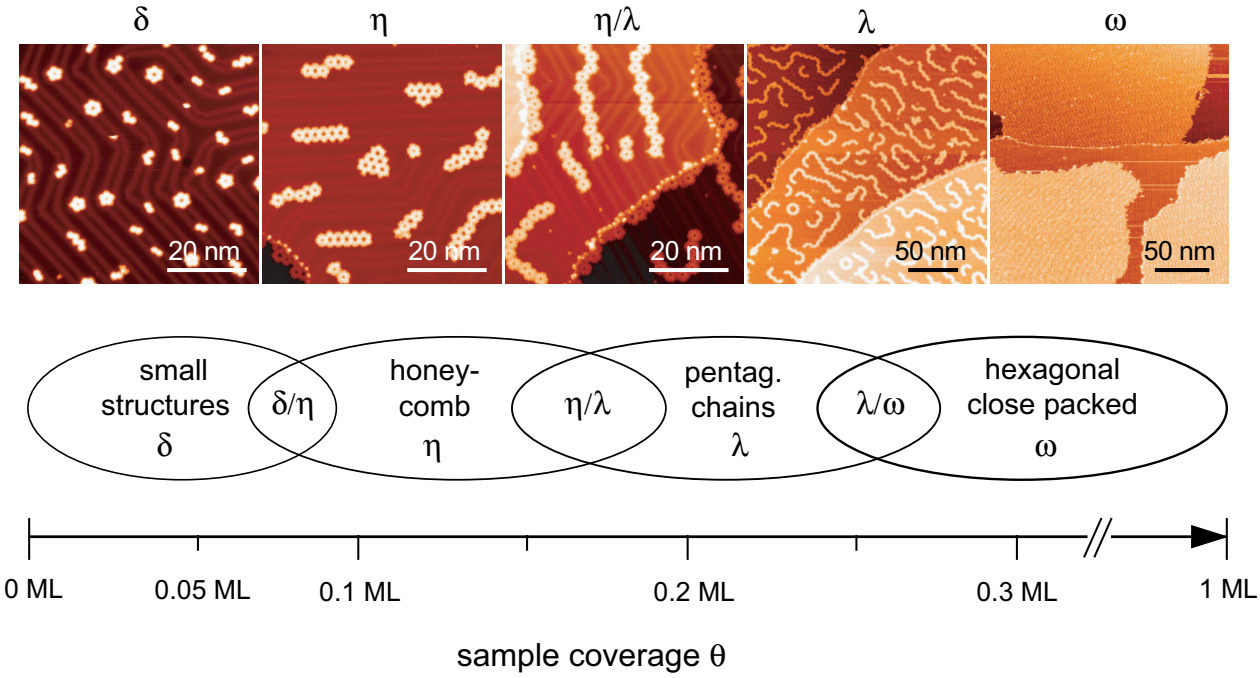

Figure 5.3: STM images showing the different supramolecular phases δ, η, λ, ω, and an example of a mixed phase η/λ. The scheme summarizes the experimental result of the correlation of the supramolecular phases with the rubrene coverage on Au(111). The different phases overlap as indicated by the ellipses, leading to mixed phases δ/η, η/λ, and λ/ω. The molecules are evaporated on the surface at T_d =5 K and subsequently annealed to T_a ≈300 K (Preparation P1).

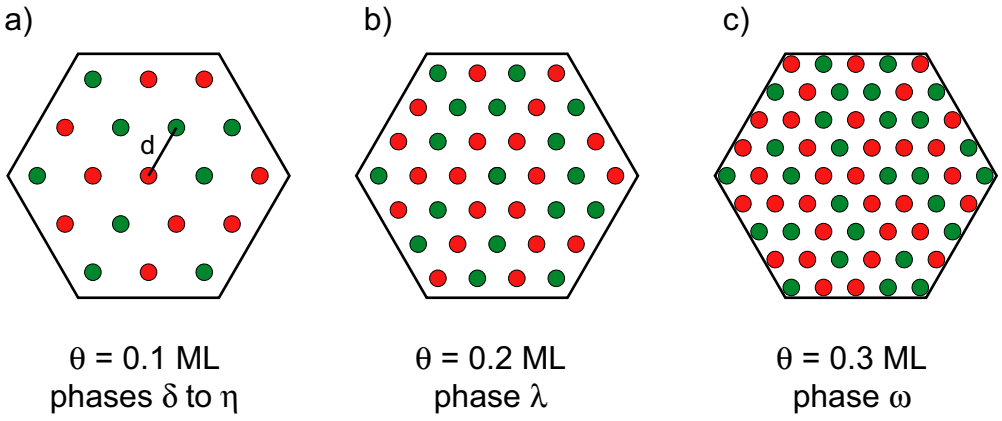

Figure 5.4: Simplified model describing the molecular densities at a surface coverage of 0.1, 0.2, and 0.3 ML, leading to different average intermolecular distances d=3.2a, 2.2a, and 1.8a for (a), (b), and (c), respectively. a=1.3 nm is the intermolecular distance of a full hcp coverage and the different colors represent the two enantiomers. The schematized initial situations result in the formation of small structures up to honeycomb islets (a), pentagonal chains (b) and hcp islands (c). The hexagonal area comprises 300 nm^2.

structures is an intuitive outcome of this process. However, for a larger coverage there is a significant difference in the geometry of the resulting assemblies, leading either to honeycomb islets ($\theta \approx 0.1$ ML) or pentagonal chains ($\theta \approx 0.2$ ML). The different initial situation preceding the assembly into supramolecular structures is presented in a very simplified manner in Fig. 5.4. The drawing shows the number of molecules present in a specific surface area of ≈ 300 nm^2 for the corresponding coverage, i.e. 19 and 37 molecules in the case of 0.1 ML and 0.2 ML, respectively[1]. Since the surface coverage constitutes a racemic mixture of both chiralities, only half of the molecules in the area are able to bond to each other. At low coverage of up to 0.1 ML (the maximal density is schematized in Fig. 5.4 (a)) causes a situation where only a small fraction of the molecules find rapidly a correct interaction partner and bond into dimers which are still surrounded by single molecules. These are subsequently attaching to the already built structures, forming trimers, tetramers, and other small structures for a coverage of ≈ 0.05 ML (phase δ). The straight geometry of the hcp troughs of the herringbone reconstruction of gold favors a linear assembly into zigzag lines which afterwards join to construct the honeycomb islets in the case of a higher density of ≈ 0.1 ML (η). However, if the surface coverage is increased to ≈ 0.2 ML, molecules of the same chirality are much closer and their diffusion leads rapidly to the creation of a large number of dimers which are surrounded by only a few single molecules. These free molecules bond to the existing dimers of the correct chirality into trimers and subsequently, these dimers and trimers present on the surface combine into pentamers which contract into pentagons, as discussed in Sec. 3.2. In a second assembly step, these closed pentagonal supermolecules interlock into pentagonal chains (λ). In the last case of a surface coverage above ≈ 0.3 ML, the chirally mixed molecular distribution is so dense (see Fig. 5.2 (c)) that the local chiral resolution into homochiral structures is hindered. Since different enantiomers do not bond to each other, the molecules continue to diffuse on the surface until they adsorb at step edges of the gold terraces. The molecules which join the first row of molecules at the step edges are subsequently stabilized into a densely packed molecular island containing both chiralities (ω). Each molecule is surrounded by six neighbors inside the structures and by four molecules at the borders of the island, leading to an efficient attraction between the molecules due to vdW forces.

This scenario describes the self-assembly in the case of an evaporation of the molecules onto a sample held at a low temperature of 5 K or 50 K, followed by an annealing to ≈ 300 K (P1). This preparation method permits a reduction of the number of parameters influencing the highly critical self-assembly of rubrene and thus leads to reproducible supramolecular phases. First of all, this procedure eliminates an influence of the deposition rate of the molecules which might vary due to small temperature fluctuations of the evaporator or the sample. Since the molecules are evaporated onto the cold sample with a reduced mobility, and self-assemble into the structures only after an annealing to higher temperature, the initial situation for the bonding of the molecules is invariably characterized by the immediate presence of all molecules on the surface at the same time. In contrast to this stable condition, a progressive molecular density which increases in the course of the assembly as it is the case for an evaporation onto a sample at room temperature (P2) changes the conditions for the supramolecular self-assembly considerably if the deposition rate is slightly varied. The second point influencing the self-organization might lay in the cooling rate of the sample, since the high mobility of the molecules suggest that the different steps of the supramolecular assembly into the hierarchy of structures takes place at temperatures between 300 K and 5 K. In the case of an annealing of the sample after the deposition at low temperature (P1), the cooling rate is more stable due to the reduced sample manipulation and transfer steps involved in this procedure than in sample preparation P2.

The one-dimensional progression of the phases as a function of the surface coverage is valid

[1] A full hcp coverage corresponds about 70 molecules per 100 nm^2.

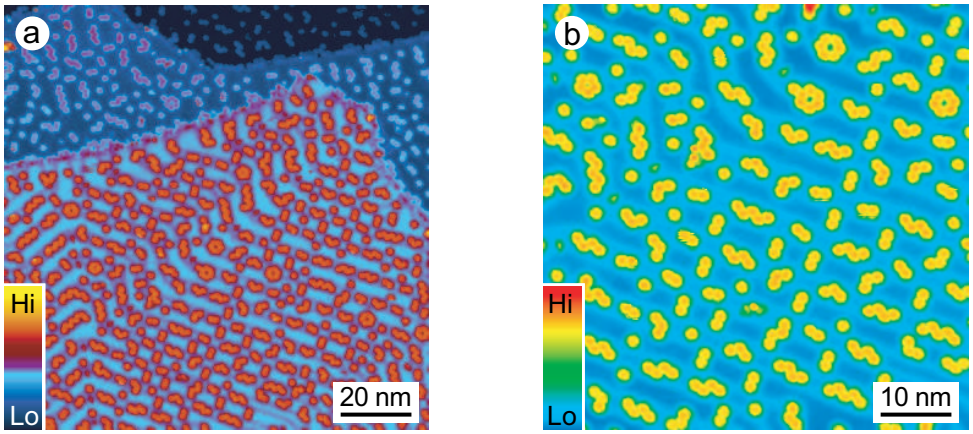

Figure 5.5: STM images of different sizes showing a distribution of small structures on Au(111) at a coverage of 0.12 ML. The phase is denoted by $\delta^{\#}$ since it represents a sample consisting of small structures like phase δ, but at a higher coverage. The molecular assemblies from trimers on are exclusively adsorbed at hcp domains including the domain boundaries. Dimers are also found at the fcc domains with an orientation perpendicular to the borders.

only for the sample preparation technique P1. The deposition of the molecules on a sample held at ambient temperature or above results furthermore in the formation of supramolecular phases which are not following the coverage dependence shown in Fig. 5.3. An example is the complete surface tiling by the patchwork phase presented in Sec. 3.6 which consists of homochiral domains despite the high coverage and is now denoted by phase χ. Another discrepancy from the one-dimensional coverage dependent assembly is shown in the STM images of Fig. 5.5 which present a supramolecular phase, denoted by $\delta^{\#}$, consisting of exclusively small structures from monomers to hexamers created by molecules at a surface coverage of 0.12 ML. This corresponds to a molecular density which already results in the formation of honeycomb islets in the case of a sample preparation P1. The STM image in Fig. 5.5 (b) reveals that the small homochiral assemblies are predominantly adsorbed at the hcp domains including the boundaries. Only monomers and part of the dimers occupy fcc stacking areas, with the orientation of the dimers being perpendicular to the domain walls. The existence of a specific supramolecular arrangement at a higher coverage than the respective value given in the phase diagram of Fig. 5.3 is furthermore found in the case of a self-assembly into large honeycomb islets ($\eta^{\#}$).

Taking into account these supramolecular phases, resulting from a sample preparation P2: $\delta^{\#}$, $\eta^{\#}$, and the patchwork phase χ, the different types of self-assembled architectures are organized in a two-dimensional phase diagram shown in Fig. 5.6. The scheme describes the dependence of the supramolecular arrangements on the sample coverage θ as well as on a parameter P which includes the conditions of the different sample preparations P1 and P2, such as sample temperature upon deposition T_{d}, the annealing temperature T_{a}, the deposition rate Ω_{d} and cooling rate Ω_c. The diagram includes the one-dimensional dependence on the coverage shown in Fig. 5.3 by the horizontal red line for the preparation method P1 which has essentially stable values of T_{d}, T_{a}, Ω_{d} and Ω_c. In contrast to P1, the deposition at ambient temperature P2 is subject to variations of these conditions, leading to a two-dimensional dispersion of the resulting phases. The indicated borders which separate the different phases are fluent, accounting for the existence of mixed phases, such as the merged hexagonal-pentagonal chain phase η/λ. All observed supramolecular assemblies, except the racemic hcp islands, are homochiral arrangements of the molecules which are bonded by directional forces to each other. The fact that the dense

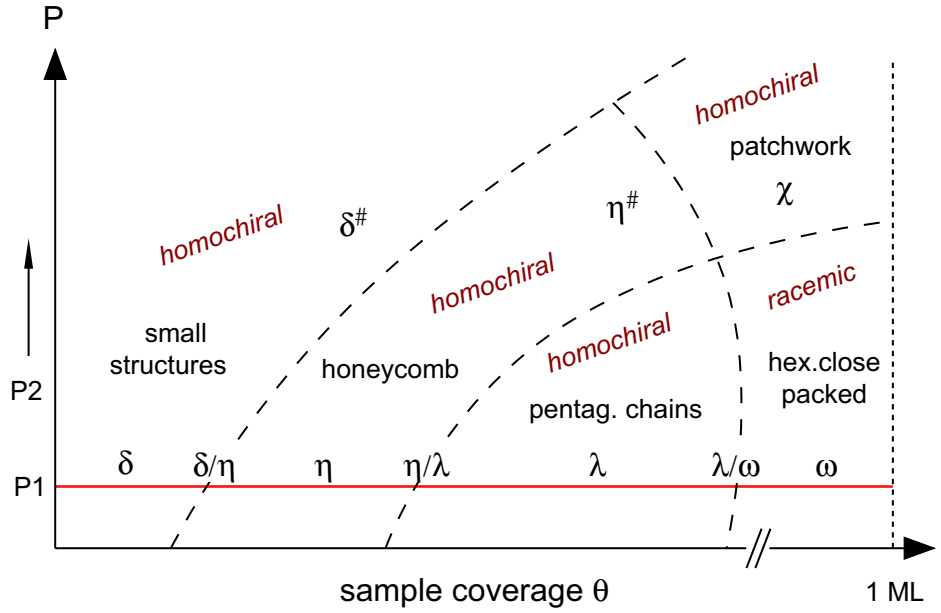

Figure 5.6: Proposed phase diagram showing the dependence of the supramolecular phases on sample coverage as well as on a parameter P which accounts for different preparation methods, leading to different values of the deposition temperature T_d, the annealing temperature T_a, the deposition rate Ω_d and the cooling rate Ω_c. The horizontal line describes the dependence of the phases on the sample coverage for the preparation method P1, leading to the one-dimensional phase diagram shown in in Fig. 5.3.

patchwork phase χ contains extended homochiral areas at a high surface coverage of > 0.7 ML suggests furthermore that in this case the enantiopure assembly is probably not due to chiral recognition leading to a chiral resolution of the racemic mixture of molecules, but rather an outcome of a flipping process [146, 156] which forces the molecules of opposite chirality to adapt to the dominant chiral character of the assembly in a certain area.

Chapter 6

Identifying and switching the electronic structure of adsorbed rubrene

The adsorption of molecules on surfaces results in the existence of different possible molecular conformations, i.e. geometric orientation and deformation of the individual molecule. The adopted steric structure might thereby diverge significantly from the gas phase or solid state conformation of the molecule. For instance, various conformers of derivatives of porphyrin [94, 23, 157, 24], decacyclene [146], phthalocyanine [158, 159, 160], as well as the so-called "Lander" [96, 161, 162], and "wheelbarrow" [163] molecules, have been detected by means of STM. On the one hand, the different adsorption geometries are observed upon varying the surface via the change of the substrate material or the crystal face. However, unequal conformations are also adopted upon adsorption onto the same surface due to the availability of different adsorption sites (e.g. bridge or on-top sites, different type of atom). The molecular conformation of adsorbed molecules can be modified with the STM by mechanical contact with the tip, inelastic tunneling into molecular vibrational levels or field-induced processes [23, 164, 158, 24]. Moreover, precise manipulations changing the chemical structure of the molecules [165, 166, 167, 168, 169, 170, 171] and complexation with metal atoms [172, 173, 174] are induced via electron tunneling leading to bond breaking or displacement of the molecules.

A local investigation of the electronic structure of the adsorbed molecules is realized by means of spectroscopic measurements (STS), as discussed in Sec. 2.2. Differential conductance (dI/dV) curves measured over the molecular adsorbates on metal surfaces and ultrathin oxide films have been recorded for various specimen, such as C_{60} [130, 175, 176, 177, 88, 178, 179, 180, 181], ethylene [19], HBC [109], PTCDA [182], Cu-Pc [183, 160, 159], Sn-Pc [184], and Zn-Etioporphyrin [157, 24]. However, the obtained spectra are either missing a clear assignment to HOMO and LUMO values of the specific molecule obtained from (combined) non-local techniques like UPS, inverse photoemission (IPES), EELS and photon absorption or reveal a perturbation of the electronic levels due to chemisorption of the molecules or a coupling of π systems lying parallel to the surface. The latter problem has been addressed by the deposition of the investigated molecules on a thin oxide layer which reduces the influence of the metal substrate on the molecular levels. With this method, HOMO and LUMO energies have been recorded for pentacene ($C_{22}H_{12}$) molecules adsorbed on NaCl, which show a close correspondence to the gas phase value for the HOMO, but a discrepancy of 1 eV in the case of the LUMO [20].

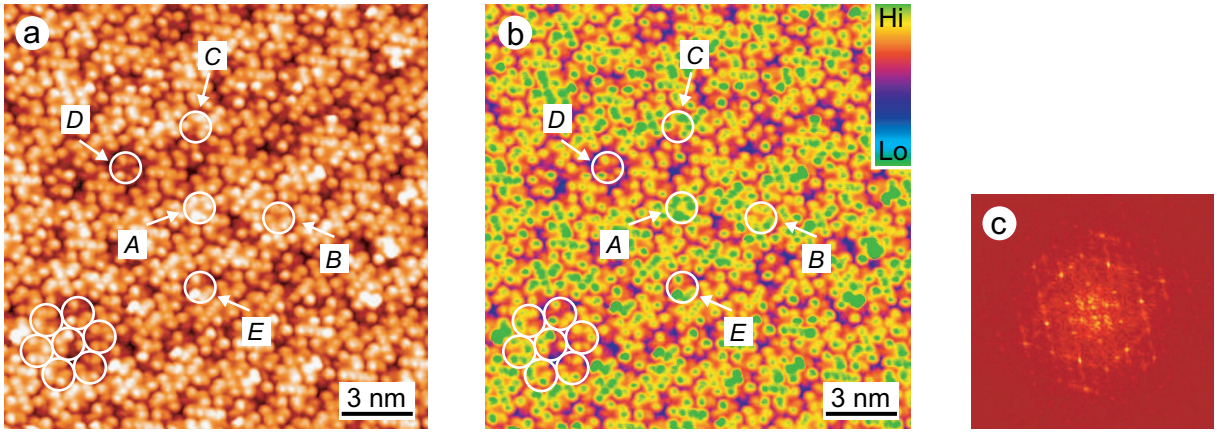

Figure 6.1: STM images represented in different color codings showing the hcp arrangement of rubrene adsorbed on Au(111). The different adsorption conformations are encircled and denoted by *A* to *E*. Closeup views of the conformers are given in Fig. 6.2. c) Result of a fast Fourier transform performed on the hcp island shown in (a) and (b), revealing the hexagonal arrangement. (Tunneling parameters: $V = -0.8$ V, $I = 50$ pA)

6.1 Conformation and intrinsic electronic structure of rubrene on Au (111)

The self-assembly of rubrene on Au(111) results in the formation of supramolecular structures of multifaceted geometry. One type of arrangement consists of hcp islands which demonstrate the weak bonding of the molecules to the underlying substrate by the preservation of the surface reconstruction of gold (see Sec. 3.5). The STM image of such an island, represented in two different color codings in Fig. 6.1, shows an inhomogeneous appearance of the densely packed molecules. A closer analysis reveals the existence of mainly five different adsorption conformations, which are encircled in the images and denoted by A to E. The respective adsorption conformations are presented in the zoomed STM images shown in Fig. 6.2 (a). The submolecular contrast reveals that each shown molecule is characterized by a different arrangement of protruding lobes. The conformers A and B possess a similar intramolecular geometry, but an additional feature distinguishes both specimen clearly. Considering the encircled molecules with respect to their six surrounding nearest neighbors, it is visible that conformers A to C form straight "bars" (indicated by the black dotted ellipses) by an alignment of their submolecular lobes to the ones of the other molecules. The number of bars, together with the submolecular appearance, determines the type of conformation: A (three), B (two), C (one), D and E (both no bars, but different submolecular contrast).

The distribution of the conformers within the shown island reveals a dominant occurrence of type C (≈ 60 %), a small number of A molecules (≈ 0.5 %), and approximately equal appearance of types B, D, and E (each ≈ 13 %). These values are however dependent on the type of sample (i.e. the presence or absence of pentagonal chains next to the hcp islands, see Sec. 3.4 and 3.5) and evolves to a disappearance of B and C, in favor of D and E in the case of an assembly into exclusively hcp islands. Furthermore, this finding is consistent with the explanation of the progression of supramolecular phases with the rubrene coverage given in Sec. 5.2. The molecules which construct the supramolecular small structures, honeycomb patterns and pentagonal chains are linked to each other with the creation of "bars" between the molecules, in the same way as

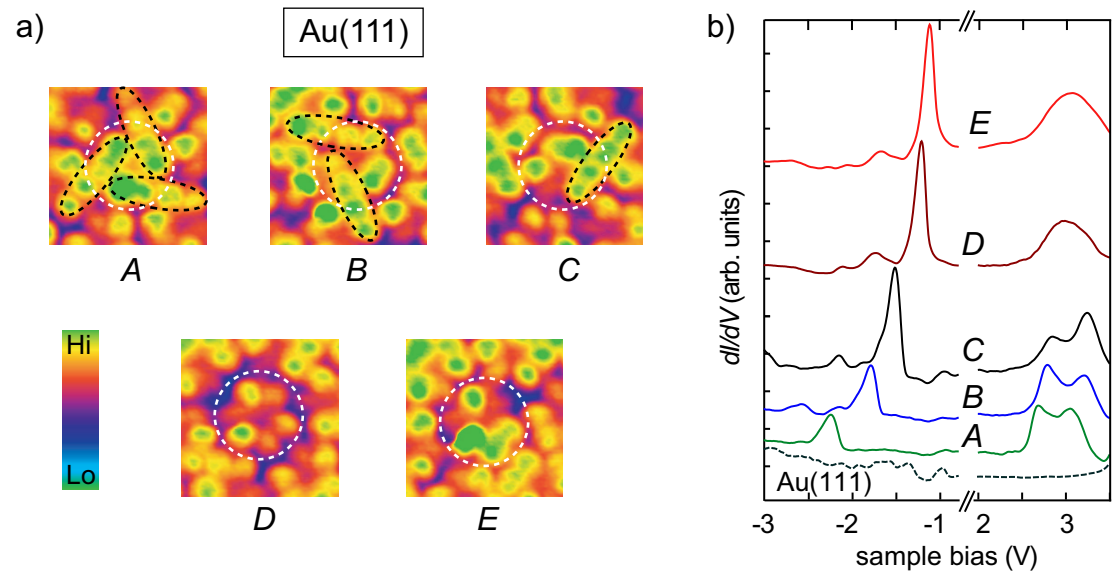

Figure 6.2: a) Closeup views of the five different conformers encircled in the STM image in Fig. 6.1. The conformations are identified by the submolecular appearance and the number of straight connection lines (indicated by the black dotted ellipses) which they form with the surrounding molecules. (2.7 nm $\times$ 2.7 nm, tunneling parameters: $V = -0.8$ V, I =50 pA) b) *dI/dV* spectra acquired with enabled feedback loop probing the HOMO and LUMO of molecules *A* - *E*. Each spectrum is an average of several spectra acquired over one conformer. The curves are offset for clarity.

conformers A, B, and C. This intermolecular bonding is only possible for low molecular coverage (allowing for chiral recognition) and vanishes for increasing densities. An analysis of the chirality of the different conformers indicates that the isolated types D and E are of opposite chirality than the surrounding molecules. This finding corroborates the previous interpretation by showing that exclusively the same enantiomers form intermolecular bonds which then build homochiral honeycomb patterns and pentagonal chains. At higher coverage, a separation of the different chiralities is inhibited and the molecules of opposite chiralities are "trapped" inside of the hcp islands where they are detected by the absence of intermolecular alignment bars.

Recording dI/dV spectra over molecules of type A to E uncovers that the specific adsorption conformations are characterized by different electronic structures. The STS measurements shown in Fig. 6.2 reveal a peak in the negative voltage range whose position is shifted towards E_F going from A to E. The positive part of the spectra exhibits two close peaks for conformers A to C which slightly shift to higher positive voltages and a broad peak for D and E. The intensity ratio of the two close peaks of curves A to C in the positive voltage range varies for different molecules of the same conformation. However, spectra acquired over different submolecular features of one molecule reproduce the same peak positions (negative and positive voltage range), but with variable intensity. The decreasing intensity of the peaks at negative polarity for voltages further away from E_F is presumably due the reduced tunneling probability from low lying occupied states of the sample originating from the increased effective barrier height for $V < 0$ (see Sec. 2.2).

The dI/dV spectra recorded over conformers D and E are characterized by close peak positions of -1.2 ± 0.1 eV and $+3.0 \pm 0.1$ eV for type D and -1.1 ± 0.1 eV and $+3.0 \pm 0.1$ eV for E[1]. Taking furthermore into account that these two adsorption conformations are moreover

[1]Concerning the experimental technique and the discussion of the uncertainty of the experimental values see Sec. 2.4.

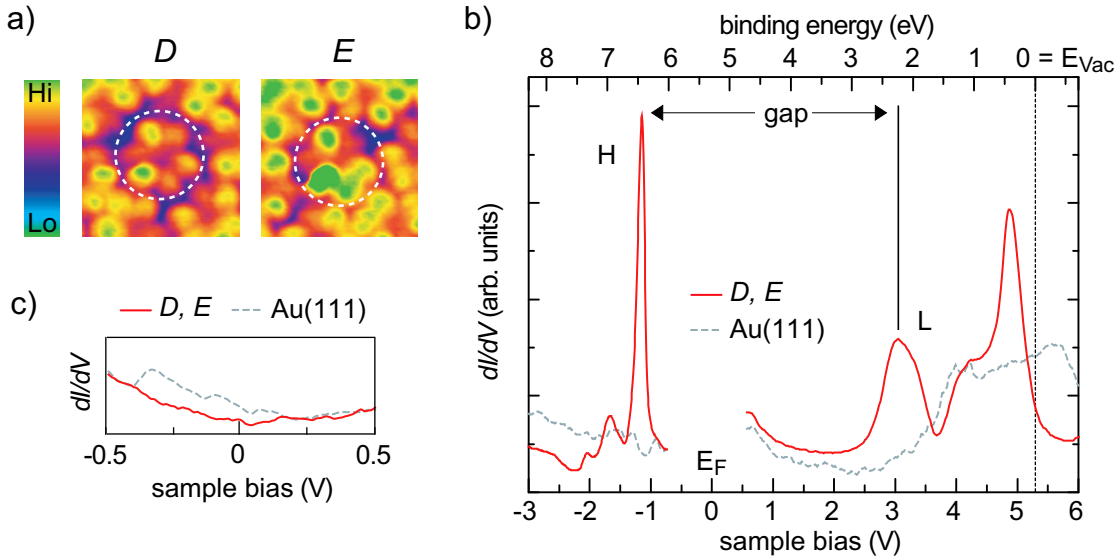

Figure 6.3: a) STM images of conformers *D* and *E* of rubrene on Au(111). (2.7 nm × 2.7 nm, tunneling parameters: $V = -0.8$ V, $I = 50$ pA) b) *dI/dV* spectra acquired with enabled feedback loop over rubrene molecules of conformation *D* and *E* and over the clean gold surface. c) *dI/dV* spectra recorded with disabled feedback loop close to E_F revealing the surface state onset of Au(111) and the absence of molecular levels in this range.

differently bonded in the hcp islands, compared to the "linked molecules" of type A to C, the spectra of conformers D and E are no longer explicitly distinguished in the following discussion. Consequently the STS measurements in Fig. 6.3 (b), acquired up to higher positive voltages, show only one representative spectrum for both conformers D and E (red solid line), together with the signal from the bare gold surface (gray dashed line). The intermediate voltage range, acquired with disabled feedback loop[2], is shown in Fig. 6.3 (c) and demonstrates the absence of molecular levels close to E_F. The rubrene spectrum shows a peak H which is separated from a peak L by a large energy gap of 4.1 ± 0.2 eV. The intense peak with a pronounced shoulder showing up at higher positive voltages originates presumably from higher lying molecular levels of rubrene. However, due to the presence of a signal from the bare substrate originating from the bulk states on Au(111) at $\approx +3.5$ eV [185], an influence of the metal cannot be excluded.

Taking into account the work function $\Phi_{Au(111)} = 5.3$ eV, [186] the position of peak H at $E_H = -1.1 \pm 0.1$ eV corresponds to a binding energy of $\Phi_{Au(111)} + E_H = 6.4 \pm 0.1$ eV. The different energy scales used here are on the one hand the energies which are measured by STS with respect to $E_F = 0$ and on the other, the binding energies (ionization potential, work function) taken from the literature which are taken positive with respect to E_{Vac}, as shown by the lower and upper scale in the dI/dV spectrum of Fig. 6.3 (b). A comparison of this value to the ionization potentials of rubrene in the gas and solid phase (see Sec. 1.2.2) uncovers an agreement of E_H to the value of the ionization potential in the gas phase IP = 6.4 eV. The electronic level H measured by STS is therefore identified with the HOMO of the adsorbed molecule. The peak L in the positive voltage range is consequently assigned to the LUMO of rubrene. The good agreement of the energetic position of the measured peak H of these types of rubrene conformers adsorbed on Au(111) with

[2]The used experimental technique with enabled feedback loop prevents a continuous measurements over the whole voltage range crossing $V = 0$ and makes it necessary to take two different spectra for negative and positive voltages (see Sec. 2.4).

Conformer	A	B	C	D	E	
E_{HOMO} [eV]	-2.3	-1.8	-1.5	-1.2	-1.1	with respect to E_{F}
	7.6	7.1	6.8	6.5	6.4	with respect to E_{Vac}

Table 6.1: Experimental values of the energetic positions of the HOMO for the five different adsorption conformations *A* to *E*. The values are given with respect to E_{F} and E_{Vac}.

the HOMO of the free molecules suggests an alignment of the vacuum levels of the molecule and the surface. This assumption is corroborated by UPS measurements showing only a small work function decrease of ≈ 0.1 eV upon adsorption of rubrene on Au(111) in the submonolayer regime of 0.1 to 0.3 ML [187], in agreement with NEXAFS studies which exclude a charge transfer between molecule and sample [39]. To reinforce this assumption of a vacuum alignment, STS measurements of rubrene adsorbed on substrates with different electronic structure are analyzed in Sec. 6.2.

The preceding discussion considered exclusively the molecules adopting conformations D and E. However, the HOMO values of conformers A to C, which are identified in Fig. 6.2 (a) by their submolecular contrast and the number of links to the surrounding molecules, are shifted to higher binding energies of 6.8 ± 0.1 eV (C), 7.1 ± 0.1 eV (B), and 7.6 ± 0.1 eV (A). These values follow from the positions of the HOMO in the dI/dV spectra in Fig. 6.2 (b) which reveal in contrast to the values for E and D at -1.1 ± 0.1 eV and -1.2 ± 0.1 eV, peak maxima at -1.5 ± 0.1 eV (C), -1.8 ± 0.1 eV (B), and -2.3 ± 0.1 eV (A). These values are summarized in Tab. 6.1. Given the fact that the influence of the surrounding molecules in a rubrene crystal decreases the HOMO energy from the gas phase value of 6.4 eV to 5.3 eV [55], the measured shift to higher binding energies of molecules of type A to C cannot be explained by a stronger interaction to the neighboring molecules.

The HOMO of rubrene is attributed to the extended π system of the molecule which is mainly concentrated on the tetracene backbone (see Sec. 1.2.2). The energy of the HOMO of rubrene is therefore related to the corresponding value of tetracene of 7.0 eV, but reduced to 6.4 eV due to the influence of the π systems of the phenyl groups (for the geometry of the molecule, see Sec. 1.2.1). This interaction of the electronic orbitals of tetracene with the substituents depends on the angle between the different parts [52]. This angular orientation of the phenyl groups with respect to the tetracene is variable due to the flexibility of the phenyls to rotate around their σ bonds and bend towards or away from the tetracene [23, 96, 188], as shown in the 3D representation of rubrene in Fig. 6.4 (a) and (b). A parallel orientation of the phenyl groups with the tetracene plane would yield a maximal coupling of the molecular orbitals and thereby a maximal decrease of the HOMO energy, compared to the value of 7.0 eV of tetracene. A minimal interaction is achieved for a perpendicular rotation of the groups, leading to a HOMO energy of rubrene which is identical to the value of tetracene. A conformational change of rubrene characterized by a stronger out-of-plane rotation of some or all of the phenyl groups from their gas phase angle of $\approx 60°$ [52] is therefore expected to result in an increase of the HOMO energy of 6.4 eV towards the value of 7.0 eV of tetracene. This mechanism would explain the shifted peaks observed in the dI/dV spectra of conformer A to C. The modification of the energy levels of rubrene, leading to an increase of the HOMO energy towards the value for tetracene should imply a shift of the LUMO closer to E_{Vac}, i.e. to higher positive voltages[3]. However, the dI/dV spectra shown in Fig. 6.2 (b) reveal a splitting of the LUMO for conformation C to A, which shifts

[3]The LUMO energy of tetracene is 1 eV with respect to E_{Vac} [189], corresponding to +4.3 eV with respect to E_{F} of Au(111).

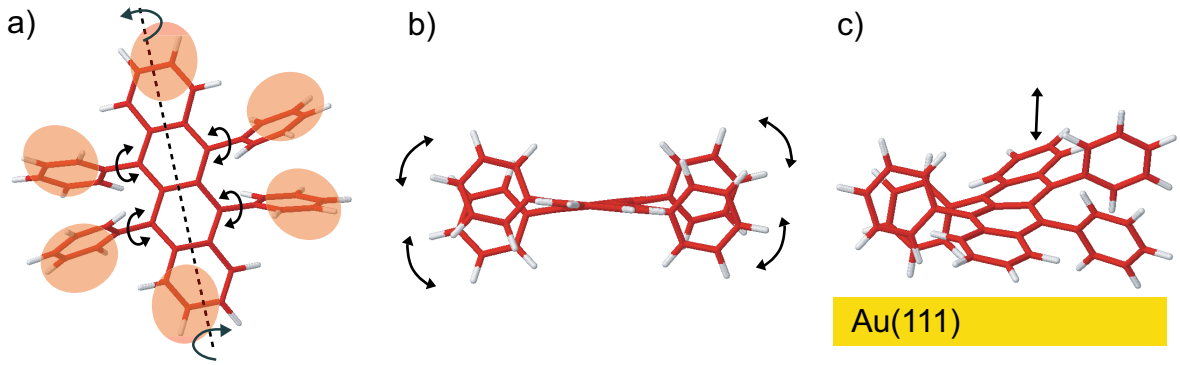

Figure 6.4: 3D representations of the geometry of rubrene showing the twisting of the tetracene backbone and the flexibility of the phenyl substituents to (a) rotate around the σ bonds leading to stronger or weaker out of plane orientation and (b) bend towards or away from the tetracene backbone. c) The inclination of the molecule on the surface can be changed.

slightly towards E_{F} and not away. This effect might be due to the increasing electronic coupling of the HOMO of these conformers with the d-band of Au(111) [65] which lies approximately between -2 eV and -6 eV [190], leading to a downshift of the molecular orbitals away from E_{Vac}. A similar phenomenon has been observed with STS for pentacene on NaCl, where the measured LUMO energy was of 1 eV higher binding energy compared to the gas phase value, while the HOMO was close to the known value from the literature [20].

The different adsorption conformations of rubrene on Au(111) are interpreted by combinations of any of the possible geometric changes of the molecule from the gas phase conformation. The already mentioned rotation and bending of the phenyl groups are likely to induce a modification of the inclination of the tetracene backbone with respect to the gold surface as indicated in Fig. 6.4 (c). An interpretation of the STM images of the different conformers in terms of an assignment of apparent features with specific parts of the molecule is difficult, taking furthermore into account the change of the submolecular contrast with the applied voltage (see Sec. 6.4). The almost circular circumference and the lateral dimensions of the molecule as well as the maximal six submolecular lobes visible in the STM images, suggests that the parts of rubrene indicated in Fig. 6.4 (a) are responsible for the contrast in the images. Depending on the applied voltage, the geometric height of the specific submolecular part and if it is in contact with the surface or not determines the tunneling current and consequently the apparent height in the STM image. Furthermore, the eventual superposition of parts of the molecule might enhance those parts, as reported for the "crossed legs" conformation of the Lander molecule in [188]. The different geometric and electronic structure of the various conformers are important for the self-assembly process of rubrene on Au(111). The STM image in Fig. 6.5 (a) shows a closeup view of a supramolecular honeycomb islet, revealing the existence of two different adsorption conformations, as indicated by the circles. The molecules in the island which are surrounded by three neighbors exhibit a conformation A^*, while conformers of type B^* are exclusively found at the edges where they are bound to only two other molecules. The STM image displayed in Fig. 6.5 uncovers that the molecules denoted by A^* form straight connection lines to its three neighbors in the same way as conformer A in the hcp islands. Furthermore, the molecules at the borders which are denoted by B^* reveal two linking bars, in analogy to conformation B in Fig. 6.2 (a). The different molecular contrasts are due to changed tunneling conditions, including change of the tip and reduced tunneling resistance. The distinction between the two adsorption

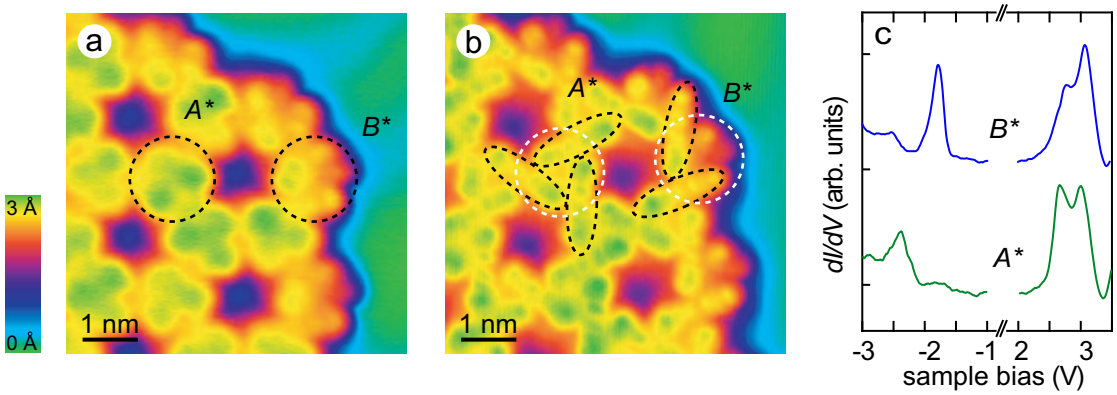

Figure 6.5: STM images of a self-assembled honeycomb islet on Au(111) revealing two different conformations *A** and *B** of the molecules. a) Conformers *A** are of symmetric threefold appearance and conformers *B** are of asymmetric shape. b) Different tunneling conditions reveal the connection bars between the molecules: three bars for *A** and two for *B**. (Tunneling parameters: a) $V = -1.0$ V, $I = 20$ pA; b) $V = -0.5$ V, $I = 100$ pA) c) *dI/dV* spectra acquired with enabled feedback loop over conformers of type *A** and *B**. The curves show the HOMO and LUMO positions of the two conformations. The curves are averages of several spectra taken over one conformer. The curves are offset for clarity.

geometries is substantiated by the different positions of the peaks in the negative voltage range of the dI/dV spectra displayed in Fig. 6.5 (c). In analogy to the results obtained for the molecules inside of the hcp islands, the features appearing at -2.4 ± 0.1 eV (A^*) and -1.8 ± 0.1 eV (B^*) are assigned to the HOMO of the molecules and the two peaks at $+2.7 \pm 0.1$ eV/$+3.0 \pm 0.1$ eV (A^*) and at $+2.8 \pm 0.1$ eV/$+3.1 \pm 0.1$ eV (B^*) to the LUMO of rubrene. The denotation of the conformations forming the honeycomb islet expresses the similarities of the HOMO and LUMO energies to the corresponding values recorded over conformers A and B found within hcp islands.

The study of the conformations adopted by the molecules in other organized supramolecular assemblies on Au(111) uncovers that all small structures from monomers to hexamers (see Sec. 3.2) appear exclusively in conformation A^*. This is shown by the submolecular contrast visible in the STM images of Fig. 6.6 (a) which resembles the one of the molecules enclosed in the honeycomb islets shown in Fig. 6.5 (a). STS measurements confirm by the characteristic position of the HOMO in the dI/dV spectrum at -2.3 ± 0.1 eV the equivalence of this adsorption conformation[4]. The STM image in Fig. 6.6 (b) shows a mixed structure formed by pentagonal supermolecules and hexagonal parts. A comparison with the submolecular appearance and the peak positions of the HOMO in the dI/dV spectra unveils that the molecules adopt either conformation A^* or B^*, just like in the case of the honeycomb islets. An investigation of the different phases obtained for varying rubrene coverage shows furthermore that the presence of molecules of type B^* found within pentagonal supermolecules increases with the number of existing pentagons on the surface. With the disappearance of honeycomb fragments and the presence of exclusively pentagonal chains (next to hcp islands), all molecules are found in conformation B^*, as shown in Fig. 6.6 (c).

The surprising dependence of the adsorption conformation of rubrene on the coverage and the type of supramolecular assembly suggest that A^* is the energetically favored conformer for isolated molecules. This adsorption conformation is observed only if the molecules have gained

[4] dI/dV spectra on monomers could only be performed down to -2 V due to the increased mobility of the single molecules. However, due to the absence of any peaks between E_F and -2 V, an assignment to any of the conformations B to E is excluded.

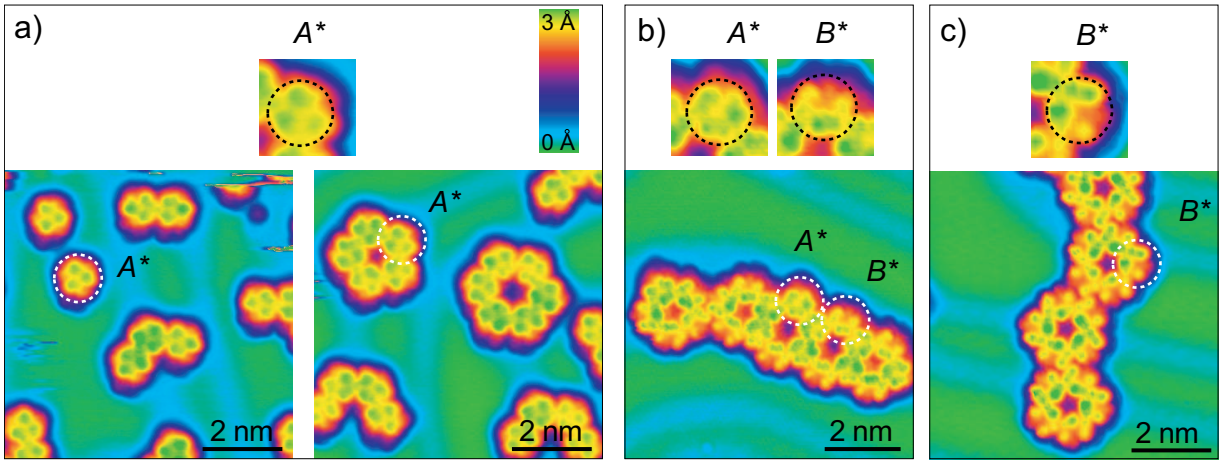

Figure 6.6: a) STM images of small structures from monomers to hexamers. All molecules adopt conformation *A**. b) STM image of a mixed structure of pentagonal supermolecules and honeycomb fragments. Both conformations *A** and *B** are present. c) STM image of a chain of pentagonal supermolecules. All molecules are in conformation *B**. (Tunneling parameters: a) $V = -0.8$ V, $I = 20$ pA; b) $V = -1.0$ V, $I = 50$ pA, c) $V = -0.8$ V, $I = 100$ pA)

enough thermal energy by an evaporation onto a sample held at room temperature or an annealing after deposition at low temperature. Without this energy supply, the rubrene molecules assemble into disordered and unstable two-dimensional clusters with a submolecular appearance resembling conformation D and E (see Sec. 3.1). The mobility of molecules which are not stabilized into clusters (even at a temperature of 5 K) unfortunately hindered reproducible spectroscopic measurements on this structures. The specific threefold adsorption conformation A^* is adopted by single molecules after annealing or upon room temperature deposition. Their self-assembly leads to the formation of dimers, trimers, and further on to pentamers and hexamers. The STM images in Fig. 6.6 (a) show that all molecules reveal an adsorption conformation A^*. However, at higher rubrene coverage, resulting in the creation of honeycomb islets and small pentagonal chains, the conformation of the molecules which are only bonded to two other neighbors at the borders of the honeycomb and inside of pentagons is either of type A^* or B^*. The fact that this transition to a different dominating conformer takes only place from a certain rubrene coverage and that the respective molecules sit at the borders of the structures suggest that this conformational change is induced by the interaction of the molecules with each other. As will be discussed in Sec. 6.6, the modification of conformer A^* to B^*, including the change of the corresponding electronic structure, can be deliberately executed with the STM.

6.2 Comparison with the results from rubrene adsorbed on Au (100), Ag (111), and Ag (100)

The deposition of rubrene on Au(100), Ag(111), and Ag(100) leads to less diverse self-assembled supramolecular structures than in the case of Au(111) (see Chapt. 7). While on both silver surfaces the molecules assemble exclusively into hcp islands, pentagonal supermolecules are present next to specially organized hcp islands in case of Au(100). However, the adsorption conformation of the molecules inside of the structures reminds some of those found on Au(111). The STM images in Fig. 6.7 show closeup views of the four different conformers observed within close packed

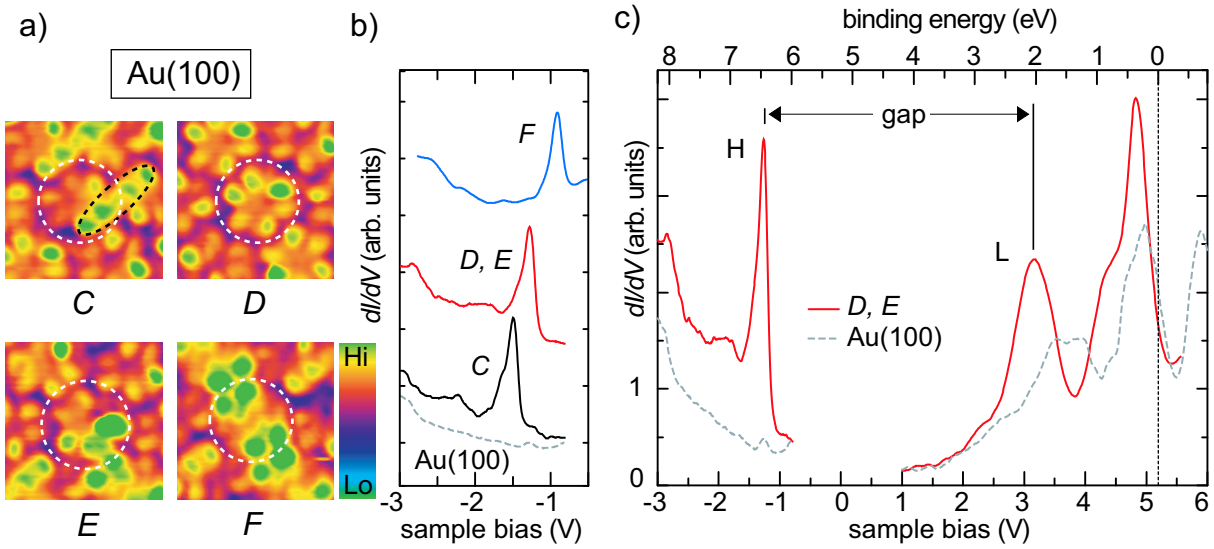

Figure 6.7: a) STM images of conformers *C* to *F* of rubrene on Au(100). (2.7 nm × 2.7 nm, tunneling parameters: $V = -1.0$ V, $I = 100$ pA) b) *dI/dV* spectra acquired with enabled feedback loop over different rubrene conformers probing the HOMO of the molecules. c) *dI/dV* spectra acquired with enabled feedback loop over rubrene molecules of conformation *D* and *E*. The dashed line shows the spectrum of the clean Au(100) surface, revealing image potential states [185].

islands on Au(100). A study of the submolecular contrasts and the presence of connection bars to the surrounding molecules (analogous to the investigation on Au(111)) reveals a correspondence of three of these molecules to the above defined conformers *C*, *D* and *E*. The fourth type, denoted by *F*, is not observed inside of the hcp islands on the (111) surface of gold, but has already been presented in Sec. 3.6 as the conformation of molecules which fill holes formed by a supramolecular heptagon.

The corresponding spectroscopic measurements probing the HOMO of the molecules reveal that the four conformers are furthermore characterized by shifted peak positions, similar to the case of Au(111). The dI/dV spectra of molecules of type *C* and *F* exhibit the HOMO at -1.5 ± 0.1 eV and -0.9 ± 0.1 eV, while conformers *D* and *E* show both the corresponding peak at -1.3 ± 0.1 eV. The complete spectrum of the latter conformations is given in Fig. 6.7 (c) and shows the HOMO (-1.3 ± 0.1 eV) and the LUMO ($+3.1 \pm 0.1$ eV), together with the signal recorded from the bare Au(100) surface. The overall shape of the spectrum, including the appearance of a higher lying unoccupied molecular level, is qualitatively similar to the spectrum measured over rubrene molecules on the (111) face of gold.

The molecular conformations observed on the (111) and (100) surfaces of silver are exclusively of type *D* and *E*. STM images of both conformers on the respective surfaces are shown in Figs. 6.8 (a) and 6.9 (a), exhibiting comparable characteristics of the submolecular features as in the case of conformation *E* and *D* on the gold surfaces. The corresponding dI/dV spectra of the conformers are presented in Figs. 6.8 (b) and 6.9 (b). They uncover the positions of the HOMO and LUMO and are characterized by the same overall shape as the spectra recorded over rubrene molecules on the Au(111) and Au(100) surfaces. However, due to the rigid shift of the spectra compared to the measurements on gold, the probed voltage range extends from -4 eV to $+5$ eV, instead of -3 eV to $+6$ eV. From the dI/dV curves, the HOMO and LUMO energies of the adsorbed rubrene molecules are determined to -1.9 ± 0.1 eV and $+2.1 \pm 0.1$ eV in the case of Ag(111)

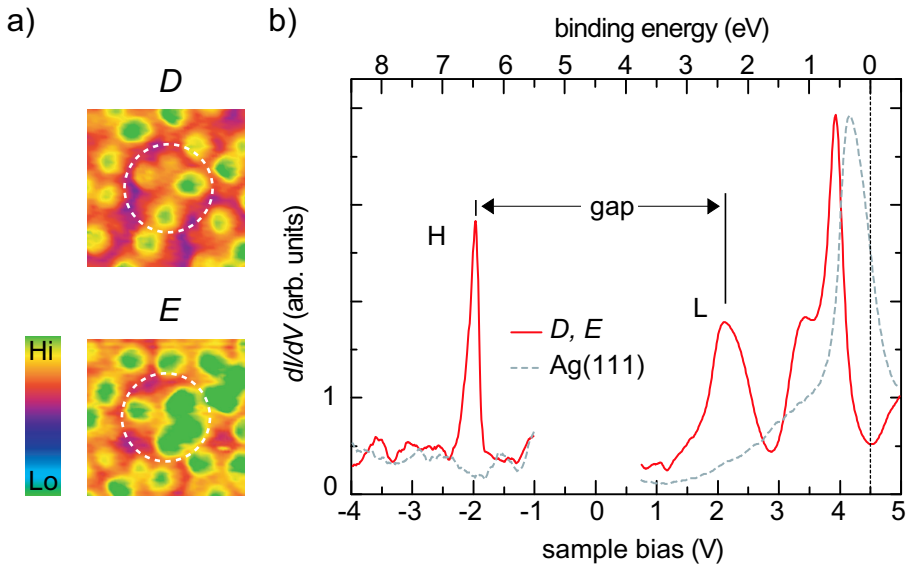

Figure 6.8: a) STM images of conformers *D* and *E* of rubrene on Ag(111). (2.7 nm $\times$ 2.7 nm, tunneling parameters: $V = +1.0$ V, $I = 100$ pA) b) *dI/dV* spectra acquired with enabled feedback loop over rubrene molecules of conformation *D* and *E*. The dashed line shows the spectrum of the clean Ag(111) surface, revealing the first image potential state [185].

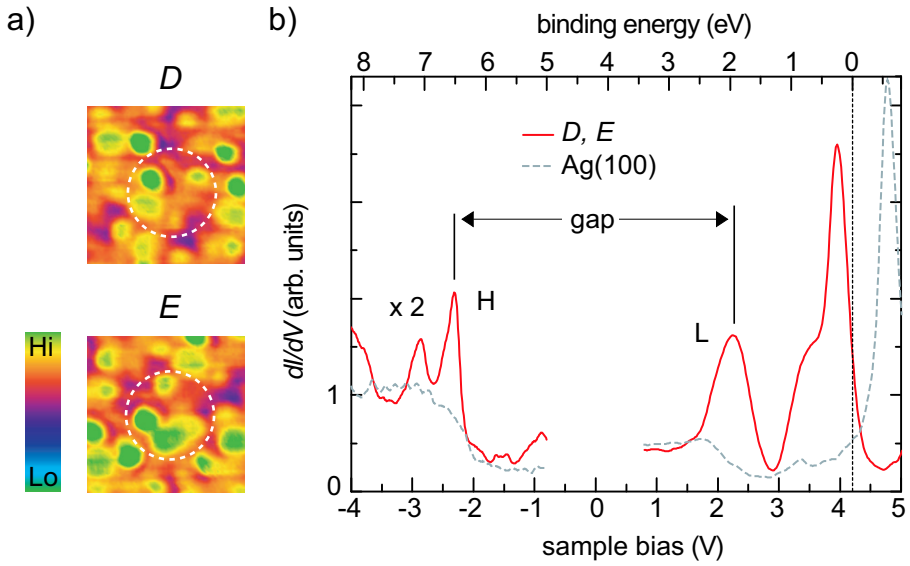

Figure 6.9: a) STM images of conformers *D* and *E* of rubrene on Ag(100). (2.7 nm $\times$ 2.7 nm, tunneling parameters: $V = -1.5$ V, $I = 50$ pA) b) *dI/dV* spectra acquired with enabled feedback loop over rubrene molecules of conformation *D* and *E*. The dashed line shows the spectrum of the clean Ag(100) surface, revealing the first image potential state [185].

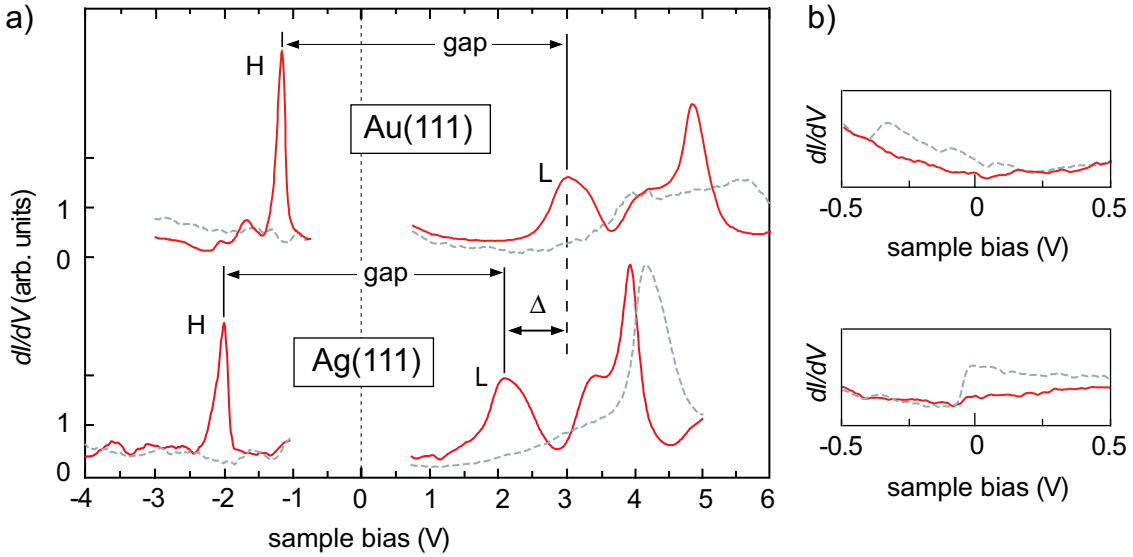

Figure 6.10: a) *dI/dV* spectra acquired with enabled feedback loop over rubrene molecules (solid lines) adsorbed on Au(111) and Ag(111) in conformations *D* and *E*. The dashed lines show the spectra from the clean surfaces. The HOMO and LUMO peaks H and L of rubrene on Ag(111) are shifted by Δ towards lower voltages, compared to the corresponding peaks of rubrene on Au(111). b) Corresponding spectra close to E_F recorded with disabled feedback loop. The signal from rubrene (solid line) shows the absence of molecular levels in the intermediate region. The surface state onsets on the bare metals are visible (dashed line).

and to -2.3 ± 0.1 eV and $+2.3 \pm 0.1$ eV for Ag(100). The fact that all four spectra recorded on rubrene show the same features of the unoccupied states which is independent of the strongly varying signals recorded on the clean substrates (i.e. the bulk states on Au(111) and the images potential state on Ag(111))[185] suggests that also the intense peak with a shoulder at high positive voltages originates from molecular states of rubrene.

Figure 6.10 (a) presents the spectra recorded over molecules of conformation *D* and *E* adsorbed on the (111) surfaces of gold and silver together in one scheme. The positions of the HOMO and LUMO peaks for the molecules on Ag(111) are shifted by Δ = 0.8-0.9 eV with respect to those recorded for molecules adsorbed on Au(111). This rigid shift Δ agrees well with the difference of the work functions Φ of Au(111) (5.3 eV [186]) and Ag(111) (4.5 eV [191]). This finding supports the assumption of an alignment of the vacuum level of rubrene to the ones of the respective surfaces and leads to the energy level schemes presented in Fig. 6.11 which are based on a common E_{Vac} of adsorbate and substrate. The diagrams are drawn for the case of resonant tunneling from the negatively biased substrate through the HOMO of rubrene into the empty states of the tip. A measurement of the unoccupied levels implies a reverse process (not shown), i.e. the application of positive bias voltage resulting in the alignment of E_F of the tip to the LUMO of rubrene. In this case, the electrons tunnel from the tip through the LUMO into the unoccupied states of the sample. Due to the alignment of the vacuum levels of rubrene and the respective substrates, the unequal work functions of Au(111) and Ag(111) lead to a different position of E_{Vac} with respect to the HOMO and LUMO of rubrene. Consequently, a larger negative bias voltage has to be applied in the case of Ag(111) to enable tunneling through the HOMO into tip. Furthermore, a smaller positive voltage for Ag(111) than for Au(111) is necessary, in order to reach the LUMO of the molecule. This schematic model describes well the

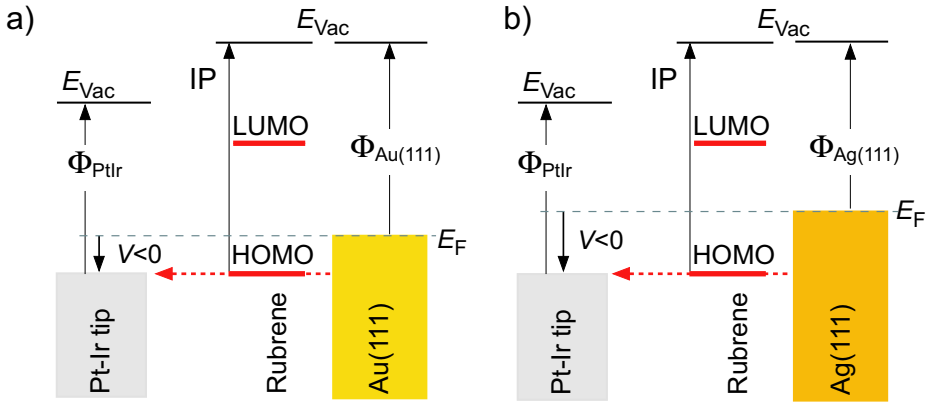

Figure 6.11: Energy level scheme for rubrene adsorbed on Au(111) (a) and Ag(111) (b) for resonant tunneling from the substrate through the HOMO of the molecule into the empty states of the tip. Due to the vacuum alignment of the adsorbate and the sample, the HOMO level of rubrene is further away from E_F on Ag(111). Consequently, a larger negative bias voltage has to be applied to enable tunneling through the HOMO into the empty states of the tip in the case of Ag(111), compared to Au(111).

different peak positions in the dI/dV spectra of Fig. 6.10 of the HOMO and LUMO of rubrene adsorbed on the (111) surfaces of gold and silver.

An analogous comparison of the HOMO and LUMO energies of rubrene measured on the Au(100) and Ag(100) surfaces gives further insight into the adsorption mechanism of the molecules. The values extracted from the dI/dV spectra of the four samples are summarized in Tab. 6.2, together with the work functions of the corresponding surfaces. The positions of E_{HOMO} and E_{LUMO} are given with respect to E_{F} and to E_{Vac}, allowing for a comparison of the deduced values with the known molecular levels of rubrene in the gas and solid phase. Furthermore, the energy gap between the HOMO and LUMO is determined to 4.1 ± 0.2 eV and 4.0 ± 0.2 eV for the (111) surfaces and larger values of 4.4 ± 0.2 eV and 4.6 ± 0.2 eV for the (100) faces of Au and Ag. The same experimental values for E_{HOMO} and E_{LUMO} are represented by the two graphs in Fig. 6.12. The energies are given as a function of Φ of the samples and expressed with respect to E_{F} in (a) and to E_{Vac} in (b). They show that E_{HOMO} of adsorbed rubrene measured by STS is close to the gas phase value of 6.4 eV for all four substrates and differs strongly from the solid state value of 5.3 eV [55]. The experimental values of E_{LUMO} vary between 1.9 eV and 2.4 eV for the different samples. They show a good agreement for the same crystal face, i.e. (111) or (100), but differ by 0.5 eV for the two silver surfaces. This yields an average value of 2.35 ± 0.10 eV for the (111) faces and 1.90 ± 0.10 eV in the case of the (100) planes. However, both values are reasonably close to the LUMO of rubrene in the gas phase, which is roughly estimated to 1.9 eV in Sec. 1.2.2.

The energy gap between HOMO and LUMO of 4.0 ± 0.2 eV for the (111) surfaces and 4.5 ± 0.2 eV for the (100) faces of gold and silver is deduced from the experimental values of E_{HOMO} and E_{LUMO}. Both values are clearly larger than the HOMO-LUMO gap of ≈ 2.7 eV measured for rubrene in the solid state and close to the gas phase value of ≈ 4.5 eV which was estimated in Sec. 1.2.2. Consequently, the results from the STS measurements of rubrene on different metal surfaces indicate that the molecular orbitals of the conformers D and E are only weakly perturbed by the presence of the substrate and the surrounding molecules. This surprising finding indicates a small charge transfer to the surface, as well as a weak polarization of the substrate and the molecular neighbors. This particular adsorption behavior is explained

	Au(111)	**Ag(111)**	**Au(100)**	**Ag(100)**	gas	
$\Phi[eV]$	5.3	4.5	5.2	4.2	phase	
E_{LUMO} [eV]	+3.0	+2.1	+3.1	+2.3	–	with respect to E_{F}
	2.3	**2.4**	**2.1**	**1.9**	$\approx$ **1.9**	with respect to E_{Vac}
E_{HOMO} [eV]	−1.1	−1.9	−1.3	−2.3	–	with respect to E_{F}
	6.4	**6.4**	**6.5**	**6.5**	**6.4**	with respect to E_{Vac}
E_{gap} [eV]	4.1	4.0	4.4	4.6	$\approx$ 4.5	$E_{\mathrm{HOMO}} - E_{\mathrm{LUMO}}$

Table 6.2: Experimental values of the energetic positions of the HOMO and LUMO of rubrene adsorbed on different surfaces and the resulting energy gap, together with the known and estimated values from theory. The values are given with respect to E_{F} of the respective metal and E_{Vac} (bold). The errors of the experimental values are discussed in Sec. 2.4. The different work functions Φ of the surfaces are noted in the first line.

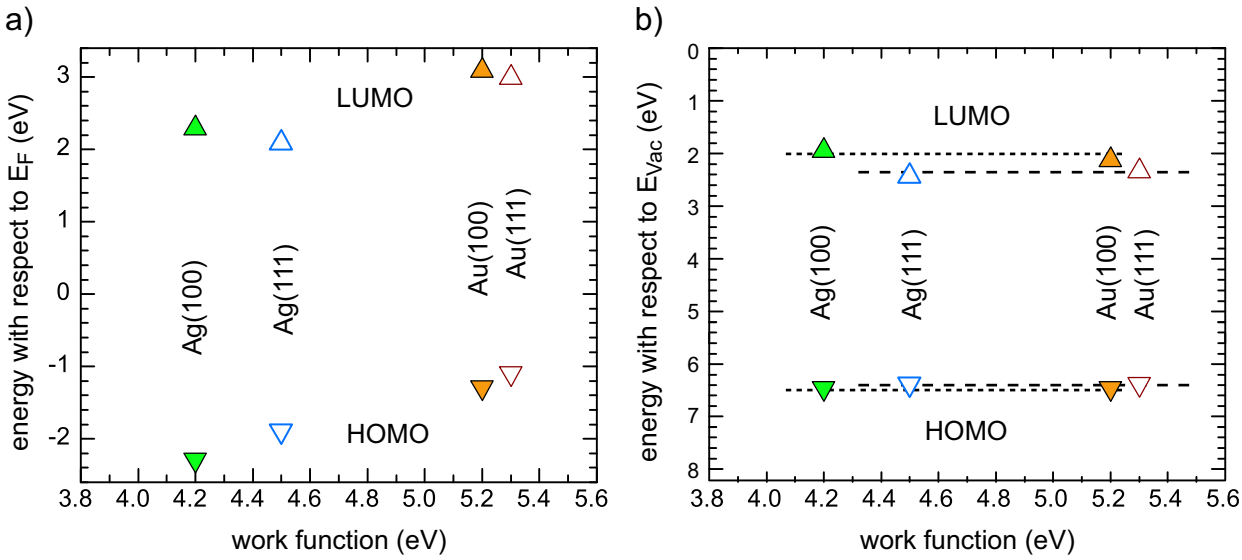

Figure 6.12: Experimental values of the HOMO ($\bigtriangledown$) and LUMO ($\bigtriangleup$) of rubrene adsorbed on Au(111), Au(100), Ag(111), and Ag(100). a) Measured energy with respect to the Fermi level $E_{\mathrm{F}} = 0$ of the corresponding metal. b) Measured energy with respect to the (common) vacuum level E_{Vac}. The dotted lines indicate the average value of the (100) surfaces ($E_{\mathrm{HOMO}} = 6.5$ eV, $E_{\mathrm{LUMO}} = 2.0$ eV) and the dashed lines the average positions of the (111) faces ($E_{\mathrm{HOMO}} = 6.4$ eV, $E_{\mathrm{LUMO}} = 2.35$ eV).

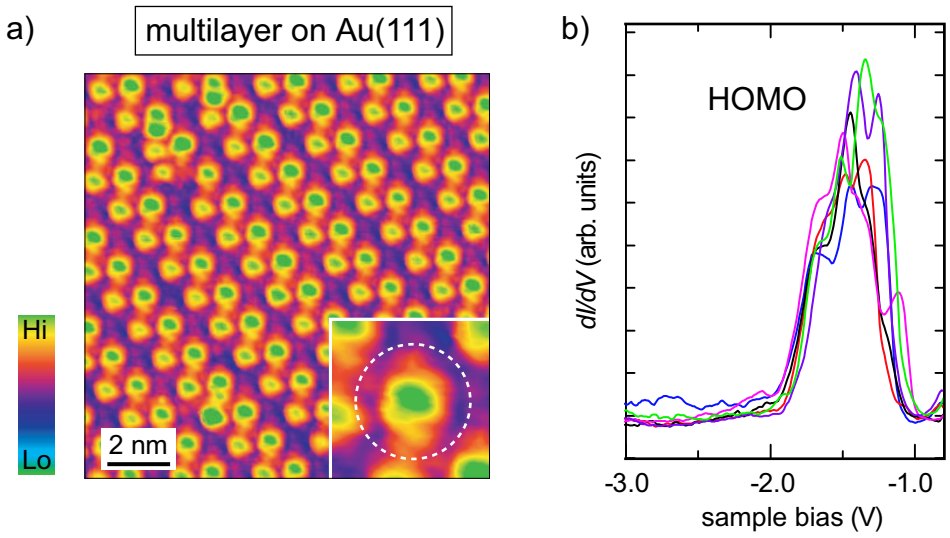

Figure 6.13: a) STM image of a multilayer of rubrene on Au(111) revealing the typical twin row arrangement. The inset shows a single molecule. (Tunneling parameters: $V = -3.3$ V, $I = 20$ pA) b) *dI/dV* spectra acquired with enabled feedback loop over different molecules in a multilayer of at least three ML. The sequence of peaks denoted by HOMO are presumably originating from the tunneling into molecules in different layers.

by a non-parallel orientation of the molecular π system with respect to the surfaces and to the adjacent molecules, due to an inclined molecular adsorption, as has been proposed for rubrene on Au(111) [39] (see Sec. 1.2.2). This inclination originates from the specific 3D geometry of rubrene, consisting of a twisted tetracene backbone and four out-of-plane rotated phenyl groups which impede a planar conformation of the central π system to the surface.

6.3 Spectroscopic results of rubrene in multilayers on Au (111)

The STM image in Fig. 6.13 (a) shows a multilayer of rubrene on Au(111). The main image reveals the typical arrangement of the molecules into twin rows (see Sec. 3.7) and the inset a zoomed image of an individual molecule inside of the surface layer. The corresponding dI/dV spectra are presented in Fig. 6.13 (b) and reveal a sequence of peaks starting from -1.1 eV on with respect to E_F. Due to the varying peak positions and intensities, several spectra recorded over different molecules are shown. The spectra are recorded over a third or fourth ML of rubrene on gold. Tunneling at positive voltages was not possible and thus prevented corresponding measurements of the unoccupied levels. In contrast to the situation of the submonolayer coverage where scanning is possible for voltages within the HOMO-LUMO gap due to the modulation of substrate states by the presence of broadened molecular metals of the molecules directly adsorbed on the gold surface,[80] the multilayers appear insulating for this voltage range. This leads to an approach of the tip to the sample in order to keep the tunneling current constant, leading to a crushing of the tip into the molecular layers.

The sequence of peaks with varying intensities and positions of the maxima between -1.1 eV and -1.7 eV forming the HOMO in the case of the multilayers of rubrene is surprising due to the apparent existence of only one type of conformer. However, the different peaks might originate from a resonant tunneling through the HOMO of molecules sitting inside of different rubrene layers forming the multilayer. The agreement between the onset of the electronic structure

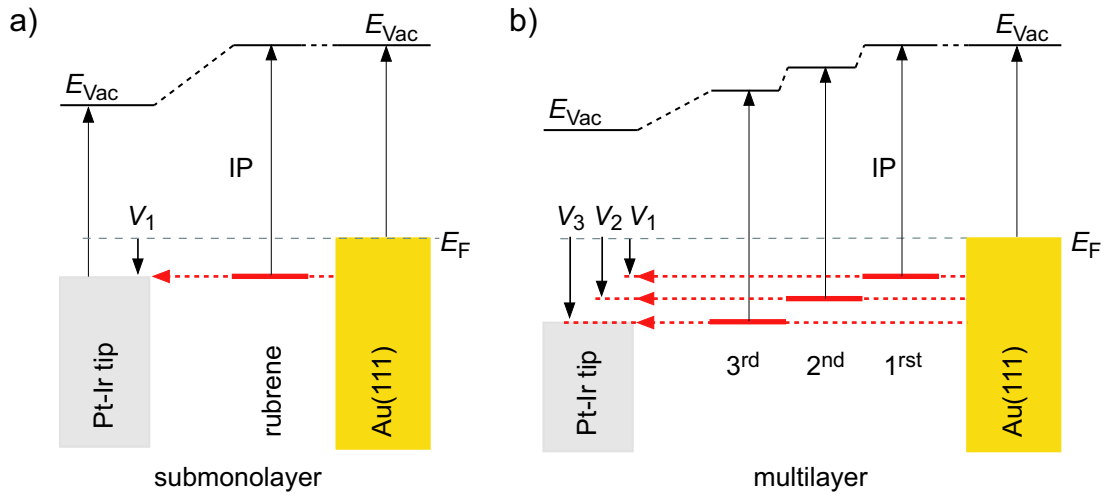

Figure 6.14: a) Energy level scheme showing resonant tunneling through the HOMO of rubrene directly adsorbed on Au(111). b) Proposed modified energy level scheme for a multilayer coverage of three layers. The electric field applied between tip and sample leads to a progressive downshift of the different molecular layers. This results in increased voltages V_2 and V_3 necessary for resonant tunneling through molecules in the second and third layer, respectively, while the bias V_1 is sufficient to reach the unchanged HOMO of the molecules in the first layer.

close to E_F with the HOMO peak position at -1.1 eV/-1.2 eV recorded for conformers D and E directly adsorbed on the bare Au(111) surface suggests that a part of the signal from the multilayer comes from molecules adsorbed in a similar manner than for the submonolayer coverage. The energy schemes in Fig. 6.14 show the situation for a submonolayer coverage (a), already discussed above, and the possible modified scheme for resonant tunneling through the different layers forming the multilayer. The applied electric field between tip and sample induces a downshift of the energy levels of the molecule within the second and third layer, which are not in contact with the metal. This leads to different positions of the HOMO with respect to E_F for the different layers, resulting in resonant tunneling through molecules for different voltages V_1, V_2, and V_3 in the case of three layers. In this way, molecules from all layers contribute to the dI/dV spectrum with different peak positions, producing a spectrum with a sequence of peaks.

6.4 Voltage dependent submolecular contrast

The different conformations which the molecules adopt determine the appearance of adsorbed rubrene in the STM images. However, this effect is strongest for tunneling voltages corresponding to energies within the HOMO-LUMO gap of the molecule. As discussed before, the width of this energy gap depends on the type of molecular conformation, in particular on the position of the HOMO of the respective molecule. The STM images showing a closeup view of a honeycomb islet in Fig. 6.15 are recorded for different bias voltages going from $+3.2$ V to -4.0 V. In this large voltage range, different changes of the submolecular appearance are visible in the corresponding 2D and pseudo 3D representations of the molecules. As discussed in Sec. 6.1, two different conformers are forming this supramolecular assembly, i.e. the molecules of type A^*, sitting inside of the islet and those of type B^* which form the outer borders. Since these molecules exhibit different submolecular features in the STM images, they are treated separately.

Voltage dependent STM images of the two conformers A^* and B^* are shown in Fig. 6.16. They

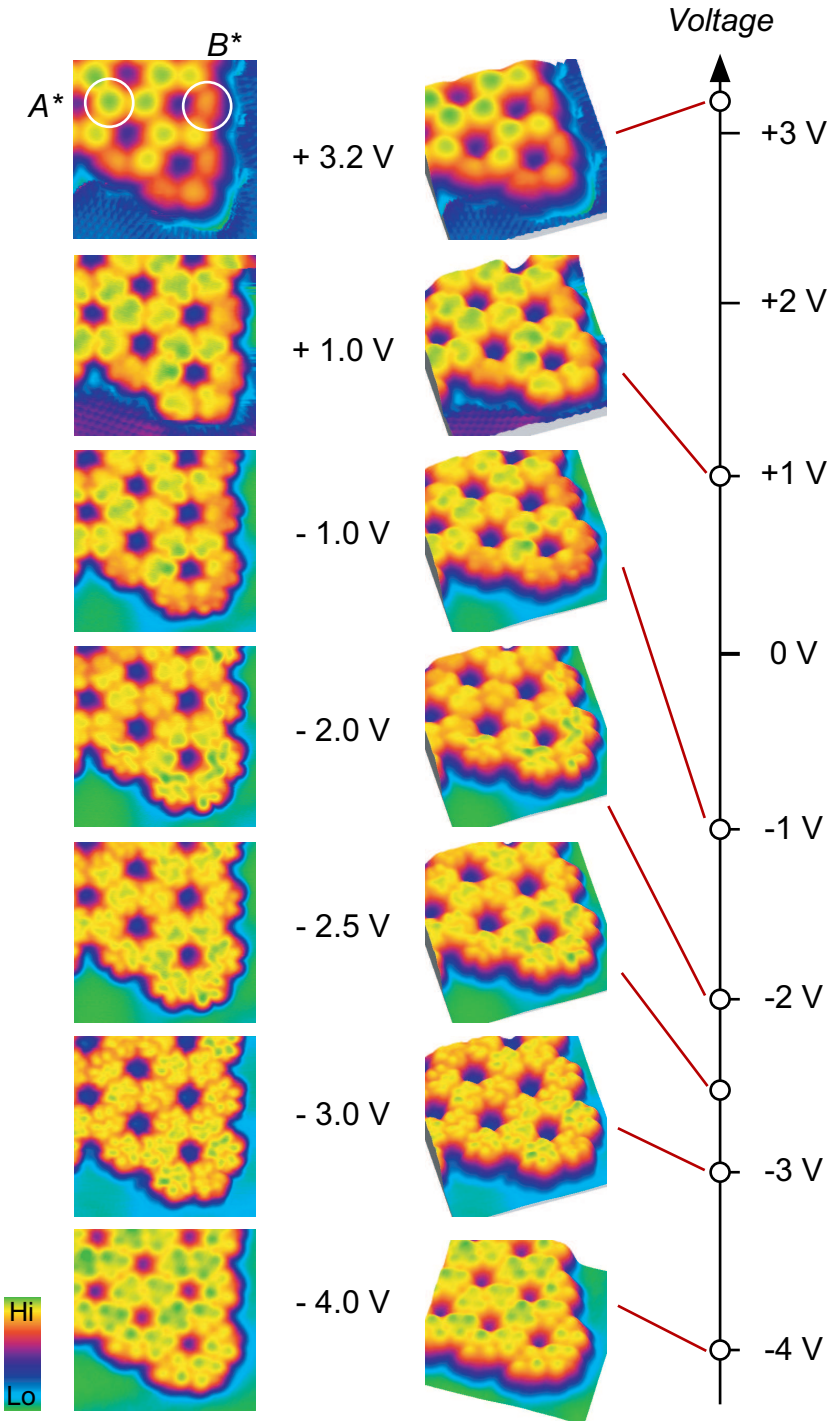

Figure 6.15: STM images showing a corner of a honeycomb islet made of conformers *A** inside and *B** at the borders of the structure. The images reveal a voltage-dependent submolecular contrast of the molecules in 2D and pseudo 3D representation. The blue contrast of increased apparent height in the images at positive voltages reveals an atomic resolution of the Au(111) surface due to the dragging of a molecule under the tip. (7.2 nm $\times$ 7.2 nm)

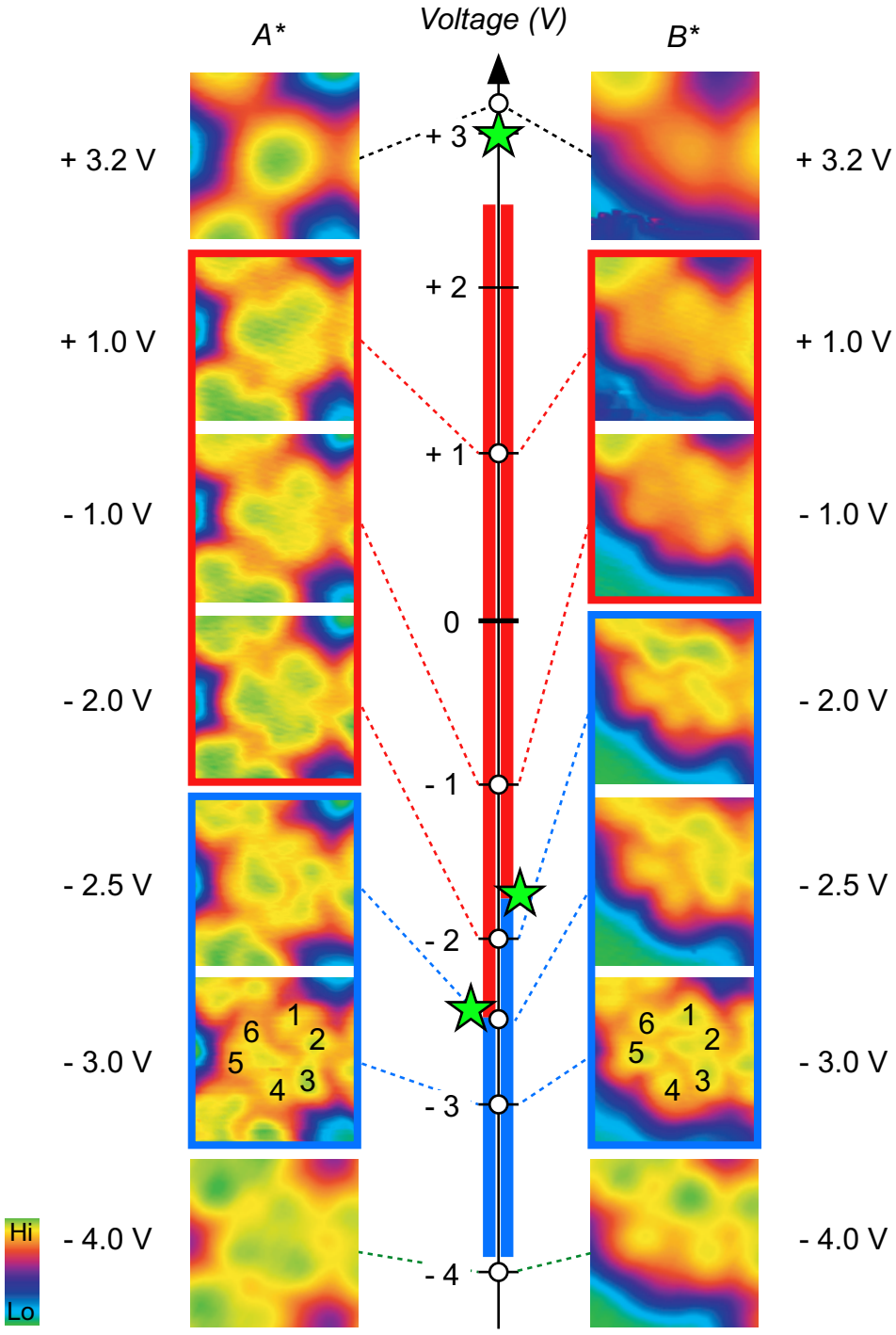

Figure 6.16: STM images showing the change of the submolecular contrast of conformer *A** and *B** with the voltage. The threefold intramolecular contrast of conformer *A** is unchanged for $+$ 2.7 V > V > $-$ 2.5 V. However the asymmetric contrast of conformer *B** is already changed at $V = -2.0$ V. The green stars indicate the positions of the HOMO and LUMO peaks measured in the *dI/dV* spectra of conformers *A** and *B**. (2.1 nm $\times$ 2.1 nm)

reveal changes of the submolecular contrast with the applied voltage and that the differences in the appearance of the two conformers depend on the considered bias. At high positive voltage of +3.2 V, both conformations appear as featureless protrusions which differ only in intensity and weakly in geometry. For a large voltage range $+2.7 > V > -1.7$ V, the STM images of A^* reveal three maxima arranged in a threefold geometry, while the molecules of type B^* appear dimmer and of asymmetric shape. However, the latter conformer changes its submolecular features at -2.0 V and preserves these with only small variations for voltages $V > -4.0$ V. In the image recorded for -3.0 V, the existence of six outer lobes of approximately equal height are indicated which are arranged pairwise. In contrast to conformer B^*, molecules of type A^* modify their appearance in the STM images only at -2.5 V. From this voltage on, the submolecular features of both conformers start resembling each other and at -3.0 V, they both reveal three pairs of two lobes in the submolecular contrast which remind the typical appearance of the molecules of conformation D which are present within the hcp islands (see Fig. 6.2 in Sec. 6.1). For voltages $V \leq -4$ V,[5] the contrast changes back to a threefold symmetry, however with a more triangular shape for A^*, compared to voltages close to E_F, and stronger intensities of all lobes for B^*.

Taking into consideration the values of the HOMO and LUMO measured over molecules of different conformations by STS, a good agreement between the peak positions in the dI/dV spectra (indicated by the green stars in Fig. 6.16) and the voltage below which the submolecular features change becomes evident. The measurements show that the conformers A^* and B^* appear dissimilar for voltages above the peak position of the HOMO. However, for scanning at voltages lower than the respective molecular level, the conformers reveal similar features than D consisting of six lobes which are arranged pairwise. Due to the fact that the HOMO of conformation D (-1.2 eV) is much closer to E_F, its submolecular appearance does not change with increasing voltage since it includes the molecular peak already at lower bias. The tunneling current at a specific voltage V is an integration over all LDOS from the E_F to V, with an enhancement of the states close to E_F compared to the states at V in the case of negative voltages. Consequently, an STM image recorded at a voltage of -3 V does include the signal from the resonant tunneling through the HOMO,[6] but is more a sum of the contribution from all states between E_F and V (see Sec. 2.2).

The fact that the molecules are imaged for voltages within the HOMO-LUMO gap suggest that the tunneling mechanism for these voltages is due to a "modulation" of the substrate states by a small tail of the molecular level reaching into the energy gap [79]. This contribution to the LDOS leads to the situation that the substrate states have a greater extension into the vacuum above the molecule than on the bare surface. This property renders the geometric features of the molecules visible in the STM images, even without a resonant tunneling into the molecular levels [80]. Consequently, the unequal appearance of the different conformers in the STM images might result from differences of actual geometric features of the molecules. As soon as the voltage corresponding to a molecular level is reached, a strong signal due to the resonant tunneling into the electronic state dominates over the modulation of the substrate states. Like this, geometrically lower-lying molecular parts become visible if they contribute to the LDOS of the respective molecular level. The featureless appearance of all conformations of the molecules at a voltage corresponding to the LUMO of adsorbed rubrene at +3 eV does presumably not reflect the spatial distribution of the molecular orbital. This molecular contrast is characterized by an increase of $\approx 30\%$ in apparent height and is explained by a field induced attraction of the molecules to the tip. This process is furthermore substantiated by the atomic resolution obtained

[5] STM imaging was possible for voltages down to -5 V.

[6] dI/dV maps give such an image of the spatial LDOS distribution at a certain energy. Unfortunately, these measurements could not be successfully performed on the presented system.

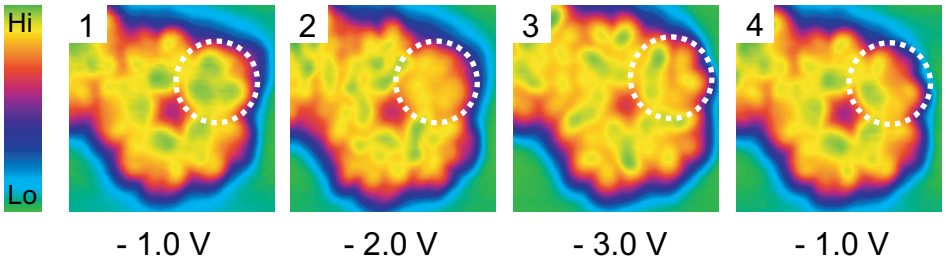

Figure 6.17: Sequence of STM images showing the switching of the molecular conformation of the encircled molecules inside of a pentagonal supermolecule by scanning at −3 V. While this molecule initially adopts a conformation *A** and appears different from the other molecules in image 1 and 2, the molecule has changed its conformation to type *B** in image 4. (4.6 nm × 4.6 nm; $I = 40$ pA (1, 2, 4) and 60 pA (3); The apparent height scale is changed from 1 to 4, to adapt to the increased heights in order to obtain the best submolecular contrast.)

on the Au(111) substrate surrounding the islet for positive voltages (see Fig.6.15), suggesting the dragging of a molecule which is captured under the tip across the surface [192, 21, 91, 112, 193].

6.5 Switching the conformation and the electronic structure of rubrene on Au(111)

An interesting phenomenon related to the two conformers which form the small supramolecular structures from dimers of molecules to the honeycomb islets and assemblies of pentagonal supermolecules is the transformation of the molecular conformation from type A^* into type B^*. As discussed in Sec. 6.1, all small structures from monomers to pentamers and hexamers consist of molecules adsorbed in conformation A^*. Only upon higher coverage, resulting in the formation of larger structures like honeycomb islets and small chains of pentagonal supermolecules which are still merged with hexagonal fragments (see Sec. 3.13), molecules of conformation B^* appear. An analysis of the STM images reveals that those molecules which form the borders of the assemblies, and which are consequently bound to only two neighbors, adopt either conformation A^* or B^* (see Fig. 6.5 (b) and Fig. 6.6 (b)).

Imaging these mixed structures by varying the voltage in the range of $-1 \geq V \geq -3$ V uncovers a surprising process which takes place by the scanning at voltages of ≈ -2.5 V. The subsequently recorded STM images displayed in Fig. 6.17 show a pentagonal supermolecule which terminates a mixed pentagonal-hexagonal structure. The first image, acquired at -1 V, unveils the presence of one molecule of conformation A^* inside of the pentagon which consists otherwise of molecules of type B^*. This different conformation is also visible in the second image[7], taken at -2 V, which shows the voltage dependent change of the appearance of conformation B^*, as discussed in Sec. 6.4. In the following image 3, all the molecules exhibit the same submolecular contrast which is typical for both conformers at this voltage of -3 V. The subsequently recorded image, acquired at the same voltage of -1 V as image 1, uncovers that the encircled molecule has changed its conformation from A^* to B^* and appears with the same submolecular contrast as the other molecules. The change of the molecular conformation consists of a modification of the geometric heights of the different submolecular lobes. The closeup views of the molecule

[7] The different apparent height of the investigated molecule is due to a change of the z scale in order to adapt to the increase in intensity of the molecules of type B^*.

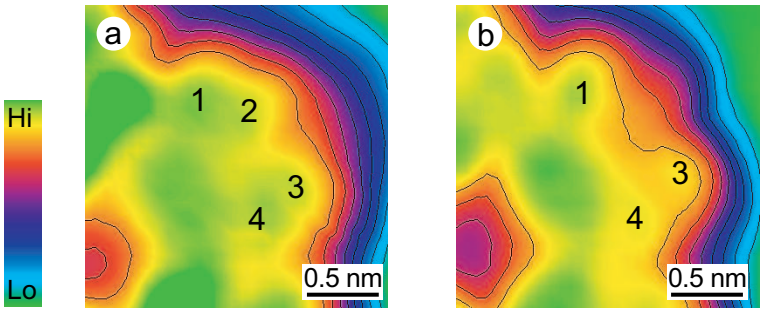

Figure 6.18: Closeup view of the molecule shown in Fig. 6.17 which experiences a switching from conformation *A** to *B**. The submolecular contrast of the molecule before the modification visible in (a) reveals four lobes, denoted by 1 to 4. A comparison with the switched molecule in (b) uncovers that feature 1 is unchanged, but that 3 and 4 are appearing lower and lobe 2 is almost invisible. The contours given in red show that this lobe still exists, however at much lower height.

undergoing the switching in Fig. 6.17 shown in Fig. 6.18 (a) before and (b) after the conformational change uncovers that mainly one lobe of the molecule has changed. The comparison of the four distinguishable outer features, denoted by 1 to 4 in Fig. 6.18 (a) with the corresponding ones visible in (b) uncovers the preservation of lobe 1, next to which the following number 2 has almost completely vanished. The contours of the molecule which appear in red uncover that the feature is still present, however at a strongly reduced height. Lobes 3 and 4 are also diminished, compared to the corresponding ones in (a). This change of the molecular conformation by imaging at voltages of ≈ -2.5 V has proven to be successful for all conformers A^* which are integrated in pentagonal supermolecules. In contrast to this, only $\approx 60\%$ of the molecules which form the borders of hexagonal structures switch into conformation B^* by an imaging at increased voltages.

The modification of the molecular conformation from type A^* to B^* is furthermore performed by applying a voltage ramp from -1 V to -3 V with the tip positioned over the respective molecule. This change is shown in Fig. 6.19 by the submolecular appearance of the encircled molecules in the STM images recorded before (a) and after (b) the voltage ramp. Furthermore, the z displacement curves of the tip are presented in Fig. 6.19 together with the simultaneously acquired dI/dV spectra. The dI/dV curve acquired over the conformer A^* shows no clear peak corresponding to the HOMO of this conformation. However, the $z(V)$ curve in (a) reveals a sudden jump τ at ≈ -2.2 V indicating a sudden withdrawal of the tip. Figure 6.19 (b) displays the subsequently recorded STM image together with the corresponding dI/dV spectrum and the $z(V)$ curve. The submolecular contrast of the studied molecule in the STM image reveals that the geometry of the molecule has been switched from conformation A^* to B^*. Furthermore, the appearance of a peak at ≈ -1.8 V in the dI/dV spectrum recorded after the second image demonstrates that a modification of the electronic structure of the molecule has occurred simultaneously with the conformational change. The z displacement curve shows only a smooth increase due to the enabled feedback loop which leads to the retraction of the tip due to the increased current corresponding to the peak in the dI/dV spectrum. Given the fact that the peak position of the HOMO of conformer A^* is located at ≈ -2.4 V, this molecular level is not observed in the dI/dV spectrum recorded from -1 V to -3 V on the unmodified conformer in Fig. 6.19 (a), since the conformation of the molecule switches to B^* before the corresponding voltage is reached. The detection of this molecular level is therefore only possible for molecules of conformation A^* which do not switch, i.e. those in the honeycomb islets which are surrounded

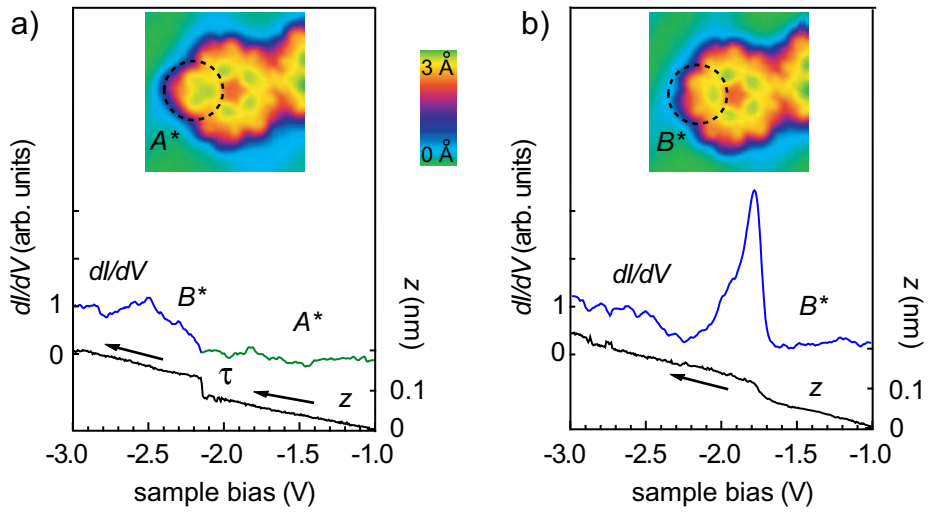

Figure 6.19: a) STM image of a pentagonal supermolecule with one molecule of conformation *A**. Simultaneously acquired *dI/dV* spectrum and *z* displacement of the tip while applying a negative voltage ramp to the molecule of type *A**. The sudden jump τ in the *z* curve indicates the switching of the molecule from conformation *A** to *B**. b) STM image displaying the switched molecule and the corresponding *dI/dV* and *z* curves. The peak at 1.8 V in the *dI/dV* spectrum evidences the modification of the HOMO of the molecule having occurred simultaneously with the conformational change. (5.2 nm $\times$ 5.2 nm; Tunneling parameters: $V = -0.5$ V, $I = 100$ pA)

by three neighbors (see Fig. 6.5). The HOMO of the modified molecule is clearly seen by the peak at -1.8 V in the corresponding spectrum and confirms that both the geometric and the electronic structure have changed to the corresponding structures of conformation B^*. This switching of conformation A^* to B^* involves by the shifting of the HOMO also a modification of the HOMO-LUMO gap. Since the LUMO position of both conformers is essentially the same (see Fig. 6.5 (c)), the shift of the HOMO closer to E_F implies a decrease of the HOMO-LUMO gap by ≈ 0.6 eV. The modified molecule keeps this conformation also under the influence of voltage ramps of negative and positive polarity. However, a switching back to conformation A^* is expected to occur upon an annealing of the sample, providing enough thermal energy to the molecules to return to their thermodynamically preferred adsorption conformation[8].

The switching from A^* to B^* is triggered by voltages of ± 2.0 V to ± 2.5 V and is performed also for positive voltages. Furthermore several molecules are modified at the same time by positioning the tip over the bare gold surface next to the self-assembled structures while performing a voltage ramp to $\approx \pm 4$ V. By this technique, also monomers and molecules in other structures having up to two neighbors have been changed. The results are exemplarily shown in Fig. 6.20 together with the original structures for a monomer, dimer, trimer, tetramer, pentamer, and hexamer which experience a modification of all their molecules. Only the last conformer A^* could not be changed to B^*. The application of the voltage ramp in the proximity of monomers induced a switching of the molecules which thereby became mobile and diffused to another adsorption site. With this technique, more than 100 molecules have been changed from conformation A^* to B^*. All molecules which are either isolated, or forming dimers, trimers, open zigzag lines or pentagons switch without failure. However, hexagonal supermolecules represent a special case,

[8] Due to the fact that the switching is performed at the nanoscale, changing only a very small fraction of molecules of the whole sample, this experiment would require a sample annealing inside of the cryostat with the tip held above the investigated area (variable temperature STM).

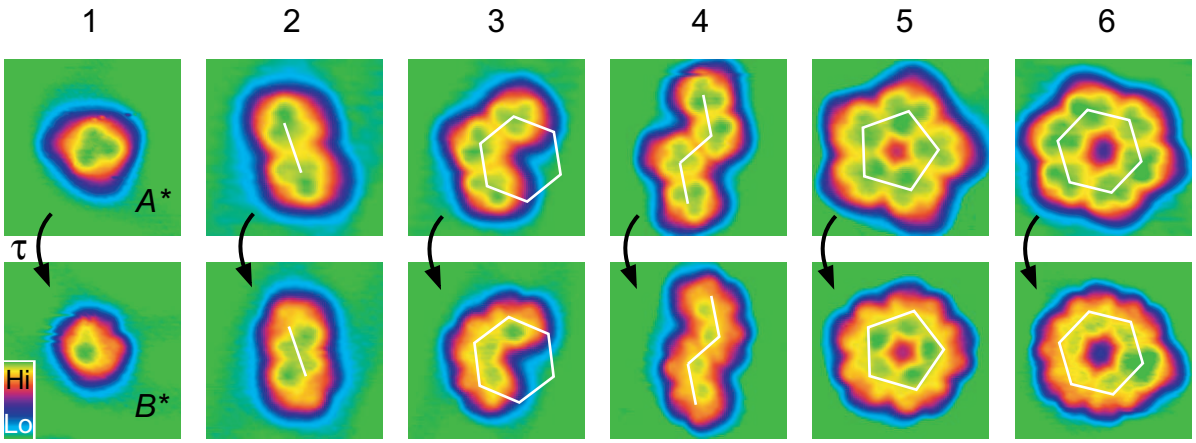

Figure 6.20: STM images of a monomer and a self-assembled dimer, trimer, tetramer, pentamer, and hexamer before and after applying positive voltage ramps on a bare gold surface area near the structures. All molecules forming the structures have changed their conformation from *A** to *B**, except one molecule inside of the hexamer. (5 nm × 5 nm; Tunneling parameters: $V = -0.8$ V, $I =$ 20 pA)

since only five out of the six conformers change to type B^*. The fact that this behavior is exclusively observed for the supramolecular hexagons indicates that the geometry of conformation B^* deviates from the almost perfect threefold shape of conformer A^*. Due to the similar angles of $\approx 60°$ of the triangular molecular shape of A^* and the inner angle of the hexagon, this type of molecules fits perfectly into hexagonal structures. However, if the conformation changes to type B^*, which is the preferred structure of the supermolecular pentagons, the geometry is no longer described by a regular triangle and is closer to a triangle with a base angle of 72° which corresponds to the inner angle of a pentagon. A switching of five molecules in a hexamer leads to a angular mismatch which results in the impossibility of the last conformer A^* to change into the wider conformation B^*, as displayed in the corresponding image in Fig. 6.20.

In principle, the switching could be induced by inelastic tunneling or field-assisted processes[24]. The fact that the conformational change is also induced with the tip held beside the molecules at lateral distances of more than one nanometer points to a minor contribution of the former mechanism due to the considerably decreased tunneling current through the molecule which is not directly under the tip apex. Therefore, we suggest that the switching is a field-assisted process [192, 21] which is triggered by an interaction of the electric field $\vec{E}$ between tip and sample with the molecule. Consequently, the polarity independent switching can be explained by the potential energy (in first order) $U = -\vec{\mu} \cdot \vec{E} - \frac{1}{2}\ \alpha\ |\vec{E}|^2$ which a molecule with a static dipole moment $\vec{\mu}$ and a polarizability α gains by the interaction with an electrical field $\vec{E}$. Given that for rubrene μ is small [53], the polarity dependent first term is negligible leading to a gain in energy which is independent of the sign of $\vec{E}$. Considering a polarizability $\alpha = 7 \cdot 10^{-39}$ $\mathrm{C^2m^2J^{-1}}$ of rubrene[9] and a tip-molecule distance of ≈ 1 nm, the electric field of $|E| \approx 2$ V/nm leads to an interaction energy of ≈ 100 meV (≈ 2 kcal/mol). This energy U is a reasonable value for an isomerization and can thus allow for a transition overcoming the energy barrier separating the local potential energy minimum of conformer A^* from the one of B^*.

[9]The value is calculated with ACD/Chemsketch and is roughly a sum of the polarizabilities of four benzenes and one tetracene.

Phase	**Small struct.** δ	**Honeycomb** η	**Mixed struct.** η/λ	**Pent. chains** λ	**Hcp** ω
Type of Conformer	A^*	inside: A^* border: A^*,B^*	inside: A^* border: A^*,B^*	B^*	A,B,C, D,E
Switch from A^* to B^* ?	yes, if # neighbors ≤ 2	yes, if # neighbors ≤ 2	yes, if # neighbors ≤ 2	–	–

Table 6.3: Types of conformers present in the different supramolecular structures self-assembled on Au(111). The switching from conformation *A** to *B** is indicated, if possible and under which conditions.

6.6 Conclusions

The investigation of the intramolecular structure of the molecules visible in the STM images allows for a classification of different adsorption conformations of rubrene. The geometric structure of the molecules depends on the underlying substrate and the type of supramolecular structures the molecules form. The largest variety of conformations is found on the Au(111) which is summarized in Tab. 6.3. A comparison of the peak positions in the dI/dV spectra with known and estimated values of the HOMO and LUMO of rubrene in the gas and solid phase shows that the adsorption conformers D and E which are present on all surfaces are characterized by electronic levels comparable to those of the "free" molecule. The spectra recorded over the distinguished molecular geometries show clearly different HOMO energies and thus demonstrate that the respective conformers are characterized by a well-defined electronic structure. The shift of the HOMO positions of conformations A, B, and C compared to the values of conformers D and E is related to the changing geometric structure of the different submolecular parts of rubrene. A switching of the conformation and the electronic structure of rubrene adsorbed on Au(111) from type A^* to B^* is deliberately induced with the STM on monomers and small supramolecular assemblies from dimers to hexamers, as well as molecules in larger structures where they possess not more than two neighbors, i.e. at the borders of honeycomb islets and in the chains of pentagonal supermolecules (see Tab. 6.3). Apart from the modification of the geometric conformation, the resulting changes involve a shift of the position of the HOMO and a reduced width of the HOMO-LUMO gap. This observation demonstrates for the first time a clear modification of the electronic structure of an adsorbed molecule with the STM without a change of the chemical composition. The process is explained by a mechanism originating from the electric field between tip and molecule acting on the strongly polarizable rubrene. The reverse switching from B^* back to A^* is expected to occur upon an annealing of the sample, resulting in a reversion of the switched conformer to the thermodynamically preferred adsorption conformation A^*.

Chapter 7

Substrate-dependent supramolecular self-assembly of rubrene

A comparison of the molecular properties on different metal surfaces offers an insight into the mechanisms which govern the adsorption and supramolecular self-organization of the molecules. The observed differences and similarities show the dependence of the molecular adsorption and self-assembly on the supporting substrate and indicate the influence of the electronic properties and the geometric structure of the metals. For instance, a change of the supramolecular organization of Cu-TBPP has been reported on Cu(100), Au(110) and Ag(110) surfaces and interpreted in terms of different molecule-substrate interactions [22]. The well-studied adsorption of C_{60} yields (quasi-) hexagonal close packed islands on the (111) surfaces of Au, Ag, Cu and Al [108]. In order to achieve commensurability with the respective surfaces, the specific intermolecular distances vary in dependence on the interatomic distance of the used substrate. Furthermore, spectroscopic measurements and DFT calculations reveal that the adsorption mechanism of the molecules is dependent on the underlying metal [194, 195, 196]. Another well-known molecule is PTCDA which arranges into overlayer structures of various symmetries on substrates such as the (111) and (110) faces of Ag [113, 112, 197], Au(111) [198], Au(100) [199], and Cu(110) [200].

The self-assembly of rubrene on Au(111), Au(100), Ag(111), and Ag(100) depends on the type of supporting metal surface. This variable assembly behavior is expected to be related to the geometric and electronic properties of the respective Ag and Au surfaces which are summarized in Tab. 7.1. The two metals possess a similar electronic structure, consisting of (almost)

	Au(111)	Au(100)	Ag(111)	Ag(100)
$\Phi[eV]^a$	5.3	5.2	4.5	4.2
d-band $[eV]^b$	-2	-2	-4	-4
$E_{\text{Surf.}}[eV]^c$	-0.48	-	-0.63	-
Reconstruction^d	$23 \times \sqrt{3}$	5×20	-	-
Distance [Å]^e	2.9	2.9	2.9	2.9

Table 7.1: Properties of the (111) and (100) surfaces of Au and Ag.
[a] Work function with respect to vacuum for gold [186] and silver [191].
[b] Upper edge of the d-band with respect to E_F [190].
[c] Surface state onset below E_F [201].
[d] Overlayer structure of the surface reconstruction.
[e] Nearest neighbor interatomic distance at the surface.

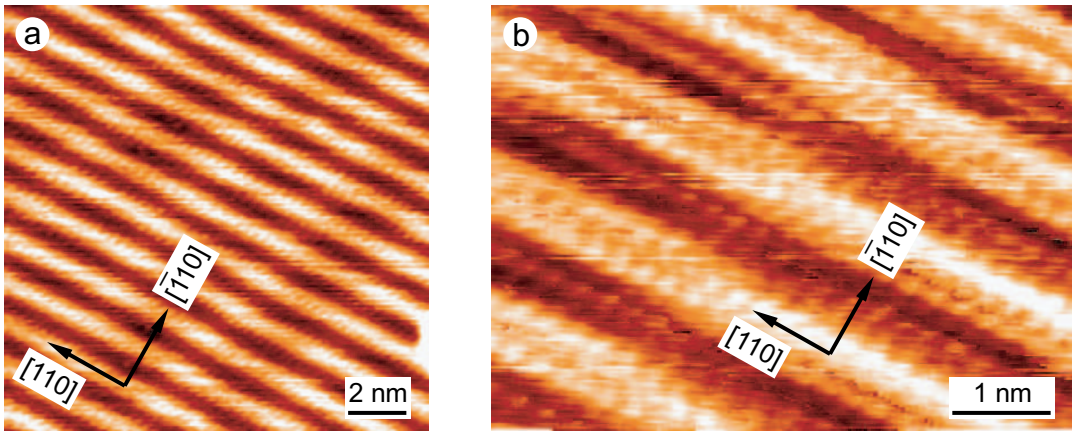

Figure 7.1: STM images showing the quasihexagonal Au(100) (5×20) (hex) reconstruction consisting of a compressed and rotated (111) overlayer on top of the square (001) surface of the fcc crystal of gold. a) Parallel running ridges along the [110] direction are separated by ≈ 1.4 nm and reveal a Moiré-pattern due to the angular mismatch of the hexagonal surface layer with respect to the [110] axis. b) The closeup view with (almost) atomic resolution of the hexagonal close packed overlayer. (Tunneling parameters: a) $V = -3$ V, $I = 20$ nA; b) $V = -0.02$ V, $I = 4$ nA)

completely filled d-bands [202] which lie significantly below E_F. Nevertheless, in the case of the gold substrate, the upper edge of the d-band is closer to E_F than for silver [190]. Furthermore, the electronic structures of the different faces of the respective Ag and Au crystals reveal a special feature for the close packed (111) planes, consisting of a sp-derived surface state at the $\overline{\Gamma}$ point of the projected bulk band structure [203]. The surface states are situated at -63 meV with respect to E_F in the case of Ag(111) and at -484 meV for the Au(111) [201]. Furthermore, the energy required to extract an electron from the surfaces to the vacuum is dependent on the type of metal and the symmetry of the crystal face. Consequently, the work functions of Au(111) and Au(100) are with 5.3 eV and 5.2 eV [186] higher than the corresponding values of 4.5 eV, and 4.2 eV for Ag(111) and Ag(100) [191]. The geometric properties of all four surfaces are characterized by an almost equal nearest neighbor distance of ≈ 2.9 Å. A strong difference consists however in the existence of a surface reconstruction in the case of the Au(111) and Au(100) faces, in contrast to the bulk-terminated corresponding Ag planes. The reconstruction of the gold surfaces introduces an additional corrugation and the presence of surface dislocation sites.

The deposition of rubrene molecules on the different samples at low temperatures of 5 K and 50 K without a subsequent annealing results in the same disordered two-dimensional clusters adsorbed on the terraces as in the case of Au(111), shown in Fig. 3.2, Sec. 3.1. The submolecular features of the molecules inside of these clusters is similar for an adsorption on all surfaces and is characterized by six-lobed structures resembling conformer D or asymmetric conformation similar to conformer E. However, the annealing to ≈ 300 K leads to different supramolecular structures for all four surfaces.

7.1 Pentagonal structures and close packed islands on Au (100)

The (100) face of a gold crystal shows a surface reconstruction consisting of a hexagonal overlayer which is incommensurate with the square lattice of the (100) truncated fcc crystal [204, 205, 206, 207, 208]. Such a reconstruction is reported for the late 5d metals Ir, Pt and Au and originates

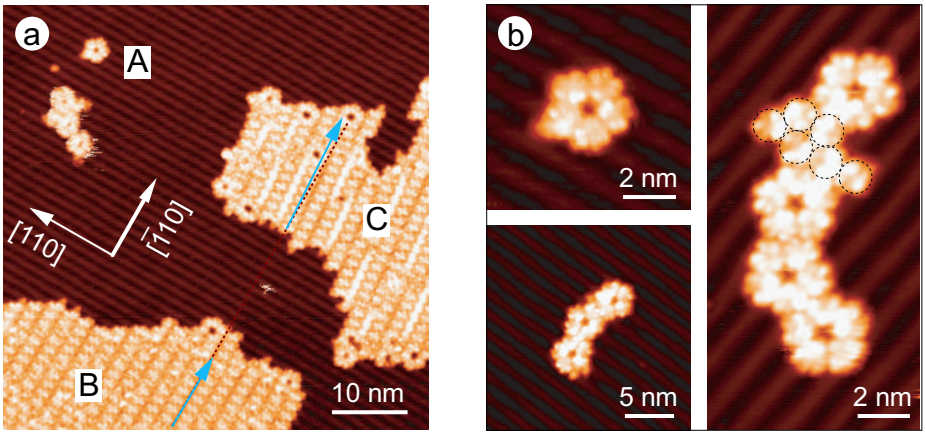

Figure 7.2: STM images showing different supramolecular structures self-assembled on Au(100). a) Overview image of three types of structures: small pentagonal (A), mixed quasi-commensurate (B) and incommensurate (C). b) Closeup views of a pentagonal supermolecule and a small supramolecular chain of pentagons, including also some close packed molecules (encircled). (Tunneling parameters: a) and b) left top: $V = -1.2$ V, $I = 100$ pA; b) left bottom: $V = -1.0$ V, $I = 20$ pA; b) right panel: $V = -1.0$ V, $I = 100$ pA)

from the surface stress of the unreconstructed last layer. In the case of Au(100), the quasi-hexagonal layer of surface atoms is characterized by an isotropic compression of the interatomic spacing by $\approx 4\%$ and a rotation of $\approx 1^\circ$ of a close-packed direction with respect to the [110] direction of the bulk. This leads to a (5×20) overlayer structure which is visible in the STM image shown in Fig. 7.1 by the parallel ridges along [110]. The reconstruction lines appear ≈ 0.5 Å higher in the STM images at a distance of ≈ 1.4 nm and are reported to inhibit strongly the molecular diffusion [209, 199]. In contrast to the (111) surface, there is no surface state on the (100) face of gold. Furthermore, the work function of Au(100) ($\Phi = 5.2$ eV) is slightly smaller than the corresponding value for Au(111) ($\Phi = 5.3$ eV) [186]. Consequently, the different properties of the electronic structure of the (111) and (100) surfaces of gold are expected to influence the adsorption and self-assembly behavior of rubrene on gold.

The deposition of rubrene onto a clean Au(100) surface held at room temperature results in three different supramolecular arrangements which are presented in the STM images shown in Fig. 7.2. The overview image in Fig. 7.2 (a) reveals small structures (A), next to regularly appearing, densely packed islands (B) and more irregularly appearing assemblies including holes (C). The indicated directions of the gold surface uncover that island of type (B) is oriented perpendicular to the ridges of the surface reconstruction, while there is a small angular mismatch between the indicated orientation of the island (C) and the [$\bar{1}$10] direction. This slight rotation of only a few degrees is characteristic for the supramolecular islands of type C.

7.1.1 Pentagonal structures

The closeup views of the small structures shown in Fig. 7.2 (b) uncover that they consist of individual or interlocked pentagonal supermolecules as the one observed on the Au(111) surface (see Sec. 3.4). The fact that these small supramolecular structures down to the individual pentagons are essentially stable and immobile on the surface at a temperature of 50 K indicates a higher diffusion barrier of rubrene on Au(100) compared to the high mobility of pentagonal supermolecules and supermolecular chains on the (111) surface. This might be due to the specific

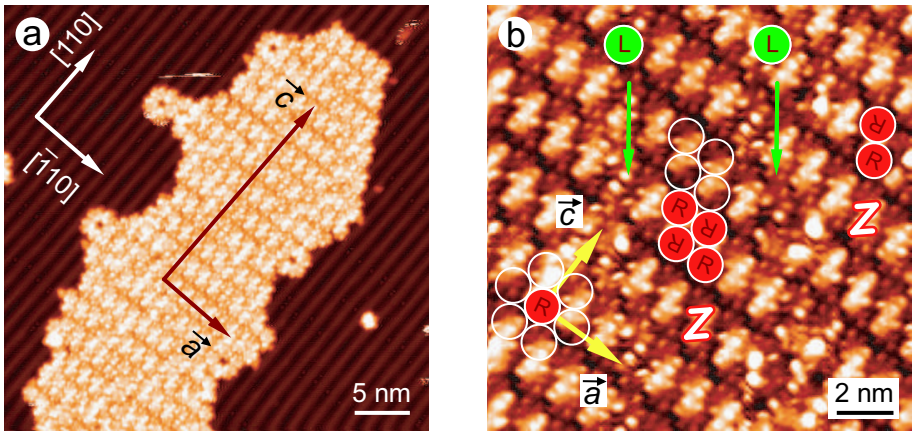

Figure 7.3: STM images showing self-assembled densely packed rubrene islands which are quasi-commensurate with the surface reconstruction of Au(100). a) Larger scale image revealing the directions of the (5×20) reconstruction and the directions $\vec{a}$ and $\vec{c}$ of the molecular island. b) Closeup view of the island showing the hcp arrangement of the molecules and the corresponding directions $\vec{a}$ (nearest neighbor) and $\vec{c}$ (second nearest neighbor) shown in (a). Three homochiral domains of type **R** are visible which are separated by molecules of **L** chirality. The *Z* shapes indicate linked molecules, forming dimers which compose the homochiral areas. (Tunneling parameters: a), b) $V = -1.0$ V, $I = 100$ pA)

hexagonal surface reconstruction [209, 199], which is characterized by a much higher corrugation than in the case of the herringbone reconstruction.

The existence of supramolecular pentagons on Au(100) gives evidence that the surprising self-assemblies are not due to properties specific for the (111) termination of the gold surface (compared to Au(100)) such as the presence of a surface state at ≈ -0.5 eV [201] or the peculiarities coming along with the herringbone reconstruction (i.e. different domains of hcp and fcc stacking and elbows forming the herringbone pattern). Just as in the case of the enantioselective hierarchical self-assembly of rubrene on Au(111) discussed in Sec. 4.2.3, the molecular organization into pentagonal supermolecules on Au(100) is driven by chiral recognition. This is seen by the study of the submolecular appearance, revealing lower lying shoulders either on the left- or on the right side of the maxima which determines the chiral signature of each molecule in the assembly. However, the precise intramolecular appearance of the molecules inside of the pentagonal structures differs from the typical appearance of conformers A^* and B^* observed on the (111) surface and is closer to the geometry of the conformers C and D, present within the hcp islands on Au(111). Unfortunately, STS measurements recording the position of the HOMO in the dI/dV spectra are missing, which would give insights into the type of conformer by the specific HOMO energy, compared to the data on Au(111). The second assembly step into pentagonal chains is following the same building rules as discussed in Sec. 4.2.4, leading to homochiral nested supramolecular chains of various shapes. However, the small number of pentagonal supermolecules present on the (100) surface does not allow for the formation of supramolecular decagons.

7.1.2 Quasi-commensurate islands

The supramolecular islands possessing the same appearance as the island denoted by (B) in Fig. 7.2 (a) reveal a basically regular arrangement of the molecules into rows along the [$\bar{1}$10] of the Au(100) surface. This alignment of $\vec{a}$ is shown in the STM image displayed in Fig. 7.3

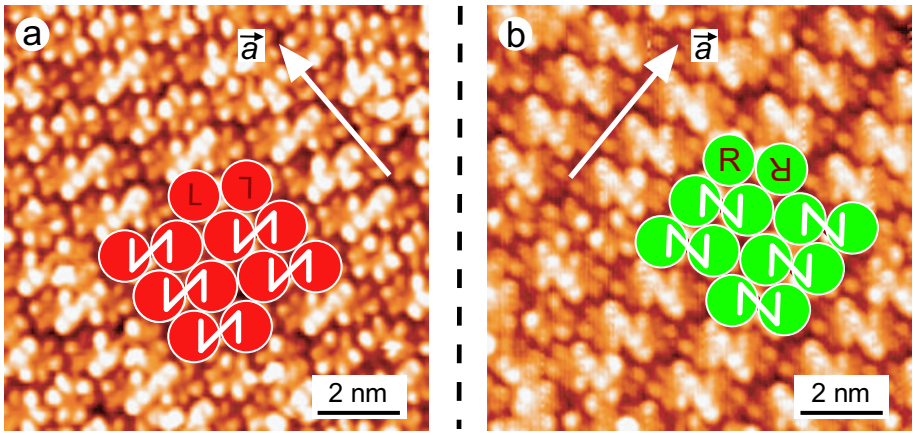

Figure 7.4: STM images showing mirror images of homochiral domains in different quasi-commensurate islands on Au(100). The molecules are enantioselectively assembled into hcp islands revealing an order into alternating rows of oriented molecules which are rotated by 180° with respect to each other. The *Z* shapes indicate the characteristic appearance of the brighter parts of the molecular dimers. (Tunneling parameters: a), b) $V = -1.0$ V, $I = 100$ pA)

(a), revealing a second apparent direction $\vec{c}$ in the island, perpendicular to $\vec{a}$, which is parallel to the [110] direction of the ridges on the surface. The closeup view of the island shown in Fig. 7.3 (b) uncovers the hcp arrangement of the molecules which are oriented in a such a way that two adjacent molecules form a *Z* shape, as indicated in the image. The long and brightest appearing line of the *Z* is oriented into the direction $\vec{c}$ of the supramolecular hexagonal packing. The STM images shows that the directions $\vec{a}$ and $\vec{c}$ which are aligned to the $[\bar{1}10]$ and [110] of the reconstruction, correspond to the nearest neighbor and second nearest neighbor directions of the close packed arrangement of the island. The submolecular appearance of the assembled molecules reveals their chirality and uncovers that the island is locally homochiral, i.e. that it is organized into uniaxial domains containing exclusively **R**-type molecules. These enantiopure domains are separated by parallel running narrow boundaries composed of molecules possessing the opposite chirality **L**. The chiral disconnection lines are oriented along the nearest neighbor direction of the molecules which form the *Z* shapes. These homochiral molecular dimers are built out of molecules with are rotated by 180° with respect to each other, as indicated by the superimposed drawings in Fig. 7.3 (b).

Taking into account the distance of 1.3 ± 0.1 nm between the molecules within the hcp islands on Au(111), a similar distance is expected for the densely packed islands on Au(100). The value is close to the separation of 1.44 nm between the trenches of the surface reconstruction of the (100) face of gold. A study of the intermolecular distances in the hcp islands on Au(100) reveals that they are close to the value of 1.3 ± 0.1 nm which is measured on Au(111). However, in order to adapt to the larger distance of the reconstruction ridges, the intermolecular distance varies slightly. In larger quasi-commensurate hcp islands on Au(100) the molecular arrangement with constant intermolecular distance of 1.3 nm is interrupted by cracking lines of larger nearest-neighbor separations which are visible in the STM images of Fig. 7.6 (a) and (b).

The smaller hcp islands of this type form quasi-commensurate, elongated patches on the Au(100) surface which are oriented with their longer axis along the [110] direction of the reconstruction ridges. The islands reveal either a dominant chirality of **L**- or **R**-type which is established by domains of parallel lines of homochiral molecular dimers, appearing in a brighter *Z* shape. This behavior leads to the presence of islands showing domains of locally enantiop-

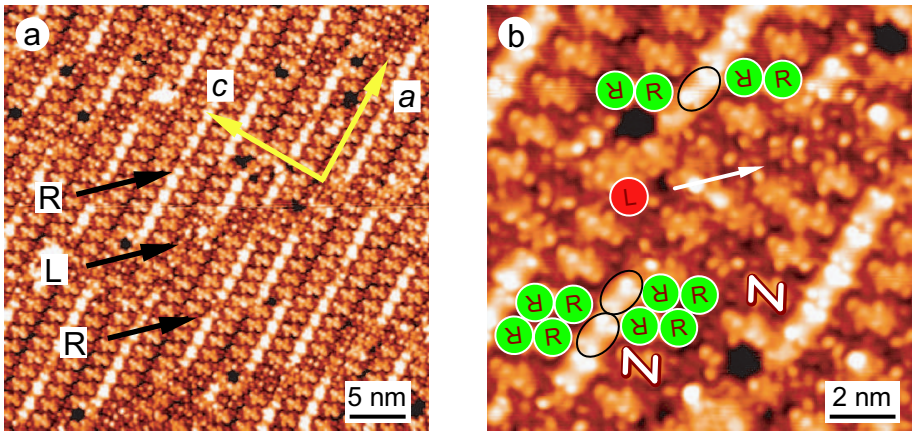

Figure 7.5: STM images showing an incommensurate hcp island on Au(100). a) Homochiral domains of **R**-type molecules are separated by transition regions of **L**-enantiomers. The holes show the presence of unfilled hexagons. b) The enantiopure domains consist of rows of molecular pairs as indicated which are interrupted by brighter appearing lines of molecules adsorbed in a special twofold conformation (encircled). (Tunneling parameters: a), b) $V = -1.0$ V, $I = 100$ pA)

ure hcp arrangement which are mirror images of each other, such as demonstrated by the STM images of Fig. 7.4.

7.1.3 Incommensurate islands

The islands which appear less regularly shaped and structured by holes and brighter lines, such as the island (C) shown in Fig. 7.2 (a) are characterized by a small misalignment of a few degrees of the molecular island with respect to the surface reconstruction of Au(100). This independence of the underlying periodicity is reflected in the shape of the islands which is not elongated into the [100] direction of the gold ridges and with straight borders like the quasi-commensurate islands, but of random shape without any preference of the growth directions. Their aspect is dominated by parallel running brighter appearing lines and the distribution of small circular openings which are scattered over the island or decorate the borders. The STM image shown in Fig. 7.5 (a) reveals the existence of ordered domains which are separated by narrow areas of fuzzy appearance.

The closeup view displayed in Fig. 7.5 (b) uncovers that part of the lines posses the same arrangement of homochiral dimers of molecules as within the quasi-commensurate islands which are indicated by the Z shapes. In contrast to the latter type of islands, the incommensurate arrangement contains a large number of unfilled hexagonal patterns, creating holes inside the island. Furthermore, every second or third row of homochiral dimers is replaced by brighter appearing rows. The thinner rows are approximately one molecule wide, but the individual parts appear different, compared to the molecules forming the dimers. This twofold, ellipsoidal molecular conformation has been presented in Sec. 3.6.1 where it filled holes created by heptagonal supramolecular structures. The geometric appearance of this conformer is achiral. Just as in the case of the quasi-commensurate islands, the transition regions which interrupt the homochiral dimer rows consist of molecules of the opposite chirality. These appear as the fuzzy areas crossing the rows of dimers and achiral bright molecules as shown in the larger scale image of Fig. 7.5 (a).

The deposition of more molecules leads to an increasing size of the quasi-commensurate and incommensurate islands. This is seen in the STM images displayed in Fig. 7.6 (a) and (c), showing

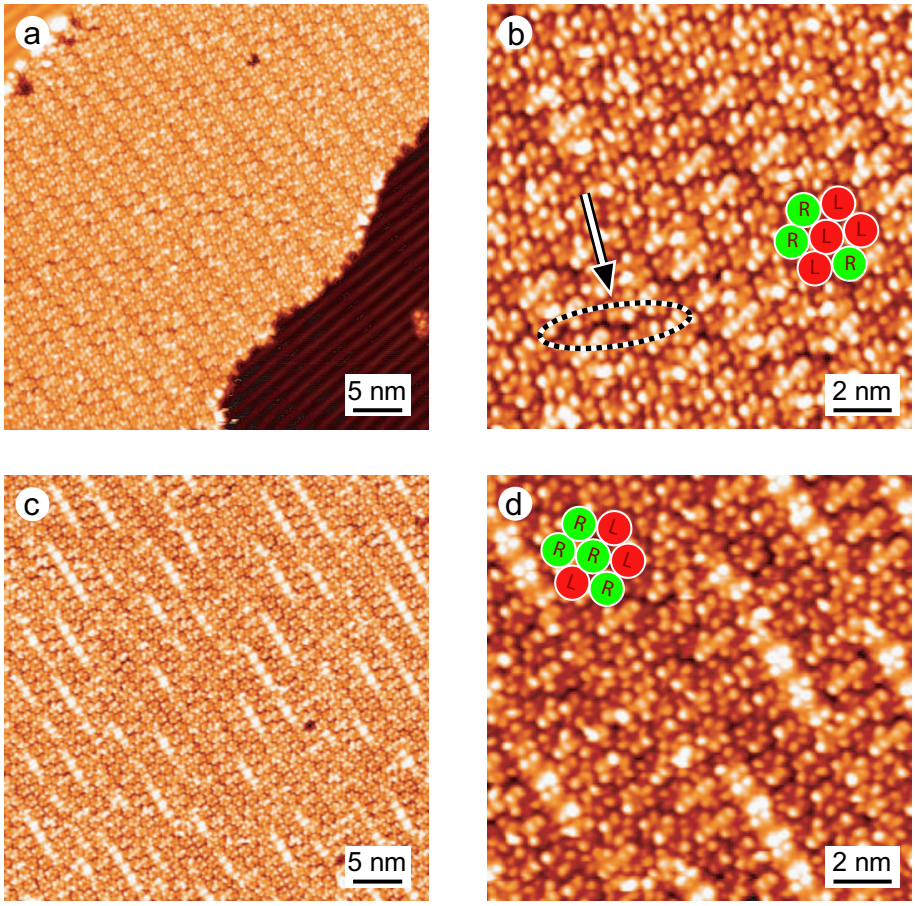

Figure 7.6: STM images showing large islands on Au(100). a), b) Quasi-commensurate island of mixed chirality. The arrow indicates a small area with slightly larger intermolecular distances, appearing like a cracking line in the island. c), d) Incommensurate island of mixed chirality and molecules in the “bright” conformation. (Tunneling parameters: a), b) $V = -1.0$ V, $I = 100$ pA)

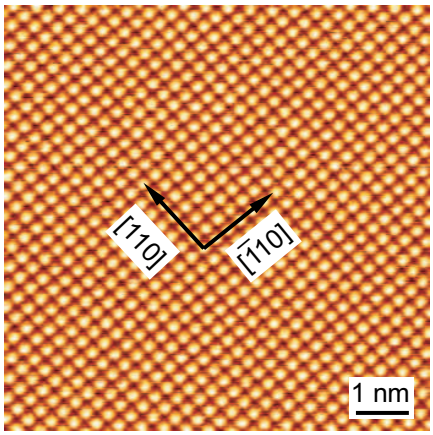

Figure 7.7: STM image with clear atomic resolution showing the square (100) surface of silver. The nearest neighbor distance along the [$\bar{1}$10] or [110] direction is a =2.89 Å. (Tunneling parameters: $V = -0.02$ V, $I = 50$ pA)

both types of islands present on Au(100). Their appearance is different from the one observed in the case of the smaller islands discussed before: the quasi-commensurate arrangements appear more homogeneous and well ordered, and the incommensurate islands contain much less circular holes. For both types, the different domains of ordered and fuzzy areas are no longer present. The smaller scale images of Fig. 7.6 (b) and (d) uncover the reason for this different aspect by showing a reduction of homochiral molecular dimers and an increased mixing of the two enantiomers. This fact leads to the absence of the strong difference of the supramolecular order between the homochiral domains and the transition regions formed by molecules of the opposite chirality. Although the brighter lines of molecules adopting the special twofold conformation are still present in the incommensurate islands, they are shorter and are partly further away from each other than in the case of the small islands. As already mentioned above, the quasi-commensurate islands which try to align the molecular dimers to the ridges of the surface reconstruction of the gold substrate, the hexagonal lattice reveals irregularities, appearing like cracking sites inside the islands.

7.2 Rubrene on Ag (111) and Ag (100): close packed islands

The hexagonal (111) surface and the square (100) surfaces of silver are characterized by lower work functions than the corresponding gold faces. In contrast to the reconstructed surfaces of Au(100) and Au(111), the corresponding silver faces are bulk-terminated. This absence of additional corrugation going along with a dislocation-free surface influences the nucleation and self-assembly behavior of adsorbed rubrene molecules. While in the case of gold, small supramolecular structures are stabilized at favorable adsorption sites of the reconstructed Au(111) and Au(100) surfaces, on the completely flat and homogenous silver substrates the high molecular diffusion of the weakly bound rubrene molecules is unhindered.

7.2.1 Rubrene on Ag (100): heterochiral extended islands

The periodicity of the square Ag(100) surface is visible in the STM image of Fig. 7.7 with atomic resolution revealing the nearest neighbor directions [$\bar{1}$10] and [110] with an interatomic distance

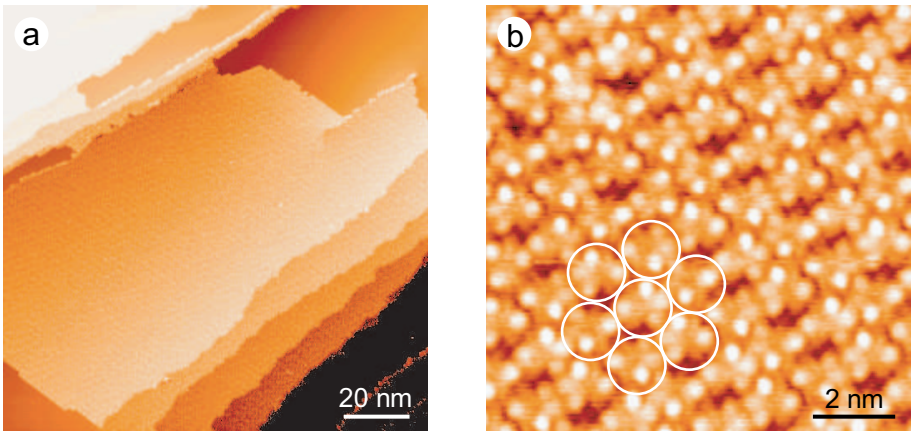

Figure 7.8: STM images showing hcp islands of rubrene on Ag(100). a) Large island covering several steps. b) Closeup view of an island, revealing the hcp packing and the ordered arrangement of oriented molecules. (Tunneling parameters: a) $V = -0.8$ V, $I = 50$ pA; b) $V = +0.4$ V, $I = 50$ pA)

of 2.89 Å. Upon deposition of rubrene at ambient temperature, the molecules decorate step edges and fill narrow terraces in a close packed arrangement. In contrast to the results obtained on the gold surfaces, there is no stable adsorption of individual molecules or small supramolecular structures on the free terraces. The self-assembly of the molecules leads exclusively to hcp islands which start their growth at the lower step edges of the terraces. At higher coverage, the densely packed islands increase in size and extend also over larger terraces. An overview of rubrene molecules, assembled into a large island on an area with several steps is shown in the STM image in Fig. 7.8 (a). In contrast to the case of an adsorption of rubrene on Au(111) (see Sec. 3.5), the molecular islands are not repelled from the upper edges of the steps and extend over several small terraces without being disturbed by the step edges.

The smaller scale STM image displayed in Fig. 7.8 (b) shows the hexagonal close packed arrangement of the molecules within the islands. The submolecular contrast shows features similar to those of the molecules in hcp islands adsorbed on Au(111) (see Sec. 3.5). However, in contrast to the case of Au(111),[1] the molecular orientations are well-defined and result in a regular order of the very homogeneously appearing molecules. The STM image in Fig. 7.9 (a) is taken at a slightly elevated voltage and reveals an arrangement of double rows of brighter appearing features. The direction $\vec{a}$ of the rows is independent of the square lattice of the underlying silver (100) surface which is demonstrated by the inset of Fig. 7.9 (b), indicating the nearest neighbor directions of Ag(100). Such as in the case of the incommensurate hcp islands of rubrene on Au(111), this property expresses the dominance of intermolecular forces over molecule-substrate interactions.

The closeup view of a small hcp area of rubrene on Ag(100) presented in Fig. 7.9 (b) offers submolecular contrast which enables a determination of the chirality of the individual molecules. Each molecule appears with three main maxima possessing lower lying lobes at either their left or right side, in analogy to the discussion in Sec. 4.2.1. This analysis uncovers that the molecules are arranged into heterochiral double rows along the direction $\vec{a}$ indicated in Fig. 7.9 (a). Each row consists of molecules oriented into the same direction, but which are of alternating chirality (i.e. **LRLRLR**..., see Fig. 7.9 (c)). The adjacent row is displaced by half an intermolecular distance to compose the hcp arrangement and follows this same scheme of alternating enantiomers. However,

[1] Excepting the special case of the hcp domains within the patchwork phase, see Sec. 3.6.4.

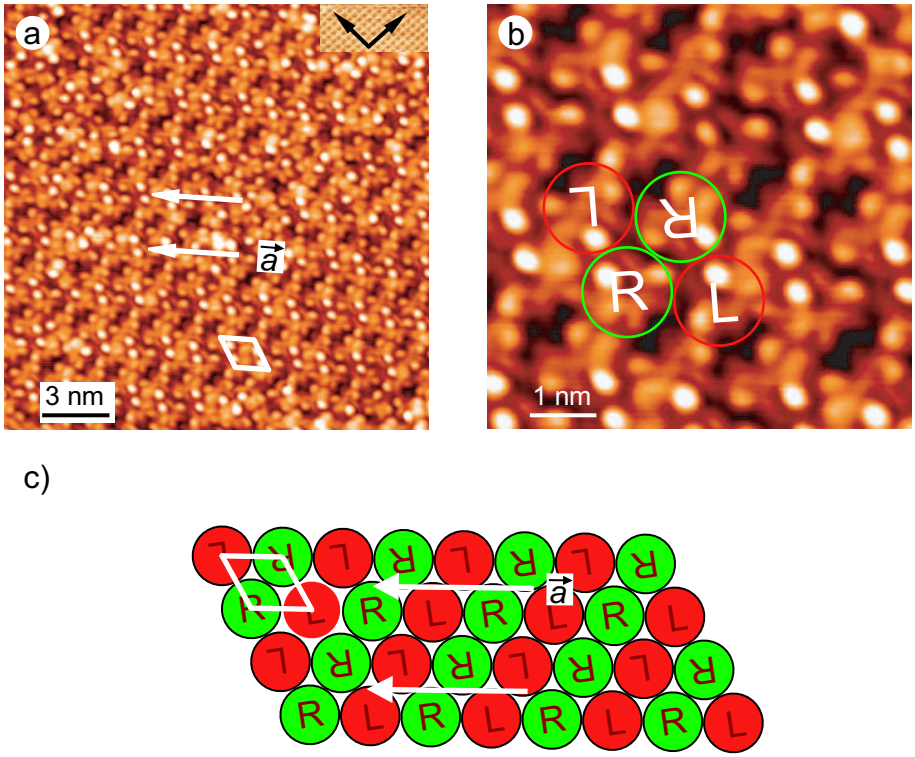

Figure 7.9: STM images showing the ordered arrangement of rubrene on Ag(100). a) The molecules form double rows oriented along $\vec{a}$, as indicated by the white arrows. The inset shows the underlying square Ag(100) surface. b) The submolecular resolution reveals the chirality of the individual molecules, as denoted by **R** and **L** and the heterochiral motif of the close packed island. c) Scheme of the supramolecular arrangement formed by heterochiral rows along $\vec{a}$ with molecules of the same orientation. Neighboring rows are rotated by 180° with respect to each other. (Tunneling parameters: a), b) $V = -2.0$ V, $I = 51$ pA)

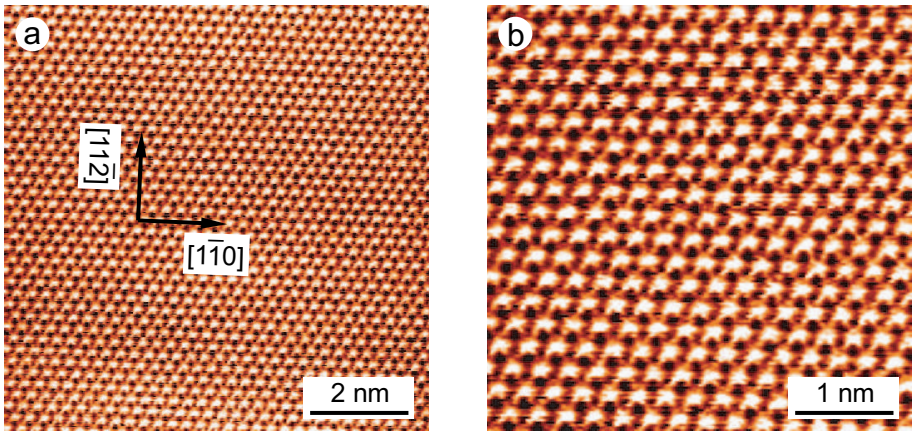

Figure 7.10: STM image with atomic resolution showing the hexagonal (111) surface of silver. The nearest neighbor distance along the direction $[1\bar{1}0]$ is a= 2.89 Å. (Tunneling parameters: $V = +0.02$ V, $I = 3$ nA)

each second row is rotated by 180° which results in the shown pattern with heterochiral molecular lines along two nearest neighbor directions and homochiral rows along the third direction. Taking into account the different chiralities and molecular orientations, each motif of the arrangement contains four molecules, as indicated by the white rhombus in Fig. 7.9 (c) and forms a heterochiral unit. Consequently, the hcp order of the island is described by a hexagonal unit cell with these supramolecular motifs at the corners and side lengths which are twice the intermolecular distance of 1.3 ± 0.1 nm.

7.2.2 Rubrene on Ag (111): locally heterochiral domains

The hexagonal Ag(111) surface is shown in the STM images of Fig. 7.10. The interatomic distance along the nearest neighbor directions is $a = 2.89$ Å. The deposition of rubrene onto the sample held at room temperature results in a similar supramolecular assembly as in the case of Ag(100) which is characterized by the absence of adsorbed monomers or small supramolecular structures on the terraces. Consequently, the molecules are exclusively found at step edges and stabilized within hcp islands which grow from the lower step edges an cover the terraces. Again, there is no repulsion by the upper edges of the steps as shown in the STM image of Fig. 7.11 (a) by the continuous hcp island growth over several step edges.

The STM images in Fig. 7.11 (b) and Fig. 7.12 show a close packed island formed by rubrene on Ag(111). The images reveal the existence of different domains of supramolecular order. While the area denoted by A in Fig. 7.12 (a) appears without any translational periodicity, the domain B shows an arrangement into lines which are directed along $\vec{a}$, as indicated by the dotted lines and the arrow. The submolecular contrast of the individual molecules in the closeup view of the area B reveals that the rubrene molecules are ordered in the same way as in the case of the heterochiral rows on Ag(100). Again, the lines consist of chirally alternating molecules and adjacent rows are rotated by 180° with respect to each other. Consequently, the domains of type B form locally restricted heterochiral arrangements surrounded by molecules without any fixed rotational orientation and chiral order.

The onset of the surface state of the Ag(111) surface is situated at −63 meV [201] with respect to the Fermi level. Scanning at voltages above this value renders standing wave patterns visible, arising from the interferences of incoming and reflected electron waves, which are scattered at

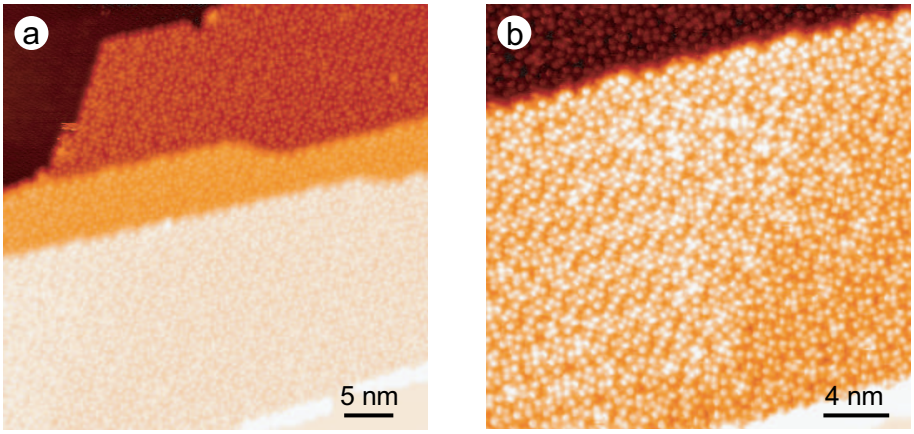

Figure 7.11: STM images showing hcp islands of rubrene on Ag(111). a) Continuous growth of the islands over several step edges. b) The molecular resolution allows a distinction of two differently ordered areas (left and right side of the image). (Tunneling parameters: a) $V = -0.5$ V, $I = 100$ pA; b) $V = +0.5$ V, $I = 100$ pA)

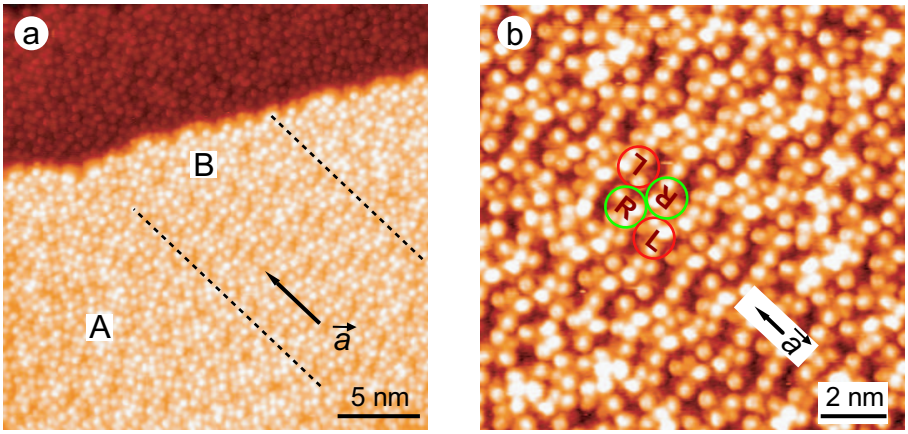

Figure 7.12: STM image showing the chiral arrangement inside the hcp islands on Ag(111). a) Overview showing two differently ordered domains A and B. The supramolecular arrangement in B consists of rows along the direction $\vec{a}$, as indicated by the dotted lines and the arrow. b) Closeup view of the domain B revealing the heterochiral arrangement with adjacent rows being rotated by 180° with respect to each other. (Tunneling parameters (a), (b): $V = -1.5$ V, $I = 100$ pA)

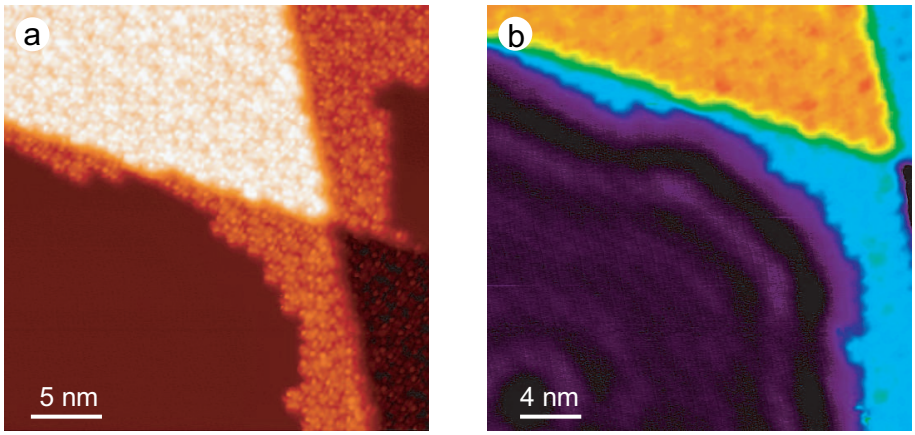

Figure 7.13: a) STM image showing the borders of an hcp island on Ag(111). b) The different false colors reveal an alternating pattern of maxima and minima showing that the surface state electrons are reflected by the borders of the hcp island. (Tunneling parameters: a) $V = -1.6$ V, $I = 20$ pA; b) $V = +0.04$ V, $I = 40$ pA)

adsorbed atoms [210, 211, 212], molecules [213], and at atomic steps [214]. The wavelength of these interfering waves (and thus the periodicity of the standing wave pattern) is related to the energy of the electrons by a parabolic dispersion relation. The STM image in Fig. 7.13 (b) demonstrates that the hcp islands of rubrene molecules self-assembled on Ag(111) scatter the surface state electrons and produce the typical pattern of alternating apparent minima and maxima in the STM images, reflecting the LDOS of the surface. The shown image is recorded at +40 meV and displays the standing waves created between the borders of the molecular island (also shown in a different color scheme in Fig. 7.13 (a)) and a surface impurity in the lower left corner of the image. The fact that the maxima and minima follow the shape of the curved border of the island suggests that the self-assembled molecules are at the origin of the reflection of the surface state electron waves. This property is due to localized perturbation of the potential energy of the underlying Ag(111) surface which is induced by the adsorption of the molecules.

7.3 Rubrene on NaCl / Au(111)

The use of an ultrathin insulating film consisting of several ML acting as a spacer layer between the metal surface and the molecules permitted successful measurements of single molecule fluorescence [157] and phosphorescence [103], vibronic states [159], and spatial maps of molecular orbitals [20]. In the two latter cases the decoupling of the electronic states of the adsorbate from the metal due to the larger separation enabled the observation of the molecule-specific features. The radiative deexcitation of an excited molecule, which is quenched in the case of an adsorption directly on the metal, became possible by the use of a spacer layer which prevented a non-radiative energy transfer to the metal[2] [215, 216, 217].

The STS measurements recorded on rubrene adsorbed directly on Au(111) shows essentially unperturbed molecular levels on the basis of a nonparallel orientation of the molecular tetracene backbone as discussed in Chapt. 6. However, STM induced light emission experiments analogous to those described in [102] did not record molecular fluorescence, but exclusively the signal

[2]The problem is equivalent to the one of a point dipole (the excited molecule) transferring energy to a volume of point dipoles (the image dipoles in the metal).

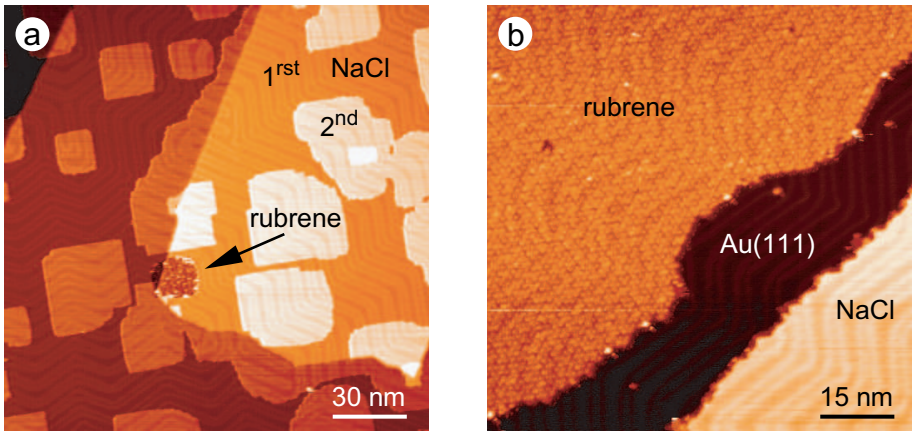

Figure 7.14: STM images showing the results of a deposition of rubrene on a NaCl covered Au(111) sample. a) Gold terraces which are almost completely covered with a first layer of NaCl and patches of a second layer. The indicated round hole in the first NaCl layer is filled with rubrene. b) Hcp island of rubrene on Au(111) separated by an area of bare Au(111) from a first layer of NaCl. (Tunneling parameters: a) $V = -1.3$ V, $I = 20$ pA, b) $V = -1.0$ V, $I = 20$ pA)

originating from the decay of a surface plasmon which is localized between the gold surface and the tip [75]. The approach of using a multilayer of rubrene as in [218], where they observed clear fluorescence from molecules which were separated from the surface by five underlying molecular layers, was not successful in the case of rubrene. At the high positive voltage required for injecting electrons into the LUMO of the molecule[3] the multilayer was damaged, either by an immersion of the tip into the molecules or by an attraction of molecules to the tip.

The evaporation of an ultrathin NaCl layer on Au(111) leads to an extended first layer with patches of a second layer, as shown in the STM image of Fig. 7.14 (a). The subsequent deposition of rubrene molecules on the NaCl covered sample at room temperature resulted in the creation of hcp islands of rubrene on the areas of bare Au(111) and a filling of holes present inside of the first layer of NaCl, as shown in Fig. 7.14 (a). The insulating layers were completely free of molecules and revealed the typical herringbone reconstructed of the underlying gold substrate. The STM image in Fig. 7.14 (b) demonstrates the unperturbed coexistence of an hcp island of rubrene on Au(111), separated by an area of the bare substrate from a first layer of NaCl. The deposition of rubrene on a NalCl covered Au(111) surface at low temperatures of 5 K and 50 K resulted in a different situation. The STM images of the NaCl areas were noisy, preventing a clear imaging of the layers. This behavior indicates the presence of very mobile rubrene molecules on the insulating films which were dragged across the surface by the scanning tip, even at very high tunneling resistances. This result is not surprising, taking into account that the adsorption of rubrene on the metallic Au(111) surface indicates already a very weak coupling of the molecular levels with the surface state. The presence of the insulating NaCl layer further decreases an electronic interaction, leading to an unstable adsorption of the molecules, even at 5 K. Consequently, no topographic, spectroscopic, and STM-induced luminescence measurements could be realized on this sample with rubrene adsorbed on NaCl/Au(111).

[3]The LUMO is situated at +3 V for the case of a submonolayer, but the value is expected to shift to higher positive voltages for the multilayer coverage, due to the influence of the electric field.

7.4 Conclusions

The self-assembly of rubrene results in fundamentally different supramolecular structures depending on the specific substrate, i.e. gold or silver. Apart from this dependence on the type of metal, the design of the architectures depends also on the surface periodicity, i.e. the (111) or (100) planes of the metals. The experimentally observed results of the supramolecular self-assembly of rubrene on the Au(111), Au(100), Ag(111), and Ag(100) surface are summarized in Tab. 7.2. The structures which are self-assembled on the (111) face of gold are multifaceted, going from small homochiral assemblies to large hcp islands. On Au(100), the only small structures observed consist of pentagonal supermolecules which link together into small chains. Next to these exist two differently organized islands which are either influenced by the ridges of the surface reconstruction and which grow independent on step edges on the terraces, in contrast to the hcp islands on Au(111), Ag(111) and Ag(100). The supramolecular phases observed on the Ag(111) and Ag(100) surfaces are less diverse and restricted to extended densely packed islands which grow from step edges on over the lower lying terraces and exhibit an extended (Ag(100)) and locally confined (Ag(100)) heterochiral order of oriented molecules showing alternating chiralities into one direction.

The conformation of the individual molecules within these latter hcp islands on silver are of type D and E, as discussed in Sec. 6.1 and 6.2. The latter conformers are characterized by a submolecular aspect which is similar to the one observed in the densely packed two-dimensional clusters measured directly after the deposition at low temperatures (see Fig. 3.2). Furthermore, these conformations reveal an electronic structure which is close to the one of the free rubrene. While all molecules adsorbed on Ag(111) and Ag(100) adopt these two conformations, the situation is different for the gold surfaces. On Au(111), the molecules change their geometry into conformations A^* and B^* upon annealing to ≈ 300 K, enabling a stable adsorption of monomers and small structures, and adopt conformations A to E within hcp islands. The occurrence of molecular deformation into A^* and B^* as a prerequisite for the formation of the small assemblies suggests that these specific conformations are energetically more favorable for a stable monomeric adsorption and an intermolecular bonding into small, low-coordinated supramolecular structures. The conformation of the molecules forming the supramolecular pentagons on Au(100) could not be clearly determined. However, for the given experimental conditions, the creation of small supramolecular structures is observed exclusively for an adsorption on both gold surfaces. This finding indicates that the different properties of Au and Ag are responsible for the characteristic self-assembly of rubrene on these two metals.

The values summarized in Tab. 7.1 in the beginning of the chapter, reveal that the silver and gold surfaces are distinguished by their electronic and geometric properties. First of all, the Au surfaces exhibit larger work functions of 5.2 eV and 5.3 eV than Ag (4.2 eV and 4.5 eV). In addition, the cutoff of the d-bands lies closer to E_F in the case of gold, compared to silver. Both properties lead to the situation that the electronic levels of the gold substrates and the HOMO of the molecules[4] are closer to each other than in the case of silver. The proximity of the electronic levels on gold might induce a change of the molecular adsorption geometry, yielding a more favorable conformation A^* of B^* with resulting HOMO positions at ≈ -2.3 eV and ≈ -1.8 eV which are close to the d-band onset of gold. This coincidence of the levels might increase the molecule-substrate interaction [65], leading to monomers and small supramolecular structures which are stable on the terraces at a temperature of 5 K.

Furthermore, the Au(111) and Au(100) surfaces are reconstructed, in contrast to the bulk-

[4]The HOMO of rubrene is located at 6.4 eV below vacuum. This corresponds to the value of -1.1 eV with respect to E_F of Au(111) and -1.9 eV for Ag(111).

Au(111)	Au(100)	Ag(111)	Ag(100)
Small structures (up to hexamers): *Homochiral assembly* Conf. *A**, *B**	Small structures (pentagons): *Homochiral assembly* Conf. not identified		
Pentagonal chains: *Homochiral assembly* Conf. *B**	Pentagonal chains: *Homochiral assembly* Conf. not identified		
Honeycomb islets and patchwork phase: *Homochiral assembly* Conf. *A**, *B**, *F*	Two types of hcp islands on terraces: *Heterochiral assembly* Conf. *D*, *E*, *F*		
Hcp island growth from step edges on: *Random chirality* Conf. *A*, *B*, *C*, *D*, *E*		Hcp island growth from step edges on: *Locally heterochiral* Conf. *D*, *E*	Hcp island growth from step edges on: *Heterochiral assembly* Conf. *D*, *E*

Table 7.2: Comparison of experimentally observed supramolecular structures on gold and silver substrates for the (111) and (100) faces. The specific chiral interaction is given as well as the dominant type of conformer (see Sec. 6.1).

terminated Ag(111) and Ag(100) faces. These surface reconstructions exhibit dislocations and lines of higher corrugation which increase the diffusion barrier for the molecules and consequently favor the stable adsorption of small structures on the terraces far away from steps. The observation that the molecular organization and conformation after the deposition at low temperatures is the same for all four substrates show that the specific supramolecular assembly and conformational changes occur during the annealing, allowing for chiral recognition processes to take place. The finding of a complete absence of any molecules and supramolecular structures on silver terraces indicate that the molecular diffusion during annealing is too high to enable stable adsorption and formation of intermolecular bonds and leads to the creation of exclusively hcp islands at step edges. The fact that the (111) surfaces of Au and Ag have a surface state, in contrast to the (100) faces of the metals excludes an influence of this electronic property on the creation of the small homochiral assemblies, since these architectures are characteristic for the Au(111) and the Au(100) plane, but not present on Ag(111). The less significant differences in the supramolecular organization of rubrene on one type of metal, but for a different crystal face might be due to the small variations of the work functions or resulting from the periodicity of the surface reconstruction. Thus, the lateral distance of the reconstruction rows of the Au(100) surface which is similar to the intermolecular separation within the rubrene islands enables the creation of well-ordered, quasi-commensurate islands. Furthermore, the higher corrugation of the surface layer structure of Au(100), compared to the herringbone reconstruction of Au(111), is reflected by a lower diffusion barrier on the (100) plane which is observed by an increased stability of individual supramolecular pentagons at 50 K.

Chapter 8

Summary

The STM and STS studies of rubrene performed within the framework of this thesis constitute the first geometric and spectroscopic analysis of the molecule at the (sub)nanoscale. The investigations of rubrene for a coverage below one monolayer yield a great diversity of results originating from the interweaved implications of different properties which determine the complex behavior of the molecule. The scheme shown in Fig. 8.1 gives an overview of the main aspects studied in the preceding chapters of this thesis and presents the obtained results together with the related dependencies. The proposed tree diagram classifies the findings into four levels:

- Investigated supporting surface: Au(111), Au(100), Ag(111), Ag(100)
- Resulting supramolecular phases: δ, η, λ, ω, ω', ω'', χ
- Adsorption conformations of the individual molecules: A, A^*, B, B^*, C, D, E, F
- Chiral organization of the two enantiomers **L** and **R** into **LL**, **RR**, **LRLR**, or randomly mixed assemblies.

The investigation of rubrene adsorbed on a herringbone reconstructed Au(111) surface uncovers an unprecedented richness of self-assembled supramolecular architectures. The observed different phases comprise small structures from monomers to hexamers (δ), honeycomb islets (η), chains and decagons of pentagonal supermolecules (λ), hcp islands (ω), as well as mixed tilings of penta-hexa-heptagonal structures (χ). Despite the fact that not all parameters which determine the creation of the specific phases are known for all sample preparation methods, a clear correlation between the rubrene coverage and the progression from δ to ω is established.

A surprising aspect of this diversity is the appearance of pentagonal and decagonal symmetries which are created by the self-organization of the molecules into perfect supramolecular pentagons (phases δ, η, and λ), joining together for the formation of perfect decagons (phase λ). Fivefold shapes are omnipresent in biological systems, but a rarity for the non-living matter which is dominated by space filling arrangements. In two dimensions, the lack of translational symmetry of the fivefold and tenfold polygon forbids however such a plane filling patterning. The STM images of domains in the patchwork phase χ show examples of periodic and non-periodic supramolecular assembly of rubrene, covering the surface without holes by the combination of slightly distorted pentagons, hexagons, and heptagons reminding the beautifully complex surfaces of quasicrystals.

A fascinating discovery is the organization of the supramolecular assemblies into a hierarchical system, whose construction plan is directly followed in the experiments by the progression of coverage dependent supramolecular growth. The STM images show that the monomers and small structures composing the δ phase constitute the building units for the further self-assembly into

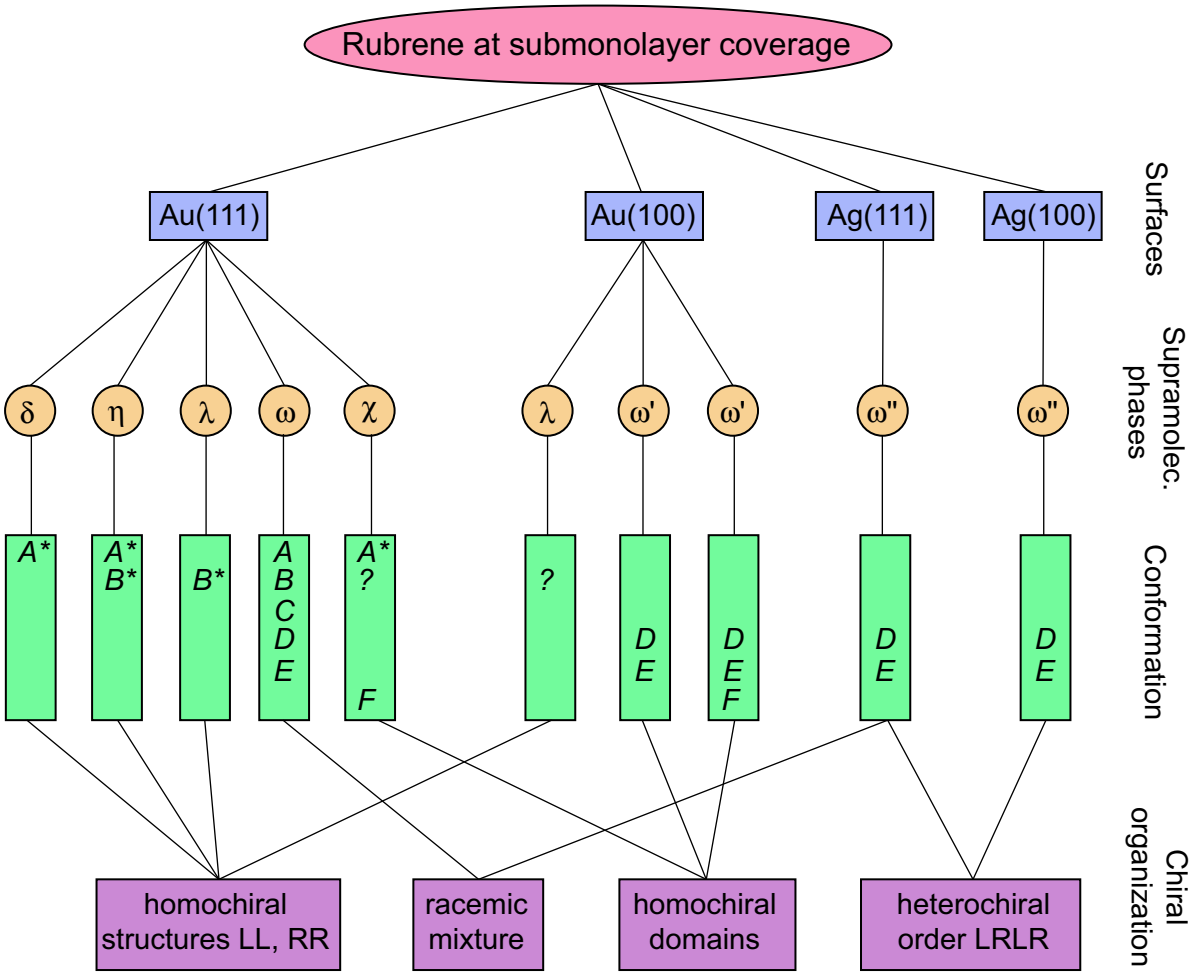

Figure 8.1: Schematic diagram summarizing the results of the combined STM/STS studies on rubrene at submonolayer coverage. On the four different surfaces, the self-assembly of rubrene into different supramolecular phases is analyzed. For each assembled structure, the molecular conformations are characterized by the submolecular appearance in the STM images and by the peak position of the HOMO in the *dI/dV* spectra obtained with STS. The submolecular contrast allows to distinguish the two enantiomers **L** and **R** of rubrene present on the surface and enables an investigation of the chiral organization of the respective supramolecular structures.

honeycomb islets (phase η) or chains and decagons of pentagonal supermolecules (phase λ). The hierarchy starts with the first generation whose constituent parts (individual molecules) join together into dimers, trimers, tetramers, pentamers, and hexagonal honeycomb islets (second generation). In the case of the supramolecular pentagons, the next assembly step links these supermolecules, which are stable but diffusing at temperatures of 50 K, into elongated, curled chains of variable shapes and sizes, forming the third generation. An especially beautiful result of this second assembly step is the formation of a supramolecular decagon, a nested structure which is built by ten pentagons interlocked like small gearwheels and which consist each of five molecules. Thus, exactly fifty molecules self-organize into this perfectly regular geometric structure combining fivefold and tenfold symmetries.

The intermediate ranges where the supramolecular phases overlap are characterized by a mixture of the adjacent supramolecular architectures and reveal that the different geometries, i.e. pentagonal, hexagonal and hcp, coexist and even coalesce. This finding (together with the existence of also heptagonal structures) indicates a certain flexibility of the intermolecular bond directions to adapt to angles of 108°, 120°, and 129° for the structures excepting the hcp organized ω phase. The initial configuration for the supramolecular assembly is however given with the creation of a trimer which exhibits 120° between the adjacent molecules. This suggests that directional forces are acting between the molecules, resulting from a combination of $\pi \cdots \pi$, $\mathrm{CH} \cdots \pi$, and quadrupole-quadrupole interactions. These anisotropic bonds notwithstanding, isotropic vdW forces which are based on the polarizability of the molecule stabilize the randomly oriented molecules in the hcp islands.

The interesting finding that the low-density phases δ, η and λ are characterized by a homochiral assembly, in contrast to the racemic hcp phase ω, fortifies this assumption of fundamentally different intermolecular forces distinguishing the assemblies with fixed molecular orientations from the unoriented case of hcp islands. Only the action of directional forces of specific submolecular parts permits the functioning of chiral recognition processes between the molecules, leading to an enantioselective supramolecular self-assembly. The chirality-dependent orientation of rotation of the homochiral molecules with respect to each other which enables the best interlocking of the submolecular parts demonstrates the action of a lock-and-key principle[1] driving the chiral recognition process. The enantioselective self-assembly of rubrene on Au(111) is observed for both steps of the supramolecular hierarchy, leading to exclusively homochiral structures. Thus, the chirality of the individual molecules which is determined from the submolecular contrast in the STM images is conserved in the assembly process and furthermore transmitted to the next stage (i.e. the pentagonal supermolecules and the honeycomb islets) and further on to the nested supramolecular decagons and the chains of pentagonal supermolecules. This mechanism results in a spontaneous separation of the racemic mixtures of rubrene molecules on the surface into enantiopure honeycomb islets, nested decagons, and pentagonal chains which extend to lengths of ≈ 150 nm. The STM observations demonstrate the potential of self-assembly techniques in view of the important quest for new processes of chiral discrimination of a racemic mixture into enantiopure compounds. The conservation of chirality over three stages of a hierarchical self-assembly exemplifies furthermore the working principle of basic processes in nature.

The investigation of the supramolecular self-assembly of rubrene on Au(100), Ag(111), and Ag(100) reveals that the principle of chiral recognition is only valid for the hexagonally reconstructed (100) of gold. Similar to the behavior on Au(111), pentagonal supermolecules are formed which interlock into chains. However, next to these structures, two different types of hcp islands (phase ω') grow on the terraces and reveal homochiral domains of oriented molecules. The deposition of rubrene on Ag(111) and Ag(100) results in both cases in exclusively hcp islands

[1] Postulated by Emil Fischer (Nobel Prize in Chemistry 1902) in 1894 as a principle for molecular recognition.

which grow from lower step edges on over the terraces (phase ω''). While the hcp arrangement formed on the (100) face is organized by strictly oriented molecules forming heterochiral dimers which construct the islands, the (111) surface of silver reveals only restricted domains of such heterochiral order which are surrounded by randomly chirally mixed hcp areas. The comparison of the specific geometric and electronic characteristics of the four investigated surfaces indicate two parameters which determine the type of supramolecular assembly realized on the different substrates. The presence of the reconstructions of the gold surfaces offers preferred nucleation sites for small clusters which are not present on the silver surfaces. Furthermore, the closer proximity of the upper edge of the *d*-band to the HOMO of the molecule in the case of gold might establish a stronger interaction of the molecular level with the substrate states and thus favors the creation of low-density supramolecular structures stabilized on the surface.

The intramolecular contrast in the STM images reveals the intriguing finding that the various supramolecular structures on the different surfaces are characterized by specific adsorption conformations of the constituent molecules. In the hcp islands on Au(111), five different conformers are distinguished (A to E). In contrast to this, the corresponding islands on Au(100) show only three of these (C to E), as well as a forth conformation (F) which is also found in the patchwork phase on Au(111). Finally, all molecules on both silver surfaces are of type D and E. The STS measurements uncover that these conformers are characterized by specific energies of the HOMO of the molecules which is detected as a clear peak appearing at shifted positions in the dI/dV spectra recorded over the different conformations. The experiments unveil that the respective HOMO energy of type D and E on all four surfaces is located at the same position with respect to E_{Vac}. The measured value of the HOMO of 6.4 ± 0.1 eV is identical with the ionization potential of rubrene in the gas phase, a finding that demonstrates the alignment of the vacuum levels of the molecule and the substrates. This result suggests a very weak interaction of the molecule with the surface which is attributed to the specific three dimensional geometry of rubrene which prevents a planar adsorption onto the surfaces due to sterically demanding phenyl groups. Consequently, the spectroscopic analysis of the molecular levels of rubrene reveals for the first time that even without the use of an inert spacer layer, a probing of the intrinsic electronic structure of individual molecules is possible.

The supramolecular structures of rubrene on Au(111) of phases δ, η, and λ exhibit different adsorption conformations A^* and B^*, which resemble conformers A and B found in the hcp islands by their submolecular appearance and the respective position of the HOMO. The STM and STS studies show that the molecules in the small structures (δ) are exclusively of type A^*, while those forming the pentagonal chains (λ) adopt all conformation B^*. The honeycomb islets (η) and the intermediate mixed structures (η/λ) are built up by both conformers. An interesting phenomenon is the switching of the geometric and electronic structure of the molecules of type A^* to conformation B^* induced with the STM. The successful realization of a switching is demonstrated by the changed intramolecular structure together with the shifted position of the HOMO. Almost all molecules in phases δ to η/λ can be modified if they are surrounded by not more than two neighboring molecules. The modification is performed by the application of higher voltages of ± 2 V to ± 4 V in the vicinity of the molecules, leading to an increased electric field between tip and sample. The observation that molecules which are not below the tip apex are successfully switched excludes a mechanism induced by inelastically tunneling electrons and therefore points towards a field-assisted process. The back-switching mechanism from B^* to A^* is expected to be activated by an annealing of the sample, providing thermal energy to the molecules to return to their initially preferred adsorption conformation A^*. This switching of rubrene adsorbed on Au(111) demonstrates the first realization of an STM induced conformational change which involves a clear modification of the electronic structure of the

molecule consisting of a decrease of the ionization potential and a reduction of the HOMO-LUMO gap.

Chapter 9

Outlook

Several interesting questions emerge from the results on the adsorption and self-assembly of rubrene presented in this thesis. A further discussion would require additional experimental investigations using a modified instrumentation as well as theoretical calculations. For instance, different assumptions inferred from the experimental data could be verified by the use of a fast-scanning variable temperature STM offering the possibility to change the temperature of the sample progressively while constantly monitoring the investigated area. This procedure could permit to verify the supposition that an annealing of the sample to temperatures higher than 5 K induces a reversion of switched molecules back to their initial conformation. The determination of the temperature required for this back-switching as well as for the creation of the different supramolecular phases which are based on a change of the molecular conformation in the unannealed clusters to the different conformers in the supramolecular assemblies, would provide values for the activation barrier of an isomerization between the various conformers.

Imaging the molecular and supramolecular motion for the different supramolecular phases at slowly increasing temperatures with high scanning speeds would furthermore give information about the various diffusion barriers as a function of the temperature, the size of the object, and the molecular conformation. In the same manner, the activation energies could be determined for breaking the intermolecular bonds between the molecules in the different assemblies, as well as the supramolecular bonds between the pentagonal supermolecules. The controlled variation of the cooling rate from the annealing temperature to the measurement temperature would give further insights into an eventual dependence of the formation of the different supramolecular phases on this value.

On the theoretical side, molecular mechanics calculations could provide helpful information for the interpretation of the different experimentally observed conformations of the molecule on the surface, taking into account the deformations induced by the tip. These studies could offer a basis for a simulation of STM images of adsorbed rubrene, enabling an assignment of the observed submolecular contrast in the experimental images to specific parts of the molecule. An appropriate technique might be the elastic scattering quantum chemistry (ESQC) approach which successfully calculated STM images of large hydrocarbon molecules with bulky side groups. Molecular dynamics simulations, including the weak intermolecular forces and the specific (chiral) conformations, could furthermore confirm the given explanation of the coverage and chirality dependent self-assembly into different supramolecular phases.

Acronyms

STM	Scanning Tunneling Microscopy
STS	Scanning Tunneling Spectroscopy
UHV	Ultrahigh Vacuum
ML	Monolayer
LDOS	Local Density of States
IP	Ionization Potential
EA	Electron Affinity
HOMO	Highest Occupied Molecular Orbital
LUMO	Lowest Unoccupied Molecular Orbital
E_{F}	Fermi Level
E_{Vac}	Vacuum Level
VdW	Van der Waals
Hcp	Hexagonal close packed
Fcc	Face centered cubic
UPS	Ultraviolet Photoelectron Spectroscopy
NEXAFS	Near Edge X-ray Absorption Fine Structure
DFT	Density Functional Theory
PAH	Polycyclic Aromatic Hydrocarbon
OLED	Organic Light Emitting Diode
OFET	Organic Field Effect Transistor
HtBDC	Hexa-*t*-Butyl Decacyclene
HBC	Hexa-*peri*-Hexabenzocoronene
HB-HPB	Hexa-*t*-Butyl-Hexaphenylbenzene
HB-HBC	Hexa-*t*-Butyl-Hexa-*peri*-Hexabenzocoronene
Pc	Phthalocyanine
PTCDA	Perylene-Tetracarboxylicacid-Dianhydride
TBPP	Tetra [3,5 di-*t*-Butylphenyl] Porphyrin

Bibliography

[1] G. Binnig, H. Rohrer, C. Gerber, and E. Weibel. Tunneling through a controllable vacuum gap. *Applied Physics Letters*, 40:178–180, 1982.

[2] G. Binnig, H. Rohrer, C. Gerber, and E. Weibel. Surface studies by scanning tunneling microscopy. *Physical Review Letters*, 49:57–60, 1982.

[3] J. K. Gimzewski, E. Stoll, and R. R. Schlittler. Scanning tunneling microscopy of individual molecules of copper phthalocyanine adsorbed on polycrystalline silver surfaces. *Surface Science*, 181:267–277, 1987.

[4] H. Ohtani, R. J. Wilson, S. Chiang, and C. M. Mate. Scanning tunneling microscopy observations of benzene molecules on the Rh(111)-(3×3)(C_6H_6+2CO) surface. *Physical Review Letters*, 60:2398–2401, 1988.

[5] F. Rosei, M. Schunack, Y. Naitoh, P. Jiang, A. Gourdon, E. Laegsgaard, I. Stensgaard, C. Joachim, and F. Besenbacher. Properties of large organic molecules on metal surfaces. *Progress in Surface Science*, 71:95–146, 2003.

[6] J. V. Barth, J. Weckesser, N. Lin, A. Dmitriev, and K. Kern. Supramolecular architectures and nanostructures at metal surfaces. *Applied Physics A-Materials Science & Processing*, 76:645–652, 2003.

[7] J. M. Brown and S. G. Davies. Chemical asymmetric-synthesis. *Nature*, 342:631–636, 1989.

[8] G. P. Lopinski, D. J. Moffatt, D. D. Wayner, and R. A. Wolkow. Determination of the absolute chirality of individual adsorbed molecules using the scanning tunnelling microscope. *Nature*, 392:909–911, 1998.

[9] H. B. Fang, L. C. Giancarlo, and G. W. Flynn. Direct determination of the chirality of organic molecules by scanning tunneling microscopy. *Journal of Physical Chemistry B*, 102:7311–7315, 1998.

[10] M. Böhringer, W. D. Schneider, and R. Berndt. Real space observation of a chiral phase transition in a two-dimensional organic layer. *Angewandte Chemie-International Edition*, 39:792–759, 2000.

[11] J. Weckesser, A. De Vita, J. V. Barth, C. Cai, and K. Kern. Mesoscopic correlation of supramolecular chirality in one-dimensional hydrogen-bonded assemblies. *Physical Review Letters*, 8709:096101, 2001.

[12] A. Kühnle, T. R. Linderoth, B. Hammer, and F. Besenbacher. Chiral recognition in dimerization of adsorbed cysteine observed by scanning tunnelling microscopy. *Nature*, 415:891–893, 2002.

[13] Q. Chen, D. J. Frankel, and N. V. Richardson. Self-assembly of adenine on Cu(110) surfaces. *Langmuir*, 18:3219–3225, 2002.

[14] M. O. Lorenzo, C. J. Baddeley, C. Muryn, and R. Raval. Extended surface chirality from supramolecular assemblies of adsorbed chiral molecules. *Nature*, 404:376–379, 2000.

[15] S. M. Barlow, S. Louafi, D. Le Roux, J. Williams, C. Muryn, S. Haq, and R. Raval. Supramolecular assembly of strongly chemisorbed size-and shape-defined chiral clusters: S- and R-alanine on Cu(110). *Langmuir*, 20:7171–7176, 2004.

[16] R. Fasel, M. Parschau, and K.-H. Ernst. Amplification of chirality in two-dimensional enantiomorphous lattices. *Nature*, 439:449–452, 2006.

[17] H. U. Blaser. Enantioselective synthesis using chiral heterogeneous catalysts. *Tetrahedron-Asymmetry*, 2:843–866, 1991.

[18] E. I. Altman and R. J. Colton. Determination of the orientation of C_{60} adsorbed on Au(111) and Ag(111). *Physical Review B*, 48:18244–18249, 1993.

[19] A. J. Mayne, A. R. Avery, J. Knall, T. S. Jones, G. A. D. Briggs, and W. H. Weinberg. An STM study of the chemisorption of C_2H_4 on Si(001)(2×1). *Surface Science*, 284:247–256, 1993.

[20] J. Repp, G. Meyer, S. M. Stojkovic, A. Gourdon, and C. Joachim. Molecules on insulating films: Scanning-tunneling microscopy imaging of individual molecular orbitals. *Physical Review Letters*, 94:026803, 2005.

[21] J. A. Stroscio and D. M. Eigler. Atomic and molecular manipulation with the scanning tunneling microscope. *Science*, 254:1319–1326, 1991.

[22] T. A. Jung, R. R. Schlittler, and J. K. Gimzewski. Conformational identification of individual adsorbed molecules with the STM. *Nature*, 386:696–698, 1997.

[23] F. Moresco, G. Meyer, K. H. Rieder, H. Tang, A. Gourdon, and C. Joachim. Conformational changes of single molecules induced by scanning tunneling microscopy manipulation: A route to molecular switching. *Physical Review Letters*, 86:672–675, 2001.

[24] X. H. Qiu, G. V. Nazin, and W. Ho. Mechanisms of reversible conformational transitions in a single molecule. *Physical Review Letters*, 93:196806, 2004.

[25] A. Aviram and M. A. Ratner. Molecular rectifiers. *Chemical Physics Letters*, 29:277–283, 1974.

[26] C. Joachim, J. K. Gimzewski, and A. Aviram. Electronics using hybrid-molecular and mono-molecular devices. *Nature*, 408:541–548, 2000.

[27] Y. Wada, M. Tsukada, M. Fujihira, K. Matsushige, T. Ogawa, M. Haga, and S. Tanaka. Prospects and problems of single molecule information devices. *Japanese Journal of Applied Physics Part 1-Regular Papers Short Notes & Review Papers*, 39:3835–3849, 2000.

[28] E. W. Meijer and A. P. H. J. Schenning. Chemistry - Material marriage in electronics. *Nature*, 419:353–354, 2002.

[29] V. Percec, M. Glodde, T. K. Bera, Y. Miura, I. Shiyanovskaya, K. D. Singer, V. S. K. Balagurusamy, P. A. Heiney, I. Schnell, A. Rapp, H. W. Spiess, S. D. Hudson, and H. Duan. Self-organization of supramolecular helical dendrimers into complex electronic materials. *Nature*, 419:384–387, 2002.

[30] Z. L. Zhang, X. Y. Jiang, S. H. Xu, T. Nagatomo, and O. Omoto. Stability enhancement of organic electroluminescent diode through buffer layer or rubrene doping in hole-transporting layer. *Synthetic Metals*, 91:131–132, 1997.

[31] Z. L. Zhang, X. Y. Jiang, S. H. Xu, T. Nagatomo, and O. Omoto. The effect of rubrene as a dopant on the efficiency and stability of organic thin film electroluminescent devices. *Journal of Physics D-Applied Physics*, 31:32–35, 1998.

[32] Y. Hamada, H. Kanno, T. Tsujioka, H. Takahashi, and T. Usuki. Red organic light-emitting diodes using an emitting assist dopant. *Applied Physics Letters*, 75:1682–1684, 1999.

[33] J. P. Yang, Y. D. Jin, P. L. Heremans, R. Hoefnagels, P. Dieltiens, F. Blockhuys, H. J. Geise, M. Van der Auweraer, and G. Borghs. White light emission from a single layer organic light emitting diode fabricated by spincoating. *Chemical Physics Letters*, 325:251–256, 2000.

[34] L. D. Wang, L. Duan, G. T. Lei, and Y. Qiu. Bright white organic light-emitting diodes based on anthracene derivatives and rubrene. *Japanese Journal of Applied Physics Part 2-Letters & Express Letters*, 43:L560–L562, 2004.

[35] V. Podzorov, V. M. Pudalov, and M. E. Gershenson. Field-effect transistors on rubrene single crystals with parylene gate insulator. *Applied Physics Letters*, 82:1739–1741, 2003.

[36] V. C. Sundar, J. Zaumseil, V. Podzorov, E. Menard, R. L. Willett, T. Someya, M. E. Gershenson, and J. A. Rogers. Elastomeric transistor stamps: Reversible probing of charge transport in organic crystals. *Science*, 303:1644–1646, 2004.

[37] R. W. I. de Boer, M. E. Gershenson, A. F. Morpurgo, and V. Podzorov. Organic single-crystal field-effect transistors. *Physica Status Solidi A-Applied Research*, 201:1302–1331, 2004.

[38] V. Podzorov, E. Menard, A. Borissov, V. Kiryukhin, J. A. Rogers, and M. E. Gershenson. Intrinsic charge transport on the surface of organic semiconductors. *Physical Review Letters*, 93:086602, 2004.

[39] D. Käfer, L. Ruppel, G. Witte, and C. Wöll. Role of molecular conformations in rubrene thin film growth. *Physical Review Letters*, 95:166602, 2005.

[40] B. A. Kowert, N. C. Dang, K. T. Sobush, and L. G. Seele. Diffusion of aromatic hydrocarbons in n-alkanes and cyclohexanes. *Journal of Physical Chemistry A*, 105:1232–1237, 2001.

[41] W. H. Taylor. X-ray measurements on diflavylene, rubrene, and related compounds. *Zeitschrift für Kristallographie*, 93:151–155, 1936.

[42] S. A. Akopyan. *Zh. Strukt. Khim.*, 3:602, 1966.

[43] D. E. Henn, W. G. Williams, and D. J. Gibbons. Crystallographic data for an orthorhombic form of rubrene. *Journal of Applied Crystallography*, 4:256, 1971.

[44] D. A. da Silva, E. G. Kim, and J. L. Bredas. Transport properties in the rubrene crystal: Electronic coupling and vibrational reorganization energy. *Advanced Materials*, 17:1072–1076, 2005.

[45] D. Käfer and G. Witte. Growth of crystalline rubrene films with enhanced stability. *Physical Chemistry Chemical Physics*, 7:2850–2853, 2005.

[46] M. Kaschke, N. P. Ernsting, and F. P. Schäfer. Rubrene, a saturable absorber for 308 nm. *Optics Communications*, 66:211–215, 1988.

[47] I. B. Berlman. *Handbook of fluorescence spectra of aromatic molecules.* Academic Press, New York, 1971.

[48] E. L. Frankevich, B. M. Rumyaptsev, and V. I. Lesin. Magnetic-field effect on the thermostimulated chemiluminescence of photoperoxidized rubrene. *Journal of Luminescence*, 11:91–106, 1975.

[49] Y. Harada, T. Takahashi, S. Fujisawa, and T. Kajiwara. Application of photoelectron-spectroscopy to the study of photo-chemical reactions of solids - Photo-oxidation of rubrene(5,6,11,12-tetraphenylnaphthacene). *Chemical Physics Letters*, 62:283–286, 1979.

[50] T. Takahashi, Y. Harada, N. Sato, K. Seki, H. Inokuchi, and S. Fujisawa. Gas and solid-phase photoelectron-spectra of 5,6,11,12-tetraphenylnaphthacene (rubrene). *Bulletin of the Chemical Society of Japan*, 52:380–382, 1979.

[51] W. Schmidt. Photoelectron-spectra of polynuclear aromatics. V. Correlations with ultraviolet-absorption spectra in catacondensed series. *Journal of Chemical Physics*, 66:828–845, 1977.

[52] A. J. Bard, K. S. V. Santhana, J. T. Maloy, J. Phelps, and L. O. Wheeler. Steric effects and electrochemistry of phenyl-substituted anthracenes and related compounds. *Discussions of the Faraday Society*, 45:167–174, 1968.

[53] H. H. Fong, S. K. So, W. Y. Sham, C. F. Lo, Y. S. Wu, and C. H. Chen. Effects of tertiary butyl substitution on the charge transporting properties of rubrene-based films. *Chemical Physics*, 298:119–123, 2004.

[54] H. Ishii, K. Sugiyama, E. Ito, and K. Seki. Energy level alignment and interfacial electronic structures at organic metal and organic organic interfaces. *Advanced Materials*, 11:605–625, 1999.

[55] N. Sato, K. Seki, and H. Inokuchi. Polarization energies of organic-solids determined by ultraviolet photoelectron-spectroscopy. *Journal of the Chemical Society-Faraday Transactions II*, 77:1621–1633, 1981.

[56] K. Hummer and C. Ambrosch-Draxl. Oligoacene exciton binding energies: Their dependence on molecular size. *Physical Review B*, 71:081202(R), 2005.

[57] I. G. Hill, A. Kahn, Z. G. Soos, and R. A. Pascal. Charge-separation energy in films of π-conjugated organic molecules. *Chemical Physics Letters*, 327:181–188, 2000.

[58] A. Schmidt, M. L. Anderson, and N. R. Armstrong. Electronic states of vapor-deposited electron and hole transport agents and luminescent materials for light-emitting-diodes. *Journal of Applied Physics*, 78:5619–5625, 1995.

[59] N. Sato, H. Inokuchi, and E. A. Silinsh. Reevaluation of electronic polarization energies in organic molecular-crystals. *Chemical Physics*, 115:269–277, 1987.

[60] J. Cohen. Biochemistry - Getting all turned around over the origins of life on earth. *Science*, 267:1265–1266, 1995.

[61] L. Pasteur. Recherches sur les relations qui peuvent exister entre la forme crystalline et la composition chimique, et le sens de la polarisation rotatoire. *Ann. Chim. Phys.*, 24:442–459, 1848.

[62] W. J. Meiring. Nuclear β-decay and the origin of biomolecular chirality. *Nature*, 329:712–714, 1987.

[63] A. Zangwill. *Physics at surfaces.* Cambridge University Press, Cambridge, 1988.

[64] N. D. Lang and A. R. Williams. Theory of atomic chemisorption on simple metals. *Physical Review B*, 18:616–636, 1978.

[65] R. Hoffmann. A chemical and theoretical way to look at bonding on surfaces. *Reviews of Modern Physics*, 60:601–628, 1988.

[66] N. D. Lang. Interaction between closed-shell systems and metal-surfaces. *Physical Review Letters*, 46:842–845, 1981.

[67] J. Bardeen. Tunnelling from a many-particle point of view. *Physical Review Letters*, 6:57–59, 1961.

[68] J. Tersoff and D. R. Hamann. Theory and application for the scanning tunneling microscope. *Physical Review Letters*, 50:1998–2001, 1983.

[69] R. S. Becker, J. A. Golovchenko, and B. S. Swartzentruber. Electron interferometry at crystal-surfaces. *Physical Review Letters*, 55:987–990, 1985.

[70] G. Binnig, K. H. Frank, H. Fuchs, N. Garcia, B. Reihl, H. Rohrer, F. Salvan, and A. R. Williams. Tunneling spectroscopy and inverse photoemission - Image and field states. *Physical Review Letters*, 55:991–994, 1985.

[71] J. A. Stroscio, R. M. Feenstra, and A. P. Fein. Electronic-structure of the Si(111)2×1 surface by scanning-tunneling microscopy. *Physical Review Letters*, 57:2579–2582, 1986.

[72] R. M. Feenstra, J. A. Stroscio, and A. P. Fein. Tunneling spectroscopy of the Si(111)2×1 surface. *Surface Science*, 181:295–306, 1987.

[73] A. Selloni, P. Carnevali, E. Tosatti, and C. D. Chen. Voltage-dependent scanning-tunneling microscopy of a crystal-surface - Graphite. *Physical Review B*, 31:2602–2605, 1985.

[74] N. D. Lang. Spectroscopy of single atoms in the scanning tunneling microscope. *Physical Review B*, 34:5947–5950, 1986.

[75] R. Berndt, J. K. Gimzewski, and P. Johansson. Inelastic tunneling excitation of tip-induced plasmon modes on noble-metal surfaces. *Physical Review Letters*, 67:3796–3799, 1991.

[76] B. C. Stipe, M. A. Rezaei, and W. Ho. Single-molecule vibrational spectroscopy and microscopy. *Science*, 280:1732–1735, 1998.

[77] A. J. Heinrich, J. A. Gupta, C. P. Lutz, and D. M. Eigler. Single-atom spin-flip spectroscopy. *Science*, 306:466–469, 2004.

[78] P. H. Lippel, R. J. Wilson, M. D. Miller, C. Woll, and S. Chiang. High-resolution imaging of copper-phthalocyanine by scanning-tunneling microscopy. *Physical Review Letters*, 62:171–174, 1989.

[79] D. M. Eigler, P. S. Weiss, E. K. Schweizer, and N. D. Lang. Imaging Xe with a low-temperature scanning tunneling microscope. *Physical Review Letters*, 66:1189–1192, 1991.

[80] A. J. Fisher and P. E. Blöchl. Adsorption and scanning-tunneling-microscope imaging of benzene on graphite and MoS_2. *Physical Review Letters*, 70:3263–3266, 1993.

[81] J. Yoshinobu, M. Kawai, I. Imamura, F. Marumo, R. Suzuki, H. Ozaki, M. Aoki, S. Masuda, and M. Aida. Direct observation of molecule-substrate antibonding states near the fermi level in Pd(110)-c(4×2)-benzene. *Physical Review Letters*, 79:3942–3945, 1997.

[82] N. D. Lang. Theory of single-atom imaging in the scanning tunneling microscope. *Physical Review Letters*, 56:1164–1167, 1986.

[83] C. Klink, L. Olesen, F. Besenbacher, I. Stensgaard, E. Laegsgaard, and N. D. Lang. Interaction of C with Ni(100) - atom-resolved studies of the clock reconstruction. *Physical Review Letters*, 71:4350–4353, 1993.

[84] P. Hu, D. A. King, M. H. Lee, and M. C. Payne. Orbital mixing in CO chemisorption on transition-metal surfaces. *Chemical Physics Letters*, 246:73–78, 1995.

[85] M. L. Bocquet and P. Sautet. STM and chemistry: A qualitative molecular orbital understanding of the image of CO on a Pt surface. *Surface Science*, 360:128–136, 1996.

[86] L. Bartels, G. Meyer, and K. H. Rieder. Controlled vertical manipulation of single CO molecules with the scanning tunneling microscope: A route to chemical contrast. *Applied Physics Letters*, 71:213–215, 1997.

[87] M. Grobis, X. Lu, and M. F. Crommie. Local electronic properties of a molecular monolayer: C_{60} on Ag(001). *Physical Review B*, 66:161408, 2002.

[88] X. H. Lu, M. Grobis, K. H. Khoo, S. G. Louie, and M. F. Crommie. Spatially mapping the spectral density of a single C_{60} molecule. *Physical Review Letters*, 90:096802, 2003.

[89] J. I. Pascual, J. Gomez-Herrero, D. Sanchez-Portal, and H. P. Rust. Vibrational spectroscopy on single C_{60} molecules: The role of molecular orientation. *Journal of Chemical Physics*, 117:9531–9534, 2002.

[90] V. M. Hallmark, S. Chiang, K. P. Meinhardt, and K. Hafner. Observation and calculation of internal structure in scanning-tunneling-microscopy images of related molecules. *Physical Review Letters*, 70:3740–3743, 1993.

[91] M. Böhringer, W. D. Schneider, and R. Berndt. Scanning tunneling microscope-induced molecular motion and its effect on the image formation. *Surface Science*, 408:72–85, 1998.

[92] M. Böhringer, K. Morgenstern, W. D. Schneider, R. Berndt, F. Mauri, A. De Vita, and R. Car. Two-dimensional self-assembly of supramolecular clusters and chains. *Physical Review Letters*, 83:324–327, 1999.

[93] J. Lagoute, K. Kanisawa, and S. Fölsch. Manipulation and adsorption-site mapping of single pentacene molecules on Cu(111). *Physical Review B*, 70:245415, 2004.

[94] T. A. Jung, R. R. Schlittler, J. K. Gimzewski, H. Tang, and C. Joachim. Controlled room-temperature positioning of individual molecules: Molecular flexure and motion. *Science*, 271:181–184, 1996.

[95] J. K. Gimzewski, C. Joachim, R. R. Schlittler, V. Langlais, H. Tang, and I. Johannsen. Rotation of a single molecule within a supramolecular bearing. *Science*, 281:531–533, 1998.

[96] T. Zambelli, H. Tang, J. Lagoute, S. Gauthier, A. Gourdon, and C. Joachim. Conformations of a long molecular wire with legs on a Cu(100) surface. *Chemical Physics Letters*, 348:1–6, 2001.

[97] P. Sautet and C. Joachim. Calculation of the benzene on rhodium STM images. *Chemical Physics Letters*, 185:23–30, 1991.

[98] P. Sautet and C. Joachim. Interpretation of STM images - Copper-phthalocyanine on copper. *Surface Science*, 271:387–394, 1992.

[99] C. Chavy, C. Joachim, and A. Altibelli. Interpretation of STM images - C_{60} on the gold(110) surface. *Chemical Physics Letters*, 214:569–575, 1993.

[100] A. D. Zhao, Q. X. Li, L. Chen, H. J. Xiang, W. H. Wang, S. Pan, B. Wang, X. D. Xiao, J. L. Yang, J. G. Hou, and Q. S. Zhu. Controlling the Kondo effect of an adsorbed magnetic ion through its chemical bonding. *Science*, 309:1542–1544, 2005.

[101] R. Gaisch, J. K. Gimzewski, B. Reihl, R. R. Schlittler, M. Tschudy, and W. D. Schneider. Low-temperature ultra-high-vacuum scanning tunneling microscope. *Ultramicroscopy*, 42:1621–1626, 1992.

[102] E. Ćavar. *Electronic and optical properties of supported C_{60} molecules studied by scanning tunneling microscopy.* PhD thesis, École Polytechnique Fédérale de Lausanne, Switzerland, 2005.

[103] E. Ćavar, M. C. Blüm, M. Pivetta, F. Patthey, M. Chergui, and W. D. Schneider. Fluorescence and phosphorescence from individual C_{60} molecules excited by local electron tunneling. *Physical Review Letters*, 95:196102, 2005.

[104] L. Limot, T. Maroutian, P. Johansson, and R. Berndt. Surface-state stark shift in a scanning tunneling microscope. *Physical Review Letters*, 91:196801, 2003.

[105] J. Kroger, L. Limot, H. Jensen, R. Berndt, and P. Johansson. Stark effect in Au(111) and Cu(111) surface states. *Physical Review B*, 70:033401, 2004.

[106] S. D. Feyter and F. C. D. Schryver. Two-dimensional supramolecular self-assembly probed by scanning tunneling microscopy. *Chemical Society Reviews*, 32:139–150, 2003.

[107] J. V. Barth, G. Costantini, and K. Kern. Engineering atomic and molecular nanostructures at surfaces. *Nature*, 437:671–679, 2005.

[108] T. Sakurai, X. D. Wang, Q. K. Xue, Y. Hasegawa, T. Hashizume, and H. Shinohara. Scanning tunneling microscopy study of fullerenes. *Progress in Surface Science*, 51:263–408, 1996.

[109] H. Proehl, M. Toerker, F. Sellam, T. Fritz, K. Leo, C. Simpson, and K. Mullen. Comparison of ultraviolet photoelectron spectroscopy and scanning tunneling spectroscopy measurements on highly ordered ultrathin films of hexa-peri-hexabenzocoronene on Au(111). *Physical Review B*, 6320:205409, 2001.

[110] T. Yokoyama, S. Yokoyama, T. Kamikado, and S. Mashiko. Nonplanar adsorption and orientational ordering of porphyrin molecules on Au(111). *Journal of Chemical Physics*, 115:3814–3818, 2001.

[111] X. Lu, K. W. Hipps, X. D. Wang, and U. Mazur. Scanning tunneling microscopy of metal phthalocyanines: d(7) and d(9) cases. *Journal of the American Chemical Society*, 118:7197–7202, 1996.

[112] M. Böhringer, W. D. Schneider, R. Berndt, K. Glockler, M. Sokolowski, and E. Umbach. Corrugation reversal in scanning tunneling microscope images of organic molecules. *Physical Review B*, 57:4081–4087, 1998.

[113] K. Glöckler, C. Seidel, A. Soukopp, M. Sokolowski, E. Umbach, M. Böhringer, R. Berndt, and W. D. Schneider. Highly ordered structures and submolecular scanning tunnelling microscopy contrast of PTCDA and DM-PBDCI monolayers on Ag(111) and Ag(110). *Surface Science*, 405:1–20, 1998.

[114] J. I. Pascual, N. Lorente, Z. Song, H. Conrad, and H. P. Rust. Selectivity in vibrationally mediated single-molecule chemistry. *Nature*, 423:525–528, 2003.

[115] L. Gross, F. Moresco, P. Ruffieux, A. Gourdon, C. Joachim, and K. H. Rieder. Tailoring molecular self-organization by chemical synthesis: Hexaphenylbenzene, hexa-peri-hexabenzocoronene, and derivatives on Cu(111). *Physical Review B*, 71:165428, 2005.

[116] R. Otero, M. Schock, L. M. Molina, E. Laegsgaard, I. Stensgaard, B. Hammer, and F. Besenbacher. Guanine quartet networks stabilized by cooperative hydrogen bonds. *Angewandte Chemie-International Edition*, 44:2270–2275, 2005.

[117] T. Yokoyama, S. Yokoyama, T. Kamikado, Y. Okuno, and S. Mashiko. Selective assembly on a surface of supramolecular aggregates with controlled size and shape. *Nature*, 413:619–621, 2001.

[118] S. Lukas, G. Witte, and C. Wöll. Novel mechanism for molecular self-assembly on metal substrates: Unidirectional rows of pentacene on Cu(110) produced by a substrate-mediated repulsion. *Physical Review Letters*, 88:028301, 2002.

[119] J. Perdereau, J. P. Biberian, and G. E. Rhead. Adsorption and surface alloying of lead monolayers on (111) and (110) faces of gold. *Journal of Physics F-Metal Physics*, 4:798–806, 1974.

[120] J. V. Barth, H. Brune, G. Ertl, and R. J. Behm. Scanning tunneling microscopy observations on the reconstructed Au(111) surface - Atomic-structure, long-range superstructure, rotational domains, and surface-defects. *Physical Review B*, 42:9307–9318, 1990.

[121] D. D. Chambliss, R. J. Wilson, and S. Chiang. Ordered nucleation of Ni and Au islands on Au(111) studied by scanning tunneling microscopy. *Journal of Vacuum Science & Technology B*, 9:933–937, 1991.

[122] D. D. Chambliss, R. J. Wilson, and S. Chiang. Nucleation of ordered Ni island arrays on Au(111) by surface-lattice dislocations. *Physical Review Letters*, 66:1721–1724, 1991.

[123] D. Fujita, T. Yakabe, H. Nejoh, T. Sato, and M. Iwatsuki. Scanning tunneling microscopy study on the initial adsorption behavior of C_{60} molecules on a reconstructed Au(111)-$(23 \times \sqrt{3})$ surface at various temperatures. *Surface Science*, 366:93–98, 1996.

[124] A. Kirakosian, M. J. Comstock, J. W. Cho, and M. F. Crommie. Molecular commensurability with a surface reconstruction:STM study of azobenzene on Au(111). *Physical Review B*, 71:113409, 2005.

[125] S. Clair, S. Pons, H. Brune, K. Kern, and J. V. Barth. Mesoscopic metallosupramolecular texturing by hierarchic assembly. *Angewandte Chemie-International Edition*, 44:7294–7297, 2005.

[126] D. Shechtman, I. Blech, D. Gratias, and J. W. Cahn. Metallic phase with long-range orientational order and no translational symmetry. *Physical Review Letters*, 53:1951–1953, 1984.

[127] G. Ehrlich and F. G. Hudda. Atomic view of surface self-diffusion - Tungsten on tungsten. *Journal of Chemical Physics*, 44:1039–1049, 1966.

[128] R. L. Schwoebel and E. J. Shipsey. Step motion on crystal surfaces. *Journal of Applied Physics*, 37:3682–3686, 1966.

[129] K. Bromann, H. Brune, H. Röder, and K. Kern. Interlayer mass-transport in homoepitaxial and heteroepitaxial metal growth. *Physical Review Letters*, 75:677–680, 1995.

[130] E. I. Altman and R. J. Colton. Interaction of C_{60} with the Au(111) $23\times\sqrt{3}$ reconstruction. *Journal of Vacuum Science & Technology B*, 12:1906–1909, 1994.

[131] J.-M. Lehn. *Supramolecular chemistry - concepts and perspectives.* VCH, Weinheim, 1995.

[132] G. R. Desiraju. Chemistry beyond the molecule. *Nature*, 412:397–400, 2001.

[133] M. Tamres. Aromatic compounds as donor molecules in hydrogen bonding. *Journal of the American Chemical Society*, 74:3375–3378, 1952.

[134] M. Nishio, M. Hirota, and Y. Umezawa. *The CH/π interaction: evidence, nature, and consequences.* Methods in stereochemical analysis. Wiley, New York, 1998.

[135] U. Samanta, P. Chakrabarti, and J. Chandrasekhar. Ab initio study of energetics of X-H$\cdots\pi$ (X = N, O, and C) interactions involving a heteroaromatic ring. *Journal of Physical Chemistry A*, 102:8964–8969, 1998.

[136] S. Tsuzuki, K. Honda, T. Uchimaru, M. Mikami, and K. Tanabe. The magnitude of the CH/π interaction between benzene and some model hydrocarbons. *Journal of the American Chemical Society*, 122:3746–3753, 2000.

[137] T. M. Schaub, D. E. Bürgler, and H.-J. Günterodt. Quasicrystalline structure of icosahedral $Al_{68}Pd_{23}Mn_9$ resolved by scanning tunneling microscopy. *Physical Review Letters*, 73:1255–1258, 1995.

[138] Z. Papadopolos, G. Kasner, J. Ledieu, E. J. Cox, N. V. Richardson, Q. Chen, R. D. Diehl, T. A. Lograsso, A. R. Ross, and R. McGrath. Bulk termination of the quasicrystalline fivefold surface of $al_{70}pd_{21}mn_9$. *Physical Review B*, 66:184207, 2002.

[139] L. Addadi and S. Weiner. Biomineralization - Crystals, asymmetry and life. *Nature*, 411:753–755, 2001.

[140] D. H. Metcalf, S. W. Snyder, S. G. Wu, G. L. Hilmes, J. P. Riehl, J. N. Demas, and F. S. Richardson. Excited-state chiral discrimination observed by time-resolved circularly polarized luminescence measurements. *Journal of the American Chemical Society*, 111:3082–3083, 1989.

[141] K. Ray, S. P. Ananthavel, D. H. Waldeck, and R. Naaman. Asymmetric scattering of polarized electrons by organized organic films of chiral molecules. *Science*, 283:814–816, 1999.

[142] R. Raval. Creating chiral architectures at metal surfaces. *Journal of Physics-Condensed Matter*, 14:4119–4132, 2002.

[143] S. M. Barlow and R. Raval. Complex organic molecules at metal surfaces: bonding, organisation and chirality. *Surface Science Reports*, 50:201–341, 2003.

[144] V. Humblot, S. M. Barlow, and R. Raval. Two-dimensional organisational chirality through supramolecular assembly of molecules at metal surfaces. *Progress in Surface Science*, 76:1–19, 2004.

[145] M. Böhringer, K. Morgenstern, W. D. Schneider, and R. Berndt. Separation of a racemic mixture of two-dimensional molecular clusters by scanning tunneling microscopy. *Angewandte Chemie-International Edition*, 38:821–823, 1999.

[146] M. Schunack, E. Laegsgaard, I. Stensgaard, I. Johannsen, and F. Besenbacher. A chiral metal surface. *Angewandte Chemie-International Edition*, 40:2623–2626, 2001.

[147] K. H. Ernst, Y. Kuster, R. Fasel, M. Muller, and U. Ellerbeck. Two-dimensional separation of [7]helicene enantiomers on Cu(111). *Chirality*, 13:675–678, 2001.

[148] R. Fasel, M. Parschau, and K. H. Ernst. Chirality transfer from single molecules into self-assembled monolayers. *Angewandte Chemie-International Edition*, 42:5178–5181, 2003.

[149] F. Vidal, E. Delvigne, S. Stepanow, N. Lin, J. V. Barth, and K. Kern. Chiral phase transition in two-dimensional supramolecular assemblies of prochiral molecules. *Journal of the American Chemical Society*, 127:10101–10106, 2005.

[150] S. Stepanow, N. Lin, F. Vidal, A. Landa, M. Ruben, J. V. Barth, and K. Kern. Programming supramolecular assembly and chirality in two-dimensional dicarboxylate networks on a Cu(100) surface. *Nano Letters*, 5:901–904, 2005.

[151] H. Spillmann, A. Dmitriev, N. Lin, P. Messina, J. V. Barth, and K. Kern. Hierarchical assembly of two-dimensional homochiral nanocavity arrays. *Journal of the American Chemical Society*, 125:10725–10728, 2003.

[152] M. Böhringer, K. Morgenstern, W. D. Schneider, M. Wuhn, C. Wöll, and R. Berndt. Self-assembly of 1-nitronaphthalene on Au(111). *Surface Science*, 444:199–210, 2000.

[153] S. Berner, M. de Wild, L. Ramoino, S. Ivan, A. Baratoff, H. J. Guntherodt, H. Suzuki, D. Schlettwein, and T. A. Jung. Adsorption and two-dimensional phases of a large polar molecule: Sub-phthalocyanine on Ag(111). *Physical Review B*, 68:115410, 2003.

[154] M. Stöhr, M. Wahl, C. H. Galka, T. Riehm, T. A. Jung, and L. H. Gade. Controlling molecular assembly in two dimensions: The concentration dependence of thermally induced 2D aggregation of molecules on a metal surface. *Angewandte Chemie-International Edition*, 44:7394–7398, 2005.

[155] G. M. Florio, T. L. Werblowsky, T. Muller, B. J. Berne, and G. W. Flynn. Self-assembly of small polycyclic aromatic hydrocarbons on graphite: A combined scanning tunneling microscopy and theoretical approach. *Journal of Physical Chemistry B*, 109:4520–4532, 2005.

[156] S. Weigelt, C. Busse, L. Petersen, E. Rauls, B. Hammer, K. V. Gothelf, F. Besenbacher, and T. R. Linderoth. Chiral switching by spontaneous conformational change in adsorbed organicmolecules. *Nature Materials*, 5:112–117, 2006.

[157] X. H. Qiu, G. V. Nazin, and W. Ho. Vibrationally resolved fluorescence excited with submolecular precision. *Science*, 299:542–546, 2003.

[158] H. Yanagi, K. Ikuta, H. Mukai, and T. Shibutani. STM-induced flip-flop switching of adsorbed subphthalocyanine molecular arrays. *Nano Letters*, 2:951–955, 2002.

[159] X. H. Qiu, G. V. Nazin, and W. Ho. Vibronic states in single molecule electron transport. *Physical Review Letters*, 92:206102, 2004.

[160] S. W. Wu, G. V. Nazin, X. Chen, X. H. Qiu, and W. Ho. Control of relative tunneling rates in single molecule bipolar electron transport. *Physical Review Letters*, 93:236802, 2004.

[161] M. Schunack, F. Rosei, Y. Naitoh, P. Jiang, A. Gourdon, E. Laegsgaard, I. Stensgaard, C. Joachim, and F. Besenbacher. Adsorption behavior of Lander molecules on Cu(110) studied by scanning tunneling microscopy. *Journal of Chemical Physics*, 117:6259–6265, 2002.

[162] L. Gross, F. Moresco, M. Alemani, H. Tang, A. Gourdon, C. Joachim, and K. H. Rieder. Lander on Cu(211) - Selective adsorption and surface restructuring by a molecular wire. *Chemical Physics Letters*, 371:750–756, 2003.

[163] L. Grill, K. H. Rieder, F. Moresco, G. Jimenez-Bueno, C. Wang, G. Rapenne, and C. Joachim. Imaging of a molecular wheelbarrow by scanning tunneling microscopy. *Surface Science*, 584:L153–L158, 2005.

[164] Z. J. Donhauser, B. A. Mantooth, K. F. Kelly, L. A. Bumm, J. D. Monnell, J. J. Stapleton, D. W. Price, A. M. Rawlett, D. L. Allara, J. M. Tour, and P. S. Weiss. Conductance switching in single molecules through conformational changes. *Science*, 292:2303–2307, 2001.

[165] G. Dujardin, R. E. Walkup, and P. Avouris. Dissociation of individual molecules with electrons from the tip of a scanning tunneling microscope. *Science*, 255:1232–1235, 1992.

[166] L. J. Lauhon and W. Ho. Control and characterization of a multistep unimolecular reaction. *Physical Review Letters*, 84:1527–1530, 2000.

[167] L. J. Lauhon and W. Ho. Single-molecule chemistry and vibrational spectroscopy: Pyridine and benzene on Cu(001). *Journal of Physical Chemistry A*, 104:2463–2467, 2000.

[168] J. R. Hahn and W. Ho. Oxidation of a single carbon monoxide molecule manipulated and induced with a scanning tunneling microscope. *Physical Review Letters*, 8716:196102, 2001.

[169] W. Ho. Single-molecule chemistry. *Journal of Chemical Physics*, 117:11033–11061, 2002.

[170] T. Komeda, Y. Kim, Y. Fujita, Y. Sainoo, and M. Kawai. Local chemical reaction of benzene on Cu(110) via STM-induced excitation. *Journal of Chemical Physics*, 120:5347–5352, 2004.

[171] M. F. Crommie. Manipulating magnetism in a single molecule. *Science*, 309:1501–1502, 2005.

[172] X. H. Qiu, G. V. Nazin, A. Hotzel, and W. Ho. Manipulation and characterization of xenon-metalloporphyrin complexation with a scanning tunneling microscope. *Journal of the American Chemical Society*, 124:14804–14809, 2002.

[173] N. Nilius, T. M. Wallis, and W. Ho. Vibrational spectroscopy and imaging of single molecules: Bonding of CO to single palladium atoms on NiAl(110). *Journal of Chemical Physics*, 117:10947–10952, 2002.

[174] G. V. Nazin, X. H. Qiu, and W. Ho. Visualization and spectroscopy of a metal-molecule-metal bridge. *Science*, 302:77–81, 2003.

[175] D. K. Kim, Y. D. Suh, K. H. Park, H. P. Noh, S. K. Kim, S. J. Oh, and Y. Kuk. Electronic and geometric structure of C_{60} molecules on Au(001). *Journal of Vacuum Science & Technology A-Vacuum Surfaces and Films*, 11:1675–1679, 1993.

[176] M. K. J. Johansson, A. J. Maxwell, S. M. Gray, P. A. Bruhwiler, D. C. Mancini, L. S. O. Johansson, and N. Martensson. Scanning tunneling microscopy of C_{60}/Al(111)-6×6: Inequivalent molecular sites and electronic structures. *Physical Review B*, 54:13472–13475, 1996.

[177] C. Rogero, J. I. Pascual, J. Gomez-Herrero, and A. M. Baro. Resolution of site-specific bonding properties of C_{60} adsorbed on Au(111). *Journal of Chemical Physics*, 116:832–836, 2002.

[178] C. Silien, N. A. Pradhan, W. Ho, and P. A. Thiry. Influence of adsorbate-substrate interaction on the local electronic structure of C_{60} studied by low-temperature STM. *Physical Review B*, 69:115434, 2004.

[179] X. H. Lu, M. Grobis, K. H. Khoo, S. G. Louie, and M. F. Crommie. Charge transfer and screening in individual C_{60} molecules on metal substrates: A scanning tunneling spectroscopy and theoretical study. *Physical Review B*, 70:115418, 2004.

[180] M. Grobis, A. Wachowiak, R. Yamachika, and M. F. Crommie. Tuning negative differential resistance in a molecular film. *Applied Physics Letters*, 86:204102, 2005.

[181] N. A. Pradhan, N. Liu, and W. Ho. Vibronic spectroscopy of single C_{60} molecules and monolayers with the STM. *Journal of Physical Chemistry B*, 109:8513–8518, 2005.

[182] M. Toerker, T. Fritz, H. Proehl, F. Sellam, and K. Leo. Tunneling spectroscopy study of 3,4,9,10-perylenetetracarboxylic dianhydride on Au(100). *Surface Science*, 491:255–264, 2001.

[183] C. Dekker, S. J. Tans, B. Oberndorff, R. Meyer, and L. C. Venema. STM imaging and spectroscopy of single copperphthalocyanine molecules. *Synthetic Metals*, 84:853–854, 1997.

[184] K. Walzer and M. Hietschold. STM and STS investigation of ultrathin tin phthalocyanine layers adsorbed on HOPG(0001) and Au(111). *Surface Science*, 471:1–10, 2001.

[185] E. V. Chulkov, M. Machado, and V. M. Silkin. Inverse lifetime of the surface and image states on Au(111). *Vacuum*, 61:95–100, 2001.

[186] G. V. Hansson and S. A. Flodstrom. Photoemission study of bulk and surface electronic-structure of single-crystals of gold. *Physical Review B*, 18:1572–1585, 1978.

[187] M. Pivetta, F. Patthey, and W.-D. Schneider. (unpublished results). 2005.

[188] J. Kuntze, R. Berndt, P. Jiang, H. Tang, A. Gourdon, and C. Joachim. Conformations of a molecular wire adsorbed on a metal surface. *Physical Review B*, 65:233405, 2002.

[189] L. Crocker, T. B. Wang, and P. Kebarle. Electron-affinities of some polycyclic aromatic-hydrocarbons, obtained from electron-transfer equilibria. *Journal of the American Chemical Society*, 115:7818–7822, 1993.

[190] S. D. Kevan and R. H. Gaylord. High-resolution photoemission-study of the electronic-structure of the noble-metal (111) surfaces. *Physical Review B*, 36:5809–5818, 1987.

[191] M. Chelvayohan and C. H. B. Mee. Work function measurements on (110), (100) and (111) surfaces of silver. *Journal of Physics C-Solid State Physics*, 15:2305–2312, 1982.

[192] L. J. Whitman, J. A. Stroscio, R. A. Dragoset, and R. J. Celotta. Manipulation of adsorbed atoms and creation of new structures on room-temperature surfaces with a scanning tunneling microscope. *Science*, 251:1206–1210, 1991.

[193] M. Böhringer, K. Morgenstern, W. D. Schneider, and R. Berndt. Reversed surface corrugation in STM images on Au(111) by field-induced lateral motion of adsorbed molecules. *Surface Science*, 457:37–50, 2000.

[194] M. Stengel, A. D. Vita, and A. Baldereschi. Adatom-vacancy mechanisms for the C_{60}/Al(111)-(6×6) reconstruction. *Physical Review Letters*, 91:166101, 2003.

[195] L. L. Wang and H. P. Cheng. Density functional study of the adsorption of a C_{60} monolayer on Ag(111) and Au(111) surfaces. *Physical Review B*, 69:165417, 2004.

[196] M. Grobis, K. H. Khoo, R. Yamachika, X. H. Lu, K. Nagaoka, S. G. Louie, M. F. Crommie, H. Kato, and H. Shinohara. Spatially dependent inelastic tunneling in a single metallofullerene. *Physical Review Letters*, 94:136802, 2005.

[197] M. Eremtchenko, J. A. Schaefer, and F. S. Tautz. Understanding and tuning the epitaxy of large aromatic adsorbates by molecular design. *Nature*, 425:602–605, 2003.

[198] T. Schmitz-Hübsch, T. Fritz, F. Sellam, R. Staub, and K. Leo. Epitaxial growth of 3,4,9,10-perylene-tetracarboxylic-dianhydride on Au(111): A STM and RHEED study. *Physical Review B*, 55:7972–7976, 1997.

[199] T. Schmitz-Hübsch, T. Fritz, R. Staub, A. Back, N. R. Armstrong, and K. Leo. Structure of 3,4,9,10-perylene-tetracarboxylic-dianhydride grown on reconstructed and unreconstructed Au(100). *Surface Science*, 437:163–172, 1999.

[200] M. Stohr, M. Gabriel, and R. Moller. Investigation of the growth of PTCDA on Cu(110): an STM study. *Surface Science*, 507:330–334, 2002.

[201] F. Reinert, G. Nicolay, S. Schmidt, D. Ehm, and S. Hufner. Direct measurements of the L-gap surface states on the (111) face of noble metals by photoelectron spectroscopy. *Physical Review B*, 63:115415, 2001.

[202] P. H. Citrin, G. K. Wertheim, and Y. Baer. Core-level binding energy and density of states from the surface atoms of gold. *Physical Review Letters*, 41:1425–1428, 1978.

[203] W. Shockley. On the surface states associated with a periodic potential. *Physical Review*, 56:317–323, 1939.

[204] D. G. Fedak and N. A. Gjostein. Structure and stability of (100) surface of gold. *Physical Review Letters*, 16:171–172, 1966.

[205] G. K. Binnig, H. Rohrer, C. Gerber, and E. Stoll. Real-space observation of the reconstruction of Au(100). *Surface Science*, 144:321–335, 1984.

[206] V. Fiorentini, M. Methfessel, and M. Scheffler. Reconstruction mechanism of fcc transition-metal (001) surfaces. *Physical Review Letters*, 71:1051–1054, 1993.

[207] Z. Gai, Y. He, X. W. Li, J. F. Jia, and W. S. Yang. Application of Moiré fringes in investigations of subsurface imperfections - A study of dislocations and strain fields under the reconstructed surface layer of Au(001) by scanning tunneling microscopy. *Surface Science*, 365:96–102, 1996.

[208] J. de la Figuera, M. A. Gonzalez, R. Garcia-Martinez, J. M. Rojo, O. S. Hernan, A. L. V. de Parga, and R. Miranda. STM characterization of extended dislocation configurations in Au(001). *Physical Review B*, 58:1169–1172, 1998.

[209] Y. Kuk, D. K. Kim, Y. D. Suh, K. H. Park, H. P. Noh, S. J. Oh, and S. K. Kim. Stressed C_{60} layers on Au(001). *Physical Review Letters*, 70:1948–1951, 1993.

[210] M. F. Crommie, C. P. Lutz, and D. M. Eigler. Imaging standing waves in a 2-dimensional electron-gas. *Nature*, 363:524–527, 1993.

[211] M. F. Crommie, C. P. Lutz, and D. M. Eigler. Confinement of electrons to quantum corrals on a metal-surface. *Science*, 262:218–220, 1993.

[212] E. J. Heller, M. F. Crommie, C. P. Lutz, and D. M. Eigler. Scattering and absorption of surface electron waves in quantum corrals. *Nature*, 369:464–466, 1994.

[213] L. Gross, F. Moresco, L. Savio, A. Gourdon, C. Joachim, and K. H. Rieder. Scattering of surface state electrons at large organic molecules. *Physical Review Letters*, 93:056103, 2004.

[214] Y. Hasegawa and P. Avouris. Direct observation of standing-wave formation at surface steps using scanning tunneling spectroscopy. *Physical Review Letters*, 71:1071–1074, 1993.

[215] R. R. Chance, A. Prock, and R. Silbey. Lifetime of an emitting molecule near a partially reflecting surface. *Journal of Chemical Physics*, 60:2744–2748, 1974.

[216] P. Avouris and B. N. J. Persson. Excited-states at metal-surfaces and their nonradiative relaxation. *Journal of Physical Chemistry*, 88:837–848, 1984.

[217] D. H. Waldeck, A. P. Alivisatos, and C. B. Harris. Nonradiative damping of molecular electronic excited-states by metal-surfaces. *Surface Science*, 158:103–125, 1985.

[218] Z. C. Dong, X. L. Guo, A. S. Trifonov, P. S. Dorozhkin, K. Miki, K. Kimura, S. Yokoyama, and S. Mashiko. Vibrationally resolved fluorescence from organic molecules near metal surfaces in a scanning tunneling microscope. *Physical Review Letters*, 92:086801, 2004.

Curriculum vitæ

Marie-Christine Blüm
Born on 13.10.1975 in Bad Ems, Germany
Nationalities: German and French

Education:

01/2002-02/2006	PhD studies/ Research and teaching assistant École Polytechnique Fédérale de Lausanne (EPFL), Switzerland
04-09/2001	Studentship of the EU: Training and mobility for young researchers Universitat Autònoma de Barcelona (UAB), Spain
11/2000	Erstes Staatsexamen (M.Sc.) in physics and mathematics
1994-2000	Studies in physics and mathematics, University of Bonn, Germany
1981-1994	School and gymnasium, Lahnstein, Germany

Languages (fluent): German, French, English

Publications:

M.-C. Blüm, M. Pivetta, F. Patthey, and W.-D. Schneider. Probing and modifying locally the intrinsic electronic structure and the conformation of supported non-planar molecules. *Submitted to Physical Review B*, 2006.

M.-C. Blüm, E. Ćavar, M. Pivetta, F. Patthey, and W.-D. Schneider. Conservation of chirality in a hierarchical supramolecular self-assembled structure with pentagonal symmetry. *Angewandte Chemie International Edition*, 117:5334-5337, 2005; *Angewandte Chemie*, 117:5468-5471, 2005.

E. Ćavar, M.-C. Blüm, M. Pivetta, F. Patthey, and W.-D. Schneider. Fluorescence and phosphorescence from individual C_{60} molecules excited by local electron tunneling. *Physical Review Letters*, 95:196102, 2005.

M. Porti, M.-C. Blüm, M. Nafría, and X. Aymerich. Imaging breakdown spots in SiO_2 films and MOS devices with a conductive atomic force microscope. *IEEE Transactions on device and materials reliability*, 2:94-1001, 2002.

M. Porti, M. Nafría, M.-C. Blüm, and X. Aymerich. Atomic force microscope topographical artifacts after the dielectric breakdown of ultrathin SiO_2 films. *Surface Science*, 532-525:727-731, 2003.

M. Porti, M. Nafría, M.-C. Blüm, X. Aymerich, and S. Sadewasser. Breakdown-induced negative charge in ultrathin SiO_2 films measured by atomic force microscopy. *Applied Physics Letters*, 81:3615-3617, 2002.